Technische Universität München

Max Planck-Institut für Biochemie

Abteilung für Molekulare Strukturbiologie

"Structural analysis of co-translational protein transport at native membranes"

Stefan Pfeffer

Vollständiger Abdruck der von der Fakultät für Chemie der Technischen Universität München zur Erlangung des akademischen Grades eines Doktors der Naturwissenschaften genehmigten Dissertation.

Vorsitzender: Univ.-Prof. Dr. Johannes Buchner

Prüfer der Dissertation:

                1. Hon.-Prof. Dr. Wolfgang Baumeister

                2. Univ.-Prof. Dr. Sevil Weinkauf

                3. Univ.-Prof. Dr. Richard Zimmermann,

                 Universität des Saarlandes

Die Dissertation wurde am 26.03.2015 bei der Technischen Universität München eingereicht und durch die Fakultät für Chemie am 13.07.2015 angenommen.

Zusammenfassung

Viele eukaryotische Proteine müssen während ihrer Synthese durch biologische Membranen hindurch transportiert oder in sie integriert werden. Im Zytoplasma werden diese Prozesse durch das in der Membran des Endoplasmatischen Retikulums (ER) lokalisierte Translokon ermöglicht. Das Translokon ist ein Multiproteinkomplex, der sich zusammensetzt aus dem universell konservierten protein-leitenden Kanal Sec61 und weiteren akzessorischen Untereinheiten, die zum Transport und Membraneinbau von entstehenden Proteinen oder deren Maturierung durch kovalente Modifikation beitragen. Aufgrund der fragilen Natur des Translokons waren strukturelle Studien bisher nur für wenige isolierte Bestandteile erfolgreich und die Gesamtstruktur des Translokons, sowie seine molekulare Architektur blieben weitgehend unbekannt. In dieser Arbeit wurden Kryoelektronentomographie und Subtomogramanalyse verwendet, um die Struktur des ribosomengebundenen Translokons in seiner nativen Membranumgebung zu studieren. Durch Verwendung dieses Ansatzes zur Analyse isolierter Vesikel des rauen ERs konnten strukturelle Einblicke in die Interaktion zwischen Ribosom und ER Membran, die Gesamtstruktur des Translokons und die räumliche Organisation membrangebundener Polyribosomen gewonnen werden. Die Manipulation der Translokonzusammensetzung mittels siRNA-vermittelten Gensilencings erlaubte weiterhin eine Lokalisierung des Sec61 Kanals, des Translokon-assoziierten Proteinkomplexes und des Oligosaccharyltransferase-Komplexes in der Struktur des nativen Translokons und ermöglichte eine detaillierte Analyse ihrer räumlichen Anordnung. Unter Verwendung neuester Direktelektronendetektoren war es möglich, die Struktur des nativen Translokons mit einer Auflösung von 9 Å abzubilden und so die Konformation von Sec61 in einem definierten funktionellen Zustand zu beschreiben. Während bisherige mechanistische Modelle für den Sec61-vermittelten Transport und Membraneinbau von Proteinen weitreichende Konformationsänderung von Sec61 annahmen, zeigen unsere Resultate, dass Sec61 im vollständig assemblierten, ribosomengebundenen Translokon Komplex unabhängig vom funktionellen Zustand nur eine einzige Konformation einnimmt.

Während das Translationssystem im Zytoplasma eukaryotischer Zellen strukturell inzwischen sehr detailliert studiert wurde, ist die mitochondriale Translationsmaschinerie erst seit kurzem zugänglich für strukturelle Analyse und deshalb noch nicht gut verstanden. Besonders kontrovers diskutiert wird die Frage, ob mitochondriale Ribosomen an die innere Mitochondrienmembran binden und auf welche Weise sie mit der mitochondrialen Maschinerie für den kotranslationalen Einbau von Membranproteinen interagieren. Unter Verwendung des bereits für die Strukturanalyse des ER Translokons eingesetzten Methodenspektrums, konnte in dieser Arbeit die supramolekulare Organisation der mitochondrialen Translationsmaschinerie und ihre Interaktion mit der inneren Mitochondrienmembran in isolierten Hefemitochondrien studiert werden. Unsere Analyse zeigte, dass mitochondriale Ribosomen entsprechend ihrer Spezialisierung auf die Synthese äußerst hydrophober Membranproteine hauptsächlich in direkter Nähe zur inneren Mitochondrienmembran lokalisiert sind. Sie interagieren mit der Membran auf definierte Weise mittels zweier unterschiedlicher Kontakte, die durch eine lange Schleife der ribosomalen RNA und einen biochemisch etablierten Rezeptor für mitochondriale Ribosomen auf der inneren Membran vermittelt werden. Unsere Resultate zeigen, dass sich die Membranassoziation mitochondrialer Ribosomen zeitgleich mit ihrem Tunnelausgang im Verlauf der Evolution radikal verändert hat.

Diese Arbeit trägt wesentlich zu unserem Verständnis der Struktur und Architektur makromolekularer Maschinen bei, die am kotranslationalen Transport und Membraneinbau von Proteinen an der ER Membran und der inneren Mitochondrienmembran beteiligt sind. Sie demonstriert die Limitationen struktureller Analyse von Membranproteinkomplexen in solubilisierter Form und zeigt eine alternative Methodik auf, die ihre Abbildung in einer natürlichen Membranumgebung und im Kontext ihrer nativen Bindungspartner erlaubt.

Summary

In eukaryotic cells, many proteins have to be translocated across or inserted into biological membranes during their synthesis. In the cytosol, these processes are facilitated by the endoplasmic reticulum (ER) protein translocon, a multi-subunit complex located in the ER membrane. The translocon comprises a universally conserved protein-conducting channel and accessory constituents that assist in protein transport and membrane integration or facilitate maturation of nascent chains by covalent modifications. Due to the fragile nature of the translocon, structural studies have succeeded for only few isolated constituents and the overall structure and molecular architecture of the translocon remain largely elusive. Here, we employed cryoelectron tomography (CET) and subtomogram analysis to study the structure of ribosome-bound translocon complexes in their native membrane environment. By applying this approach to isolated rough ER vesicles, we obtained structural insights into membrane attachment of ribosomes via several previously unknown contact sites, the overall structure of the native translocon, and the specific three-dimensional arrangement of ribosomes on the ER membrane induced by polyribosome formation. Using siRNA mediated gene silencing to manipulate the translocon composition in human cells, we could identify the protein-conducting channel Sec61, the translocon associated protein complex (TRAP) and the oligosaccharyl-transferase complex (OST) in our structure of the native translocon and describe their spatial organization in unprecedented detail. Using latest direct electron detector technology, we were able to refine our structure of the native translocon to subnanometer resolution and determine the conformation of Sec61 at a defined functional state. While previous mechanistic models for peptide translocation and membrane insertion via Sec61 assumed extensive conformational changes of the protein-conducting channel, our results imply, that Sec61 adopts only one major conformation in the fully assembled ribosome-bound translocon complex, independent of its functional state.

While the cytosolic translation system is structurally well characterized for over a decade, the mitochondrial translation machinery has become accessible to structural analysis only very recently and is consequently not well understood, yet. In particular, it is controversial how mitoribosomes interact with the inner mitochondrial membrane and the machinery, necessary for co-translational membrane protein insertion in mitochondria. Thus, applying the same set of methodologies as used for structural analysis of the ER protein translocon, we studied the supramolecular organization of the mitochondrial translation machinery and its association with the inner membrane in isolated mitochondria from yeast. Our study revealed that mitoribosomes are predominantly located in immediate proximity of the inner mitochondrial membrane, in line with their specialization on the synthesis of highly hydrophobic membrane proteins. Mitoribosomes interact with the inner membrane in a defined manner via two distinct contact sites, formed by a long ribosomal RNA expansion segment and a biochemically established mitoribosome receptor on the inner membrane. Our results demonstrate, that concomitant with the remodeling of the mitoribosomal polypeptide exit tunnel, the mode of membrane association has been radically reshaped during evolution.

This work makes a substantial contribution to our understanding of the structure and architecture of macromolecular machineries involved in co-translational protein transport and membrane insertion at the endoplasmic reticulum and the inner mitochondrial membrane. It demonstrates the limitations of analyzing membrane protein complexes in an isolated, detergent-extracted form and advocates structural studies in a native membrane environment and in context of their native interaction partners.

Contents

Preface

My doctoral work resulted in four manuscripts, of which three have been published already as research articles in major peer-reviewed journals [1-3]. Since the four manuscripts together represent the main body of work undertaken in the course of my Ph.D. project, this thesis is written in cumulative style. The first chapter contains an introduction to the biological and methodological background and the current state of research. The second chapter includes the classical "Results" and "Material and methods" sections in form of the original manuscripts. The last chapter features a comprehensive discussion and outlook that integrates the main aspects from all four manuscripts.

1 Introduction

In eukaryotic cells, many proteins have to be translocated across or inserted into biological membranes during their synthesis. The first two chapters contain an introduction to the biological background of co-translational protein transport at the endoplasmic reticulum (section 1.1) and the inner mitochondrial membrane (section 1.2) and describe the current state of research with a focus on structural biology. The fragile nature of transport machineries involved in these processes favors approaches that capture their structures without detergent extraction and in a native membrane environment. Thus, in the third chapter (section 1.3), Cryo electron tomography (CET) is introduced as a methodology that allows obtaining three-dimensional (3D) structural information for a wide range of cryo-preserved specimens and, in combination with advanced image processing techniques, can provide detailed information about the organization and structure of large macromolecular complexes in a native context.

1.1 Co-translational protein transport at the endoplasmic reticulum

1.1.1 Synthesis of secretory and membrane proteins in eukaryotes

In eukaryotic cells, almost all proteins are synthesized by the cytosolic 80S ribosome, a 3-4 MDa RNA-protein complex consisting of two subunits (Fig. 1.1a): the 40S subunit, responsible for binding and decoding of messenger RNA (Fig. 1.1b), and the 60S subunit, harbouring the peptidyl-transferase activity necessary to form peptide bonds and [4] (Fig. 1.1c). Translation of an mRNA can be divided into three phases: initiation, elongation and termination. During translation initiation, the 40S subunit and initiator Methionyl-tRNA form a complex on the 5'-end of an mRNA molecule and scan the mRNA for the starting codon [5]. Binding of the 60S subunit to this complex forms the 80S initiation complex ready for translational elongation. Translational elongation is iteratively repeated for each incorporated amino acid.
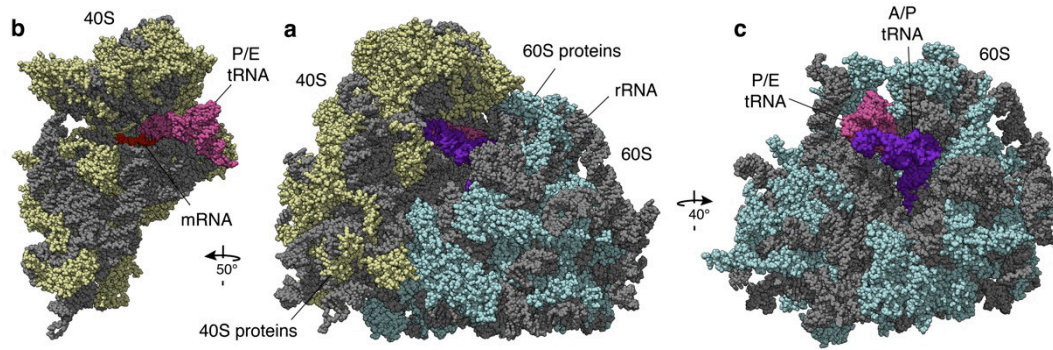
Figure 1.1: Structure of the mammalian 80S ribosome. a, Overall structure visualized using atomic models derived from a single particle cryo-EM reconstruction (PDB 3J7R) [6]. Proteins of the large (blue) and small (yellow) ribosomal subunits, ribosomal RNA (gray), mRNA (red), and tRNA molecules in the A/P (magenta) and P/E (pink) orientations are depicted. **b,** Rotated view on the 40S subunit, depicting interaction between mRNA and the tRNA in P/E orientation. The 60S subunit and A/P tRNA are not shown. **c,** Rotated view on the 60S subunit, depicting how the A/P tRNA reaches down to the peptidyl-transferase centre on the 60S subunit. The 40S subunit and mRNA are not shown.

While the growing polypeptide occupies the ribosomal P-site (Fig. 1.2a), the next aminoacyl-tRNA is brought to the ribosomal A-site by GTP-dependent eukaryotic elongation factor (eEF) 1 (Fig. 1.2b). In case of a complementary base pairing between mRNA and aminoacyl-tRNA, eEF1-bound GTP is hydrolysed and eEF1 dissociates from the ribosomal complex (Fig. 1.2c). In the next step, the peptidyl-transferase activity of the 60S subunit transfers the growing polypeptide chain onto the aminoacyl-tRNA bound in the A-site, elongating the nascent peptide by one amino acid (Fig. 1.2d). Binding and GTP hydrolysis of eEF2 leads to a translocation of the mRNA molecules by exactly one codon (three nucleotides) in 3' direction (Fig. 1.2e). The now vacant tRNA originally positioned in the ribosomal P-site moves to the E-site or dissociates and the elongated peptidyl-tRNA molecule takes over the P-site, clearing the A-site for another round of elongation [7]. The end of a polypeptide chain is coded on the mRNA by a termination codon, which recruits termination factors and leads to hydrolytic release of the polypeptide from the P-site tRNA [8].

3
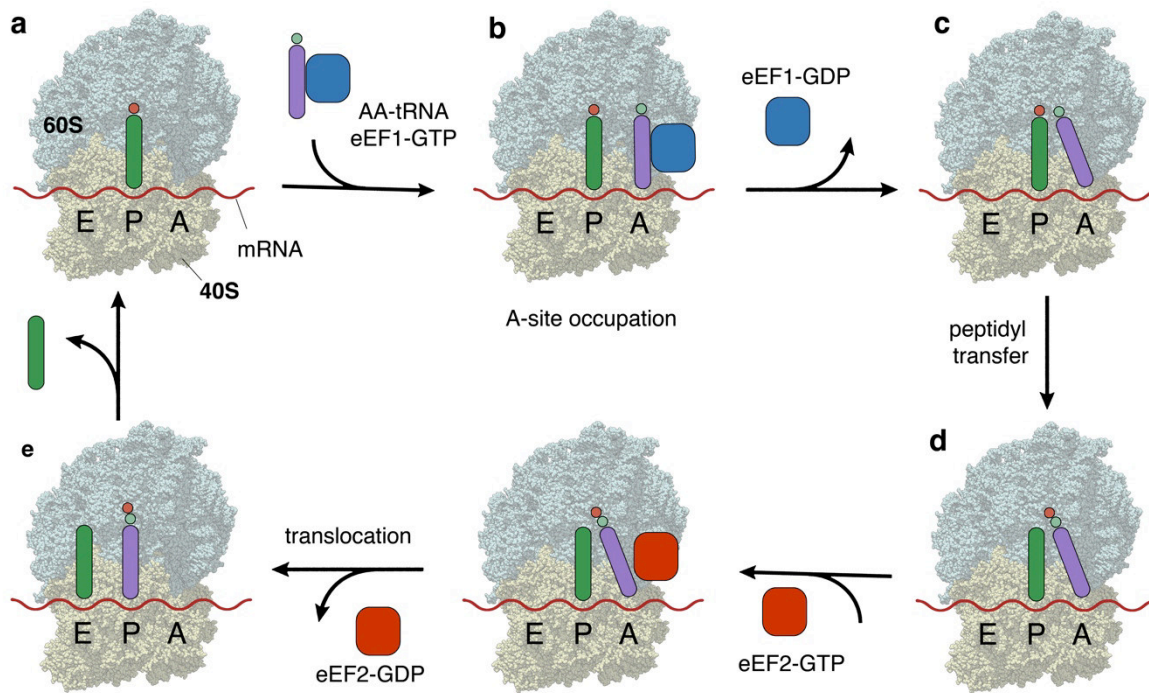
Figure 1.2: Translational elongation cycle in eukaryotes. a, The 40S (yellow) and 60S (blue) subunit of the mammalian ribosome, the mRNA (red) and a peptidyl-tRNA molecule (green) in the ribosomal P-site are depicted. **b,** eEF1 (blue) delivers an aminoacyl-tRNA molecule (magenta) to the ribosomal A-site. **c,d** The A-site tRNA reorients and the growing polypeptide is transferred from the P-site tRNA to the A-site tRNA. **e,** Binding and GTP hydrolysis of eEF2 translocates the mRNA molecule in concert with both tRNAs by one codon. After dissociation of the E-site tRNA, a new round of elongation can start.

For efficient translation, often more than one ribosome initiates on the same mRNA molecule, giving rise to a polyribosome. Due to varying translation speed on different regions of the mRNA [9], ribosomes often come into spatial proximity and form tightly packed macromolecular assemblies with a defined 3D organization in the cytosol and on the endoplasmic reticulum membrane. Polyribosomes were first described using conventional transmission electron microscopy [10-12]. However, lacking 3D information about their defined arrangements, they could not be described in detail until CET was established.
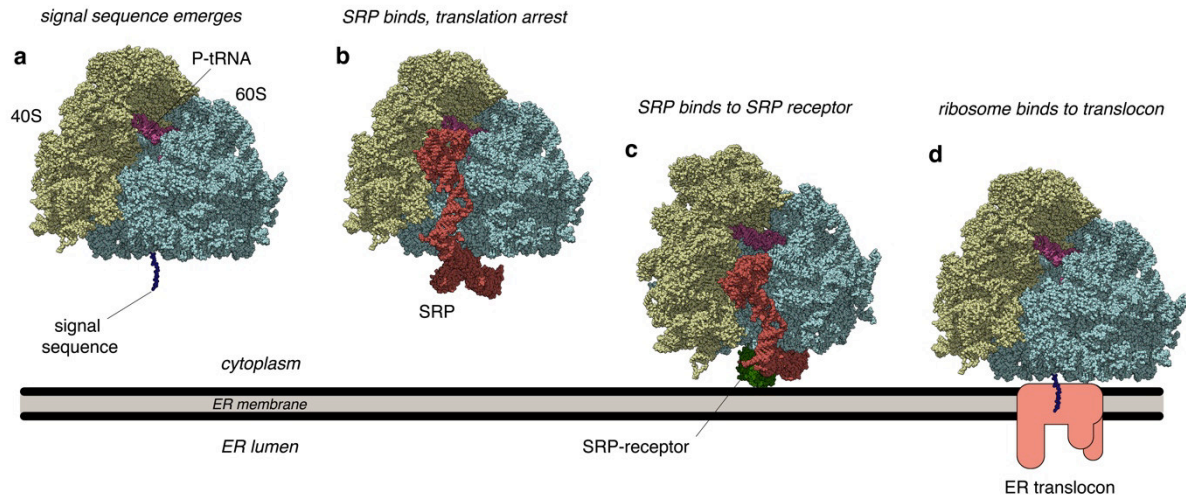
Figure 1.3: Formation of the ribosome translocon complex. a, The 40S (yellow, PDB 3J7R) and 60S (blue, PDB 3J7R) subunit of the mammalian ribosome, the emerging signal sequence (dark blue) and a peptidyl-tRNA molecule (magenta, PDB 3J7R) in the ribosomal P-site are depicted. **b,** SRP (red, PDB 1RY1) binds to the emerging signal sequence and arrests translation. **c,d** SRP binds to the ER-resident SRP-receptor (green, PDB 2GO5) and the RNC complex is transferred to the ER translocon (light red) for transport of the nascent peptide across or insertion into the ER membrane.

The precursors of secretory proteins typically carry an N-terminal hydrophobic signal sequence of 20-30 amino acids in length [13], which commits them to the 'secretory pathway' [14]. As this signal sequence emerges from the ribosomal tunnel exit during translation (Fig. 1.3a), it is bound by the signal recognition particle (SRP), a universally conserved RNA-protein complex abundant in the cytosol (Fig. 1.3b). Binding of SRP to the ribosome nascent chain (RNC) complex slows down protein synthesis and targets the RNC complex to the endoplasmic reticulum [15]. Upon interaction with the ER-resident SRP receptor (Fig. 1.3c), SRP is released into the cytosolic pool and the RNC complex is transferred to the ER translocon [16], a multi-subunit complex located in the ER membrane (Fig 1.3d). Alternatively, synthesis of secretory and membrane proteins can be initiated on ribosomes already bound to the ER translocon, bypassing SRP-dependent recruitment [17].

1.1.2 The translocon core - a protein-conducting channel

The ER translocon is a multi-subunit complex located in the ER membrane. The core of the translocon is formed by the universally conserved protein-conducting channel Sec61, which functions as a dynamic aqueous pore and binds to translating ribosomes for co-translational protein transport. The structure of the prokaryotic Sec61 ortholog, the SecY complex, has been extensively studied by X-ray crystallography [18,19]. Single particle cryo-EM studies have provided high-resolution structures of eukaryotic solubilized and purified ribosome-Sec61 complexes [6,20,21].

Sec61 is a hetero-trimeric complex, consisting of the central Sec61α subunit and two much smaller peripheral subunits Sec61β and Sec61γ (Fig 1.4a). Sec61α establishes contact with the ribosome via two cytosolic loops L5/6 and L7/8 that bind to the ribosome close to the peptide tunnel exit. Based on its structure, Sec61α can be divided into an N- and C-terminal half, each comprising five transmembrane helices with a pseudo two-fold symmetry axis in the membrane plane. The two sets of helices are connected by a short 'hinge' helix (Fig. 1.4b), allowing movement of the N- and C-terminal halves with respect to each other (Fig. 1.4c). A ring of bulky hydrophobic residues and a short 'plug' helix are thought to prevent excessive passive ion flow through the channel. Sec61β and Sec61γ are located at the periphery of the protein-conducting channel and consist of one transmembrane helix, each.

On the basis of the available structural information, a detailed model for protein translocation through a central pore and protein membrane insertion via a lateral gate, formed by two adjacent transmembrane helices of Sec61α, has been proposed [18,21]. Specifically, two global conformations are thought to underlie the two fundamentally distinct functional states of Sec61: (I) in the 'non-inserting state' (idle or translocating a soluble domain), Sec61 is

6
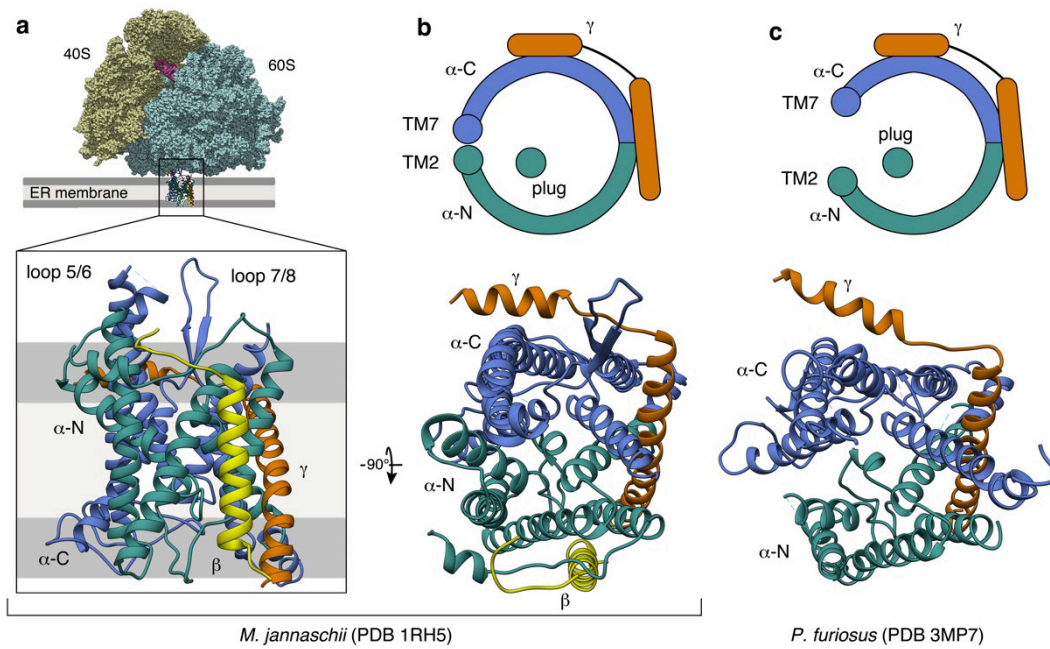
Figure 1.4: X-Ray crystallographic structures of the prokaryotic protein-conducting channel in two different conformations. a, Sec61 binds to the ribosome (PDB 3J7R) via two highly conserved cytosolic loops L5/6 and L7/8 close to the peptide tunnel exit. The N- and C-terminal halves of Sec61α (α-N, α-C), Sec61β (β) and Sec61γ (γ) are indicated. **b,** Sec61 seen from the cytosol with the ER membrane in the paper plane. Sec61 adopts a compact, closed conformation that is represented in the schematic. **c,** Sec61 adopting an open conformation, in which the N- and C-terminal halves of Sec61α have moved with respect to each other, resulting in a gap between transmembrane helices (TM) 2 and 7, as represented in the schematic.

thought to adopt a compact conformation with a closed lateral gate ('closed' conformation) (Fig. 1.5a,b); (II) in the 'inserting state' (integration of a TMH into the membrane), Sec61 is thought to adopt a less compact conformation with an open lateral gate ('open' conformation) (Fig. 1.5c). Recently, structures of the solubilized ribosome-Sec61 complex purified from porcine pancreas were determined for the two non-inserting conditions to unprecedented resolution (3.4 and 3.9 Å resolution, respectively), revealing subtle differences between the idle and translocating states that were not observed in the previous lower resolution studies [6]. In summary, all structural studies focused on the detergent solubilized protein-conducting channel in isolation from all other canonical translocon components to date, but the structure of Sec61 in its native context remained uncharted.
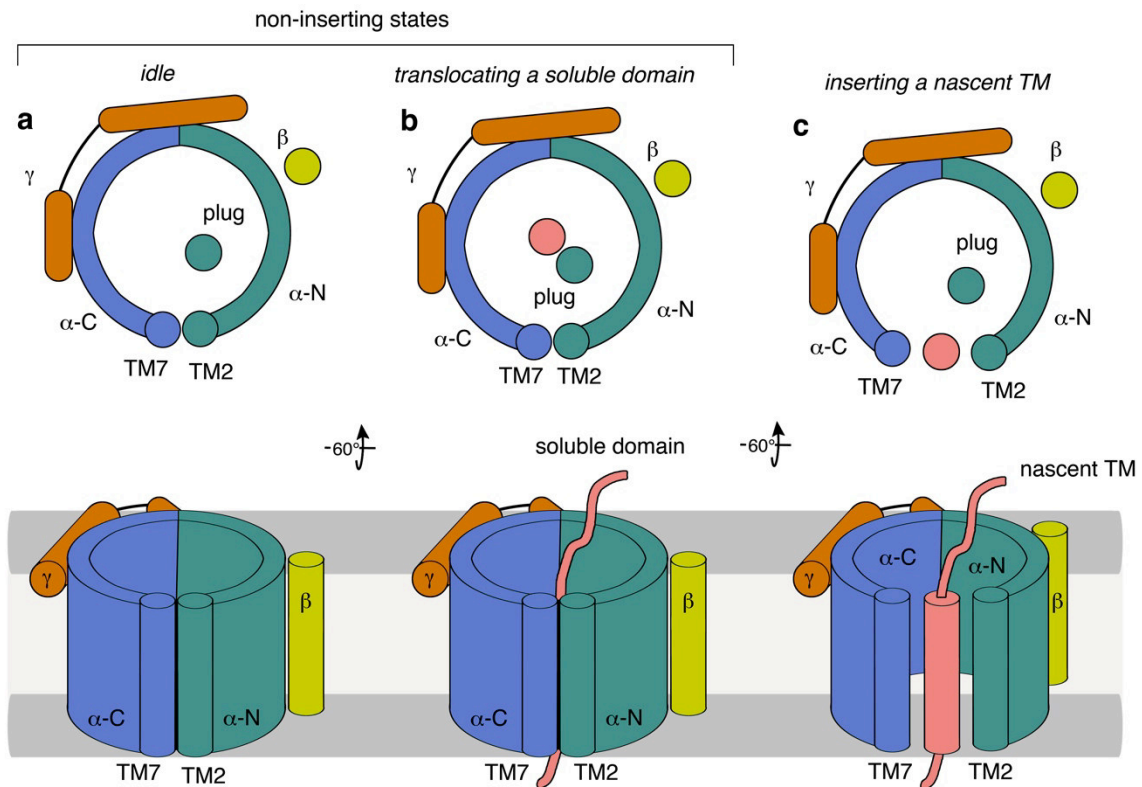
**Figure 1.5: Current model for co-translational protein transport and membrane insertion by Sec61.** Schematic representations of Sec61, seen either from the cytosol (top) or in a view perpendicular to the membrane (bottom). The N- and C-terminal halves of Sec61α (α-N, α-C), Sec61β (β) and Sec61γ (γ) are indicated. In the two non-inserting states (**a,b**), Sec61 adopts a conformation with a close lateral gate between TM2 and TM7. A nascent soluble domain is thought to pass through a central pore of Sec61α (**b**). In the inserting state (**c**), Sec61 adopts a conformation with an open lateral gate, though which a nascent TM is inserted into the membrane. The hydrophilic head groups of the ER membrane phospholipids are shown in grey.

1.1.3 Accessory translocon components

The basic functions of Sec61 are complemented by accessory translocon components, which have been found physically associated with Sec61 using biochemical methods [22-24] and assist in protein transport and membrane integration or facilitate maturation of nascent chains by covalent modifications. It is unclear, however, how transient these accessory translocon components associate with the translocon.

The most prominent examples of nascent chain modifying translocon components are the signal peptidase (SPC) complex [25], cleaving off signal peptides from translocating or translocated proteins, and the oligosaccharyl-transferase (OST) complex, catalyzing co-translational N-glycosylation [26-28], which is one of the most common covalent protein modifications in eukaryotic cells. OST is an elaborate multi-subunit complex integrated into the ER protein translocon [27]. The catalytic OST subunit is present in two paralogous forms, STT3A and B. The structure of a prokaryotic homolog of STT3, which functions as a monomer in the cell, has been solved by X-ray crystallography, revealing how polysaccharides are transferred from their dolichol-carrier to glycosylation substrates (Fig. 1.6). STT3 is joined by at least six accessory subunits of poorly understood function: Ribophorin I (RibI), Ribophorin II (RibII), OST48, DAD1, N33 or IAP, and OST4. The N33/IAP subunits of OST have oxido-reductase activity and are thought to increase the efficiency of glycosylation by slowing down glycoprotein folding via formation of a mixed disulfide with glycosylation substrates [29]. Sequence analysis and proteinase protection assays [30] suggest that all OST subunits are integral membrane proteins and many possess substantial lumenal domains, adding up to nearly 200 kDa [27].

Two other commonly detected components of the translocon are the translocon associated membrane protein (TRAM) and the translocon associated protein complex (TRAP) [24]. Their functions are not well understood, but recent studies suggest that they assist Sec61 in membrane protein insertion [31] and assembly of the correct topology for polytopic membrane proteins [32]. The Hsp40 chaperone Sec63 is thought to associate with the translocon and recruit the lumenal Hsp70 chaperone BiP in a substrate-specific manner [33]. BiP binds to unfolded proteins in the ER lumen and thereby supports Sec61 in the transport of nascent proteins across the membrane in a ratchet-like manner [34].
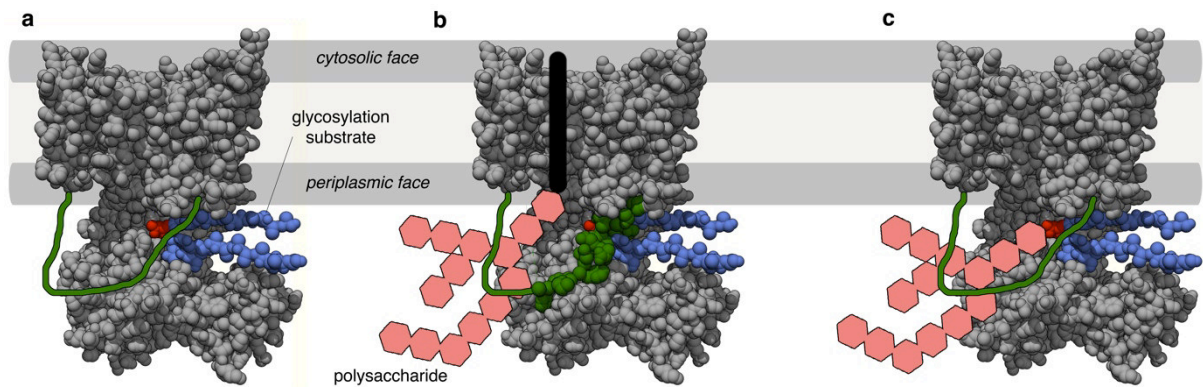
Figure 1.6: Model for protein glycosylation by a prokaryotic oligosaccharyl-transferase. a, X-ray structure of the prokaryotic STT3-homologue PglB (gray, PDB 3RCE) with a bound glycosylation substrate (blue, PDB 3RCE). The acceptor Asparagine is depicted in red. An unordered periplasmic loop of PglB is depicted in green. **b,** The disordered loop becomes partly ordered and positions the glycosylation substrate in the active site for transfer of a polysaccharide moiety (pink) from the lipid carrier (black) to the acceptor Asparagine. **C,** After transfer of the polysaccharide, the glycosylated substrate is released.

Despite their essential functions, structural information on these accessory translocon components and their spatial organization in the native translocon is comparably sparse and often inconclusive, because they are difficult to study by X-ray crystallography and single particle cryo-EM. When solubilized from their native membrane, these components become disordered and often completely dissociate from Sec61, favoring their study in a native context.

1.2   Co-translational protein transport in mitochondria

Mitochondria are essential organelles of eukaryotic cells that produce ATP by aerobic respiration. They possess an outer and inner membrane, separated by the intermembrane space and are further compartmentalized by invaginations of the inner membrane, forming the so-called cristae [35]. The inner mitochondrial membrane encloses the matrix, which houses several copies of the mitochondrial genome. Mitochondria maintained their own genome along with their own translation machinery, for the synthesis of a few highly hydrophobic

membrane proteins that have to be inserted into the inner mitochondrial membrane co-translationally and cannot be productively imported from the cytosol. These membrane proteins form the central reaction centers of the respiratory chain and the ATP synthase complexes [36].

Only recently, a number of high-resolution cryo-EM structures for mammalian and yeast large mitoribosomal subunits [37-40] were published. These structures confirmed that mitoribosomes have significantly diverged from their bacterial counterparts and show high variability between different species (Fig. 1.7a). Mitoribosomes contain a number of mitoribosome-specific proteins. Canonical ribosomal proteins are considerably larger in mitochondria [37], resulting in a significantly increased network of inter-protein interactions, likely to structurally compensate for the loss of rRNA. The divergence of mitoribosomes between different species is exemplified by a completely remodeled pathway of the polypeptide exit tunnel specific for yeast mitoribosomes [37] (Fig. 1.7b) and the integration of a mitochondrial tRNA molecule into the central protuberance to compensate for loss of the 5S rRNA specifically in mammalian mitoribosomes [39,40] (Fig. 1.7c).

Mitoribosomes have specialized in the synthesis of highly hydrophobic membrane proteins that are integrated into the inner mitochondrial membrane during their synthesis by Oxa1, a homolog of the bacterial YidC insertase [41-44]. The oligomeric state of Oxa1 in the native inner mitochondrial membrane is controversial, but recent structural studies of the YidC insertase using X-ray crystallography and cryo-EM single particle analysis strongly suggest that Oxa1 is functional as a monomer [45-47]. For efficient integration of membrane proteins, Oxa1 cooperates with Mba1, a membrane-associated mitochondrial protein, which has been characterized as a mitoribosome receptor on the inner membrane [48,49]. Biochemical studies

suggest that the mitoribosome remains associated to the inner membrane even in mutants lacking both Oxa1 and Mba1, indicating the presence of additional, so far unidentified membrane tethers [49,50]. Since the mitoribosomes used in previous single particle cryo-EM experiments were recovered from salt-washed detergent extracts, membrane-binding sites of the mitoribosome remained hypothetical. Based on earlier cryo-EM studies it was speculated that the mitoribosome might be partially embedded into the lipid bilayer [51], whereas the recent high-resolution studies led to different hypotheses: the mitoribosome might contact the inner membrane either via a mitoribosome-specific protuberance of the large subunit [37] or the mitoribosome receptor protein Mba1 [38]. In light of these numerous hypotheses, it proves mandatory to use an alternative approach that allows studying mitoribosomes in intact mitochondria in order to obtain a faithful description of how the mitochondrial translation machinery associates with the inner membrane for co-translational protein insertion.
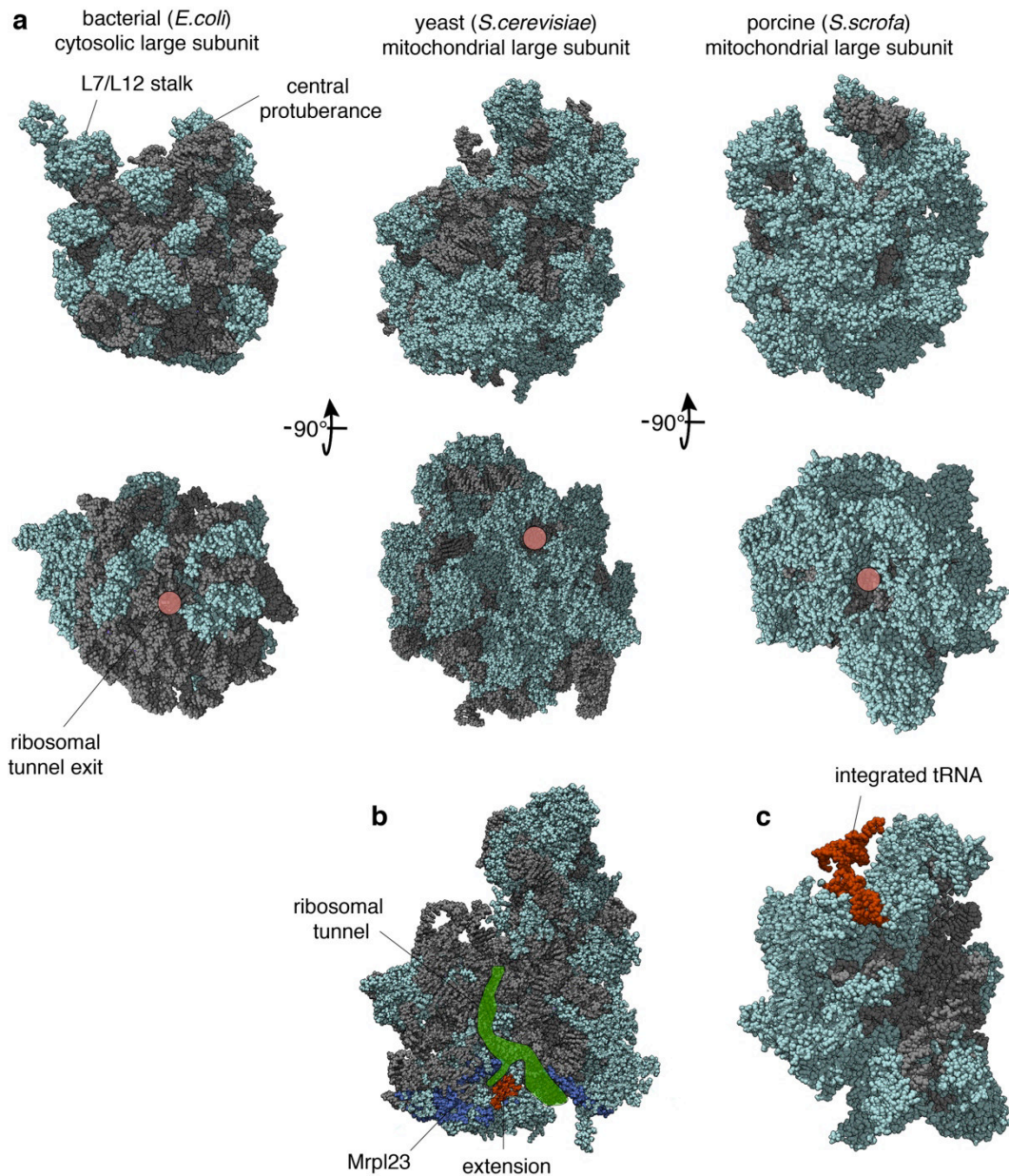
Figure 1.7: Structural divergence of ribosomal large subunits from mitochondria. a, Comparison of atomic models for the large ribosomal subunit from *E.coli* cytosol and *S.cerevisiae* / *S.scrofa* mitochondria. The ribosomal large subunits were aligned to each other according to their rRNA. Ribosomal proteins (blue), rRNA (gray) and the position of the ribosomal tunnel exit (red) are depicted. **b,** The ribosomal tunnel (green) has been remodelled in the yeast mitoribosome, because an extension (red) of Mrpl23 (dark blue) blocks the canonical ribosomal tunnel exit. The large subunit was cut to allow for a better view on the ribosomal tunnel. **c,** A mitochondrial tRNA molecule (red) has been integrated into the central protuberance of the mammalian mitoribosome to compensate for loss of the 5S rRNA. The central protuberance was cut to allow for a better view on the tRNA.

13

1.3 Structural analysis of native specimens using CET

1.3.1 Basics of CET

CET can provide a 3D view on the structure and organization of a wide range of cryo-preserved specimens under near-to-native conditions [52]. It is applicable to a variety of cell-free translation systems [53-57], isolated cellular organelles [58-64] and even intact cells [65-68] that do not exceed 0.5 μm in thickness. In combination with Focused Ion Beam (FIB) milling techniques and correlative light microscopy, even structures deeply embedded in much thicker cells can be targeted [69-72]. In combination with advanced image processing methods, the location, orientation and structure of larger macromolecular complexes can be mined from tomographic data. Specific macromolecular complexes that have been analysed in their native context using CET include ribosomal complexes [53-57], the nuclear pore complex [64,73], the ATP-Synthase [58-61] and microtubules [74-76]. CET often complements structural biology methods aiming to acquire high-resolution structures of isolated components (X-ray crystallography, cryo-EM single particle analysis) and puts them into a cellular context. However, with the recent advances in direct electron detector technology [77] and more advanced data processing software [78,79], CET now slowly advances into resolution regimes that were typically only accessible to cryo-EM single particle analysis [80-82].

In CET, two-dimensional projections of the specimen under scrutiny are used to reconstruct an approximation of its 3D volume (Fig. 1.8a). By tilting the specimen along an axis perpendicular to the electron beam, the necessary projections along different angles (under otherwise constant acquisition conditions) can be obtained. Since small lateral motions of the object during data acquisition are unavoidable, the projections have to be aligned to a common coordinate system prior to reconstruction, most commonly with the help of fiducial markers [83].

14
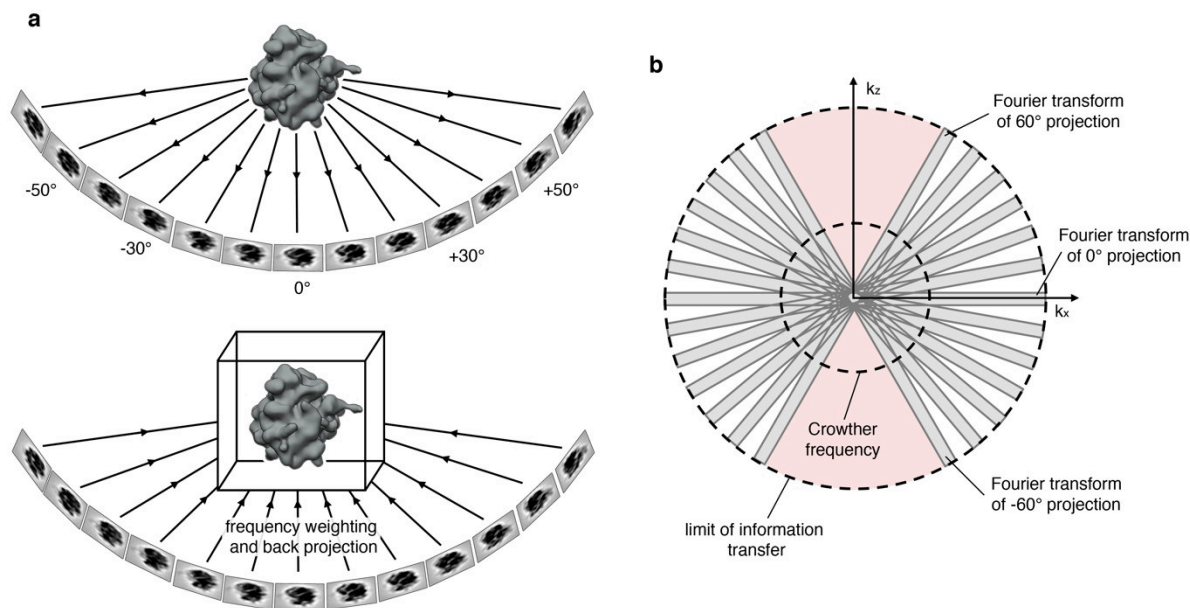
Figure 1.8: Principle of tomography. a, Projections of the specimen are acquired along different tilt angles under otherwise constant acquisition conditions (top). After frequency weighting and alignment, the tilt images are computationally back projected into a 3D volume (bottom). **b,** Each projection corresponds to a thin slice (gray) in Fourier space. Spatial information is sampled continuously up to the Crowther frequency. The restricted tilt range results in a wedge of missing information in Fourier space (red).

The reconstruction process can be explained best in Fourier space: the Fourier transform of each projection corresponds to a slice with constant thickness in Fourier space (Fig. 1.8b). Acquiring projections with a regular tilt increment, the 3D information of the specimen is sampled continuously up to a certain spatial frequency ('Crowther criterion') [84]. For lower frequencies, slices of the acquired projections overlap in Fourier space and simple summation would artificially enhance the signal. To correct for this signal enhancement, spatial frequencies of the projections are weighted accordingly in Fourier space [85]. Typically, the accessible tilting range for tomogram acquisition is restricted to -60° to 60° by the microscope stage and the thickness of the sample. The missing projections for the rest of the tilting range result in a 'missing wedge' in Fourier space and thus an anisotropic resolution and a slight elongation of the object in the direction of the electron beam in real space. According to the

15

above projection-slice theorem a 3D reconstruction by direct interpolation of the measured Fourier components onto the Fourier space Cartesian grid of the 3D volume would be most straightforward. However, interpolation in real-space tends to be easier to implement and less memory intensive making weighted back projection the most common reconstruction method in CET.

1.3.2   Acquisition of CET data

Acquisition of tomographic data is a considerable challenge for vitrified samples: it is necessary to find a balance between the high dose sensitivity of vitrified samples and the acquisition of a whole tomogram consisting of 60 projection images or more. By automation of all necessary steps, the electron dose applied to a specimen can be reduced to a minimum ('low dose' acquisition). Aside from acquiring the projections used for reconstructing the tomogram, various parameters have to be monitored and adjusted for each tilt angle [86]. For each tilting step, it is necessary to compensate for the specimen drift and changes in defocus. To minimize exposure of the object of interest, these processes are performed on a spot located a few micrometres away along the tilt axis (Fig. 1.9). The standard procedure for low dose data acquisition consists of four steps: tilt the sample; compensate for specimen drift by acquiring a tracking image and correlating it with the previous one; adjusting the defocus by acquiring and correlating a pair of projections with different beam tilt; acquisition of the projection image for tomogram reconstruction. Typically, the electron dose does not exceed 80-120 $e^-/Å^2$ for the whole tomogram to avoid specimen alteration due to dose damage.
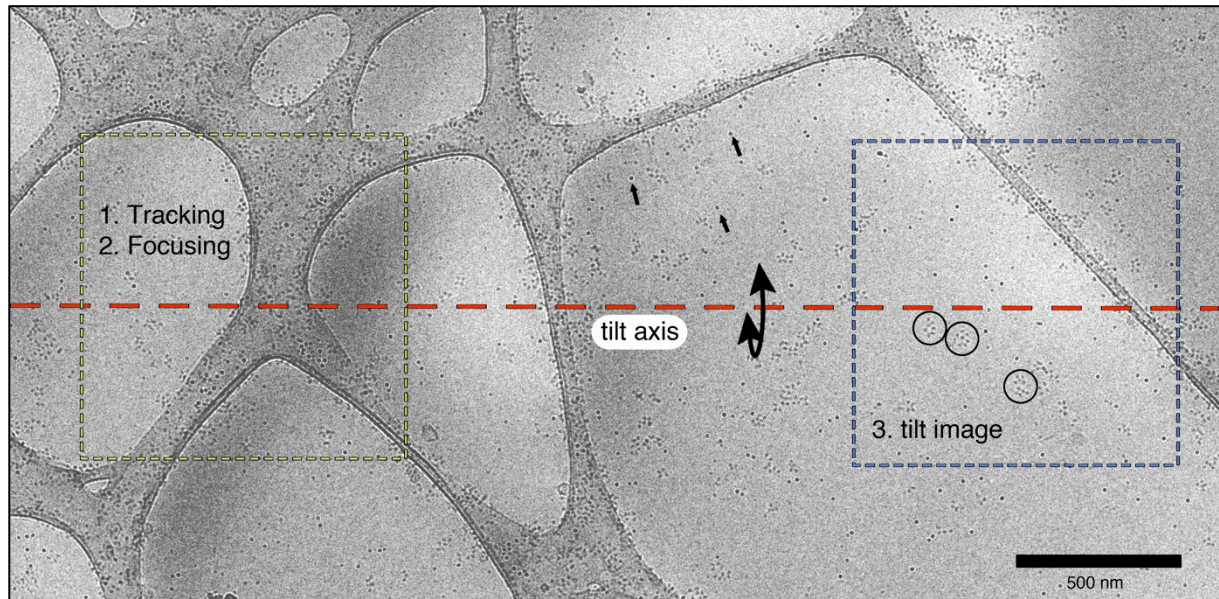
Figure 1.9: Setup for low dose acquisition of a cryo electron tomogram. For acquisition of a tomogram under low dose conditions, two acquisition areas are defined in sufficient distance from each other along the tilt axis (red): a record area (blue), where the tilt images for tomogram reconstruction are acquired, and a tracking and focus area (yellow), where lateral movement of the sample during tilting is compensated (tracking) and nominal defocus is set (focusing). Exemplary yeast polyribosomes (black circles) and gold fiducials (black arrows) for tilt series alignment are highlighted. The scale bar corresponds to 500 nm.

For structural studies using subtomogram analysis (section 1.3.3), acquisition of a high number of tomograms is often a prerequisite. Automation for the comparably simple procedures involved in data acquisition for single particle cryo-EM has been established more than a decade ago in a variety of software packages [87]. They include cross-correlation based functions for automatic tracking and feature centring, focusing and acquisition of electron micrographs. The more complex procedures involved in acquiring tomographic data ('low dose scheme') require an extension of the basic functions used for single particle analysis and in particular a very stable microscope. Using dedicated software packages (Serial EM [88], FEI tomography, UCSF tomo [89]) in combination with modern electron microscopic equipment, automatic batch acquisition of tomograms is possible nowadays and yields 40 cryo-tomograms and more in one day.

1.3.3 Structural biology *in situ* using subtomogram analysis

Template matching

Although the signal-to-noise ratio is typically very small in CET, it is possible to locate macromolecular structures of 500 kDa or more with acceptable specificity using a cross-correlation based pattern recognition algorithm ('template matching') [90]. For optimal performance of the algorithm, the provided reference structure has to be adapted to the acquisition conditions, in particular the average defocus modulating the phase contrast and the information loss due to the missing wedge. The pattern recognition algorithm provides a measure of similarity between the reference structure and the subvolume of the tomogram. For that purpose, the reference structure is shifted throughout the tomogram in all three spatial directions pixel by pixel. By assigning the determined cross-correlation coefficient to the respective central voxel in the tomographic subvolume, an initial correlation volume is created. Since the macromolecular complexes of interest can be oriented arbitrarily in the tomogram, the pixel-wise cross correlation is determined with a set orientations for the reference structure, sampling its orientation space and only the highest cross correlation coefficient is retained for each voxel (Fig. 1.10a).

From the resulting 3D correlation volume, a list of peaks can be extracted from the cross correlation function, indicating positions of candidates for the macromolecular complex of interest [90]. Mostly due to the low signal-to-noise ratio in the data, high cross correlation values are not exclusively obtained for the macromolecular complex of interest, but in certain cases also for other structures ('false positives'). To distinguish between true and false positive peaks of the cross correlation function, a variety of methods is available [90]. A straightforward way of assessing the identity of a cross correlation peak is to manually inspect the corresponding position in the tomogram having been queried. Another option for distinguishing true and false positive
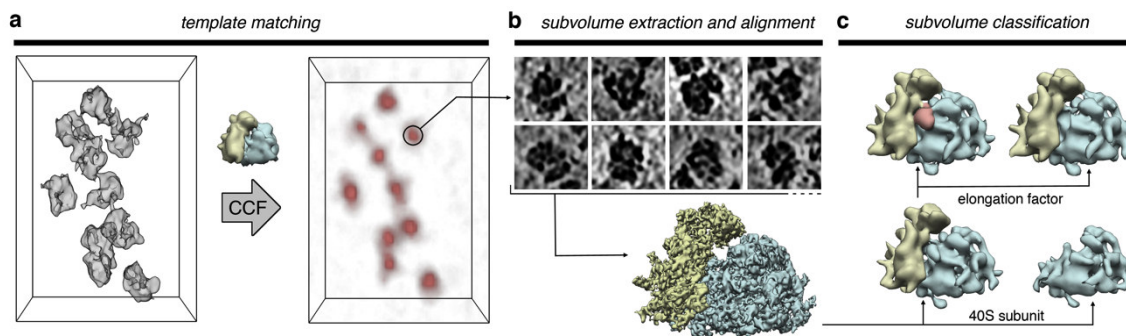
Figure 1.10: Typical workflow for subtomogram analysis. a, Localization of ribosomes in a tomogram (left) by template matching. Peaks of the cross correlation function (red, right) correspond to putative ribosome positions. **b,** Subvolumes (top) are extracted for peaks of the cross correlation function and iteratively aligned to obtain a higher resolution subtomogram average (bottom). **c,** By several rounds of classification, structural and conformational heterogeneity of the sample can be disentangled. As an example, enrichment of subtomograms depicting fully assembled 80S ribosomes with an elongation factor (red) bound to the stalk base is shown.

peaks is to repeat cross-correlation based pattern recognition with a mirrored reference structure. For false positive peaks, cross-correlation coefficients for the right- and wrong-handed reference are typically similar. In contrast, in case of a true positive peak, a much higher correlation coefficient can be expected for the right-handed reference structure. Finally, classification approaches of subvolumes extracted from the tomogram at the corresponding positions is a vey powerful tool to distinguish true and false positive peaks, in particular, if the subvolumes can be classified according to features that are not included in the reference structure.

Subtomogram alignment

By iterative alignment and averaging of subtomograms, depicting the same macromolecular complex, the signal-to-noise ratio and resolution of structural information can be increased (Fig. 1.10b) [91]. The basic principle for iterative subtomogram alignment is to sample different rotations and translations of subtomograms in order to maximize a score, which is based on cross correlation with a reference constrained to commonly sampled regions in Fourier space

19

('constrained cross correlation') [92]. Taking into consideration the newly determined rotations and translations, subtomograms are averaged and the resulting structure is used as a reference for the next round of alignment. This procedure, which is a quasi-expectation maximization algorithm, is repeated until rotations and translations of subtomograms have converged. In order to reduce the risk of aligning to noise ('over fitting') or getting caught in local minima during the alignment, an adaptive bandpass filter can be applied to the reference. This bandpass filter is set according to the resolution determined by Fourier Shell Correlation for the subtomogram average originating from the previous iteration [79].

Typically, translational search is carried out in Fourier space, while rotational search can be performed either in real space ('real space alignment') [79] or using spherical harmonics ('fast rotational matching alignment') [78]. Since rotational search using spherical harmonics is orders of magnitude faster than in real space, it provides the unique opportunity to sample rotations globally in a sensible amount of time, while in real space, rotational search is usually focused around a predetermined starting angle (e.g. from template matching). Sampling rotations globally allows a reference-free alignment approach, in which subtomograms are initially aligned to a featureless sphere, instead of an external reference structure. This minimizes template bias during the subtomogram alignment and allows determining the structure of unknown macromolecular complexes without using a reference. A way to further reduce the influence of noise on subtomogram alignment is to split the dataset into two halves that are processed completely independently from each other ('gold standard alignment') [93,94]. By determining the adaptive bandpass filter that is applied to the reference for alignment by Fourier Shell Correlation of the two completely independent halfsets of the data, resolution can be assessed without contribution of artificially correlated noise.

Classification of subtomograms

Classification approaches can be used to disentangle compositional and conformational heterogeneity of the macromolecular complex of interest (Fig. 1.10c). However, the incomplete spatial information originating from the missing wedge, the low signal-to-noise ratio, the unknown number of classes and the often-unbalanced class occupation in tomographic data make a reliable classification of subtomograms challenging. Several approaches have been proposed. For classification by constrained principal-component analysis (CPCA), a matrix of constrained correlation coefficients is computed for all pairs of subtomograms and subsequently analysed by principal-component analysis (PCA) and k-means clustering [95,96]. While this approach is computationally very expensive and only applicable to medium-sized datasets (< 10.000 subtomograms), it allows classification without bias introduced by reference structures. In order to recover also small populations of structurally or conformationally distinct macromolecular complexes, the number of output classes typically strongly oversamples the number of expected distinct classes in the data. Redundant classes can then be merged to reduce the number of classes and increase the signal-to-noise ratio of the individual structures.

CTF correction of tilted projections

A prerequisite for the determination of high-resolution cryo-EM structures is correction of phase reversals in contrast introduced by the contrast transfer function (CTF). The CTF modulates both phase and amplitude of contrast as a function of spatial frequency and is determined by acquisition parameters (mostly defocus and acceleration voltage) and properties of the electron microscope (lens aberration and beam coherence). While CTF correction is well established for the non-tilted, high-dose projections obtained in cryo-EM single particle analysis, CTF correction in CET is much more problematic. On the one hand, the very low electron dose spent on each tilt image significantly restricts the accuracy of

defocus determination. On the other hand, tilting of the sample results in a linear defocus gradient perpendicular to the tilt axis and thus additionally restricts the area of the tilt image usable for CTF determination. As a consequence, precise defocus determination on single projection images was impossible for tomographic data acquired on a regular CCD camera and only the CTF averaged over the whole tilt series could be determined. As defocus typically varies significantly between consecutive tilt images, an average CTF is very inaccurate and thus restricts attainable resolution. In contrast, with the much more sensitive direct electron detectors, signal on even the high-tilt images is sufficient to reliably determine the applied defocus for every projection independently and thus obtain a much more accurate CTF correction of the data.

CTF determination is typically performed by means of periodogram averaging [97], a procedure in which each tilt image is subdivided into tiles, for which power spectra are calculated and averaged. Defocus values are then determined from the averaged power spectrum by cross correlation with a set of theoretical CTF spectra. For CTF correction, the tilt image is again subdivided into small tiles, which are each corrected for a defocus value calculated according to a geometrical model based on the defocus value of the tilt image, the respective tile's distance to the tilt axis and the tilt angle [98].

1.3.4 Extracting supramolecular structure information from CET data

In general, cryoelectron tomograms of vitrified samples represent a 3D snapshot of the native structures and interactions of all imaged macromolecules. Thus, they contain data beyond plain structural information of single macromolecular complexes and allow a detailed dissection of 3D distribution and arrangement of these complexes with respect to each other and additional cellular structures.

The relative positioning and orientation of different copies of a macromolecule was used for an analysis of the supramolecular organization of ribosomes revealing the compact organization of bacterial and eukaryotic cytosolic polyribosomes [53,65]. In these studies, neighboring ribosomes exhibit preferred arrangements, resulting in pseudoplanar or pseudohelical organizations (Fig. 1.11a). While the transcript is sequestered on the inside of the polyribosome, polypeptide exit sites of individual ribosomes are well separated and face the cytosol, presumably to limit aggregation of nascent peptides and promote productive folding. Another specific macromolecular arrangement that has been structurally characterized using CET is the 100S ribosome pair that transiently forms in bacterial cells under nutritional stress [66]. The 3D configuration of these ribosome pairs is well preserved and results in close contact between the small ribosomal subunits (Fig. 1.11b). In a recent study using CET, the chloroplast morphology of a green algae has been analysed, revealing hexagonally packed RuBisCO complexes within the pyrenoid [69], the site of light independent carbon fixation. Finally, the arrangement of mitochondrial ATP synthases in long double rows along the inner mitochondrial membrane was described using CET (Fig 1.11c) [60].
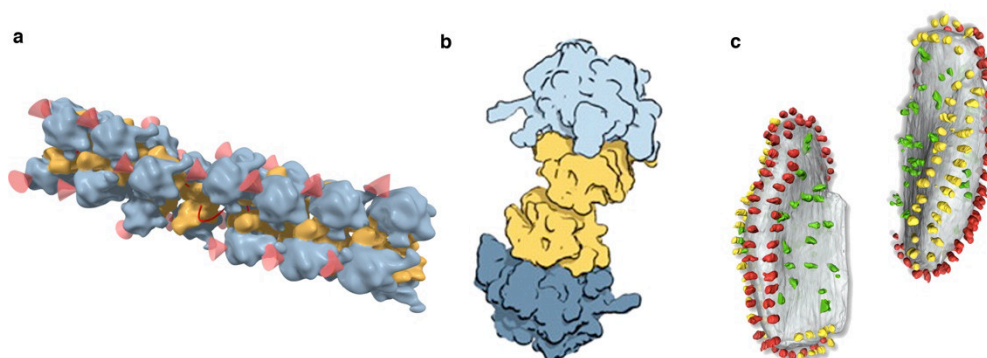
Figure 1.11: Supramolecular assemblies analysed using CET. a, Pseudohelical organization of bacterial cytosolic polyribosomes. The small (yellow) and large subunits (blue) of neighbouring ribosomes and the position of the peptide tunnel exit (red cones) are depicted (adapted from [53]). **b,** 3D configuration of 100S ribosome pairs. The small (yellow) and large subunits (light and dark blue) of two neighbouring ribosomes are depicted (adapted from [66]). **c,** Double row assemblies of ATP-synthase dimers (yellow, red) on the inner mitochondrial membrane (adapted from [61]).

1.4   Scope of this work

The fragile nature of transport machineries involved in co-translational protein translocation, membrane insertion and maturation at the ER and the inner mitochondrial membrane has hampered their structural study substantially. Consequently, this work aims to shed light on the structure and molecular architecture of these co-translational transport machineries without detergent extraction and in their native membrane environment using CET and advanced image-processing techniques.

Particular questions to be addressed are: What is the overall structure of the ER protein translocon and how do ribosomes interact with it? Which translocon components are stably associated to the core translocon and how are they spatially organized? Is there compositional heterogeneity? Do current mechanistic models for protein transport and membrane insertion via Sec61 faithfully describe the situation *in situ*? How is the mitochondrial translation machinery organized in general and do mitoribosomes directly bind to the inner membrane? Do membrane-associated polyribosomes on the ER and the inner mitochondrial membrane adopt specific topologies?

2   Results

2.1   Structure and 3D arrangement of ER membrane-associated ribosomes

This article was published in 2012 in Structure (Issue 20(9), pages 1508-18). The supplemental material is attached at the end of the article (pages 37-49).

Summary

In this article, we used CET and subtomogram analysis to provide a three-dimensional reconstruction of 80S ribosomes attached to functional canine pancreatic ER microsomes *in situ*. In the resulting subtomogram average at 31 Å resolution, we observed membrane attachment of ribosomes via previously unknown contact sites, including a long ribosomal RNA expansion segment, and distinguished several membrane-embedded and lumenal complexes, including Sec61, TRAP and another large complex that was identified as the OST complex in following studies (section 2.2). Most membrane-associated ribosomes observed in our tomograms adopted a preferred three-dimensional arrangement that is likely specific for membrane-bound polyribosomes and may explain the high translation efficiency of ER-associated ribosomes compared to their cytosolic counterparts. In summary, this study allowed us to obtain first structural insights into membrane attachment of ribosomes, the molecular architecture of the ER translocon, and polyribosome formation on the ER membrane

Contribution

For this article, I carried out polyribosome profiling using sucrose gradient centrifugation, functional assays using a cell-free system, grid preparation for electron microscopy, acquisition of CET data and the complete workflow for data processing and map interpretation. I wrote major parts of the manuscript and prepared most of the figures.

Structure and 3D Arrangement of Endoplasmic Reticulum Membrane-Associated Ribosomes

Stefan Pfeffer,[1] Florian Brandt,[1] Thomas Hrabe,[1] Sven Lang,[2] Matthias Eibauer,[1] Richard Zimmermann,[2] and Friedrich Förster[1,*]
[1]Department of Molecular Structural Biology, Max-Planck Institute of Biochemistry, D-82152 Martinsried, Germany
[2]Medical Biochemistry and Molecular Biology, Saarland University, D-66421 Homburg, Germany
*Correspondence: foerster@biochem.mpg.de
http://dx.doi.org/10.1016/j.str.2012.06.010

SUMMARY

In eukaryotic cells, cotranslational protein translocation across the endoplasmic reticulum (ER) membrane requires an elaborate macromolecular machinery. While structural details of ribosomes bound to purified and solubilized constituents of the translocon have been elucidated in recent years, little structural knowledge of ribosomes bound to the complete ER protein translocation machinery in a native membrane environment exists. Here, we used cryoelectron tomography to provide a three-dimensional reconstruction of 80S ribosomes attached to functional canine pancreatic ER microsomes in situ. In the resulting subtomogram average at 31 Å resolution, we observe direct contact of ribosomal expansion segment ES27L and the membrane and distinguish several membrane-embedded and lumenal complexes, including Sec61, the TRAP complex and another large complex protruding 90 Å into the lumen. Membrane-associated ribosomes adopt a preferred three-dimensional arrangement that is likely specific for ER-associated polyribosomes and may explain the high translation efficiency of ER-associated ribosomes compared to their cytosolic counterparts.

INTRODUCTION

The 80S ribosome, a 3.6 MDa riboprotein-complex in mammals, translates messenger RNA (mRNA) to polypeptides (Armache et al., 2010a, 2010b; Ben-Shem et al., 2010; Rabl et al., 2011). It is composed of the large 60S subunit (approximately 50 proteins and three rRNA molecules) and the small 40S subunit (approximately 30 proteins and one rRNA molecule). Compared to prokaryotic ribosomes, the ribosomal RNA (rRNA) of eukaryotic ribosomes contains various insertions, referred to as expansion segments (ESs) (Gray and Schnare, 1990). To date, no function has been assigned to any of the ESs. However, ES27 of the large subunit rRNA (ES27L), one of the largest insertions, has been shown to be essential (Sweeney et al., 1994).

In mammalian cells, ribosomes that synthesize proteins of the secretory pathway are typically associated with the rough endoplasmic reticulum (ER), where most nascent chains are cotranslationally translocated across the ER membrane through the heterotrimeric Sec61-translocation channel (Blobel and Dobberstein, 1975a, 1975b; Görlich and Rapoport, 1993). During translocation, nascent transmembrane helices are proposed to be inserted into the ER membrane through a lateral gate formed by two transmembrane helices of the Sec61α subunit (Van den Berg et al., 2004). Several additional proteins are known to be associated with the Sec61 translocon. The translocon-associated protein (TRAP) complex is a commonly detected component of the translocation complex and binds stoichiometrically to Sec61 in vitro (Hartmann et al., 1993; Ménétret et al., 2008). TRAP is a heterotetrameric protein complex that is required for efficient translocation of various proteins, but its precise function and mechanism are not known. Tightly associated to Sec61 and essential for processing of translocated proteins are the heterooctameric oligosaccharyl-transferase (OST), which mediates asparagine-linked glycosylation of nascent proteins (Kelleher and Gilmore, 2006; Potter and Nicchitta, 2002) and the heteropentameric signal-peptidase (SP), which cleaves the signal sequence from translocated proteins (Evans et al., 1986). The Hsp40 chaperones Sec63 and ERj1 are integral membrane proteins that are associated to the translocon and recruit the lumenal Hsp70 chaperone BiP. ERj1 presumably regulates translation by binding to the universal adaptor site at the ribosomal peptide exit in a BiP-dependent manner (Dudek et al., 2005). Sec63 forms a complex with Sec62 and both proteins are stoichiometrically bound to Sec61 in canine pancreatic rough microsomes, i.e., vesicles that were derived from the rough ER (Tyedmers et al., 2000). Moreover, the translocon-associated membrane protein (TRAM) is part of the translocation complex (Görlich et al., 1992). It is proposed to support insertion of electrostatically nonoptimal transmembrane helices into the ER membrane (Saurí et al., 2007).

To date, most structural studies of ribosomes focused on isolated soluble or solubilized ribosomes, i.e., on ribosomes that are not associated to membranes and not engaged in polyribosomes. Recently, the structure of the wheat germ 80S ribosome was resolved to 5.5 Å by cryo-EM single-particle analysis (Armache et al., 2010a, 2010b) and X-ray crystallography revealed the structures of the yeast 80S ribosome to 3.0 Å (Ben-Shem et al., 2011) and the small (Rabl et al., 2011) and large
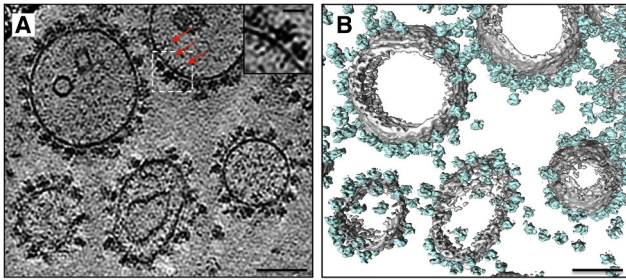
Figure 1. Cryoelectron Tomograms of Rough ER-Derived Microsomes

(A) Slice (thickness 1.88 nm) through a representative tomogram, filtered to 7 nm resolution. The imaged vesicles are densely populated with membrane-bound ribosomes. Inside the ER lumen, elongated membrane-associated electron densities are resolved (red arrows), which colocalize with the membrane binding sites of ER-associated ribosomes. The insert shows a magnified and rotated region of the 3D reconstruction (marked by dashed frame). Scale bars in the image and the magnified region correspond to 100 and 25 nm, respectively.

(B) Isosurface representation of the segmented volume. The microsomal membrane is depicted in gray and localized ribosomes are depicted in cyan. Scale bar correspond to 100 nm.

See also Figure S1 for biochemical and functional characterization of the imaged microsomes.

(Klinge et al., 2011) subunits of the *Tetrahymena thermophila* ribosome to 3.9 and 3.5 Å, respectively. As a result, atomic models for more than 90% of all known ribosomal proteins and rRNA molecules exist for these species. In addition, high-resolution single-particle reconstructions of ribosome-nascent chain complexes (RNCs) bound to solubilized Sec61 led to an atomic model of the heterotrimeric complex in its active and idle state (Becker et al., 2009). Importantly, the nascent chain was resolved in a previously hypothesized intramolecular channel, which suggested that only a single Sec61 complex is required for translocation in the reconstituted system. Moreover, a cryo-EM single-particle reconstruction of the reconstituted solubilized 80S-Sec61-TRAP complex revealed the low-resolution density of TRAP in this complex (Ménétret et al., 2008). Our structural knowledge of the native ER translocation machinery, however, is comparably sparse because membrane-proteins, let alone functional, ribosome-bound translocation complexes are difficult to study by single-particle analysis and/or crystallographic methods. Thus, no detailed structural information of translating 80S ribosomes bound to the entire ER translocation machinery in its native membrane environment does yet exist.

Cryoelectron tomography (CET) has emerged as a method for structural analysis of macromolecular complexes under physiological conditions, e.g., in whole cells or lysates (Lucić et al., 2005). In cryoelectron tomograms large macromolecular complexes such as ribosomes can be distinguished. Their individual positions and orientations can be determined accurately based on structural templates ("template matching") (Frangakis et al., 2002). Moreover, medium-resolution structures of specific complexes can be obtained by averaging subtomograms containing the macromolecule of interest (Bartesaghi and Subramaniam, 2009; Förster and Hegerl, 2007). CET studies have shown that ribosomes adopt distinct topologies in cytosolic

polyribosomes in vitro (Brandt et al., 2009) and in vivo (Brandt et al., 2010). In the observed "pseudohelical" and "pseudoplanar" arrangements, the exposure of mRNA to the cytosol is minimized by positioning the mRNA entry and exit sites of adjacent ribosomes in close proximity. Moreover, the different tunnel exit sites of adjacent ribosomes are distant from each other, presumably to avoid interference of nascent peptides during folding. Notably, none of the arrangements observed for cytosolic polyribosomes is compatible with membrane-association of polyribosomes because the peptide exits do not point into the same direction, as would be required for co-translational insertion of peptides into the approximately planar ER membrane.

Here, we used CET to provide a 3D reconstruction of 80S ribosomes attached to rough ER microsomes in situ. These studies allowed us to provide structural insights into membrane attachment of ribosomes, the molecular architecture of the ER translocation machinery, and polyribosome formation on membranes.

RESULTS

Structure of the ER-Associated Ribosome in Its Native Membrane Environment

Prior to CET, isolated rough microsomes were characterized by western blotting. Typical ER membrane proteins and complexes (Sec61, Sec62, Sec63, TRAM, TRAP, OST, SP, ERj1, SRP receptor) and ER-lumenal proteins (Grp170, Grp94, Grp78 [BiP], PDI) are present in the preparation (Figure S1A available online), which is in agreement with previous proteomics analysis of microsomes isolated according to the same protocol (Zahedi et al., 2009). Furthermore, the isolated microsomes were verified to be competent for translocation and cotranslational processing of protein substrates using an in vitro translation-translocation assay (Figure S1B). In 3D reconstructions of vitrified samples, microsomes were approximately 100–300 nm in diameter and their surface was densely covered with ribosomes. Inside the microsomal lumen, elongated electron densities protrude from the membrane binding sites of the ER-associated ribosomes (Figures 1A and 1B).

Ribosome positions and orientations were determined by template matching with an appropriately filtered density of the human ribosome as determined by single-particle analysis (Spahn et al., 2004) in eight different tomograms (Figure 2A). Particles were reconstructed individually and subsequently sorted by two consecutive classification steps (Figure 2B) to (1) separate ER-associated ribosomes from false positive matches (Figure S2A) and (2) to obtain a set of ER-associated ribosomes with homogenous translocation machinery and well-defined membrane region (Figure S2B). Thus, from approximately 8,000 candidates obtained by template matching we retained approximately 1,000 ER-associated ribosomes after the last classification step. Subsequently, we aligned and averaged these 1,000 particles to obtain a subtomogram average of the membrane-bound ribosome (Figure 3). The resolution of the subtomogram average was determined to 31 Å by Fourier Shell Correlation (Figure S3A). In addition to the 80S ribosome, the average includes a slightly curved membrane and two distinct densities inside the microsomal lumen, which we refer to as
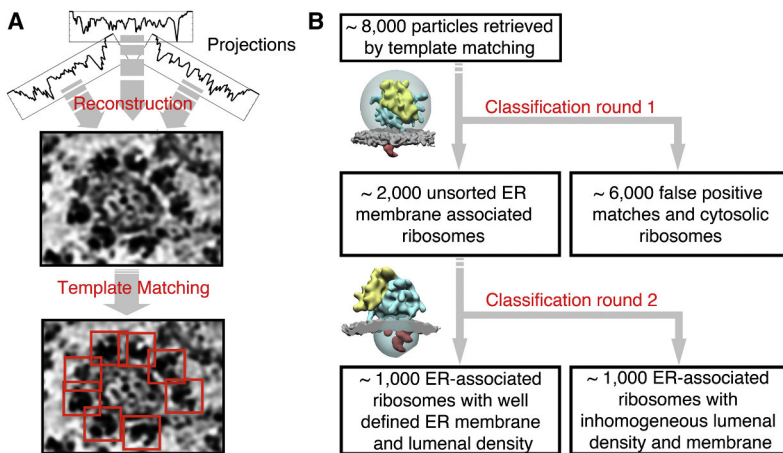
Figure 2. Overview of the Processing Workflow

(A) Particle localization. Demagnified (binned) volumes were reconstructed from phase-corrected projections. Ribosomes were localized by template matching in PyTom (Hrabe et al., 2012) using a single-particle reconstruction of the human 80S ribosome as a template (Spahn et al., 2004). (B) Particle classification by constrained principal component analysis (CPCA). Unbinned particles were sorted by two consecutive classification steps. For the first classification step, subtomograms were masked by a spherical mask encapsulating the entire ribosome and a small proportion of the ER membrane. Classification separated ER-associated ribosomes from false-positive matches, such as gold markers, microsomal membrane and 60S ribosomal subunits, as well as free ribosomes (Figure S2A). The resulting 2,000 ER-associated ribosomes were subjected to a second round of classification with a mask focused on the ER-lumenal and membrane region to obtain a data set with well-defined membrane and lumenal density (Figure S2B).

See also Figure S2 for individual classes obtained by classification.

---

lumenal density 1 (LD1) and LD2 in the following. The membrane reveals its typical bilayer-like appearance (Figure S3B), which is consistent with the determined resolution. As a control for the reference-based alignment, we performed a reference-free alignment, which resulted in an essentially identical density (Figure S3C).

Structure of the ER Translocation Machinery In Situ

Within the ER membrane, marked density variations could be distinguished (Figure 4A). When superposing the single-particle reconstruction of the reconstituted canine 80S-Sec61-TRAP complex (Ménétret et al., 2008) (EMDB 1528) onto the averaged map, we observed colocalization of one area of high density with the Sec61 complex (Figure S4A). Moreover, we were able to

identify a second area of high density within the ER membrane as the transmembrane region of TRAP (Figure S4B). In addition to these two identified integral membrane complexes, we can observe electron density for a number of additional integral membrane proteins/complexes, which probably correspond to other subunits of the translocation complex, such as OST, SP, ERj1, Sec62, Sec63, and TRAM.

In addition, two distinct electron densities, LD1 and LD2, were detected in the microsomal lumen (Figure 3). Superposition of the CET map onto the single-particle reconstruction of reconstituted 80S-Sec61-TRAP complex (Ménétret et al., 2008) (EMDB 1528) suggests that LD1 exclusively corresponds to the TRAP complex (Figure S4C). LD2 is considerably larger than LD1 and protrudes approximately 9 nm into the ER lumen. It
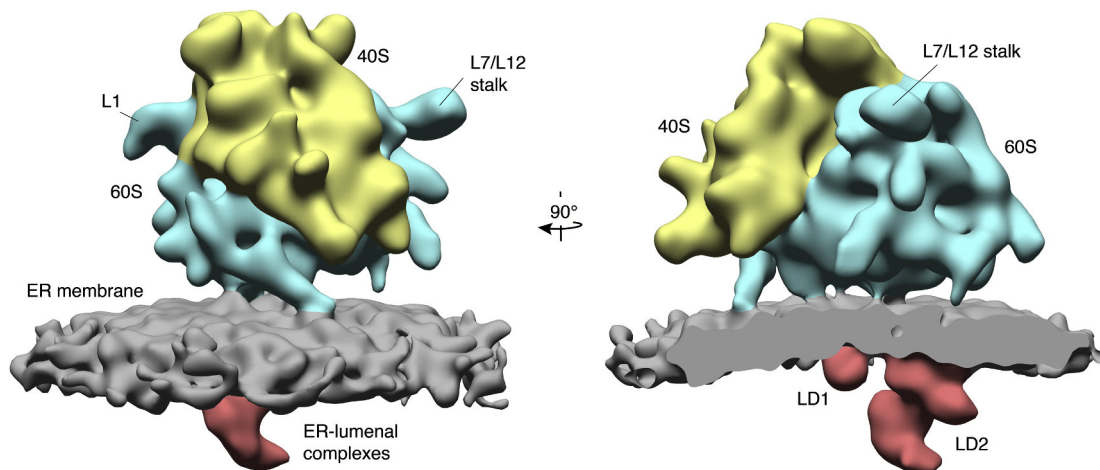
Figure 3. Overview of the In Situ Structure of the ER-Associated Ribosome

Left: the 31 Å subtomogram-average includes the large (blue) and small (yellow) ribosomal subunit, the ER membrane (gray), and the ER-lumenal electron densities LD1 and LD2 (red).

Right: the ER membrane was cut for better visibility of the ER-lumenal densities.

See also Figure S3 for resolution assessment and reference-free alignment.
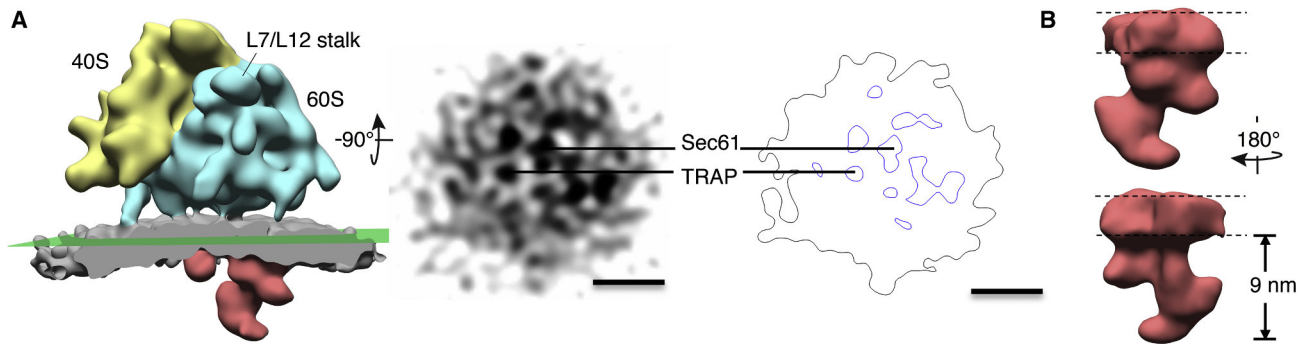
Figure 4. Structural Details of the ER Translocation Machinery In Situ

(A) Density variations within the ER-derived membrane. For a slice through the membrane region of the EM map (green, left-hand panel), a density (middle panel) and isoline representation (right-hand panel) is shown. In the isoline representation, blue lines surround high-density features (e.g., proteins), and black lines at a lower threshold level encapsulate also lower-density features (e.g., lipid). Sec61 and TRAP are assigned based on single-particle reconstructions (Figures S4A–S4C). Scale bar corresponds to 10 nm.

(B) Electron density of the ER-lumenal complex LD2. LD2 is oriented as in A, left panel (top) and rotated by 180° (bottom). Dashed lines indicate the membrane embedded region of LD2.

See also Figure S4 for assignment of Sec61 and TRAP in the CET map.

adopts a complex hook-like overall structure with its basis embedded in the ER membrane (Figure 4B).

Ribosomal Expansion Segment ES27L Is a Major ER Membrane Contact Site

One major ER membrane contact site of the ribosome is a rod-shaped density protruding from the front of the large ribosomal subunit. By superposing the single-particle reconstruction of the canine ribosome (Chandramouli et al., 2008) (EMDB 1480) onto the in situ CET map we assigned this region to expansion segment ES27L (Figure 5A): the observed rod-shaped density coincides with ES27L of the detergent-extracted ribosome at its basis near the ribosomal core, but deviates from the single-particle reconstruction in a further extension toward the membrane. The conformation of ES27L is not completely homogeneous, as revealed by classification of the underlying subtomograms (Figures S5A and S5B): ES27L is predominantly found in a conformation establishing a contact between the 80S ribosome and the membrane approximately 15 nm away from the ribosomal tunnel exit (80% of particles), and in a second conformation it contacts the membrane approximately 9 nm away from the ribosomal tunnel exit (20% of particles).

In addition to the contact by ES27L, we observe a second density that connects the ribosome to the membrane approximately 16 nm away from the ribosomal peptide exit (Figure 5B). However, the density of this connection is markedly lower than that of ES27L and it is only visible at a lower isosurface level. The low density suggests that different conformations contribute to the subtomogram average, but the density is too small to untangle these states by classification at the resolution of the in situ CET map. By superposing the single-particle reconstruction of the canine ribosome (Chandramouli et al., 2008) (EMDB 1480) to the in situ CET map we assigned this region to expansion segment ES7 of the large subunit rRNA (ES7L). The density of ES7L in our map largely colocalizes with the corresponding density in the single-particle reconstruction;

i.e., there is no indication of a conformational difference at the resolution of our map.

Ribosome-Membrane Interactions near the Universal Ribosomal Adaptor Site

In addition to the ER membrane contact by ES27L, we observed marked contacts between the ER membrane and the ribosome near the universal ribosomal adaptor site, i.e., in the vicinity of the ribosomal peptide exit (Figure 5C). A set of these interactions could be attributed to the Sec61 complex (Figure S5C). The ribosome-Sec61 interface observed in the in situ CET map corresponds to the interactions observed in the single-particle reconstruction of the reconstituted canine 80S-Sec61-TRAP complex. A connection of similar intensity between ribosomal components and the microsomal membrane was attributed to an interaction of the ribosome and the transmembrane region of the TRAP complex (Figure S5D). Two more ribosome-membrane interactions seem to be mediated by unidentified integral membrane proteins in proximity to LD2 (Figure S5E) and Sec61 (Figure S5F), respectively.

3D Arrangement of ER-Associated Ribosomes

In the in situ CET map of the microsome-associated ribosome, we can clearly observe density of neighboring ribosomes (Figure 6A). This density is very pronounced in specific regions around the central ribosome, suggesting that neighboring ribosomes adopt a preferred arrangement with respect to each other. A possible reason for induced ordering of neighboring ribosomes on the ER membrane is their supramolecular organization in polyribosomes. Consistently, we detected a high proportion of ER-associated ribosomes (approximately 65%) to be organized in polyribosomes by sucrose gradient centrifugation (Figure 6B), which is in agreement with previous results obtained for other ER preparations (Potter and Nicchitta, 2002).

For a detailed analysis of the 3D arrangement of ribosomes on the microsomal membrane, we used a coordinate system with
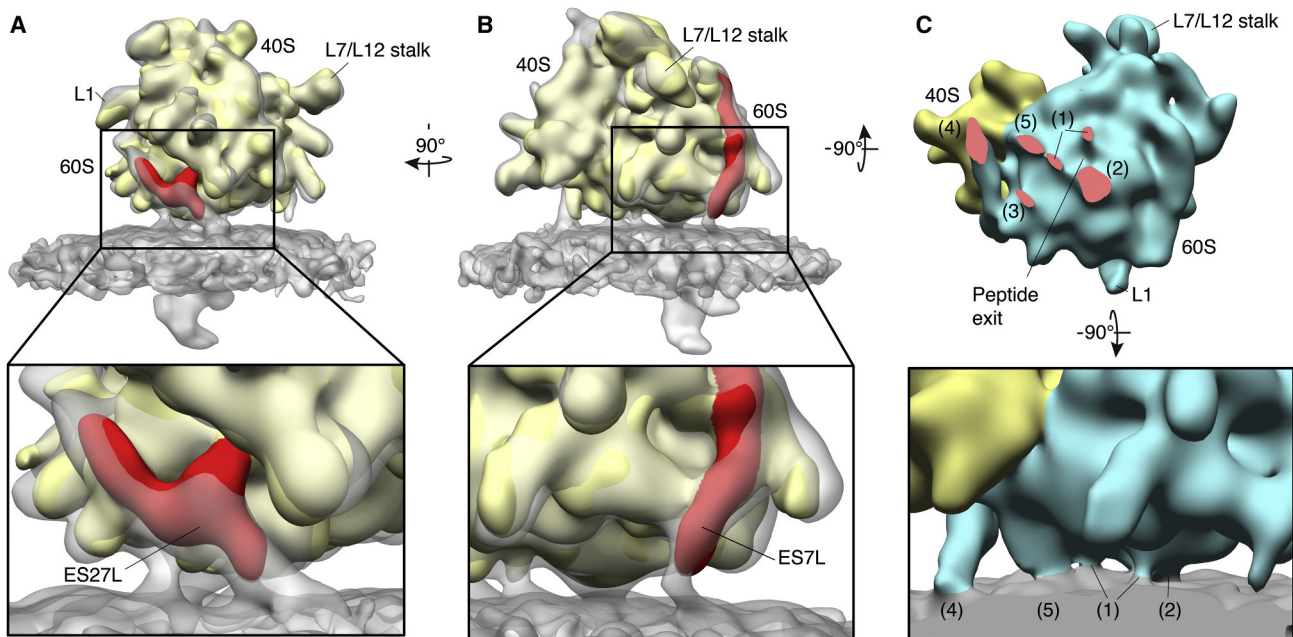
Figure 5. Structural Details of the Ribosome-Membrane Interface

(A and B) Assignment of ES27L and ES7L. A single-particle reconstruction of the canine ribosome (yellow) (Chandramouli et al., 2008) (EMDB 1480), filtered to 30 Å resolution, is superposed onto the in situ CET map. In the single-particle reconstruction, resolved segments of ES27L (A) and ES7L (B) are depicted in red. For the assignment of ES7L, a lower isosurface level was used.

(C) Overview of the observed interactions between ribosome and the ER membrane. Top: EM map seen from the ER lumen, capped at the ribosome-membrane interface. The observed interaction areas (red) are annotated based on single-particle reconstructions (A, B, and Figure S4): (1) Sec61, (2) unknown, (3) TRAP, (4) ES27L, and (5) unknown. Bottom: magnified view of the cytosolic ER interface of the EM map as shown in (B).

See also Figure S5 for further details on ribosome-membrane interactions and classification of ES27L conformations.

the z axis perpendicular to the microsomal membrane. For each ribosome, we calculated the relative Euclidean distances and relative orientations of its ten nearest neighbors. To reduce the background of nonspecific neighbors (e.g., ribosomes from adjacent microsomes), we restricted further analysis to those neighbors that reside in a preferred distance range (20–37 nm, Figure S6A) and membrane inclination range (0°–40°, Figure S6B). For these neighbors, we calculated an angle α, which describes their positions relative to the central ribosome, and an angle β, which describes their in-plane rotations (orientations) relative to the central ribosome (Figure 6C). To detect preferred arrangements, we plotted α against β and clustered these coordinates (Figure 6D). The clustering revealed two strongly populated classes and an approximately evenly distributed background (Figure S6C). To visualize the ribosome arrangements represented by these two classes, we generated replicates of the CET map using the expectation values of positions and orientations of neighbors assigned to the two classes. The replicates reveal that the two classes represent the right and left neighbors of essentially the same chain-like spatial arrangement. In this major next-neighbor configuration, mRNA entry and exit sites of adjacent ribosomes are in spatial proximity (approximately 19 nm) and their relative positions and orientations would allow threading an interconnecting mRNA molecule from one ribosome to the next on a smooth path without major bends (Figure 6E). Thus, the observed arrangement would allow for simultaneous translation of the same mRNA molecule and concurrent protein translocation across the ER membrane by multiple membrane-bound ribosomes (polyribosomes).

DISCUSSION

ER Membrane Attachment of ES27L

In our subtomogram average ES27L is in physical contact to the ER membrane. The conformations of ES27L, which we can distinguish by classification of subtomograms, are different from those observed in the absence of the ER membrane (Chandramouli et al., 2008) (EMDB 1480). Conformational changes of ES27L are not unexpected; in solution, ES27L has been shown to be highly variable in yeast and wheat germ ribosomes (Armache et al., 2010a). In both cases, ES27L adopts two preferred orientations, one pointing toward the L1 stalk (ES27L$_{in}$) and one pointing toward the peptide exit tunnel (ES27L$_{out}$), as well as a broad range of intermediate orientations. The orientations of ES27L$_{in}$ and ES27L$_{out}$ differ more than 90° and the tip of ES27L moves more than 19 nm between both conformations.

It is possible that the ES27L-membrane interaction is simply fortuitous due to the positioning of the ribosome on the ER-membrane and that the interaction has a minor stabilizing effect. However, it seems unlikely that ES27L adopts a well-defined conformation that is different from that in solution if ES27L did not bind with notable affinity to the ER membrane. Thus, we assume that ES27L stabilizes the association of
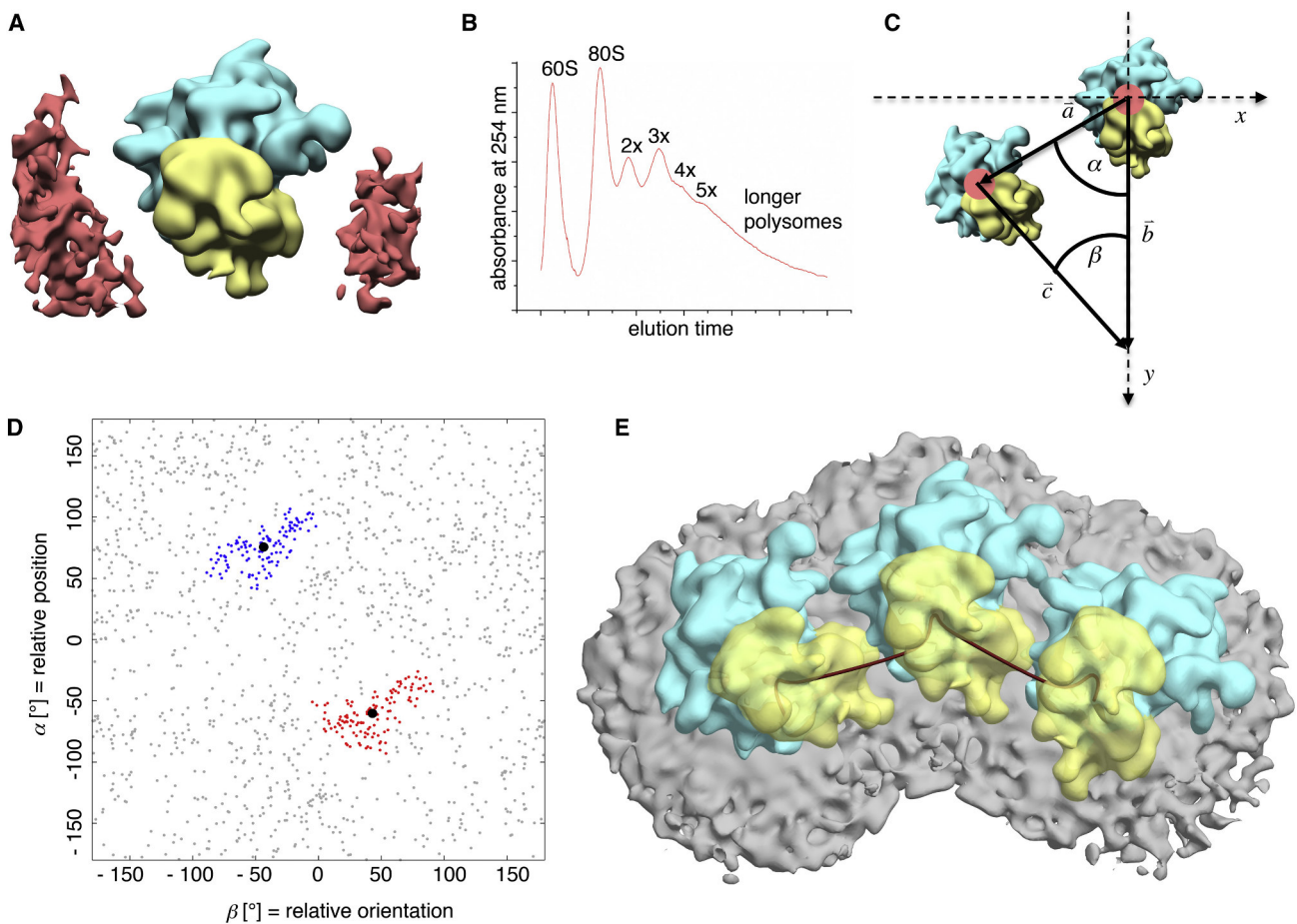
Figure 6. 3D Arrangement of ER-Associated Ribosomes

(A) Density of adjacent ribosomes in the CET map. In the in situ CET map, electron density for neighboring ribosomes (red) can be observed in specific regions around the central ribosome. For better dissection of the additional electron density, the ER membrane (oriented parallel to the drawing plane) was removed.

(B) Polyribosome profile of solubilized membrane-bound ribosomes. The analyzed microsomes contain a high proportion of ER-associated polyribosomes (65%).

(C) Definition of arrangement parameters. For the analysis of the 3D distribution of ribosomes we defined two angles: the angle α between the y axis of the ribosome under scrutiny and the center-to-center vector $\vec{a}$ of another ribosome describes their relative positions while the angle β between the vectors $\vec{b}$ and $\vec{c}$ of the two ribosomes captures their relative orientation.

(D) Clustering of arrangement parameters. The plot of α against β and subsequent clustering of the data set reveals two highly populated classes (red and blue) that represent the left and right neighbor in the same 3D arrangement.

(E) Preferred 3D arrangement of membrane-bound ribosomes visualized by replicates of the in situ CET map. A flexible rod was fitted to mRNA entry and exit site and the codon recognition site of adjacent ribosomes to visualize a possible pathway for interconnecting mRNA. Small ribosomal subunits are depicted transparently for visualization of the mRNA pathway.

See also Figure S6 for further details on the distribution analysis of ER-associated ribosomes.

ribosomes to the ER membrane. How is ES27L attached to the ER membrane? ES27L could either bind directly to lipid or to an integral membrane protein. Direct interaction between the negatively charged phosphate groups of the rRNA backbone and predominantly positively charged head groups of ER membrane lipids would be a possible model and it was recently proposed that rRNA-membrane interactions occur close to the peptide exit tunnel of prokaryotic ribosomes (Frauenfeld et al., 2011).

Alternatively, several membrane proteins have been suggested to bind rRNA and thus these are genuine candidates for ES27L interaction. The Sec62/Sec63 complex (Müller et al.,

2010) and ERj1 (Dudek et al., 2005; Dudek et al., 2002) have been reported to bind ribosomes in an RNase-sensitive manner. In a single-particle study of solubilized ribosomes, ES27L has indeed been shown to bind to the cytosolic domain of ERj1 (Blau et al., 2005). Due to the simultaneous binding of ERj1 to the ribosomal tunnel exit in the single-particle reconstruction, the conformation of ES27L observed in the solubilized sample differs fundamentally from the one observed in the in situ CET map. However, according to the mechanistic model proposed by Blau et al. (Blau et al., 2005), ERj1 rearranges or even dissociates from the ribosomal tunnel exit after recruiting BiP to the lumenal side of the translocation complex to enable Sec61

31

binding to the ribosome. Another candidate for ES27L binding is the ER membrane protein p180/Ribosome Receptor protein (RRp) (Savitz and Meyer, 1990), which is highly abundant in the ER membrane (Shibata et al., 2010) and has been shown to bind to both, the ER translocation machinery and the large subunit rRNA (Ueno et al., 2012). P180's C-terminal, cytosolic domain contains 54 repeats of a 10 amino acid consensus motif, which is thought to be responsible for rRNA binding (Wanker et al., 1995). As a result, the ubiquitous p180/RRp could provide a suitable platform for stable binding of ES27L. In the in situ CET map, we observe higher density levels in the microsomal membrane in the vicinity of ES27L, but the resolution of our map is not sufficient to unambiguously conclude the presence of a protein contacting ES27L.

Ribosome-membrane interactions mediated by ribosomal ESs may explain a fundamental difference between prokaryotic and eukaryotic ribosomes after completion of translocation. Eukaryotic ribosomes have been reported to remain associated to the ER membrane and to only dissociate when programmed for a soluble protein (Potter and Nicchitta, 2000). In fact, it was hypothesized that ES27L triggers dissociation of ribosomes from the ER membrane (Potter and Nicchitta, 2002). Our findings suggest that ES27L contributes directly to ribosome association with the ER membrane and, accordingly, conformational changes of ES27L may indeed be responsible for dissociation. In contrast, prokaryotic ribosomes, which lack ESs, dissociate after translocation of the nascent chain across the inner bacterial plasma membrane (du Plessis et al., 2011).

Structure of the ER Translocation Machinery In Situ

There has been a long-standing debate over the exact copy number of translocon subunits in the native holocomplex. In particular, the copy number of Sec61 and its prokaryotic homolog SecYEG has been controversial (Becker et al., 2009; Beckmann et al., 2001; Breyton et al., 2002; Mitra et al., 2005). Recent subnanometer resolution single particle reconstructions provide compelling evidence that the ribosome binds to a Sec61/SecYEG monomer in reconstituted RNC-Sec61 and RNC-SecYEG complexes (Becker et al., 2009; Frauenfeld et al., 2011). However, it has not been addressed to date whether the oligomeric state of Sec61/SecYEG in the reconstituted complex is identical to that in the native ER membrane. For example, antibody-mediated FRET measurements suggested that Sec61 predominantly oligomerizes in the ER membrane (Snapp et al., 2004). A model has been suggested that reconciles both findings (Schaletzky and Rapoport, 2006): RNCs target a minority population of monomeric Sec61 in the ER membrane and RNC-binding induces oligomerization. In the in situ CET map of microsome-bound ribosomes reported here, clear densities colocalize with the positions of monomeric Sec61 and TRAP complexes in single-particle reconstructions of reconstituted, solubilized samples (Becker et al., 2009; Ménétret et al., 2008). The excellent agreement of our in situ map with these single-particle reconstructions suggests that Sec61 is monomeric in the native translocon as well. However, higher resolution reconstructions will be required to make an unambiguous determination of the oligomeric state.

In addition to Sec61 and the TRAP complex, we observe distinct electron densities corresponding to unidentified membrane-integral and ER-lumenal components of the translocation machinery in the in situ CET map. Most prominent among these unidentified components is a density we designated LD2, a large complex that protrudes approximately 9 nm into the ER lumen. According to the analysis of RAMPs (Potter and Nicchitta, 2002), Sec61, TRAP, and OST are the most abundant complexes physically associated to the membrane-bound ribosome and thus should represent the largest, most pronounced densities observed in the tomographic reconstruction. High-resolution single-particle reconstructions allow a straightforward assignment of Sec61 and TRAP outside LD2. Hence, the OST complex is the most likely candidate to correspond to substantial parts of the LD2 density. Further considering that the OST active site is located approximately 3–4 nm away from the ER membrane surface (Nilsson and von Heijne, 1993), it is plausible that LD2 encompasses OST. At this point we cannot be certain about the identity of the LD2 density, because that would require labeling or gene silencing experiments to specifically target single components of the translocation machinery. Future experiments with systems, such as cell lines that can be readily manipulated may enable unambiguous assignment of the LD2 components by CET.

Albeit being inferior to many single-particle and X-ray crystallography ribosome studies in terms of resolution, the structure of ER-associated ribosomes presented here benefits from a general advantage of CET compared to other methods for structural analysis of large membrane-associated complexes. The imaged specimen represents a functional, near-to-native state without extensive biochemical purification and reconstitution, as required for single-particle analysis and X-ray crystallography. Thus, in addition to the obvious advantage of studying the native set of molecules and interactions, the laborious and often unsuccessful solubilization and reconstitution of the complexes of interest is circumvented. Hence, we could image the ribosome associated to the translocon with all of its subunits and accessory components, whereas prior structural work using single-particle analysis focused on subcomplexes. The analysis of the in situ map of the membrane-bound ribosome suggests an interaction between ES27L and the ER membrane approximately 15 nm away from the ribosome-Sec61 interface. Thus, in this specific case, the topology of the surrounding membrane environment proves to be critical for essential observations; in a reconstituted system, e.g., using detergent micelles or lipid nanodiscs (Frauenfeld et al., 2011), the spread and curvature of the membrane environment is severely restricted and the interaction between ES27L and the ER membrane as reported here probably would not have been observed, even if the reconstituted system contained all necessary protein components.

It would be desirable to analyze ribosome and in particular polyribosome structures in whole cells rather than microsomes and some progress has been made recently in the preparation of thin vitrified cellular samples. In tomograms of focused-ion-beam milled vitrified cells ER-associated ribosomes could be discerned (Rigort et al., 2012). Alternatively, thin (<100 nm) sections of cells can be obtained by cryosectioning, which leaves the structure of 80S ribosomes unaltered, at least to low resolution (Pierson et al., 2011). The SNR in tomograms of cell sections is generally worse than in our microsome tomograms

due to molecular crowding in the cytoplasm, which favors microsome tomography for structural studies of the translocation machinery. We do not anticipate significant structural changes of the translocation machinery in microsomes compared to whole cells because they are transport-competent. However, when cryo-ET studies of cell sections are well established their application will be valuable for the study of polyribosome structures, which might be affected by the microsome preparation.

3D Arrangement of ER-Associated Ribosomes

As is expected with microsomal preparations, a high density of ER-associated ribosomes is detected in tomographic reconstructions of vitrified samples. When analyzing the membrane-bound ribosome fraction for preferred organizations of polyribosomes, as previously reported for cytosolic polyribosomes in vitro (Brandt et al., 2009) or in situ (Brandt et al., 2010), the high density of membrane-bound ribosomes poses a particular challenge: numerous unspecific proximities may occur due to adjacent ribosomes not belonging to the same polyribosome. Nevertheless, we observe a preferred 3D arrangement and it is plausible that this arrangement of neighboring membrane-bound ribosomes is specific for ER-associated polyribosomes for four reasons: (1) Biochemical verification indicates that a large portion (approximately 65%) of the ER-associated ribosomes is organized in polyribosomes. (2) It is unlikely that crowding of ribosomes on the ER membrane induces preferred arrangements; if preferred orientations were induced by surface crowding, we would expect a plane-filling pattern, e.g., a hexagonal arrangement with more than one specific neighbor density occurring in the ribosome average, rather than a single preferred arrangement of neighbors, which results in a chain-like organization. (3) The observed arrangement is consistent with the expected topological requirements for membrane-bound polyribosomes: peptide exits are arranged in a plane and point toward the ER membrane; mRNA entry and exit sites of adjacent ribosomes are positioned along a smooth path, which would allow threading the interconnecting mRNA molecule without major bends. (4) An extrapolation of the observed arrangement would be consistent with the spiral-like organization of ribosomes, which was described earlier for ER-associated polyribosomes imaged by TEM of plastic-embedded thin sections of eukaryotic cells (Lee et al., 1971). Based on these data, we suggest that the observed arrangement is specific for membrane-bound polyribosomes.

Compared to the well-defined 3D arrangement of cytosolic polyribosomes (Brandt et al., 2010), the spatial organization of ER-associated polyribosomes appears to be more flexible. While we observe a comparably sharp positioning of neighboring ribosomes (SD ±16°), their relative orientation is relatively flexible (±23°). Given the high density of ribosomes on the microsomal membrane, it is, however, not surprising to find a higher degree of flexibility in the 3D arrangement of ER-associated polyribosomes: during formation, the spatial organization of a growing polyribosome has to adopt to the locally available space, while preserving the basic topological requirements for membrane-bound polyribosomes. The fluid-like nature of biological membranes, in which embedded complexes can rotate and diffuse laterally, provides a physical basis for the observed flexibility in spatial organization of ER-associated polyribosomes.

A defined 3D arrangement of ribosomes on the ER-membrane may be a reason for higher translation efficiency of ER-associated ribosomes compared to their cytosolic counterparts (Stephens and Nicchitta, 2008). After completion of translation ribosomes stay associated to the ER membrane (Potter and Nicchitta, 2002) and photobleaching experiments (Rolls et al., 2002) suggest that their spatial organization should remain essentially invariant. The immobilization of ribosomes on the ER membrane would then facilitate rapid "threading" of newly arriving mRNA molecules through the "preformed" polyribosome.

EXPERIMENTAL PROCEDURES

Preparation of Rough ER Microsomes

Rough ER microsomes (RMs) were prepared from dog pancreas as described earlier (Watts et al., 1983) but omitting the nuclease treatment. The microsomes were characterized by western blotting and in functional assays (Figure S1). All subsequent steps were carried out on ice unless stated otherwise.

Polysome Profiling

Canine microsomes (15 eq) were resuspended in 50 μl of polysome buffer (5 mM MgCl$_2$, 140 mM KCl, 10 mM HEPES [pH 7.4], 1 mM DTT, protease inhibitor) and lysed by adding 0.3% (f.c.) Triton X-100. The sample was then layered on a linear sucrose gradient (15%–45%) prepared in polysome buffer, which was subsequently centrifuged for 2 hr at 38,000 rpm in a SW41 rotor (Beckman Coulter). The gradients were eluted from top to bottom (Gradient Master, Biocomp, Netherlands) while the absorption of 254 nm light was monitored (Econo UV Monitor, Bio-Rad). The proportion of ribosomes engaged in polyribosomes was estimated based on the ratio of the summed integral of 60S and 80S peaks (Gaussian fit) and the integral of the complete profile.

Cryoelectron Tomography

Diluted microsomes (3 μl) in polysome buffer (2 eq/25 μl) were applied to lacey carbon molybdenum grids (Ted Pella, USA). After an incubation time of 60 s, 3 μl of 10 nm colloidal gold in polysome buffer were added to the grid and the sample was vitrified in liquid ethane using a Vitrobot Mark IV (FEI, Netherlands). Tilt series were acquired using a FEI Tecnai Polara TEM equipped with a GIF 2002 energy filter (Gatan) housing a 2kx2k CCD-Camera. The TEM was operated at an acceleration voltage of 300 kV. Single-axis tilt series were recorded from $-60°$ to $+60°$ with an angular increment of 3° at a nominal defocus of 4 μm and an object pixel size of 4.7 Å using the FEI tomography acquisition software. The cumulative electron dose did not exceed 60 electrons/Å^2.

Data Processing

Phase restoration of the tilt series was performed as previously described (Fernández et al., 2006) implemented in in-house developed software (M.E., C. Hoffmann, J.M. Plitzko, W. Baumeister, S. Nickell, and H. Engelhardt, unpublished data). The phase-corrected projections were aligned with the help of interactively located gold markers and demagnified (object pixel size: 1.88 nm) tomograms (512 × 512 × 128 voxels) were reconstructed by weighted back projection using the av3 (Förster et al., 2005) and TOM toolboxes (Nickell et al., 2005).

Ribosomes were localized by template matching in PyTom (Hrabe et al., 2012). As a template, we used the single-particle reconstruction of the human 80S ribosome (Spahn et al., 2004), which was filtered to 4 nm resolution, convoluted with an approximate CTF, and scaled to 1.88 nm voxel size (Förster et al., 2010). Different rotations of the template were sampled with an angular increment of 12.85°. Peaks of the resulting cross-correlation function (distance of distinct peaks >18.8 nm) indicated positions of putative ribosomes. Unbinned subtomograms (128^3 voxels), centered at the identified coordinates, were reconstructed individually from the weighted back projections and aligned to the template using PyTom (Hrabe et al., 2012). Particles were sorted in two consecutive classification steps by constrained principal component

33

analysis (CPCA) (Förster et al., 2008). First, subtomograms were masked by a spherical mask encapsulating the entire ribosome and a small proportion of the ER membrane (Figure S2A). Classification separated ER-associated ribosomes from false-positive matches, such as gold markers, microsomal membrane and 60S ribosomal subunits, as well as non-membrane bound ribosomes. The resulting 1,950 ER-associated ribosomes were subjected to a second round of classification with a mask focused on the ER-lumenal and membrane region of the average (Figure S2B) to obtain a data set with well-defined membrane and lumenal density. The resulting 1,004 particles were subjected to further alignment and averaging using PyTom until convergence. The resolution of the resulting average was determined by Fourier shell correlation (FSC) using FSC = 0.5 as the resolution measure.

EM-Map Analysis

For EM-map analysis and visualization we used the UCSF Chimera software package (Goddard et al., 2007). The isosurface level was chosen such that the approximate molecular weight of the lumenal proportion of the TRAP complex (assuming a protein density of 1.21 Da/$\mathring{A}^3$ (Goddard et al., 2007)) corresponds to its molecular weight. For structure comparison, the respective single-particle reconstructions (filtered to 30 $\mathring{A}$ resolution) were manually superposed onto our EM-map prior to automated refinement of the fit.

Analysis of the 3D Arrangement of ER-Associated Ribosomes

The analysis was carried out in a coordinate system with the z axis perpendicular to the microsomal membrane using the full data set of 1,950 classified ER-associated ribosomes. First, a Gaussian distribution was fitted to the radial pair distribution function of the ten nearest ribosomes in a radius of 100 nm. Only ribosomes within two standard deviations around the mean distance were used for further analysis. Next, a Gaussian distribution was fitted to the distribution of membrane inclination angles θ in the retained ribosome pairs and only ribosomes within two standard deviations of the mean value were used for further analysis. For each ribosome, we calculated the angle α, describing the relative position of neighboring ribosomes, and the angle β, describing the relative orientation of neighboring ribosomes (Figure 6C). The data set was clustered hierarchically in these two dimensions in MATLAB (Mathworks) using "single" linkage and "distance" clustering criterion.

Polyribosome Models

To obtain the average 3D arrangement of neighboring ribosomes in the clusters, we computed the expectation values of their positions and orientations. Using the averaged positions and orientations, we generated replicates of the in situ CET map to visualize the preferred 3D arrangement. The putative interconnecting mRNA molecule was modeled as a flexible rod joining mRNA entry and exit and the codon recognition site of adjacent ribosomes in 3 ds max (Autodesk) as previously described (Brandt et al., 2009). The approximate coordinates of mRNA entry and exit and codon recognition site in the in situ CET map were chosen according to the crystal structure of the yeast 80S ribosome (Ben-Shem et al., 2010) (PDB 3O2Z and 3O30).

Tomogram Visualization

For the visualization of a whole tomogram in Figure 1, a representative reconstruction was filtered to a resolution of 7 nm. The ER membrane was segmented manually in Amira (Visage Imaging) and ribosomes were marked by spheres of 15 nm radius positioned according to the coordinates determined by template matching. Tomogram and segmentation masks were multiplied and isosurface rendering was done in Amira.

ACCESSION NUMBERS

The in situ structure of the ER-associated ribosome has been deposited in the EMDB with accession code 2099.

SUPPLEMENTAL INFORMATION

Supplemental Information includes six figures and Supplemental References and can be found with this article online at http://dx.doi.org/10.1016/j.str.2012.06.010.

REFERENCES

Armache, J.P., Jarasch, A., Anger, A.M., Villa, E., Becker, T., Bhushan, S., Jossinet, F., Habeck, M., Dindar, G., Franckenberg, S., et al. (2010a). Cryo-EM structure and rRNA model of a translating eukaryotic 80S ribosome at 5.5-Å resolution. Proc. Natl. Acad. Sci. USA *107*, 19748–19753.

Armache, J.P., Jarasch, A., Anger, A.M., Villa, E., Becker, T., Bhushan, S., Jossinet, F., Habeck, M., Dindar, G., Franckenberg, S., et al. (2010b). Localization of eukaryote-specific ribosomal proteins in a 5.5-Å cryo-EM map of the 80S eukaryotic ribosome. Proc. Natl. Acad. Sci. USA *107*, 19754–19759.

Bartesaghi, A., and Subramaniam, S. (2009). Membrane protein structure determination using cryo-electron tomography and 3D image averaging. Curr. Opin. Struct. Biol. *19*, 402–407.

Becker, T., Bhushan, S., Jarasch, A., Armache, J.P., Funes, S., Jossinet, F., Gumbart, J., Mielke, T., Berninghausen, O., Schulten, K., et al. (2009). Structure of monomeric yeast and mammalian Sec61 complexes interacting with the translating ribosome. Science *326*, 1369–1373.

Beckmann, R., Spahn, C.M., Eswar, N., Helmers, J., Penczek, P.A., Sali, A., Frank, J., and Blobel, G. (2001). Architecture of the protein-conducting channel associated with the translating 80S ribosome. Cell *107*, 361–372.

Ben-Shem, A., Jenner, L., Yusupova, G., and Yusupov, M. (2010). Crystal structure of the eukaryotic ribosome. Science *330*, 1203–1209.

Ben-Shem, A., Garreau de Loubresse, N., Melnikov, S., Jenner, L., Yusupova, G., and Yusupov, M. (2011). The structure of the eukaryotic ribosome at 3.0 Å resolution. Science *334*, 1524–1529.

Blau, M., Mullapudi, S., Becker, T., Dudek, J., Zimmermann, R., Penczek, P.A., and Beckmann, R. (2005). ERj1p uses a universal ribosomal adaptor site to coordinate the 80S ribosome at the membrane. Nat. Struct. Mol. Biol. *12*, 1015–1016.

Blobel, G., and Dobberstein, B. (1975a). Transfer of proteins across membranes. I. Presence of proteolytically processed and unprocessed nascent immunoglobulin light chains on membrane-bound ribosomes of murine myeloma. J. Cell Biol. *67*, 835–851.

Blobel, G., and Dobberstein, B. (1975b). Transfer of proteins across membranes. II. Reconstitution of functional rough microsomes from heterologous components. J. Cell Biol. *67*, 852–862.

Brandt, F., Etchells, S.A., Ortiz, J.O., Elcock, A.H., Hartl, F.U., and Baumeister, W. (2009). The native 3D organization of bacterial polysomes. Cell *136*, 261–271.

Brandt, F., Carlson, L.A., Hartl, F.U., Baumeister, W., and Grünewald, K. (2010). The three-dimensional organization of polyribosomes in intact human cells. Mol. Cell *39*, 560–569.

Breyton, C., Haase, W., Rapoport, T.A., Kühlbrandt, W., and Collinson, I. (2002). Three-dimensional structure of the bacterial protein-translocation complex SecYEG. Nature *418*, 662–665.

Chandramouli, P., Topf, M., Ménétret, J.F., Eswar, N., Cannone, J.J., Gutell, R.R., Sali, A., and Akey, C.W. (2008). Structure of the mammalian 80S ribosome at 8.7 A resolution. Structure *16*, 535–548.

du Plessis, D.J., Nouwen, N., and Driessen, A.J. (2011). The Sec translocase. Biochim. Biophys. Acta *1808*, 851–865.

34

Dudek, J., Volkmer, J., Bies, C., Guth, S., Müller, A., Lerner, M., Feick, P., Schäfer, K.H., Morgenstern, E., Hennessy, F., et al. (2002). A novel type of co-chaperone mediates transmembrane recruitment of DnaK-like chaperones to ribosomes. EMBO J. 21, 2958–2967.

Dudek, J., Greiner, M., Müller, A., Hendershot, L.M., Kopsch, K., Nastainczyk, W., and Zimmermann, R. (2005). ERj1p has a basic role in protein biogenesis at the endoplasmic reticulum. Nat. Struct. Mol. Biol. 12, 1008–1014.

Evans, E.A., Gilmore, R., and Blobel, G. (1986). Purification of microsomal signal peptidase as a complex. Proc. Natl. Acad. Sci. USA 83, 581–585.

Fernández, J.J., Li, S., and Crowther, R.A. (2006). CTF determination and correction in electron cryotomography. Ultramicroscopy 106, 587–596.

Förster, F., and Hegerl, R. (2007). Structure determination in situ by averaging of tomograms. Methods Cell Biol. 79, 741–767.

Förster, F., Medalia, O., Zauberman, N., Baumeister, W., and Fass, D. (2005). Retrovirus envelope protein complex structure in situ studied by cryo-electron tomography. Proc. Natl. Acad. Sci. USA 102, 4729–4734.

Förster, F., Pruggnaller, S., Seybert, A., and Frangakis, A.S. (2008). Classification of cryo-electron sub-tomograms using constrained correlation. J. Struct. Biol. 161, 276–286.

Förster, F., Han, B.G., and Beck, M. (2010). Visual proteomics. Methods Enzymol. 483, 215–243.

Frangakis, A.S., Böhm, J., Förster, F., Nickell, S., Nicastro, D., Typke, D., Hegerl, R., and Baumeister, W. (2002). Identification of macromolecular complexes in cryoelectron tomograms of phantom cells. Proc. Natl. Acad. Sci. USA 99, 14153–14158.

Frauenfeld, J., Gumbart, J., Sluis, E.O., Funes, S., Gartmann, M., Beatrix, B., Mielke, T., Berninghausen, O., Becker, T., Schulten, K., and Beckmann, R. (2011). Cryo-EM structure of the ribosome-SecYE complex in the membrane environment. Nat. Struct. Mol. Biol. 18, 614–621.

Goddard, T.D., Huang, C.C., and Ferrin, T.E. (2007). Visualizing density maps with UCSF Chimera. J. Struct. Biol. 157, 281–287.

Görlich, D., and Rapoport, T.A. (1993). Protein translocation into proteoliposomes reconstituted from purified components of the endoplasmic reticulum membrane. Cell 75, 615–630.

Görlich, D., Hartmann, E., Prehn, S., and Rapoport, T.A. (1992). A protein of the endoplasmic reticulum involved early in polypeptide translocation. Nature 357, 47–52.

Gray, M.W., and Schnare, M.N. (1990). Evolution of the modular structure of rRNA, W.E. Hill, A. Dahlberg, R.A. Garrett, P.B. Moore, D. Schlessinger, and J.R. Warner, eds. (Washington, D.C.: American Society for Microbiology), pp. 589–597.

Hartmann, E., Görlich, D., Kostka, S., Otto, A., Kraft, R., Knespel, S., Bürger, E., Rapoport, T.A., and Prehn, S. (1993). A tetrameric complex of membrane proteins in the endoplasmic reticulum. Eur. J. Biochem. 214, 375–381.

Hrabe, T., Chen, Y., Pfeffer, S., Kuhn Cuellar, L., Mangold, A.V., and Forster, F. (2012). PyTom: a python-based toolbox for localization of macromolecules in cryo-electron tomograms and subtomogram analysis. J. Struct. Biol. 178, 177–188.

Kelleher, D.J., and Gilmore, R. (2006). An evolving view of the eukaryotic oligosaccharyltransferase. Glycobiology 16, 47R–62R.

Klinge, S., Voigts-Hoffmann, F., Leibundgut, M., Arpagaus, S., and Ban, N. (2011). Crystal structure of the eukaryotic 60S ribosomal subunit in complex with initiation factor 6. Science 334, 941–948.

Lee, S.Y., Krsmanovic, V., and Brawerman, G. (1971). Attachment of ribosomes to membranes during polysome formation in mouse sarcoma 180 cells. J. Cell Biol. 49, 683–691.

Lucić, V., Förster, F., and Baumeister, W. (2005). Structural studies by electron tomography: from cells to molecules. Annu. Rev. Biochem. 74, 833–865.

Ménétret, J.F., Hegde, R.S., Aguiar, M., Gygi, S.P., Park, E., Rapoport, T.A., and Akey, C.W. (2008). Single copies of Sec61 and TRAP associate with a nontranslating mammalian ribosome. Structure 16, 1126–1137.

Mitra, K., Schaffitzel, C., Shaikh, T., Tama, F., Jenni, S., Brooks, C.L., 3rd, Ban, N., and Frank, J. (2005). Structure of the E. coli protein-conducting channel bound to a translating ribosome. Nature 438, 318–324.

Müller, L., de Escauriaza, M.D., Lajoie, P., Theis, M., Jung, M., Müller, A., Burgard, C., Greiner, M., Snapp, E.L., Dudek, J., and Zimmermann, R. (2010). Evolutionary gain of function for the ER membrane protein Sec62 from yeast to humans. Mol. Biol. Cell 21, 691–703.

Nickell, S., Förster, F., Linaroudis, A., Net, W.D., Beck, F., Hegerl, R., Baumeister, W., and Plitzko, J.M. (2005). TOM software toolbox: acquisition and analysis for electron tomography. J. Struct. Biol. 149, 227–234.

Nilsson, I.M., and von Heijne, G. (1993). Determination of the distance between the oligosaccharyltransferase active site and the endoplasmic reticulum membrane. J. Biol. Chem. 268, 5798–5801.

Pierson, J., Ziese, U., Sani, M., and Peters, P.J. (2011). Exploring vitreous cryo-section-induced compression at the macromolecular level using electron cryo-tomography; 80S yeast ribosomes appear unaffected. J. Struct. Biol. 173, 345–349.

Potter, M.D., and Nicchitta, C.V. (2000). Regulation of ribosome detachment from the mammalian endoplasmic reticulum membrane. J. Biol. Chem. 275, 33828–33835.

Potter, M.D., and Nicchitta, C.V. (2002). Endoplasmic reticulum-bound ribosomes reside in stable association with the translocon following termination of protein synthesis. J. Biol. Chem. 277, 23314–23320.

Rabl, J., Leibundgut, M., Ataide, S.F., Haag, A., and Ban, N. (2011). Crystal structure of the eukaryotic 40S ribosomal subunit in complex with initiation factor 1. Science 331, 730–736.

Rigort, A., Bäuerlein, F.J., Villa, E., Eibauer, M., Laugks, T., Baumeister, W., and Plitzko, J.M. (2012). Focused ion beam micromachining of eukaryotic cells for cryoelectron tomography. Proc. Natl. Acad. Sci. USA 109, 4449–4454.

Rolls, M.M., Hall, D.H., Victor, M., Stelzer, E.H., and Rapoport, T.A. (2002). Targeting of rough endoplasmic reticulum membrane proteins and ribosomes in invertebrate neurons. Mol. Biol. Cell 13, 1778–1791.

Saurí, A., McCormick, P.J., Johnson, A.E., and Mingarro, I. (2007). Sec61alpha and TRAM are sequentially adjacent to a nascent viral membrane protein during its ER integration. J. Mol. Biol. 366, 366–374.

Savitz, A.J., and Meyer, D.I. (1990). Identification of a ribosome receptor in the rough endoplasmic reticulum. Nature 346, 540–544.

Schaletzky, J., and Rapoport, T.A. (2006). Ribosome binding to and dissociation from translocation sites of the endoplasmic reticulum membrane. Mol. Biol. Cell 17, 3860–3869.

Shibata, Y., Shemesh, T., Prinz, W.A., Palazzo, A.F., Kozlov, M.M., and Rapoport, T.A. (2010). Mechanisms determining the morphology of the peripheral ER. Cell 143, 774–788.

Snapp, E.L., Reinhart, G.A., Bogert, B.A., Lippincott-Schwartz, J., and Hegde, R.S. (2004). The organization of engaged and quiescent translocons in the endoplasmic reticulum of mammalian cells. J. Cell Biol. 164, 997–1007.

Spahn, C.M., Jan, E., Mulder, A., Grassucci, R.A., Sarnow, P., and Frank, J. (2004). Cryo-EM visualization of a viral internal ribosome entry site bound to human ribosomes: the IRES functions as an RNA-based translation factor. Cell 118, 465–475.

Stephens, S.B., and Nicchitta, C.V. (2008). Divergent regulation of protein synthesis in the cytosol and endoplasmic reticulum compartments of mammalian cells. Mol. Biol. Cell 19, 623–632.

Sweeney, R., Chen, L., and Yao, M.C. (1994). An rRNA variable region has an evolutionarily conserved essential role despite sequence divergence. Mol. Cell. Biol. 14, 4203–4215.

Tyedmers, J., Lerner, M., Bies, C., Dudek, J., Skowronek, M.H., Haas, I.G., Heim, N., Nastainczyk, W., Volkmer, J., and Zimmermann, R. (2000). Homologs of the yeast Sec complex subunits Sec62p and Sec63p are abundant proteins in dog pancreas microsomes. Proc. Natl. Acad. Sci. USA 97, 7214–7219.

35

Ueno, T., Kaneko, K., Sata, T., Hattori, S., and Ogawa-Goto, K. (2012). Regulation of polysome assembly on the endoplasmic reticulum by a coiled-coil protein, p180. Nucleic Acids Res. *40*, 3006–3017.

Van den Berg, B., Clemons, W.M., Jr., Collinson, I., Modis, Y., Hartmann, E., Harrison, S.C., and Rapoport, T.A. (2004). X-ray structure of a protein-conducting channel. Nature *427*, 36–44.

Wanker, E.E., Sun, Y., Savitz, A.J., and Meyer, D.I. (1995). Functional characterization of the 180-kD ribosome receptor in vivo. J. Cell Biol. *130*, 29–39.

Watts, C., Wickner, W., and Zimmermann, R. (1983). M13 procoat and a pre-immunoglobulin share processing specificity but use different membrane receptor mechanisms. Proc. Natl. Acad. Sci. USA *80*, 2809–2813.

Zahedi, R.P., Völzing, C., Schmitt, A., Frien, M., Jung, M., Dudek, J., Wortelkamp, S., Sickmann, A., and Zimmermann, R. (2009). Analysis of the membrane proteome of canine pancreatic rough microsomes identifies a novel Hsp40, termed ERj7. Proteomics *9*, 3463–3473.

Supplemental Information

Structure and 3D arrangement of ER membrane associated ribosomes

Stefan Pfeffer[1], Florian Brandt[1], Thomas Hrabe[1], Matthias Eibauer[1], Sven Lang[2], Richard Zimmermann[2], Friedrich Förster[1*]

1: Max-Planck Institute of Biochemistry, Department of Molecular Structural Biology, D-82152 Martinsried, Germany
2: Saarland University, Medical Biochemistry and Molecular Biology, D-66421 Homburg, Germany

Inventory of the Supplemental Information

- Figure S1, related to Figure 1: Functional characterization of the imaged microsomes.

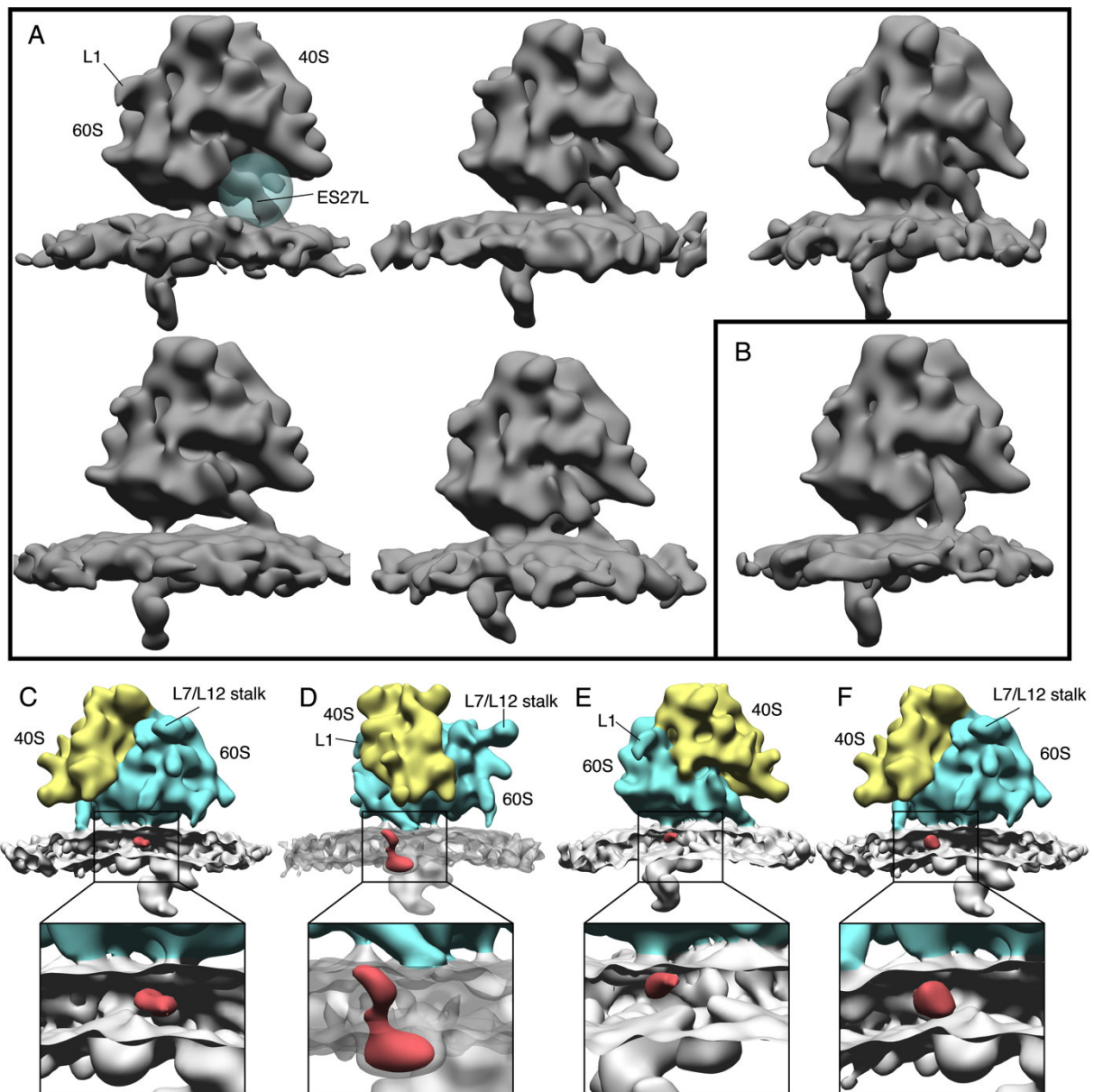- Figure S2, related to Figure 2: Classification of subtomograms by CPCA.

- Figure S3, related to Figure 3: Resolution assessment of the subtomogram average of the ER-associated ribosome *in situ* and reference-free alignment.

- Figure S4, related to Figure 4: Assignment of Sec61 and TRAP in the subtomogram average.

- Figure S5, related to Figure 5: Classification of ES27L conformations and interaction partners of the membrane-bound ribosome in the ER membrane.

- Figure S6, related to Figure 6: Distribution analysis of ER-associated ribosomes.
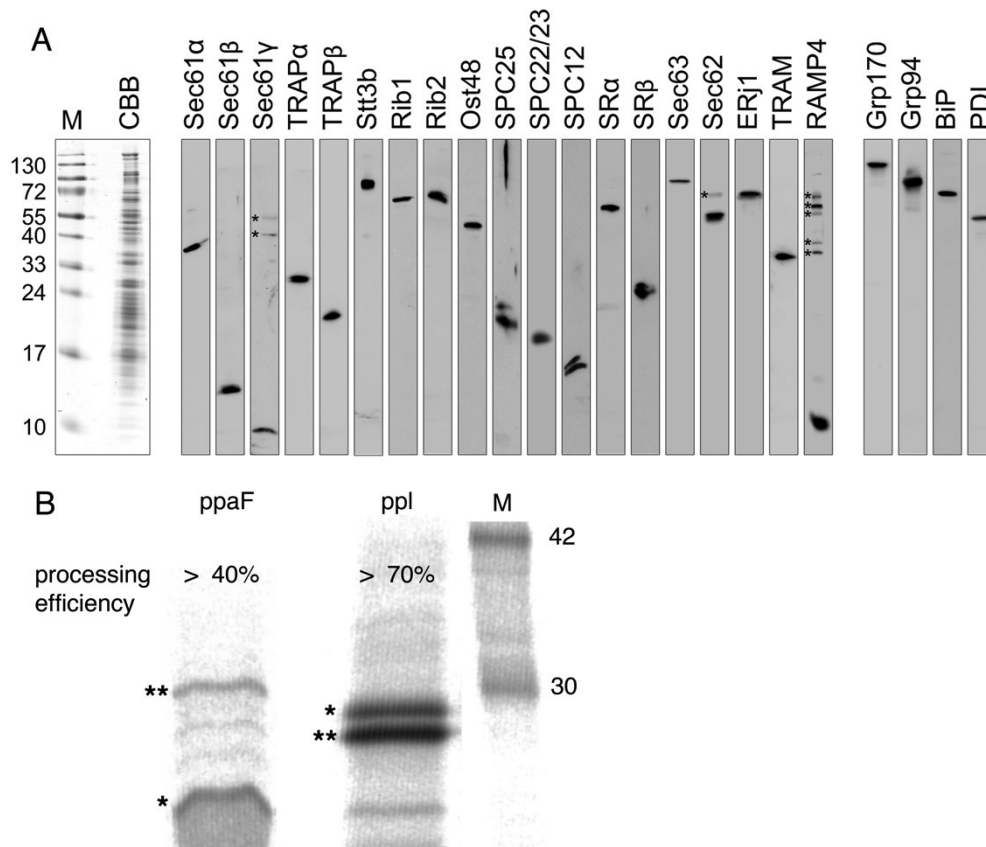
Figure S1, related to Figure 1. Functional characterization of imaged microsomes. Prior to CET, we verified that the isolated rough canine microsomes contain the proteins of interest and are competent for translocation and processing of protein substrates using an *in vitro* translation-translocation assay. **(A)** Microsomes were subjected to SDS-PAGE in combination with protein staining (CBB) or western blot analysis using antibodies that were directed against BiP (directed against the N-terminal 12-mer), ERj1 (directed against the purified protein), Grp94 (directed against the purified protein), Grp170 (directed against the N-terminal 11-mer), OST48 (kind gift from S. High, Manchester), PDI (directed against the purified protein), RAMP4 (directed against the N-terminal 10-mer), Ribophorin I (D. Meyer, Los Angeles), Ribophorin II (D. Meyer), Sec61α (directed against the C-terminal 14-mer), Sec61β (directed against the N-terminal 9-mer), Sec61γ (S. High), Sec62 (directed against the C-terminal 11-mer), Sec63 (directed against the C-terminal 14-mer), SPC25 (directed against

the C-terminal 11-mer), SPC22/23 (directed against the C-terminal 14-mer), SPC12 (directed against the N-terminal 15-mer), SRP receptor α (D. Meyer), SRP receptor ß (directed against the N-terminal 12-mer), STT3B (S. High), TRAM (directed against the C-terminal 12-mer), TRAPα (M. Wiedmann, New York), TRAPβ (directed against the N-terminal 15-mer). ER lumenal proteins are shown on the right; cross-reactions are indicated by asterisk. **(B)** Pre-pro-lactin (ppl) mRNA was prepared *in vitro* (Ambion, USA) from pB4-plasmid (Volkmer et al, 1997) and pre-pro-α-factor (ppaF) mRNA was purchased from Promega (USA). *In vitro* translation-translocation reactions were performed at 30°C in Flexi rabbit reticulocyte lysate (Promega, USA) in the presence of 1 mM L-^{35}S-methionine (Perkin Elmer, USA). Reactions were supplemented with 100 nM exogenous mRNA and canine microsomes at a concentration of 2 eq/25μl. After one hour, reactions were stopped on ice with 100 μg/μl cycloheximide (Sigma-Aldrich, Germany). Aliquots of the *in vitro* reactions were analyzed by SDS-PAGE and autoradiography. For ppaF, at least 40% of the synthesized protein (*) was translocated and processed by N-glycosylation (**). For ppl, at least 70% of the synthesized protein (*) was translocated and processed by cleavage of the signal sequence (**). Thus, we conclude that the imaged microsomes are functional and the translocation machinery is intact.
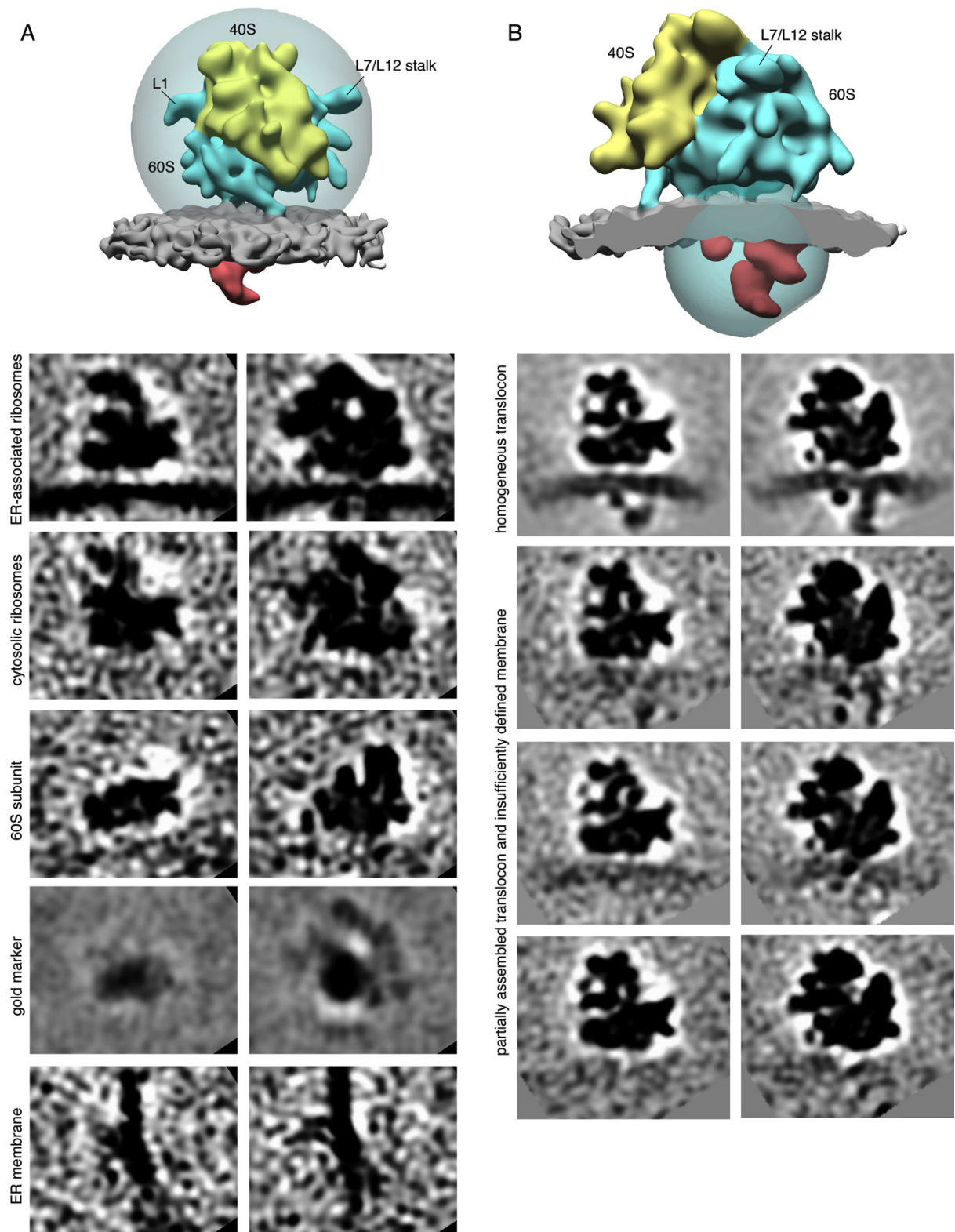
Figure S2, related to Figure 2. Classification of subtomograms by CPCA (Forster et al, 2008).

(A) Classification of subtomograms of the best 1,000 matches retrieved from template matching in one representative tomogram. The classification mask (upper panel, transparent blue) includes the central ribosome and a small proportion of the microsomal membrane. ER-

associated ribosomes could be separated from unwanted matches, such as cytosolic ribosomes, 60S ribosomal subunits, gold markers, and microsomal membrane.

(B) Classification of subtomograms containing ER-associated ribosomes. The classification mask (upper panel, transparent blue) includes lumenal electron densities and parts of the ER membrane and the large ribosomal subunit. By classification, we obtained a set of ER-associated ribosomes with homogeneous translocation machinery and well-defined membrane region.
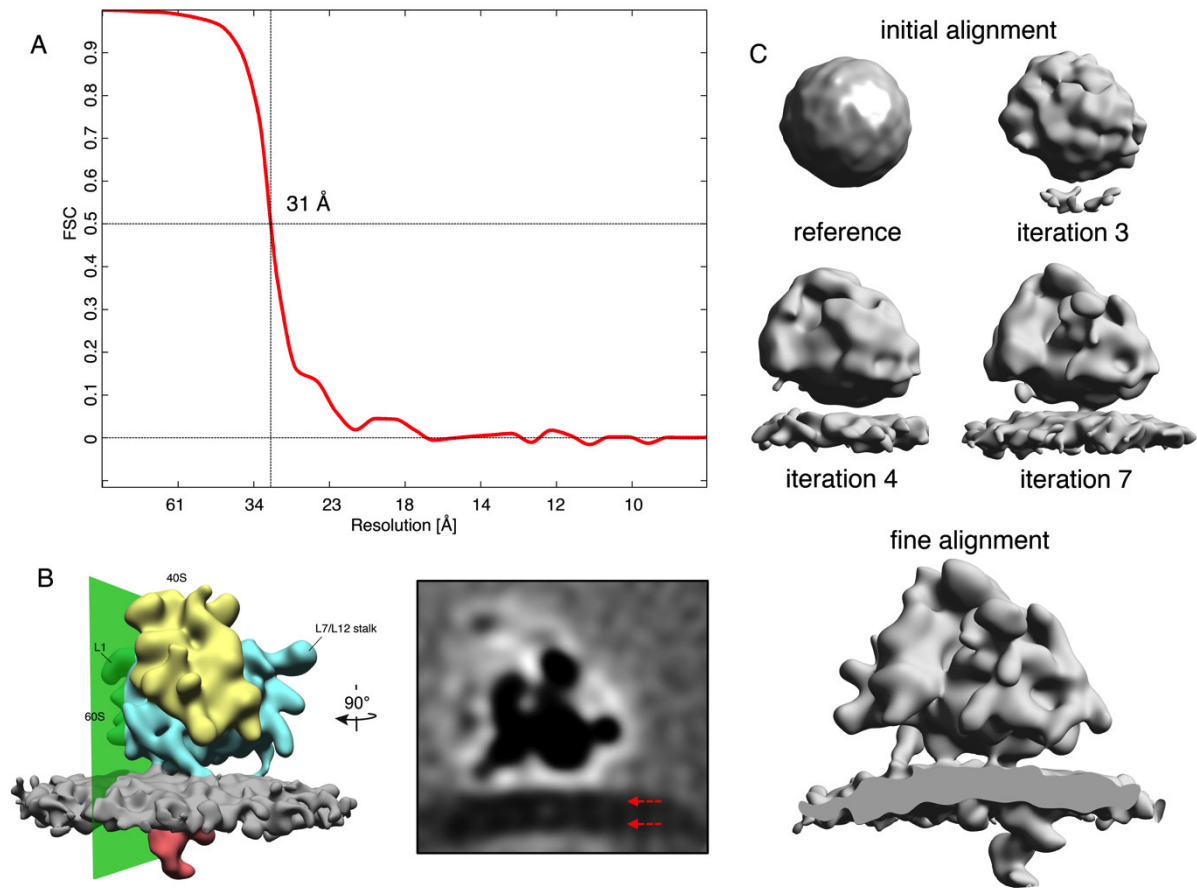
Figure S3, related to Figure 3. Resolution assessment of the subtomogram average of the ER-associated ribosome *in situ* and reference-free alignment. **(A)** Resolution determination by Fourier Shell Correlation (FSC) of two masked averages generated from each 50 % of the particles. Horizontal gray lines indicate FSC = 0 and FSC = 0.5. The vertical gray line indicates the resolution at FSC = 0.5 (31 Å). **(B)** Lipid bilayer-like morphology of the ER membrane. We extracted a slice of the subtomogram average of the membrane-associated ribosome (left, green plane). In the slice (right), the membrane reveals its typical bilayer-like appearance. Red arrows indicate the positioning of the two leaflets of the membrane bilayer. **(C)** Reference-free alignment. Reference-free subtomogram alignment was performed in PyTom. Initially, random orientations were assigned to all subtomograms and the resulting featureless average was used as a starting reference for subsequent alignment. Within each alignment iteration, global orientation sampling (angular increment: 20°) was followed by a finer local search around the highest scoring orientation from the global search (angular

increment: 10°). Starting reference and averages of selected iterations are shown (upper panel). After 7 iterations, the alignment converged into a structure, which was used as reference for final alignment of subtomograms with identical parameters as for the reference-based alignment. Three rounds of fine alignment with local angular sampling yielded a structure essentially identical to the result of the reference-based alignment (lower panel). The ER membrane was cut for better visibility of the ER-lumenal densities.
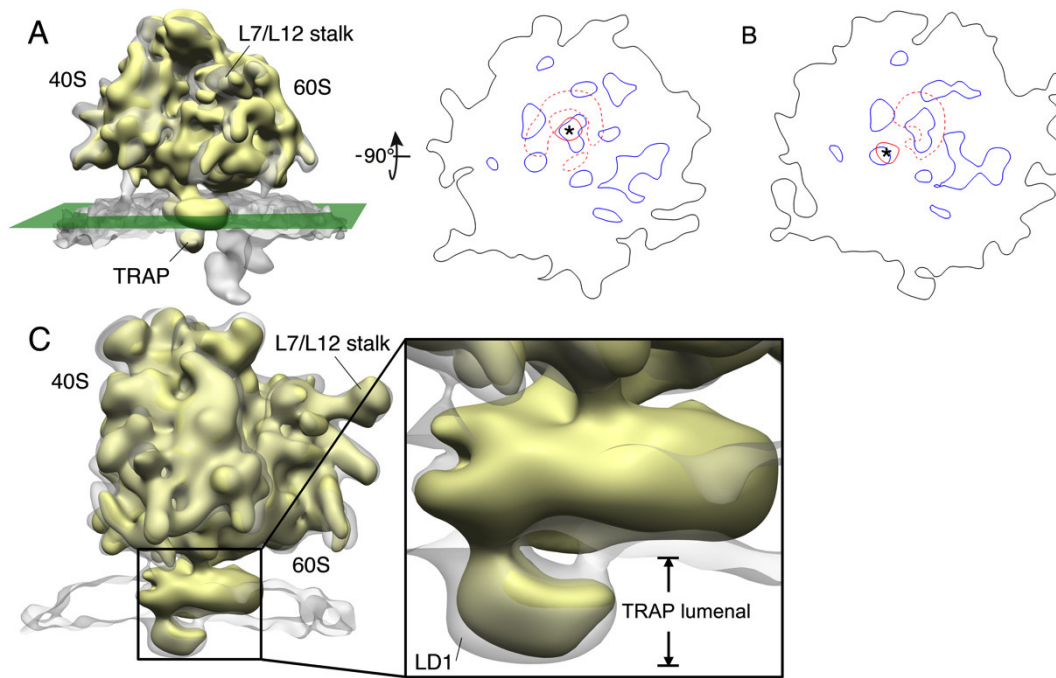
Figure S4, related to Figure 4. Assignment of Sec61 and TRAP in the subtomogram average. A single-particle reconstruction (yellow) of solubilized canine ribosome-Sec61-TRAP complex (Menetret et al, 2008) (EMDB 1528) was filtered to 30 Å resolution and superposed to the *in situ* CET map of the ER-associated ribosome (transparent). **(A)** Assignment of Sec61 in the ER membrane. The slice through the membrane region is oriented as indicated by the green plane. In the slice, density originating from proteins in the single-particle reconstruction is enclosed by solid red lines and the detergent micelle in the single-particle reconstruction is framed by dashed red lines. Blue and black isolines surround high-density (e.g. proteins) and low-density features (e.g. membrane), respectively, in the *in situ* CET map. Density assigned to the Sec61 complex in the single-particle reconstruction (asterisk) co-localizes with a specific region of high density in the *in situ* map. **(B)** Assignment of TRAP in the ER membrane. The slice is located 9 Å closer to the lumenal face of the ER membrane than in (A). Density assigned to the trans-membrane region of the TRAP complex in the single-particle reconstruction (asterisk) co-localizes with a second specific region of high density in the *in situ* CET map. **(C)** Assignment of TRAP in the ER lumen. The density assigned to the lumenal region of the TRAP complex in the single-particle reconstruction corresponds to

LD1. For better dissection of the LD1 complex, only a section of the ER membrane region of

the *in situ* map is depicted.

Figure S5, related to Figure 5**.** Classification of ES27L conformations and interaction partners of the membrane-bound ribosome in the ER membrane. **(A,B)** Classification of ES27L conformations. The classification mask, which was applied prior to classification, is superposed to the upper left average in transparent blue. Averages are filtered to a resolution of 35 Å. Classification (Förster et al, 2008) of subtomograms reveals various conformations of ES27L. ES27L predominantly (80 % of subtomograms) adopts a conformation, contacting the ER membrane approximately 15 nm away from the ribosomal tunnel exit (A). In a second, less abundant (20 % of subtomograms) conformation, ES27L interacts with the ER membrane approximately 9 nm away from the ribosomal tunnel exit (B). **(C-F)** Interactions between

ribosome and components of the ER membrane. Interaction partners within the ER membrane are shown in red. Detailed view on the interactions between the large ribosomal subunit and (C) Sec61 (as identified in Figure S4A), (D) the TRAP complex (as identified in Figure S4B and S4C), (E) an unidentified integral membrane protein close to LD2 and (F) an unidentified integral membrane protein close to Sec61.
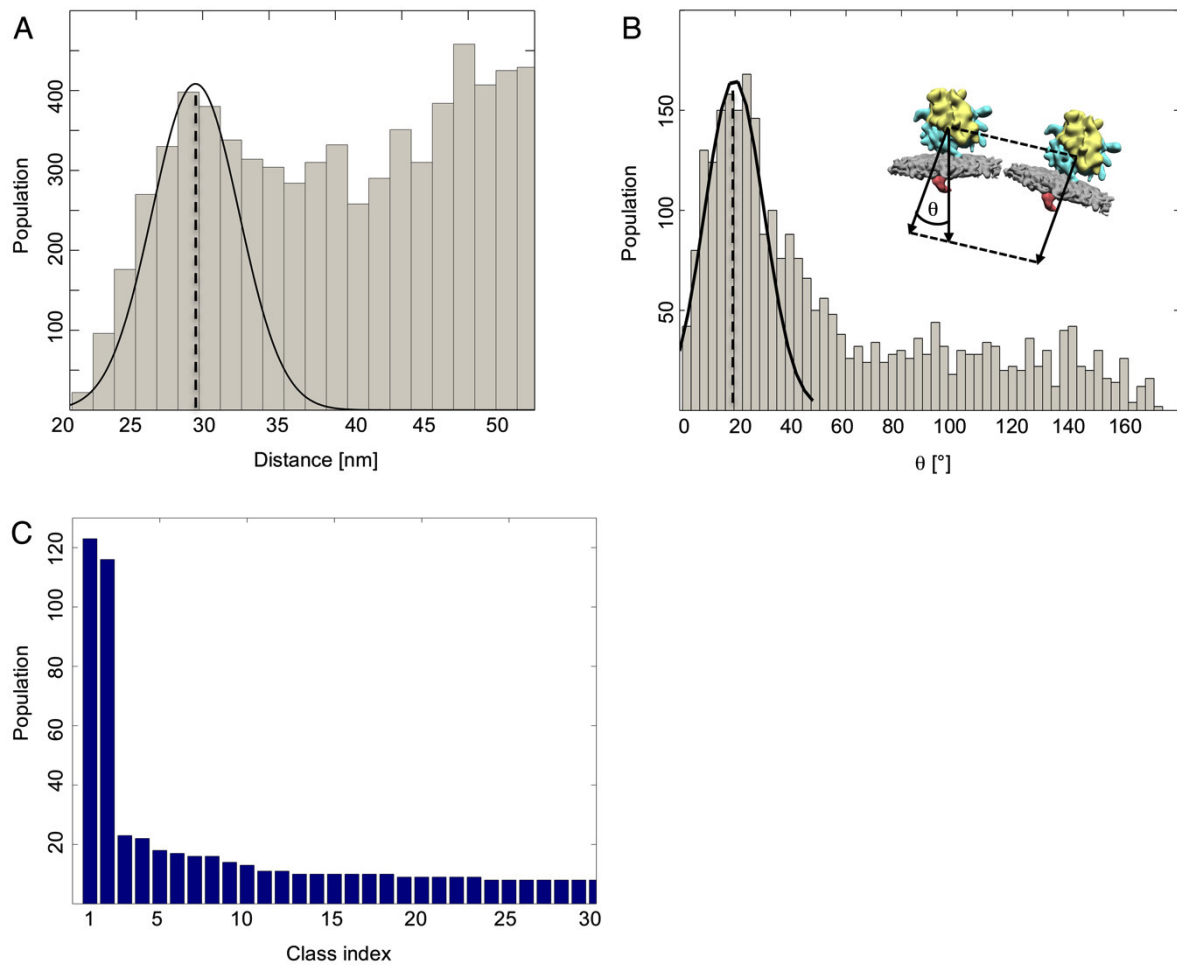
Figure S6, related to Figure 6**.** Distribution analysis of ER-associated ribosomes.

(**A**) Distance distribution of adjacent ribosomes. For each ribosome, the center-to-center distance distribution of its ten nearest neighbors was analyzed. We observed a Gaussian-like distribution with a preferred distance of 29.5 nm and a standard deviation of 3.3 nm, overlaid with the background signal of non-specifically positioned ribosomes. We restricted further analysis, to ribosomes within a distance of 20-37 nm (approximately mean plus two standard deviations). (**B**) Distribution of the ER membrane inclination between adjacent ribosomes. We analyzed the distribution of the angle θ, describing the ER membrane inclination between the central ribosome and its neighbors (see insert). We observed a Gaussian-like distribution with a preferred ER membrane inclination of 19.8° and a standard deviation of 10.9°. Further analysis was restricted to ribosomes with a membrane inclination of 0-40° (approximately mean plus two standard deviations). (**C**) Absolute populations of classes obtained from the

48

clustering in Figure 6D. We observe two highly populated classes and an evenly populated background.

Supplemental References

Volkmer J, Guth S, Nastainczyk W, Knippel P, Klappa P, Gnau V, Zimmermann R (1997) Pancreas specific protein disulfide isomerase, PDIp, is in transient contact with secretory proteins during late stages of translocation. *FEBS Lett* **406:** 291-295

2.2 Structure of the mammalian oligosaccharyl-transferase complex in the native ER protein translocon

This article was published in 2014 in Nature Communications (doi: 10.1038/ncomms4072). The supplemental material is attached at the end of the article (pages 59-80).

Summary

In this article, we combined CET with siRNA-mediated gene silencing to study translocon structure in human cells with manipulated translocon composition. Using this approach, we could verify the position of TRAP and determined the overall structure, oligomeric state and position of OST in the native ER protein translocon of human cells. Using first generation direct electron detectors for CET data acquisition, we obtained a subtomogram average of the ER-associated ribosome at 22 Å resolution, which allowed reliable dissection of lumenal and transmembrane segments of TRAP, OST and Sec61. This allowed dissecting the spatial organization of these three major translocon constituents in unprecedented detail. Finally, cryo-EM single particle analysis of detergent solubilized ribosome-translocon complexes allowed accurate positioning of an atomic model for Sec61 in the native translocon and revealed its interaction with OST in more detail. In conclusion, our study provides a basic understanding of how protein translocation into the ER and glycosylation of nascent proteins are structurally coupled.

Contribution

For this article, I carried out microsome stripping via puromycin-high salt treatment, ribosome programming with a stalling nascent peptide using a cell-free system, grid preparation for electron microscopy, acquisition of CET data and the complete workflow for data processing and map interpretation. I wrote major parts of the manuscript and prepared most of the figures.

ARTICLE

Structure of the mammalian oligosaccharyl-transferase complex in the native ER protein translocon

Stefan Pfeffer[1,*], Johanna Dudek[2,*], Marko Gogala[3], Stefan Schorr[2], Johannes Linxweiler[2], Sven Lang[2], Thomas Becker[3], Roland Beckmann[3], Richard Zimmermann[2] & Friedrich Förster[1]

In mammalian cells, proteins are typically translocated across the endoplasmic reticulum (ER) membrane in a co-translational mode by the ER protein translocon, comprising the protein-conducting channel Sec61 and additional complexes involved in nascent chain processing and translocation. As an integral component of the translocon, the oligosaccharyl-transferase complex (OST) catalyses co-translational N-glycosylation, one of the most common protein modifications in eukaryotic cells. Here we use cryoelectron tomography, cryoelectron microscopy single-particle analysis and small interfering RNA-mediated gene silencing to determine the overall structure, oligomeric state and position of OST in the native ER protein translocon of mammalian cells in unprecedented detail. The observed positioning of OST in close proximity to Sec61 provides a basis for understanding how protein translocation into the ER and glycosylation of nascent proteins are structurally coupled. The overall spatial organization of the native translocon, as determined here, serves as a reliable framework for further hypothesis-driven studies.

[1] Department of Molecular Structural Biology, Max-Planck Institute of Biochemistry, Am Klopferspitz 18, D-82152 Martinsried, Germany. [2] Department of Medical Biochemistry and Molecular Biology, Saarland University, D-66421 Homburg, Germany. [3] Gene Center and Center for integrated Protein Science Munich, Department of Biochemistry, University of Munich, D-81377 Munich, Germany. * These authors contributed equally to this work. Correspondence and requests for materials should be addressed to F.F. (email: foerster@biochem.mpg.de).

51

In mammalian cells, co-translational N-glycosylation is one of the most common covalent protein modifications. This essential reaction is catalysed by the oligosaccharyl-transferase complex (OST)[1–3], an elaborate multisubunit complex integrated into the endoplasmic reticulum (ER) protein translocon. The catalytic OST subunit is present in two paralogous forms, STT3A and B, joined by at least six accessory subunits of poorly understood function: ribophorin I (RibI), ribophorin II (RibII), OST48, DAD1, N33 or IAP, and OST4. Sequence analysis and proteinase protection assays[4] suggest that all OST subunits are integral membrane proteins and many possess substantial lumenal domains, adding up to nearly 200 kDa[2] (Supplementary Fig. 1). Despite its essential function, structural information on OST and its integration into the ER protein translocon is sparse and inconclusive. Recently, we gained first insights into the organization of the native translocon from a reconstruction of endogenous 80S ribosomes, attached to canine pancreatic rough microsomes (RMs), obtained using cryoelectron tomography (CET) and subtomogram analysis[5]. In the ribosome-associated density corresponding to the translocon, we discerned several membrane-embedded and lumenal complexes, including the protein-conducting channel Sec61, the translocon-associated protein complex (TRAP) and a large lumenal density, protruding 9 nm into the lumen.

In this work, we localize OST in the native mammalian ER protein translocon using CET in combination with small interfering RNA (siRNA)-mediated gene silencing in human cells. Determining the structure of ribosome nascent chain complexes (RNCs) bound either to the native or solubilized translocon of canine pancreatic microsomes using CET and single-particle analysis (SPA) allows dissecting the structure and integration of OST in the mammalian translocon in unprecedented detail.

Results

Confirming the position of TRAP in the native translocon. As a control for following silencing experiments, we first analysed RMs from HeLa cells that were treated with non-silencing siRNA. Classification of automatically located and iteratively aligned subtomograms depicting ER membrane-associated ribosomes revealed that two distinct populations of translocons were present in the data, including (42%) and lacking (58%) a large lumenal density (LD) (Supplementary Fig. 2a). For the final subtomogram average (Fig. 1a), only particles including LD were retained, yielding a resolution of 40 Å. The average shares all low-resolution features with the map of the canine ER-associated ribosome we previously reported[5], and was used as a control map for the evaluation of different knockdown structures in the following.

As a proof-of-principle for the gene-silencing approach, TRAPβ was chosen as a target due to the previously established position of TRAP in the detergent-extracted translocon by cryoelectron microscopy (cryo-EM) SPA[6]. TRAPβ (SSR2) gene silencing for 96 h did not have major effects on cell growth (88 ± 7% s.e.m. of control siRNA-treated cells; n = 4), ER integrity (Table 1), ER morphology (Supplementary Fig. 3b), protein translocation and substrate processing (Supplementary Fig. 4a). Western blotting indicates a nearly quantitative depletion of the target protein as well as all other TRAP subunits (Fig. 1b and Table 2), as previously observed[7]. As there was no decrease in the transcription of the TRAPα (SSR1) gene (Supplementary Fig. 5a), depletion of non-target TRAP subunits was most likely to be due to destabilization of TRAP and subsequent degradation of subunits. Consistent with the control data set, translocons including (43%) and lacking (57%) LD were present in the TRAPβ knockdown data (Supplementary Fig. 2b). Again, only
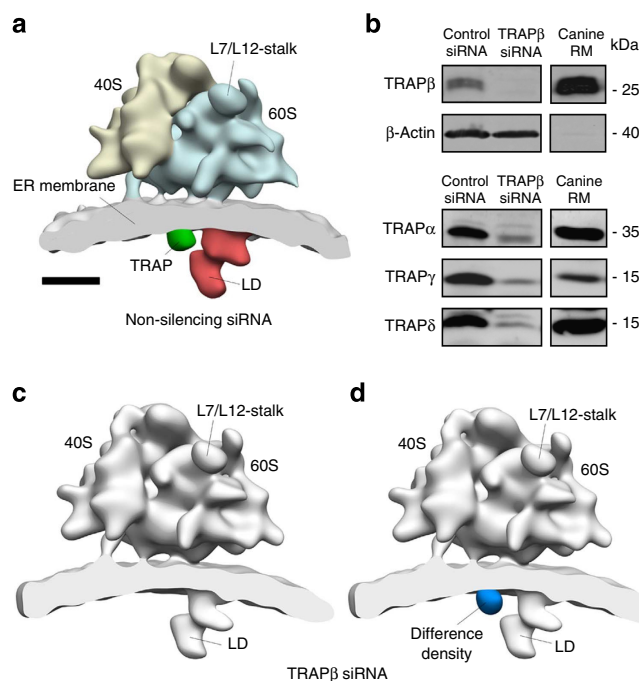
Figure 1 | Localization of TRAP in a subtomogram average of the human ER membrane-associated ribosome. (**a**) Subtomogram average for microsomes, isolated from HeLa cells treated with non-silencing control siRNA. Only particles including LD were retained for the average (Supplementary Fig. 2a). Scale bar, 10 nm. (**b**) HeLa cells were treated with TRAPβ or control siRNA. Protein levels of the target protein, as well as of TRAPα, γ and δ after TRAPβ gene silencing were analysed by SDS–PAGE and western blot analysis. As a positive control for the TRAP antibodies, an aliquot of rough canine microsomes (RMs) was run in parallel. The differences in intensity in the canine RMs compared with HeLa total lysate are due to the different concentrations of ER proteins in the samples and species differences in antibody affinity. (**c,d**) The subtomogram average for microsomes, isolated from TRAPβ-depleted HeLa cells is shown with (**d**) and without (**c**) the difference density to the control, isosurface rendered at 6σ (blue). All structures were filtered to a resolution of 40 Å.

particles including LD were retained for the final average. Different from the control, essentially the entire density assigned to TRAP disappeared (Fig. 1c), which is also highly significant in the difference map to the control (Fig. 1d). Thus, the position of TRAP, previously assigned based on the purified and solubilized ribosome–Sec61–TRAP complex[6], was confirmed in situ and we concluded that a 60-kDa lumenal density can be localized accurately using in situ CET in combination with gene silencing.

Identification and localization of OST in the native translocon. On the basis of its size and position close to Sec61, we speculated that LD might represent the nascent-chain-processing OST complex. Therefore, we depleted HeLa cells of either RibI or RibII, both integral OST subunits. Silencing of RPN1 and RPN2, coding for RibI and RibII, respectively, for 72 h only had mild effects on cell growth (88 ± 5% s.e.m. (n = 6) and 76 ± 16% s.e.m. (n = 3) of control siRNA-treated cells for RibI and RibII, respectively), ER integrity (Table 1), ER morphology (Supplementary Fig. 3c,d) and protein translocation activity (Supplementary Fig. 4b). For the RibI knockdown, western blotting indicates a strong reduction of the target protein (<10% residual protein) and also partial depletion of at least four other OST subunits (RibII, STT3B, OST48 and DAD1; Fig. 2a and

Table 1 | Relative protein content of selected ER-resident proteins after silencing with the indicated siRNA.

Protein	TRAPβ siRNA	RibI siRNA	RibII siRNA
ER membrane proteins			
Sec61α	102 ± 5 (9)	122 ± 8 (6)	122 ± 7 (2)
SPase25	96 ± 10 (2)	113 ± 0 (1)	240 ± 29 (2)
SPase22/23*	84 ± 2 (6)	122 ± 8 (4)	170 ± 10 (4)
Sec62	105 ± 4 (10)	104 ± 8 (3)	106 ± 10 (4)
Sec63	107 ± 6 (6)	101 ± 9 (4)	91 ± 8 (4)
Calnexin	115 ± 5 (4)	104 ± 4 (3)	111 ± 3 (3)
SRα	111 ± 9 (8)	110 ± 2 (2)	127 ± 0 (1)
ERj1	107 ± 9 (8)	112 ± 7 (4)	129 ± 2 (2)
Lumenal proteins			
BiP	100 ± 5 (9)	181 ± 15 (4)	151 ± 25 (2)
GRP170*	103 ± 6 (10)	89 ± 4 (5)	87 ± 9 (3)
GRP94*	89 ± 9 (8)	87 ± 16 (4)	89 ± 17 (3)
ERp57	95 ± 7 (7)	93 ± 13 (4)	92 ± 19 (3)

ER, endoplasmic reticulum; RibI, ribophorin I; RibII, ribophorin II; siRNA, small interfering RNA.
Protein content given as % of control siRNA-treated cells; normalized to β-actin; mean values ± s.e.m; *n* given in parenthesis.
*Glycosylated protein.

Table 2 | Relative protein content of TRAP and OST subunits after silencing with the indicated siRNA.

Protein	TRAPβ siRNA	RibI siRNA	RibII siRNA
TRAP complex			
TRAPα*	21 ± 7 (7)	64 ± 0 (2)	89 ± 10 (2)
TRAPβ*	6 ± 2 (7)	100 ± 18 (4)	117 ± 14 (3)
TRAPγ	21 ± 1 (5)	159 ± 11 (3)	118 ± 0 (1)
TRAPδ	6 ± 2 (5)	111 ± 1 (3)	103 ± 0 (1)
OST			
RibI*	90 ± 18 (2)	8 ± 2 (6)	94 ± 14 (5)
RibII*	99 ± 13 (3)	24 ± 6 (5)	9 ± 2 (7)
STT3B*	ND	40 ± 3 (6)	38 ± 5 (3)
OST48	97 ± 6 (4)	25 ± 6 (6)	33 ± 9 (4)
DAD1	74 ± 8 (2)	27 ± 6 (4)	30 ± 7 (3)

ND, not determined; OST, oligosaccharyl-transferase complex; RibI, ribophorin I; RibII, ribophorin II; siRNA, small interfering RNA; TRAP, translocon-associated protein complex.
Protein content given as % of control siRNA-treated cells; normalized to β-actin; mean values ± s.e.m; *n* given in parenthesis.
*Glycosylated protein.

Table 2), analogous to knockdown studies of other OST subunits[8]. For the RibII knockdown, nearly quantitative depletion of the target protein and strong reduction of three out of the four other OST subunits (STT3B, OST48 and DAD1) was observed, whereas RibI was only moderately affected (Fig. 2c and Table 2). Reverse transcription–PCR (RT–PCR) data indicate that depletion of non-target OST subunits is due to protein degradation for both knockdowns (Supplementary Fig. 5b,c). As reported previously[9], depletion of RibI resulted in only a mild and selective glycosylation defect (Supplementary Fig. 4b). We suggest that single catalytically active STT3 subunits may be able to independently perform N-glycosylation after RibI depletion. The subtomogram averages of both knockdown samples and their difference maps to the control are largely identical (Fig. 2b,d): essentially all density assigned to LD in the control map disappeared, confirming our hypothesis that LD represents or at least includes OST. A second, significant reduction of density in the knockdowns can be observed at the cytosolic face of the ER membrane, directly opposed to LD. This density

may correspond to cytosolic domains of OST and possibly associated proteins.

The only further known component of the translocon that contains notable lumenal segments (47 kDa) is the signal peptidase complex (SPase)[10]. To rule out the possibility that LD corresponds to an OST–SPase supercomplex, we also depleted SPase subunits from HeLa cells and analysed the derived microsomes by CET. Comparison with the control structure revealed no significant reduction of density in the resulting subtomogram average (Supplementary Fig. 6). Consistent with CET analysis of the SPase knockdown, depletion of OST subunits did not affect the stability of SPase subunits, as judged by western blotting (Table 1). In conclusion, LD does not comprise SPase and thus most probably corresponds to OST alone. This positioning of OST in the native translocon allows for concomitant scanning of a nascent polypeptide for glycosylation sites, while it is conducted into the ER lumen, thus providing a basic understanding of how protein translocation into the ER and glycosylation of nascent proteins are structurally coupled. From the good agreement of the approximate molecular weight of LD (170–200 kDa) with the lumenal mass of OST, as well as the absence of multiply-occurring structural features in LD, we furthermore conclude that OST is present in only one copy in the native translocon, in contrast to previous hypotheses of a dimeric OST organization[11].

Structure and integration of OST in the native translocon. To resolve native OST and its surroundings at a greater level of detail, we used a cell-free translation/translocation system to populate vacant translocons of ribosome-stripped canine pancreatic microsomes with homogenous RNCs stalled on the regulatory peptide of the human cytomegalovirus (CMV) gp48 upstream open-reading frame 2 (ref. 12). Quantitative stalling and high translocation efficiency (~95%) in the cell-free system were verified by SDS–polyacrylamide gel electrophoresis (SDS–PAGE) and western blotting (Supplementary Fig. 7).

ER membrane-associated ribosomes from tomographic reconstructions (Supplementary Fig. 8) were iteratively aligned and classified, confirming the presence of two distinct populations of translocons, including (63%) and lacking (37%) OST (Supplementary Fig. 2e). The ribosome bound to the OST-containing translocon (Fig. 3a) was resolved to 22 Å (Supplementary Figs 9 and 10) and shares all low-resolution features with the endogenous human ER membrane-associated ribosome (Fig. 1a). The translocon is embedded into a well-resolved membrane bilayer and dense regions that transverse the membrane can be distinguished (Fig. 3b–e), likely to be corresponding to tightly packed transmembrane segments of integral membrane proteins, referred to as membrane anchors (MAs) in the following. In the density, the hook-shaped lumenal part of OST is connected to the ER membrane by two MAs (Fig. 3d,e), one of them likely to be corresponding to the tightly packed 13-transmembrane helices of the catalytic subunit STT3 (ref. 13).

To locate the Sec61 protein-conducting channel in the subtomogram average, a single-particle reconstruction of the canine ribosome (EMD 1480)[14] and an aligned atomic model of the nascent-chain-translocating canine Sec61 complex[15] were fitted into the subtomogram average as one rigid body. Near the ribosomal tunnel exit, a high-density region of the subtomogram average (Fig. 3b) exactly co-localizes with the fitted atomic model of Sec61 (Supplementary Fig. 11), allowing an unambiguous identification of Sec61 in the translocon density. Directly adjacent to the density attributed to Sec61, TRAP is resolved with its prominent ER-lumenal domain and one MA (Fig. 4c).

To visualize their spatial organization in the native translocon, lumenal and transmembrane segments of OST, Sec61 and TRAP

53
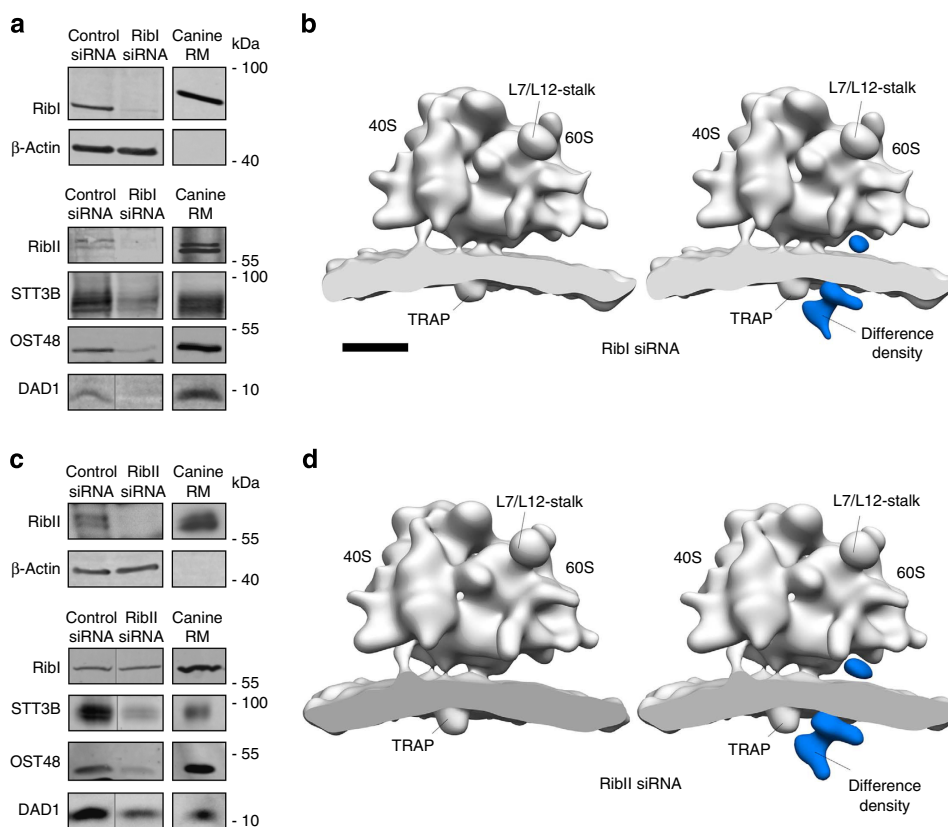
Figure 2 | Localization of OST in subtomogram averages of the human ER membrane-associated ribosome. HeLa cells were treated with RibI (**a**,**b**) or RibII (**c**,**d**) and control siRNA. Protein levels of the target proteins, as well as non-target OST subunits after RibI (**a**) or RibII (**c**) gene silencing were analysed by SDS–PAGE and western blot analysis. As a positive control for the OST antibodies, an aliquot of rough canine microsomes (RMs) was run in parallel. The differences in intensity in the canine RMs compared with HeLa total lysate are due to the different concentrations of ER proteins in the samples and species differences in antibody affinity. The subtomogram averages for microsomes, isolated from RibI- (**b**) or RibII- (**d**) depleted HeLa cells are shown with (right) and without (left) the difference density to the control, isosurface rendered at 6σ (blue). All structures were filtered to a resolution of 40 Å. Scale bar, 10 nm.

were automatically segmented from the subtomogram average (Fig. 3f and Supplementary Movie 1), revealing a potential interface between Sec61 and OST within the ER membrane (Supplementary Fig. 12). To analyse this interaction in more detail, we compared the subtomogram average to a reconstruction by cryo-EM SPA of wheatgerm RNCs bound to the mammalian translocon. Although detergent solubilization yielded primarily RNC–Sec61 complexes[15], particle sorting also revealed an additional less-populated class that is similar to the subtomogram average (Fig. 4a). It is known that TRAP and OST co-purify under mild solubilization conditions with Sec61 as part of the so-called RAMP fraction (ribosome-associated membrane proteins)[16], and mass spectrometry (MS) analysis indeed confirmed that among the 100 most abundant proteins in the sample, there are almost exclusively ribosomal proteins and subunits of the Sec61, TRAP and OST complexes (Supplementary Data 1). Therefore, the observed similarity strongly suggests that this particle population corresponds to RNCs bound to the Sec61–OST–TRAP complex.

The local resolution of Sec61 is in the range of the global resolution of the single-particle reconstruction (10 Å), but TRAP and OST are less well resolved, probably due to underrepresentation or a higher degree of flexibility in the detergent micelle. Secondary structure elements of Sec61 that are resolved in several areas of the map (Fig. 4b and Supplementary Fig. 13) allowed us to accurately position the protein-conducting channel in the translocon and to fit an atomic model of the

nascent-chain-translocating heterotrimeric Sec61 complex (Supplementary Fig. 13)[15]. Notably, the position and overall arrangement of the Sec61 complex in the presence of TRAP and OST remain indistinguishable from the canonical position observed previously for the ribosome-bound Sec61 or SecYEG complexes alone[17,18]. Superposition of the subtomogram average and the single-particle reconstruction showed a spatial coincidence of the translocon densities (Fig. 4c,d) and allowed accurate positioning of Sec61 in relation to OST and TRAP in the subtomogram average. Here, one of the two MAs of OST is in direct proximity to the carboxy-terminal region of Sec61γ and a hinge helix between the amino- and the C-terminal halves of Sec61α (Fig. 5 and Supplementary Fig. 13), suggesting that this interface contributes to the stable integration of OST into the translocon.

Discussion

In this work, we used CET, SPA and siRNA-mediated gene silencing to determine the overall structure, oligomeric state and position of OST in the native ER protein translocon of mammalian cells. The position of OST in close proximity to Sec61 (Fig. 5) agrees well with crosslinking studies, indicating proximity of OST to both the large ribosomal subunit[19] and the Sec61 complex[20], and it is also consistent with negative-stain EM images of ribosomal particles, showing additional density close to the ribosomal tunnel exit on complex formation with OST[21].

54
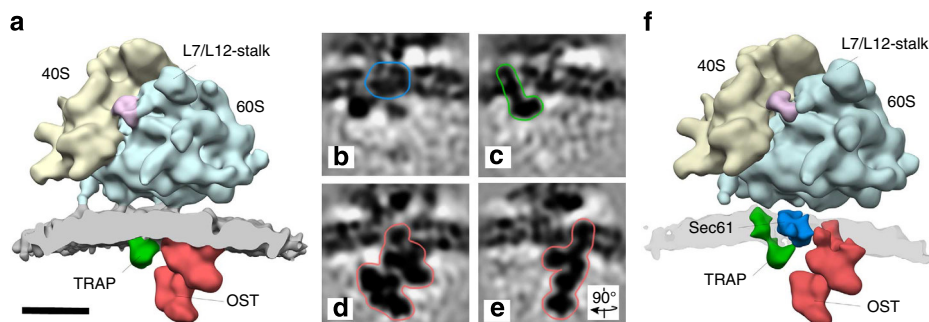
Figure 3 | Subtomogram average of the stalled mammalian ribosome bound to canine pancreatic microsomes. (**a**) Subtomogram average at 22 Å resolution. On the ribosomal stalk base, additional non-ribosomal density is resolved (magenta) that potentially corresponds to canonical translation, elongation or termination factors. Scale bar, 10 nm. (**b**–**e**) Structural details of the membrane and ER lumenal region of the subtomogram average after alignment focused on this region. Lumenal and/or transmembrane segments (outlined) of Sec61 (**b**) (as identified in Supplementary Fig. 11), TRAP (**c**) and OST (**d**,**e**) can be discerned. Slices in **b**–**d** are oriented as in **f**, the slice in **e** is rotated by 90°. (**f**) Lumenal and transmembrane segments of OST (red), Sec61 (dark blue) and TRAP (green) were automatically segmented from the subtomogram average.
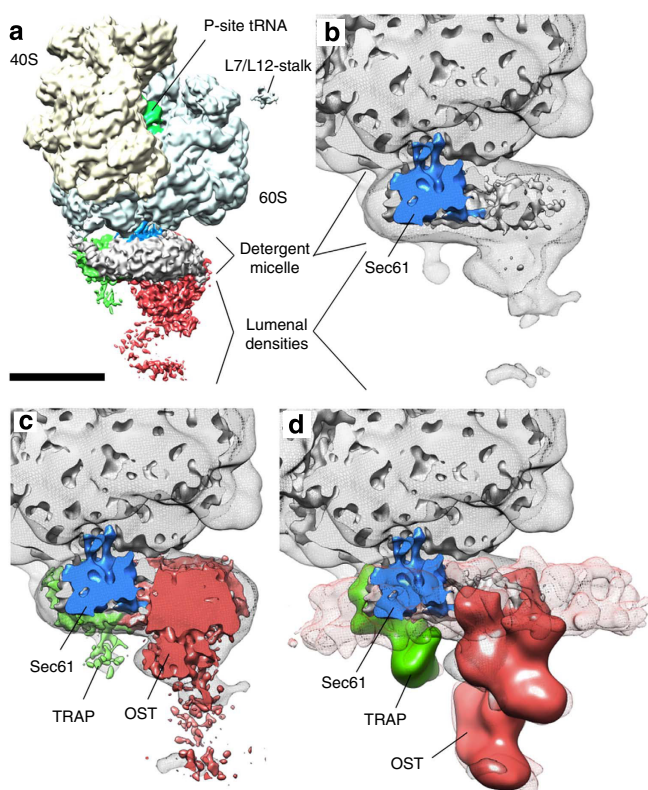
Figure 4 | Single-particle reconstruction of stalled ribosomes bound to solubilized canine Sec61–OST–TRAP complexes. (**a**) Reconstruction filtered to 10 Å resolution. Colouring as in Fig. 3f. Scale bar, 10 nm. (**b**) Magnified view of the reconstruction with Sec61 segmented from the map (blue). The overall density is shown at two different resolutions and threshold levels (grey) to visualize the high-resolution details of Sec61, but also the overall structure of the translocon. (**c**,**d**) Additional densities in the single-particle reconstruction (**c**) co-localize with the isolated TRAP and OST densities from the subtomogram average (**d**).

In the overall arrangement of the translocon determined here (Fig. 5), the directly adjacent OST and TRAP complexes spatially confine the C-terminal segment of Sec61α. This is in agreement with a rigid positioning of the C-terminal half of Sec61 on the ribosome in different functional states[15]. The N-terminal segment of Sec61α, in contrast, is spatially less constrained, which may be

required to adopt the observed more open states during peptide translocation or membrane insertion[15]. Notably, the Sec61 lateral gate, through which transmembrane helices of nascent membrane proteins are released into the membrane bilayer, points away from OST (Fig. 5). The resulting distant positioning of OST from nascent transmembrane helices may explain why glycosylation consensus motifs have to be located more than 12–15 amino acid residues ($\sim$3–5 nm) away from a transmembrane helix to be glycosylated efficiently during translocation into the ER lumen[22].

In contrast to the excellent agreement of the position of OST in the native translocon determined here with previously established biochemical information, the structure of native mammalian OST itself (Fig. 3) is difficult to reconcile with a previous single-particle study of detergent-solubilized, isolated yeast OST[23]. In the latter reconstruction, the overall shape of OST appears much more compact than determined here, while the surface appears unusually ragged. The structural discrepancy between the native mammalian OST structure and the single-particle reconstruction of detergent-solubilized, isolated yeast OST may be due to interspecies differences in the size of the RibI and RibII subunits, different conformational states of the complex, destabilization of OST in the detergent micelle, or the high error margin in cryo-EM single-particle reconstructions of small detergent-extracted complexes. Cryo-EM single-particle reconstructions can bear significant errors, as recently discussed[24,25]. This holds true in particular for detergent-extracted complexes, because the particles tend to be heterogeneous due to the formation of micelles, and for small complexes (traditionally below $\sim$300–500 kDa), because the amount of signal may be insufficient for accurate alignment of the single particles[26].

An unexpected finding in our analysis of the translocon is that in all microsome data sets analysed in this work, two distinct translocon populations—including and lacking OST—were present (excluding the RibI and RibII knockdown tomograms, of course; Supplementary Figs 2 and 6). Albeit it cannot be entirely ruled out that partial dissociation of OST is induced by microsome formation at this point, the fact that OST remains partially associated to Sec61 even after detergent solubilization, and the tight interaction between Sec61 and OST observed in our subtomogram average, both suggest that translocon populations including and lacking OST also coexist in the cell. Whether OST is recruited transiently to the translocon during translocation of nascent peptides or whether two stable, specialized species of translocon complexes exist and how co-translational glycosylation of nascent peptides is assured remains subject to future studies.
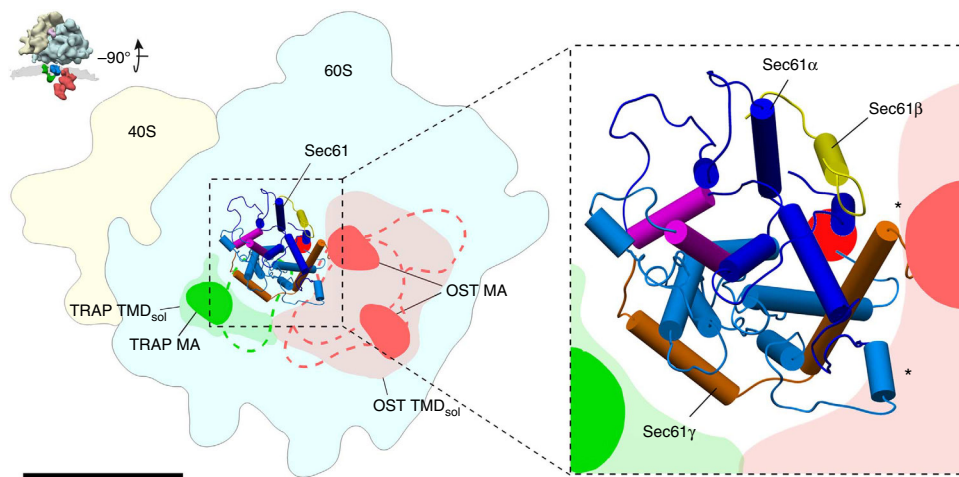
Figure 5 | Spatial organization of OST, Sec61 and TRAP in the translocon seen from the ER lumen. For TRAP (green) and OST (red), MAs and lumenal segments (dashed lines) from the native translocon, as well as transmembrane density from the solubilized translocon (TMD$_{sol}$) were projected onto the membrane plane. Atomic models for Sec61α (N-terminal half: dark blue; C-terminal half: light blue), Sec61β (yellow) and Sec61γ (orange), as well as the position of the peptide exit tunnel (red dot) on the large ribosomal subunit and the Sec61 lateral gate (magenta helices), are depicted. One of the two MAs of OST is in proximity to the C-terminal region of Sec61γ and a hinge helix between the N- and the C-terminal halves of Sec61α (asterisks). Scale bar, 10 nm.

In summary, the spatial organization of the translocon described here provides a basis for understanding how protein translocation into the ER and N-glycosylation of nascent proteins are structurally coupled and it serves as a reliable framework for further hypothesis-driven functional studies. In conjunction with orthogonal structural data, our density of the translocon may also allow dissecting the TRAP and OST complexes in further detail using integrative approaches in the future[27].

Methods

Cell culture. HeLa cells (ATCC number CCL-2) were cultured in DMEM (Gibco-Invitrogen, Karlsruhe, Germany) containing 10% FBS (Biochrom, Berlin, Germany) and 1% penicillin and streptomycin (PAA, Pasching, Austria) in a humidified environment with 5% CO_2 at 37 °C.

Gene silencing of HeLa cells. For gene-silencing experiments, 1.2×10^6 HeLa cells were seeded per 10-cm culture dish and transfected with RibI siRNA (5'-CGU ACA UUG AGA AUG AGA AdTdT-3'; Qiagen, Hilden, Germany) for silencing of *RPN1* gene, RibII siRNA (5'-GGC UAU CUU GCG GUU GCA AdTdT-3'; Qiagen) for silencing of *RPN2* gene or SPC25 siRNA (5'-CCA UGA CAG UCU UGC CAU AdTdT-3'; Qiagen) for silencing of *SPC25* gene, respectively, at a final concentration of 25 nM using HiPerFect Reagent (Qiagen). After 24 h, the medium was changed and the cells were transfected a second time. SSR2 gene silencing was carried out according to the same protocol with TRAPβ siRNA (5'-AAG GGU AUC UUA AAU GCA AdTdT-3'; Qiagen) at a final concentration of 10 nM. The non-silencing AllStars Negative Control siRNA (Qiagen) served as control siRNA. Silencing was evaluated by RT–PCR and western blot analysis as described.

Quantitative RT–PCR analysis. Cells were harvested and total RNA was isolated using the QIAamp RNA Blood Kit (Qiagen). Reverse transcription of mRNA was performed with Superscript II RT (Invitrogen, Darmstadt, Germany) and oligo(dT) primers (Invitrogen), and the resulting complementary DNA was purified using the PCR Purification Kit (Qiagen). TaqMan Gene Expression Assays (Applied Biosystems, Darmstadt, Germany) were used for quantitative real-time RT–PCR of *TRAPα* (Hs00162340_m1), *TRAPβ* (Hs00162346_m1), *RPN1* (Hs00161446_m1), *RPN2* (Hs00955802_m1), *STT3B* (Hs00385811_m1), *DDOST* (Hs00193263_m1) and *DAD1* (Hs02912874_m1) in a StepOne Plus 96-well system (Applied Biosystems). Relative gene expression was calculated using the comparative C_T method[28] with *ACTB* (Hs00357333_g1) serving as internal control. ΔCt values were then normalized to control siRNA-treated cells.

Semi-quantitative western blot analysis. Rabbit antibodies were raised against the C-terminal peptides of human Sec61α (14-mer), SPase22/23 (14-mer), SPase25 (11-mer), Sec62 (11-mer) and TRAPα (15-mer), or the N-terminal peptides of human BiP (12-mer), human SPase12 (15-mer) and Grp170 (11-mer) plus an N- or C-terminal cysteine, human TRAPβ (aa 18–32) and human SRα (aa 137–150),

plus a C-terminal cysteine, dog GRP94, human Sec63-ΔN380 and murine ERj1C-ΔN21 (ref. 29). Antibodies directed against RibI, RibII, STT3B and DAD1 were a kind gift from S. High (Manchester, UK). The ERp57 antibody was a kind gift from T. Wileman (Norwich, UK). Antibodies directed against OST48 (Santa Cruz Biotechnology, Heidelberg, Germany), Calnexin (Stressgene, Hamburg, Germany) and TRAPγ, TRAPδ and β-actin (Sigma, Taufkirchen, Germany) were obtained from commercial sources. The primary antibodies were visualized using peroxidase-conjugated anti-rabbit IgG-goat antibodies (Sigma), ECL Plex goat anti-rabbit IgG-Cy5 conjugate or ECL Plex goat anti-mouse IgG-Cy3 conjugate (GE Healthcare, Freiburg, Germany) and X-ray films (GE Healthcare), or the Typhoon-Trio imaging system (GE Healthcare) in combination with Image Quant TL software 7.0 (GE Healthcare). Full scans of all western blottings are shown in Supplementary Figs 14–18. Working dilutions of all antibodies and catalogue numbers of purchased antibodies are listed in Supplementary Table 1.

Protein transport assays. Precursor polypeptides were synthesized in reticulocyte lysate (nuclease treated; Promega, Heidelberg, Germany) in the presence of [^{35}S]methionine (Perkin Elmer, Rodgau-Jügesheim, Germany) plus buffer or semipermeabilized cells for 60 min at 30 °C. Semipermeabilized cells were prepared from identical cell numbers according to a published procedure[30]. All samples were analysed by SDS–PAGE and phosphorimaging using the Typhoon-Trio imaging system (GE Healthcare) in combination with Image Quant TL software 7.0 (GE Healthcare). Full phosphorimaging scans are shown in Supplementary Fig. 19.

Immunofluorescence microscopy. Cells were fixed with paraformaldehyde, washed and an indirect immunofluorescence staining was performed with an affinity-purified rabbit anti-peptide antibody directed against the human Sec62 (C-terminal 11-mer plus an N-terminal cysteine) and Alexa-Fluor-594-coupled secondary antibody from goat (Invitrogen). We note that the anti-Sec62 antibody is specific for Sec62 under denaturing as well as native conditions (that is, western blotting and fluorescence microscopy signals were quenched after silencing of the *SEC62* gene)[31]. Cells were analysed by microscopy using an Elyra SIM (Carl Zeiss MicroImaging, Göttingen, Germany). Synthesis of the Sec62 protein was not affected by *RPN1*, *RPN2* and *TRAPβ* gene silencing (Table 1).

Preparation of RMs from culture cells. siRNA-treated cells (30×10^6) were harvested and washed once with PBS and twice with HEPES buffer (50 mM HEPES/KOH, pH 7.5; 0.25 M sucrose; 50 mM KOAc; 6 mM MgOAc; 4 mM phenylmethylsulphonyl fluoride; 1 mM EDTA; 1 mM dithiothreitol (DTT); 0.1 mg ml^{-1} cycloheximide; 0.3 U ml^{-1} RNAsin (Promega, Heidelberg, Germany); protease inhibitor cocktail). After homogenization using a glass/Teflon homogenizer, the suspension was centrifuged at 1,000 g for 10 min. The supernatant was centrifuged at 10,000 g for 10 min. The new supernatant was layered onto a 0.6-M sucrose cushion (50 mM HEPES/KOH, pH 7.5; 0.6 M sucrose; 100 mM KOAc; 5 mM MgOAc; 4 mM DTT; 0.1 mg ml^{-1} cycloheximide; 40 U ml^{-1} RNAsin) and centrifuged at 230,000 g for 90 min. The resulting membrane pellet was resuspended in HEPES buffer and stored at −80 °C. All steps after the first washing step were carried out on ice.

Preparation of stripped canine pancreatic RMs. RMs were prepared from dog pancreas as previously described[5]. RMs in buffer A (20 mM Hepes, pH 7.6; 50 mM KCl; 2 mM MgCl$_2$; 200 mM sucrose; 2 mM DTT; protease inhibitor) were incubated for 30 min at 20 °C in the presence of 0.5 mM GTP (Sigma-Aldrich, Germany), 2 mM puromycin (Sigma-Aldrich), 750 mM KOAC (Sigma-Aldrich) and subsequently pelleted (TLA 100 rotor, 160,000 g, 35 min, 20 °C). The microsomal pellet was resuspended in buffer B (50 mM HEPES, pH 7.6; 1.25 M sucrose; 800 mM CsCl; 15 mM Mg(OAc)$_2$; 3 mM DTT; protease inhibitor) and layered on the bottom of a two-step gradient consisting of buffer C (buffer B, only 0.8 M sucrose) and buffer A. After flotation (TLA 120.2 rotor, 350,000 g, 70 min, 20 °C), microsomes could be retrieved from the interphase between buffer A and C. Ribosome-stripped microsomes were pelleted (TLA 100 rotor, 160,000 g, 35 min, 4 °C), resuspended in buffer A at a concentration of 1 eq µl^{-1}, flash frozen in liquid nitrogen and stored at −80 °C.

Cell-free system for CET. The pre-pro-lactin (ppl) construct with C-terminal CMV stalling sequence (ppl-CMV) was generated using a primer extension PCR reaction based on the pB4 plasmid[32] with forward primer 5′-TAT TTA GGT GAC ACT ATA GAA GAG GCC GCC ACC ATG GAC AGC AAA GGT TCG TC-3′ and reverse primer 5′-TTA AGG AGG AAT ATA TTT GCA GGT CAG CAG GCT GCT CAG TTT TTT CGC ACT CAG CAC CAG CGG TTC CAT GCA GTT GTT GTT GTA GAT GAT TCT G-3′. Stalling ppl-CMV mRNA was prepared *in vitro* (mmessage mmachine SP6 Kit, Ambion, USA). Cell-free reactions were performed at 30 °C in Flexi rabbit reticulocyte lysate (Promega, USA) in the presence of 1 mM biotinylated Lysyl-transfer RNA (Transcend tRNA Kit, Promega, USA). Reactions were supplemented with 200 nM of non-stalling ppl or stalling ppl-CMV mRNA and puromycin/high-salt-treated rough membrane (PK-RM) at a concentration of 4 eq per 25 µl, where indicated. After 20 min, reactions were stopped on ice. For RNAse digestion assays, 20 µl of cell-free reaction were supplemented with 0.1 mg ml^{-1} (f.c.) RNAse A (Sigma-Aldrich, Germany) and incubated for 30 min at 30 °C. Ribosome association of ppl-CMV chains was analysed by pelleting ribosomes from 20 µl of cell-free reaction (without PK-RM) through a 0.25 M sucrose cushion (TLA 100, 30 min, 150,000 g, 4 °C). Translocation of ppl-CMV nascent chains was analysed by pelleting microsomes from 20 µl of cell-free reaction (eppendorf Centrifuge 5417R, 3 min, 16,000 g, 4 °C). Samples were analysed by SDS–PAGE and western blotting using streptavidin-coupled horseradish peroxidase (Transcend tRNA Kit, Promega, USA). Relative amounts of protein were quantified using AIDA two-dimensional densiometry software (Raytest, Germany).

Cryoelectron tomography. Twenty-five microlitres of *in vitro* reaction were centrifuged in an eppendorf Centrifuge 5417R (3 min, 16,000 g, 4 °C) to pellet microsomes. The pellet was resuspended in 25 µl of ribosome buffer (20 mM Hepes, pH 7.6; 50 mM KCl; 2 mM MgCl$_2$) and 3 µl were applied to lacey carbon molybdenum grids (Ted Pella, USA). After an incubation time of 60 s, 3 µl of 10-nm colloidal gold in ribosome buffer were added to the grid and the sample was vitrified in liquid ethane using a Vitrobot Mark IV (FEI Company, The Netherlands). Tilt series were acquired using a FEI Titan Krios TEM equipped with a 4k × 4k FEI Falcon direct electron detector. The TEM was operated at an acceleration voltage of 300 kV. Single-axis tilt series were recorded from −60° to +60° with an angular increment of 3° at a nominal defocus of 4 (canine pancreatic microsomes) or 8 µm (HeLa cell microsomes), and an object pixel size of 0.288 nm using the FEI tomography acquisition software. The cumulative electron dose did not exceed 60 electrons per Å^2.

Image processing for CET. Phase correction of the tilt series, tomogram reconstruction (object pixel: 2.30 nm) and template matching (object pixel: 2.30 nm) were performed as described[5]. For tomograms obtained from canine pancreatic microsomes, subtomograms (32^3 voxels, object pixel: 2.30 nm) centred at the coordinates of the 1,000 highest-scoring peaks of the cross correlation function were classified using constrained principal component analysis[33] focusing on the large ribosomal subunit and the ER membrane. Classification separated ER membrane-associated ribosomes from most false-positive matches, such as gold markers, ER membrane or carbon edges. For tomograms obtained from HeLa cell microsomes, cross correlation peaks in areas containing rough ER were visually inspected to identify true-positive matches. For the selected coordinates, unbinned subtomograms (200^3 voxels, object pixel: 0.288 nm) were reconstructed individually from the weighted backprojections and aligned to the template using PyTom[34]. With a second round of constrained principal component analysis, translocons including and lacking the OST complex were sorted. Using aligned coordinates and angles, the reconstruction centre was moved to the centre of the translocon and unbinned subtomograms (96^3 voxels, object pixel: 2.88 Å) were reconstructed and aligned. The resolution of the resulting averages was determined by Fourier shell correlation (FSC) on appropriately masked averages (FSC = 0.5) and cross resolution (FSC = 0.33). We performed an independent reference-free alignment described in ref. 35 to rule out reference bias in the alignment process. This alternative alignment procedure divided the data into two halves that were aligned independently and assessed by FSC, commonly referred to as 'gold standard FSC'[36]. Normalized electron-density difference maps were generated from normalized tomographic reconstructions, filtered to their respective resolution.

EM map analysis. For EM map analysis, fitting of atomic models, segmentation and visualization, we used the UCSF Chimera software package[37]. Colouration of the EM maps was done either on single images in Photoshop by applying coloured layers ('multiply' style) to the image or in chimera on segmented densities.

Sample preparation and data processing for SPA. *Bona fide* translocating ribosome–Sec61 complexes were obtained using constructs based on the well-characterized Lep93 (here referred to as LepT) by Saaf et al.[38] These constructs contain glycosylation sites to precisely monitor the translocation state. We modified these constructs to generate and stabilize translocation and insertion intermediates by introducing a C-terminal ribosomal stalling sequence (CMV gp48 upstream open-reading frame)[12], a streptavidin tag for affinity purification and an haemagglutinin tag for immunodetection. LepT-mRNA was used in a self-made wheatgerm translation system in the presence of PK-RM and signal recognition particle from dog pancreas[15]. After *in vitro* translation, ribosome-bound membranes were isolated and solubilized with digitonin. Programmed ribosomes containing the glycosylated LepT-peptide engaged with Sec61, OST and TRAP were affinity purified using the Strep-tag. For sample preparation, freshly prepared samples were applied to Quantifoil grids precoated with 2 nm carbon on top and flash frozen using the Vitrobot Mark IV (FEI Company).

Data were collected on a Titan Krios TEM (FEI Company) under low-dose conditions at 200 keV and magnification of ×148,721 at the plane of the charge-coupled device using a TemCam-F416 CMOS camera (TVIPS GmbH), resulting in an image pixel size of 1.049 Å per pixel on the object scale. EM-TOOLS software was used for automated data collection and data were recorded in a defocus range of 1.3–4.0 µm. SPA and three-dimensional reconstruction was performed using the SPIDER software package[39]. Automated particle selection was performed using the programme Signature[40], which was followed by a second automated particle classification step using the MAPPOS software[41]. Particles (487,470) were sorted for the presence of Sec61 complex and P-site tRNA, and remaining 'non-particles' representing noisy images or aggregated particles, which could not be excluded before. For sorting, in brief, references representing an empty ribosome, a programmed ribosome and a programmed ribosome bound to Sec61 were offered as references for supervised classification. 'Non-particles' were sorted out using a reference map derived from noise particles. After sorting, three-dimensional maps were obtained for a data subset (53,248 particles; 10.92%) containing highly enriched peptidyl–tRNA and Sec61 complex. From this data subset, a further subpopulation of 15,705 particles could be isolated, which contained a density larger than the Sec61 complex at the exit site. By MS analysis of the sample, the additional density was identified as the OST and TRAP complexes (Supplementary Data 1). The RNC–Sec61–OST–TRAP data set could be refined to a global resolution of 9.3 Å, although the densities for TRAP and OST are not as well resolved.

References

1. Mohorko, E., Glockshuber, R. & Aebi, M. Oligosaccharyltransferase: the central enzyme of N-linked protein glycosylation. *J. Inherit. Metab. Dis.* **34,** 869–878 (2011).
2. Kelleher, D. J. & Gilmore, R. An evolving view of the eukaryotic oligosaccharyltransferase. *Glycobiology* **16,** 47R–62R (2006).
3. Chavan, M. & Lennarz, W. The molecular basis of coupling of translocation and N-glycosylation. *Trends Biochem. Sci.* **31,** 17–20 (2006).
4. Crimaudo, C., Hortsch, M., Gausepohl, H. & Meyer, D. I. Human ribophorins I and II: the primary structure and membrane topology of two highly conserved rough endoplasmic reticulum-specific glycoproteins. *EMBO J.* **6,** 75–82 (1987).
5. Pfeffer, S. *et al.* Structure and 3D arrangement of endoplasmic reticulum membrane-associated ribosomes. *Structure* **20,** 1508–1518 (2012).
6. Menetret, J. F. *et al.* Single copies of Sec61 and TRAP associate with a nontranslating mammalian ribosome. *Structure* **16,** 1126–1137 (2008).
7. Nagasawa, K., Higashi, T., Hosokawa, N., Kaufman, R. J. & Nagata, K. Simultaneous induction of the four subunits of the TRAP complex by ER stress accelerates ER degradation. *EMBO Rep.* **8,** 483–489 (2007).
8. Roboti, P. & High, S. The oligosaccharyltransferase subunits OST48, DAD1 and KCP2 function as ubiquitous and selective modulators of mammalian N-glycosylation. *J. Cell Sci.* **125,** 3474–3484 (2012).
9. Wilson, C. M., Roebuck, Q. & High, S. Ribophorin I regulates substrate delivery to the oligosaccharyltransferase core. *Proc. Natl Acad. Sci. USA* **105,** 9534–9539 (2008).
10. Evans, E. A., Gilmore, R. & Blobel, G. Purification of microsomal signal peptidase as a complex. *Proc. Natl Acad. Sci. USA* **83,** 581–585 (1986).
11. Chavan, M. *et al.* Dimeric organization of the yeast oligosaccharyl transferase complex. *Proc. Natl Acad. Sci. USA* **103,** 8947–8952 (2006).

12. Bhushan, S. *et al.* Structural basis for translational stalling by human cytomegalovirus and fungal arginine attenuator peptide. *Mol. Cell* **40,** 138–146 (2010).

13. Lizak, C., Gerber, S., Numao, S., Aebi, M. & Locher, K. P. X-ray structure of a bacterial oligosaccharyltransferase. *Nature* **474,** 350–355 (2011).

14. Chandramouli, P. *et al.* Structure of the mammalian 80S ribosome at 8.7 A resolution. *Structure* **16,** 535–548 (2008).

15. Gogala, M. *et al.* Cryo-EM structures of the Sec61-complex engaged in nascent peptide translocation or membrane insertion. *Nature* (in press).

16. Gorlich, D. & Rapoport, T. A. Protein translocation into proteoliposomes reconstituted from purified components of the endoplasmic reticulum membrane. *Cell* **75,** 615–630 (1993).

17. Frauenfeld, J. *et al.* Cryo-EM structure of the ribosome-SecYE complex in the membrane environment. *Nat. Struct. Mol. Biol.* **18,** 614–621 (2011).

18. Becker, T. *et al.* Structure of monomeric yeast and mammalian Sec61 complexes interacting with the translating ribosome. *Science* **326,** 1369–1373 (2009).

19. Kreibich, G., Freienstein, C. M., Pereyra, B. N., Ulrich, B. L. & Sabatini, D. D. Proteins of rough microsomal membranes related to ribosome binding. II. Cross-linking of bound ribosomes to specific membrane proteins exposed at the binding sites. *J. Cell Biol.* **77,** 488–506 (1978).

20. Chavan, M., Yan, A. & Lennarz, W. J. Subunits of the translocon interact with components of the oligosaccharyl transferase complex. *J. Biol. Chem.* **280,** 22917–22924 (2005).

21. Harada, Y., Li, H. & Lennarz, W. J. Oligosaccharyltransferase directly binds to ribosome at a location near the translocon-binding site. *Proc. Natl Acad. Sci. USA* **106,** 6945–6949 (2009).

22. Nilsson, I. M. & von Heijne, G. Determination of the distance between the oligosaccharyltransferase active site and the endoplasmic reticulum membrane. *J. Biol. Chem.* **268,** 5798–5801 (1993).

23. Li, H., Chavan, M., Schindelin, H. & Lennarz, W. J. Structure of the oligosaccharyl transferase complex at 12 A resolution. *Structure* **16,** 432–440 (2008).

24. Cohen, J. Structural biology. Is high-tech view of HIV too good to be true? *Science* **341,** 443–444 (2013).

25. Murray, S. C. *et al.* Validation of cryo-EM structure of IP(3)R1 channel. *Structure* **21,** 900–909 (2013).

26. Henderson, R. The potential and limitations of neutrons, electrons and X-rays for atomic resolution microscopy of unstained biological molecules. *Q. Rev. Biophys.* **28,** 171–193 (1995).

27. Lasker, K. *et al.* Molecular architecture of the 26S proteasome holocomplex determined by an integrative approach. *Proc. Natl Acad. Sci. USA* **109,** 1380–1387 (2012).

28. Schmittgen, T. D. & Livak, K. J. Analyzing real-time PCR data by the comparative C(T) method. *Nat. Protoc.* **3,** 1101–1108 (2008).

29. Dudek, J. *et al.* ERj1p has a basic role in protein biogenesis at the endoplasmic reticulum. *Nat. Struct. Mol. Biol.* **12,** 1008–1014 (2005).

30. Wilson, R. *et al.* The translocation, folding, assembly and redox-dependent degradation of secretory and membrane proteins in semi-permeabilized mammalian cells. *Biochem. J.* **307**(Pt 3): 679–687 (1995).

31. Greiner, M. *et al.* Silencing of the SEC62 gene inhibits migratory and invasive potential of various tumor cells. *Int. J. Cancer* **128,** 2284–2295 (2011).

32. Volkmer, J. *et al.* Pancreas specific protein disulfide isomerase, PDIp, is in transient contact with secretory proteins during late stages of translocation. *FEBS Lett.* **406,** 291–295 (1997).

33. Förster, F., Pruggnaller, S., Seybert, A. & Frangakis, A. S. Classification of cryo-electron sub-tomograms using constrained correlation. *J. Struct. Biol.* **161,** 276–286 (2008).

34. Hrabe, T. *et al.* PyTom: a python-based toolbox for localization of macromolecules in cryo-electron tomograms and subtomogram analysis. *J. Struct. Biol.* **178,** 177–188 (2012).

35. Chen, Y., Pfeffer, S., Hrabe, T., Schuller, J. M. & Forster, F. Fast and accurate reference-free alignment of subtomograms. *J. Struct. Biol.* **182,** 235–245 (2013).

36. Scheres, S. H. & Chen, S. Prevention of overfitting in cryo-EM structure determination. *Nat. Methods* **9,** 853–854 (2012).

37. Goddard, T. D., Huang, C. C. & Ferrin, T. E. Visualizing density maps with UCSF chimera. *J. Struct. Biol.* **157,** 281–287 (2007).

38. Saaf, A., Wallin, E. & von Heijne, G. Stop-transfer function of pseudo-random amino acid segments during translocation across prokaryotic and eukaryotic membranes. *Eur. J. Biochem.* **251,** 821–829 (1998).

39. Frank, J. *et al.* SPIDER and WEB: processing and visualization of images in 3D electron microscopy and related fields. *J. Struct. Biol.* **116,** 190–199 (1996).

40. Chen, J. Z. & Grigorieff, N. SIGNATURE: a single-particle selection system for molecular electron microscopy. *J. Struct. Biol.* **157,** 168–173 (2007).

41. Norousi, R. *et al.* Automatic post-picking using MAPPOS improves particle image detection from cryo-EM micrographs. *J. Struct. Biol.* **182,** 59–66 (2013).

Acknowledgements

Author contributions

Additional information

58

Supplementary Figure S1. Schematic representation of size and membrane topology of the mammalian OST subunits. Membrane topology was predicted based on sequence analysis, proteinase protection assays and structural information. A scale bar, corresponding to 100 amino acids (AA) is depicted. TMH, Transmembrane helices.

all subtomograms   including LD   lacking LD

a   control siRNA (31 tomograms)

LD   LD

704   295 (42%)   409 (58%)

b   TRAPβ siRNA (32 tomograms)

LD   LD

577   251 (43%)   326 (57%)

c   RibI siRNA (13 tomograms)

no classes
including LD

417

d   RibII siRNA (17 tomograms)

no classes
including LD

833

e   dog pancreatic microsomes (45 tomograms)

LD   LD

4597   2896 (63%)   1701 (37%)

60
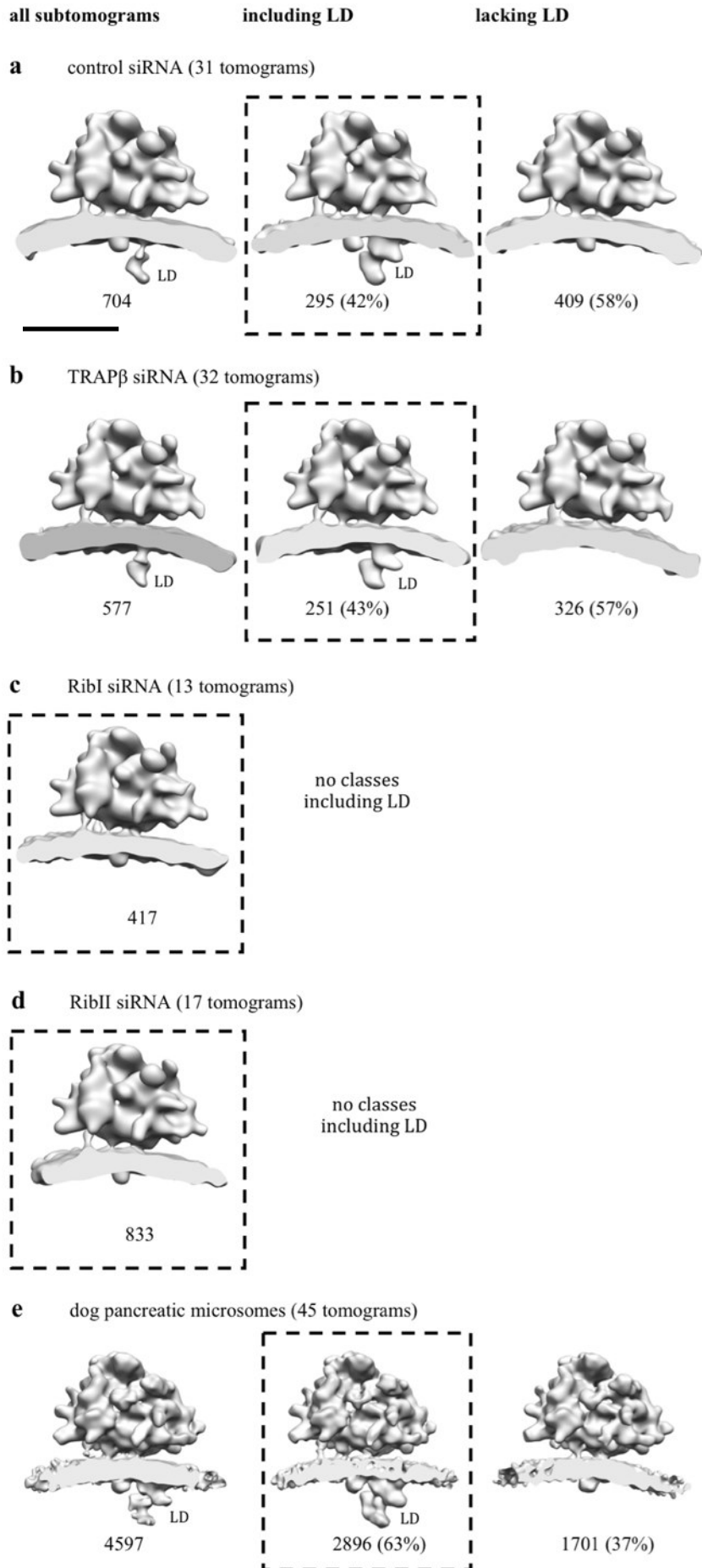
Supplementary Figure S2. Two translocon populations are present in the data. For control (a) and TRAPβ (b) siRNA treated HeLa cells as well as canine pancreatic microsomes (e), averages of the unclassified data and the states including and lacking LD are shown together with absolute number of particles and relative amount of particles contributing to the maps. For the RibI (c) and RibII (d) siRNA treatment, no classes including LD were observed. Boxed structures were used for further analysis. Scale bar corresponds to 20 nm.
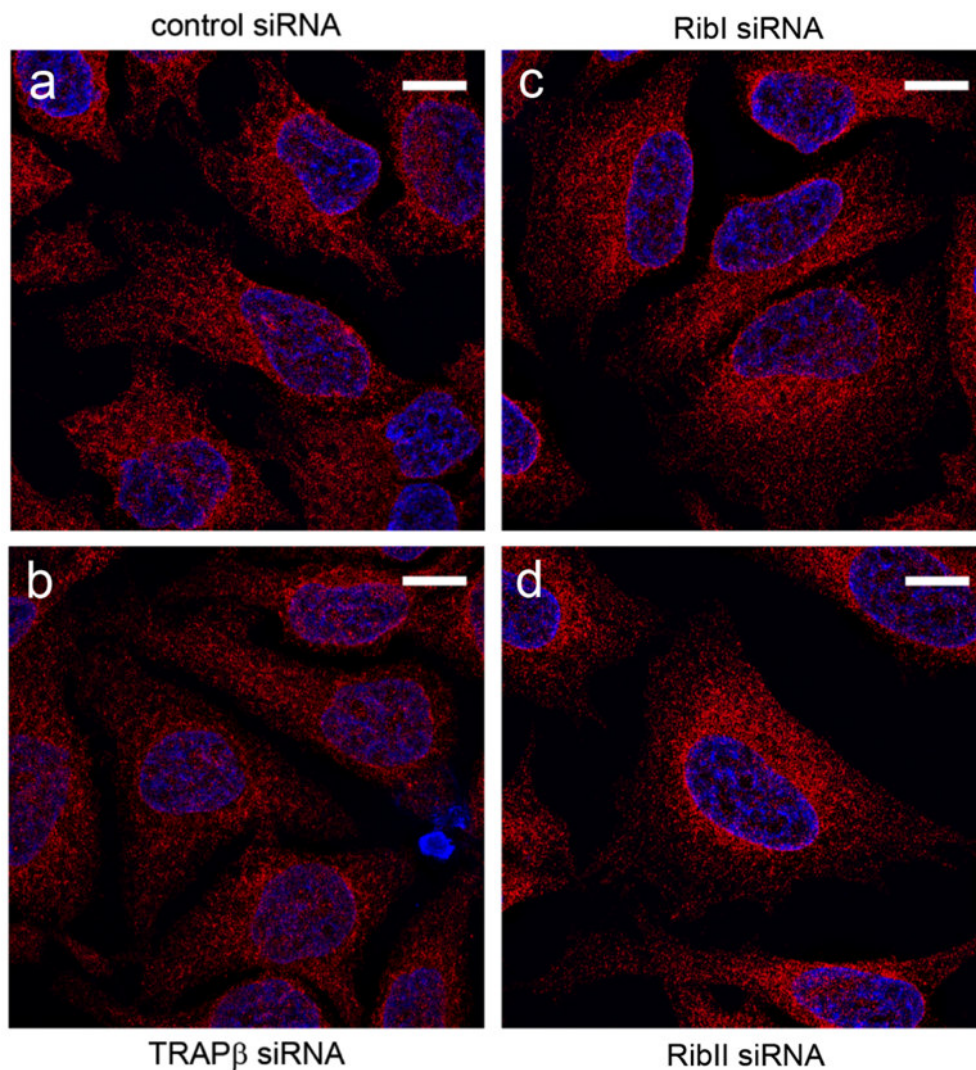
Supplementary Figure S3. Effect of RibI, RibII, and TRAPβ gene silencing on ER integrity. 96 h after control (a) and TRAPβ (b) siRNA treatment and 72 h after RibI (c) and RibII (d) siRNA treatment, HeLa cells were fixed with paraformaldehyde and stained with antibodies directed against the Sec62 protein and Alexa-Fluor-594-coupled secondary antibodies. Nuclei were counterstained with DAPI. Cells were analyzed on an Elyra SIM and are shown in maximum intensity projection. The bar corresponds to 10 μm.
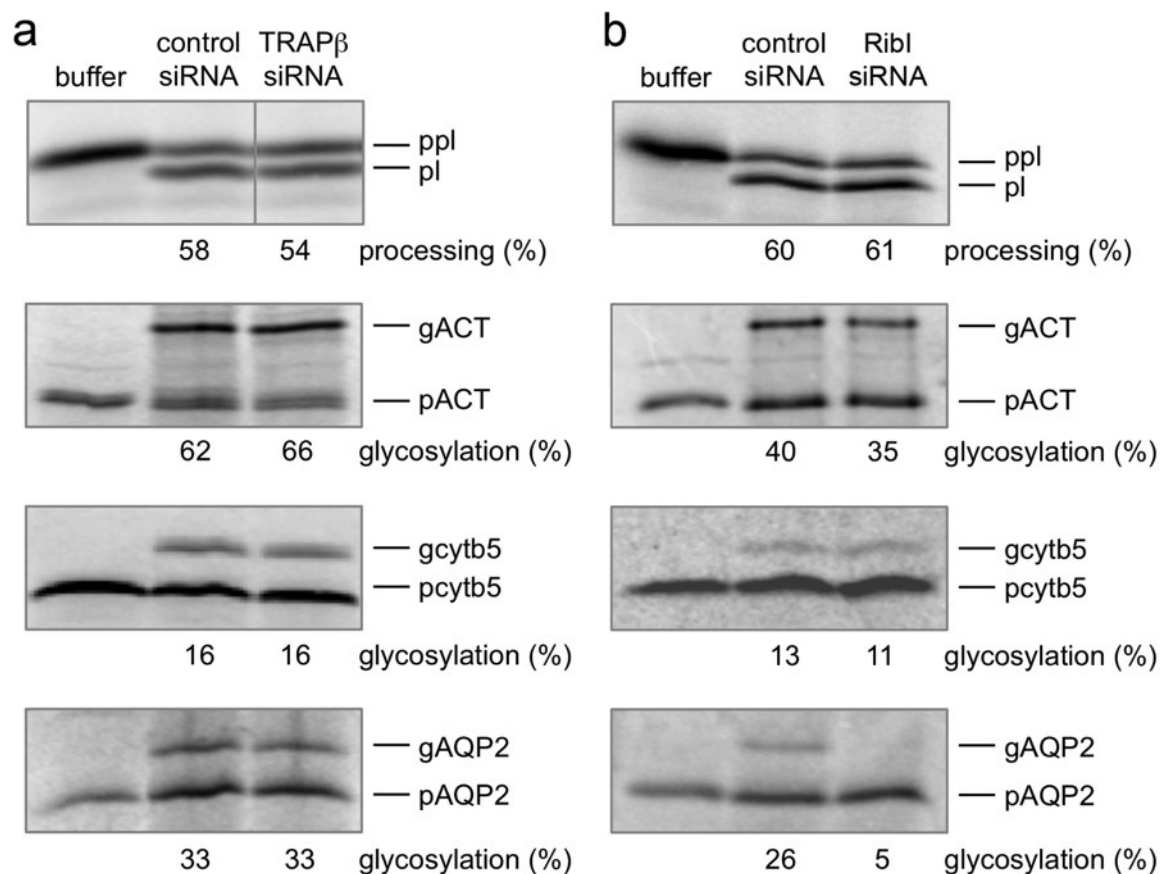
Supplementary Figure S4. Effect of TRAPβ and RibI gene silencing on glycosylation and ER protein transport. a, **b** Before treatment with digitonin for preparation of semi-permeabilized cells, HeLa cells were treated with the indicated siRNAs for 96 h (a) or 72 h (b). The indicated precursor polypeptides were imported into ER fractions or incubated in the presence of buffer as negative controls. Transport reactions were analyzed by SDS-PAGE and phosphorimaging. The efficiencies of modification by OST or signal peptidase are indicated for the mature proteins and shown as percentage of precursor plus mature protein. g, glycosylated polypeptide; p, precursor.
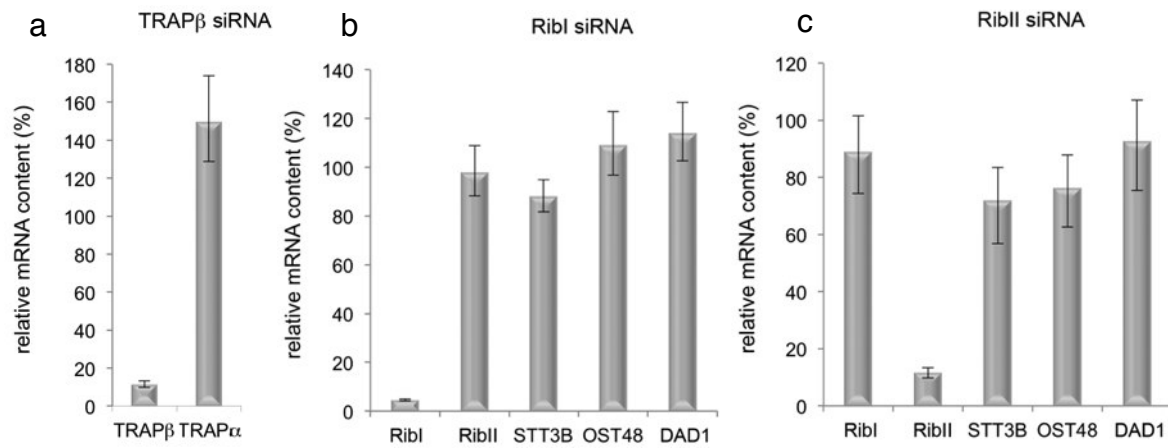
Supplementary Figure S5. Effect of TRAPβ, RibI, and RibII gene silencing on mRNA levels. 96 h after TRAPβ (a) and control siRNA treatment and 72 h after RibI (b), RibII (c), and control siRNA treatment of HeLa cells, RT-PCR was performed. The respective value of control siRNA treated cells was set to 100%; mean ± s.d.; n = 3 per gene.
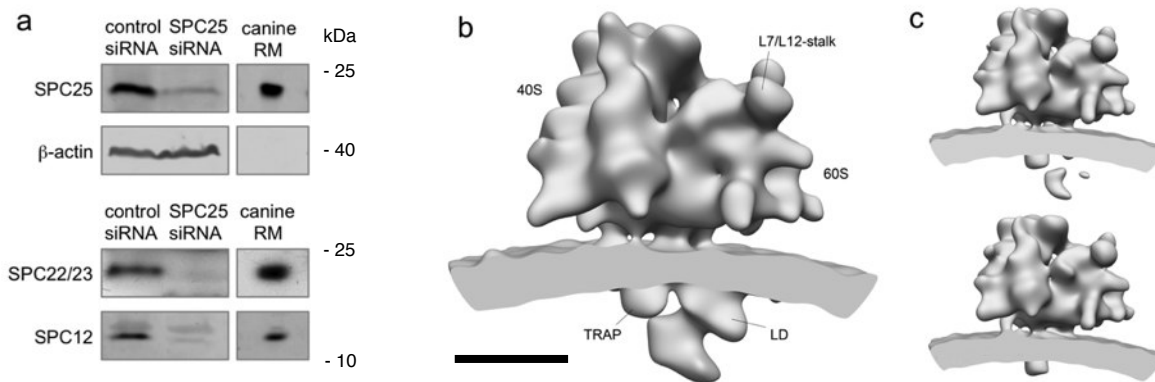
Supplementary Figure S6. Depletion of SPase subunits from HeLa cells does not affect LD. a, HeLa cells were depleted of SPase subunit SPC25 as described in methods. The efficiency of SPC25 gene silencing was evaluated by western blotting, which indicates a nearly quantitative depletion of the target protein (7 ± 2 % s.e.m residual protein (n=4)) and at least two other SPase subunits (SPC22/23: 9 ± 3 % s.e.m residual protein (n=4) and SPC12: 5 ± 1 s.e.m % residual protein (n=4)). As a positive control for the SPC antibodies, an aliquot of rough canine microsomes (RM) was run in parallel. The differences in intensity in the canine RMs compared to HeLa total lysate are due to the different concentrations of ER proteins in the samples and species differences in antibody affinity. **b,** Subtomogram average of the ER membrane-associated ribosome from SPC25 depleted HeLa cells. Only particles including LD were retained (453 particles, 37 % of dataset). Upon SPC25 depletion, no significant change of electron density can be discerned in the region of the translocon at a threshold level of 6σ of the difference map to the control. Scale bar corresponds to 10 nm. **c,** Subtomogram averages of the unclassified dataset (upper panel, 1,219 particles) and the population lacking LD (lower panel, 766 particles, 63 % of dataset) are shown.
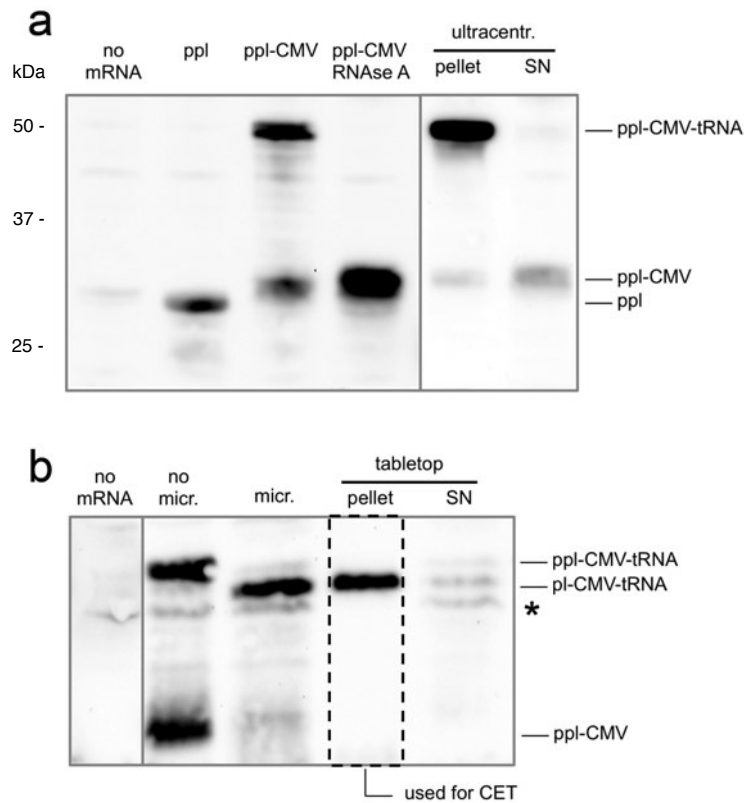
Supplementary Figure S7. Stalling (a) and translocation efficiency (b) in the cell-free system. a, In vitro translation of mRNA coding for pre-pro-lactin not containing a CMV stalling sequence (ppl) yielded a single translation product, corresponding to regularly terminated ppl. Addition of the 20 amino acid CMV stalling sequence to the C-terminus of pre-pro-lactin (ppl-CMV) yielded two translation products: the first product, corresponding to regularly terminated ppl-CMV (22%) and the second product migrating at significantly higher molecular weight, corresponding to ppl-CMV with a tRNA moiety (ppl-CMV-tRNA) still bound (78%). Upon treatment with RNAse A, tRNA moieties were degraded and ppl-CMV-tRNA was converted to ppl-CMV. To demonstrate that ppl-CMV-tRNA chains are still ribosome bound after the reaction, ribosomes were pelleted by ultracentrifugation and equal amount of the pellet and supernatant fraction were analyzed. While ppl-CMV was mainly present in the supernatant (SN), ppl-CMV-tRNA was quantitatively recovered from the ribosomal pellet (pellet) and thus was still in complex with ribosomes when the reaction was

stopped. **b,** After addition of ribosome stripped microsomes to the cell-free system (micr.), 94% of nascent chains migrated at slightly lower molecular weight due to cleavage of the 30 amino acid N-terminal signal sequence by the ER-lumenal signal peptidase complex, already indicating efficient translocation of nascent chains. To further substantiate this result, microsomes were pelleted under conditions leaving cytosolic ribosomes in the supernatant. When equal amounts of the pellet (pellet) and supernatant (SN) fraction were analyzed, nascent chains were nearly quantitatively recovered from the pellet, confirming efficient translocation. We note, that under these conditions, which were also used for tomographic analysis, quantitative stalling can be observed, possibly yielding a highly homogenous population of ER membrane associated ribosomes. (*) unspecific binding of streptavidin coupled horseradish peroxidase.
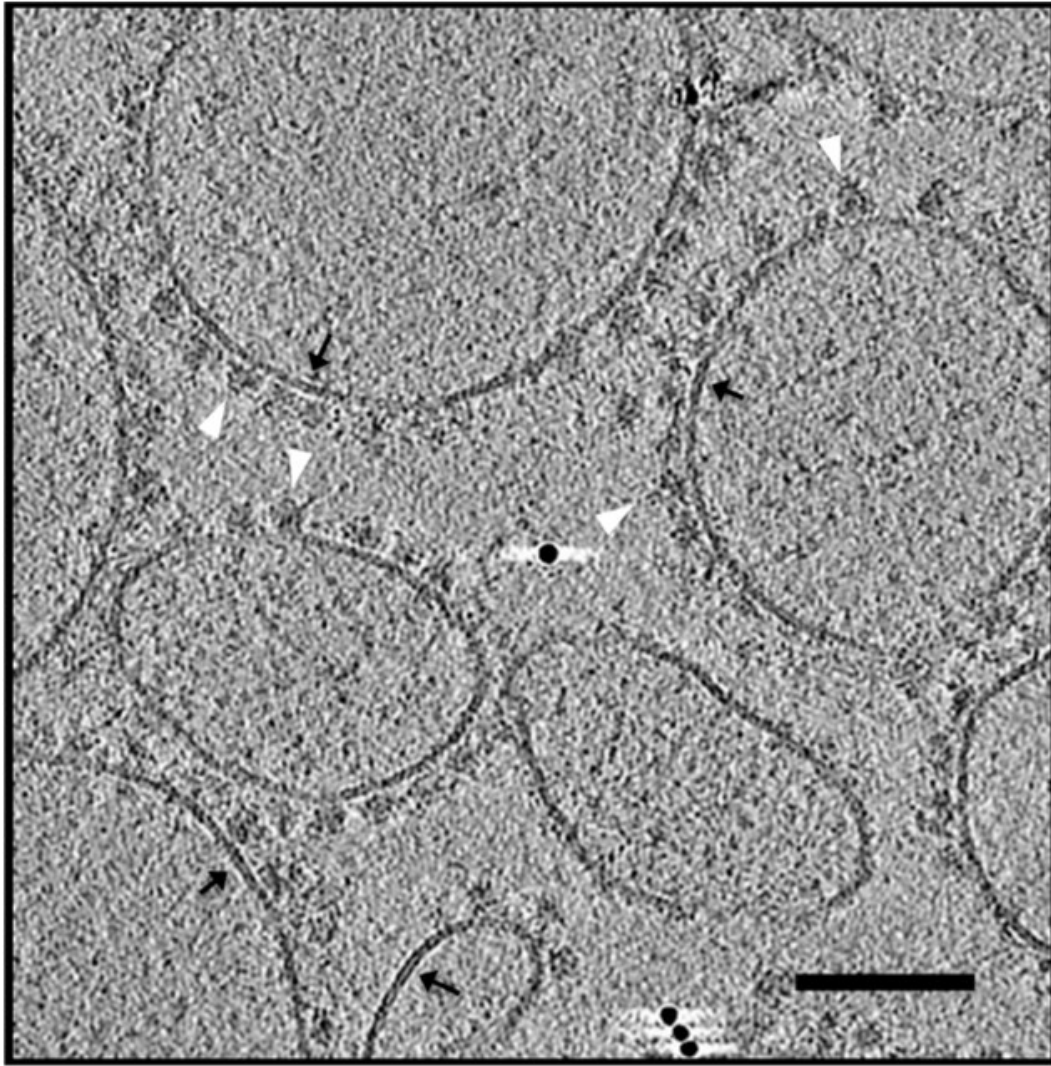
Supplementary Figure S8. Tomographic reconstruction of canine pancreatic microsomal vesicles loaded with stalled RNCs *in vitro*. Slice (10 nm thickness) through a representative tomogram. ER membrane associated ribosomes (white arrow heads) and the lipid bilayer (black arrows) can be discerned. Scale bar corresponds to 100 nm.
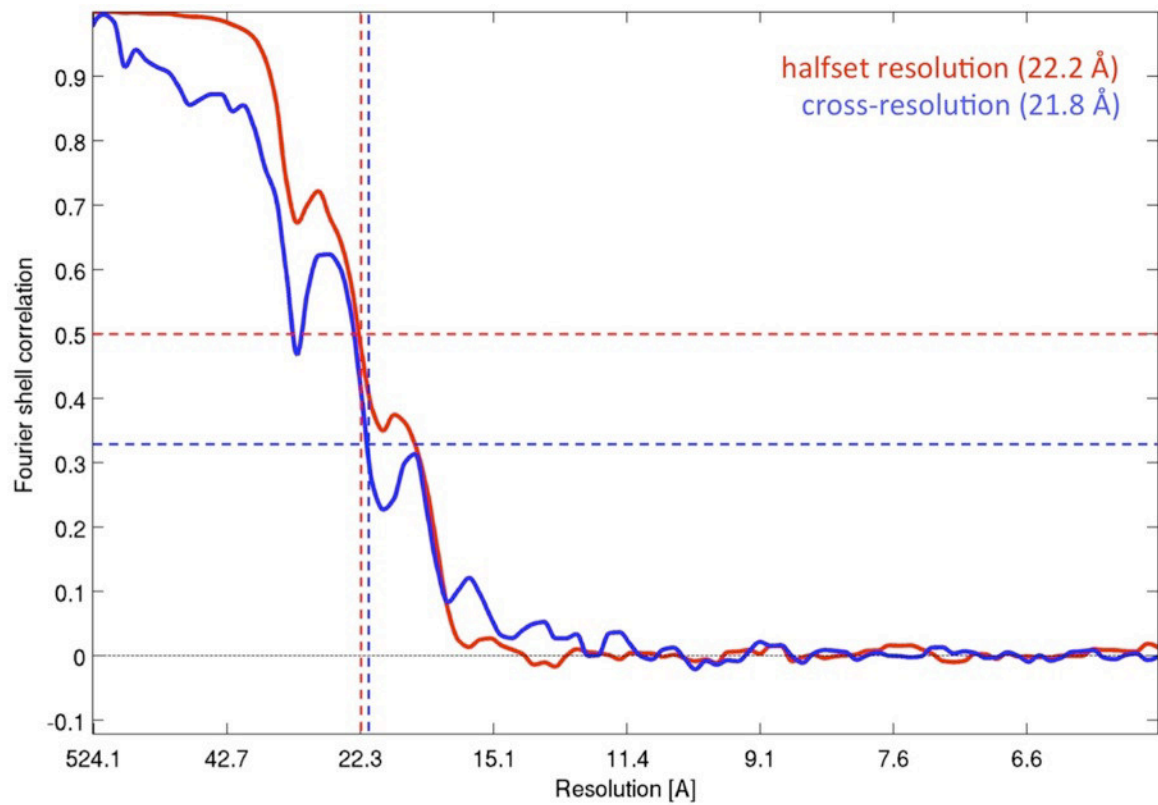
Supplementary Figure S9. Resolution determination via Fourier Shell Correlation and cross-resolution. The resolution of the final subtomogram average was determined to 22.2 Å by Fourier Shell Correlation (0.5 FSC criterion) and to 21.8 Å by cross resolution (0.33 FSC criterion) with a single particle reconstruction of the canine 80S ribosome (EMD 1480).
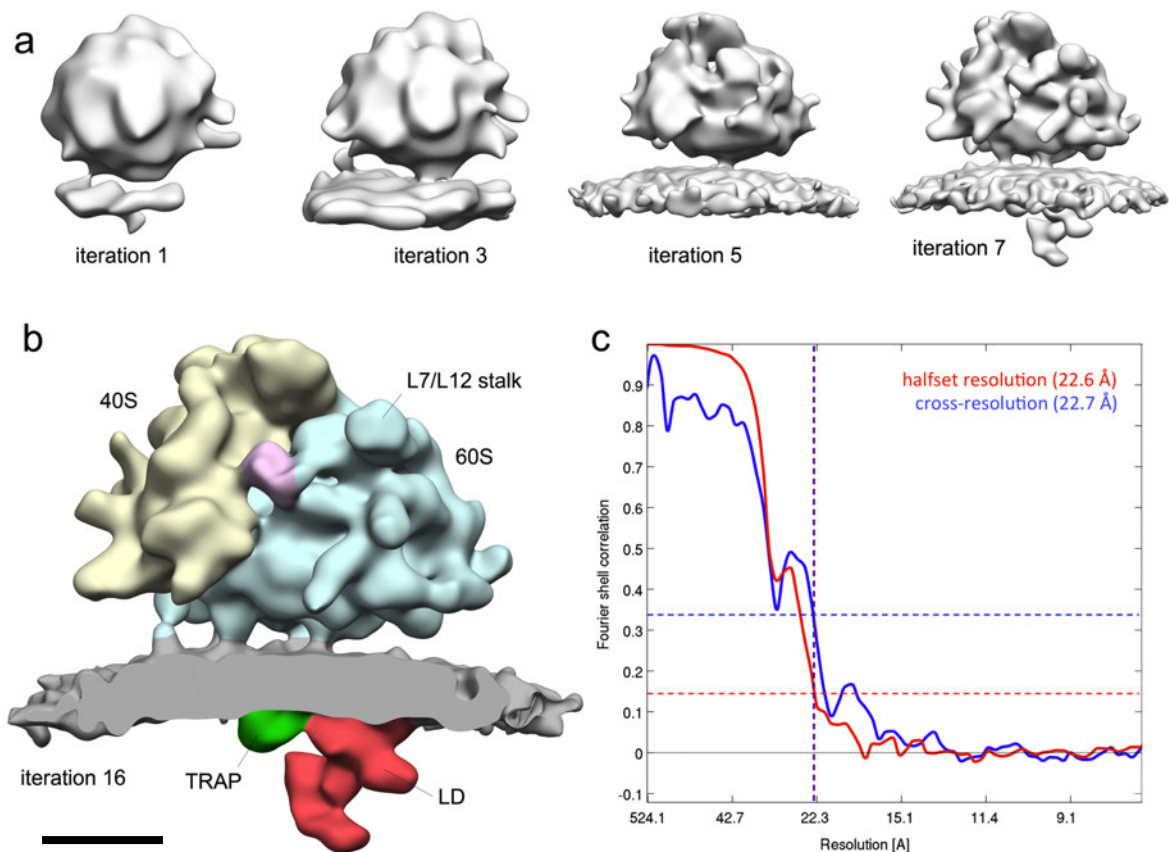
Supplementary Figure S10. Resolution determination via reference-free gold standard alignment [35]. a, Over the course of 7 iterations, a well-defined ER membrane-associated ribosome evolves from an initially featureless blob. **b,** After 16 iterations, the alignment converges into a structure, which is essentially identical to the result of the reference-based alignment (Fig. 3a). Scale bar corresponds to 10 nm. **c,** The resolution of the subtomogram average was determined to 22.7 Å by cross-resolution (FSC=0.33) with a single particle reconstruction of the canine 80S ribosome (EMD 1480), and 22.6 Å by Fourier Shell Correlation of the two completely independent halfsets (FSC=0.143).
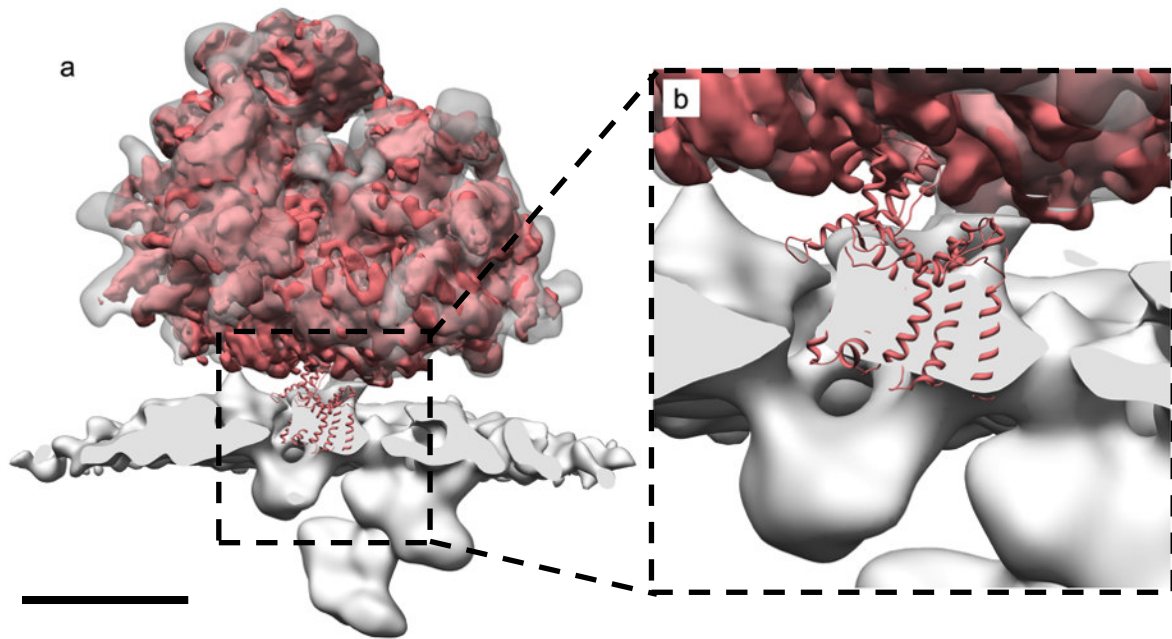
Supplementary Figure S11. Sec61 is resolved in the subtomogram average. a, A single particle reconstruction of the canine ribosome (EMD 1480) and an aligned atomic model of the nascent chain translocating canine Sec61 complex [15] (red) were fitted into the subtomogram average (gray) as a rigid body. A high-density region in the ER membrane colocalizes with Sec61. Scale bar corresponds to 10 nm. **b,** Magnified view of the Boxed area in a.
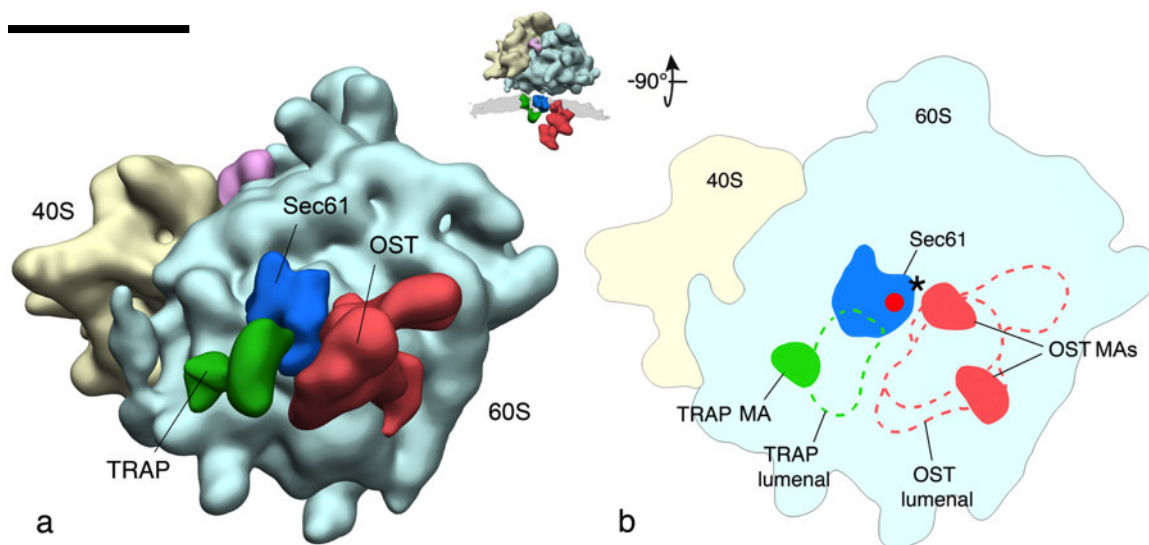
Supplementary Figure S12. Spatial organization of OST, Sec61 and TRAP in the native translocon seen from the ER lumen and represented either as **(a)** a surface model of the segmented densities (colored as in Fig. 3f) or as **(b)** a projection of membrane anchors (MA) and lumenal segments of TRAP (green), OST (red) and Sec61 (dark blue) onto the membrane plane. The positions of the peptide exit tunnel (red dot) on the large ribosomal subunit and a potential interaction site of Sec61 with OST (asterisk) are indicated in **b**. Scale bar corresponds to 10 nm.
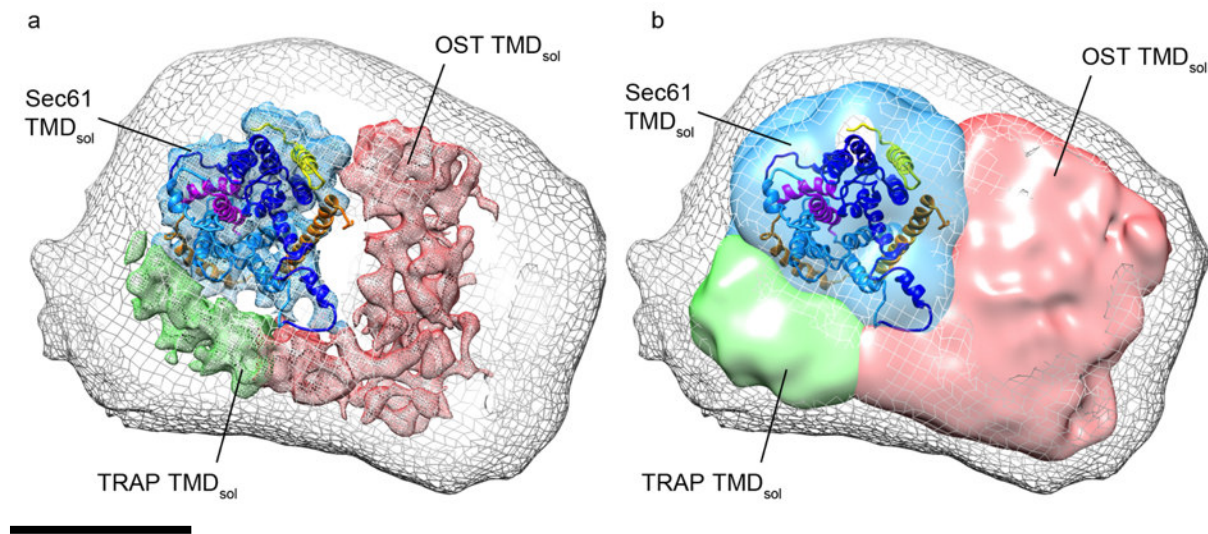
Supplementary Figure S13. Spatial organization of OST, Sec61 and TRAP in the solubilized translocon seen from the ER lumen. Transmembrane density from the solubilized translocon (TMD_{sol}) assigned to Sec61 (blue), OST (red) and TRAP (green) depicted at 10 Å **(a)** and 30 Å **(b)** resolution, respectively. Atomic models [15] for nascent chain translocating Sec61α (N-terminal half: dark blue, C-terminal half: light blue), Sec61β (yellow) and Sec61γ (orange) were fitted into the density at 10 Å resolution. Rod-like features in the Sec61 density co-localize with α-helices in the atomic model in several areas of the map. The lateral gate of Sec61α is depicted (magenta helices). Scale bar corresponds to 5 nm.

anti-TRAPβ and -β-actin antibody decoration of TRAPβ silenced cells
+ canine RM as antibody control

Figure 1b

SDS gel 12 %

anti-TRAPα, -TRAPγ and -TRAPγ antibody decoration of TRAPβ silenced cells
+ canine RM as antibody control

Figure 1b

SDS gel 17,5 %
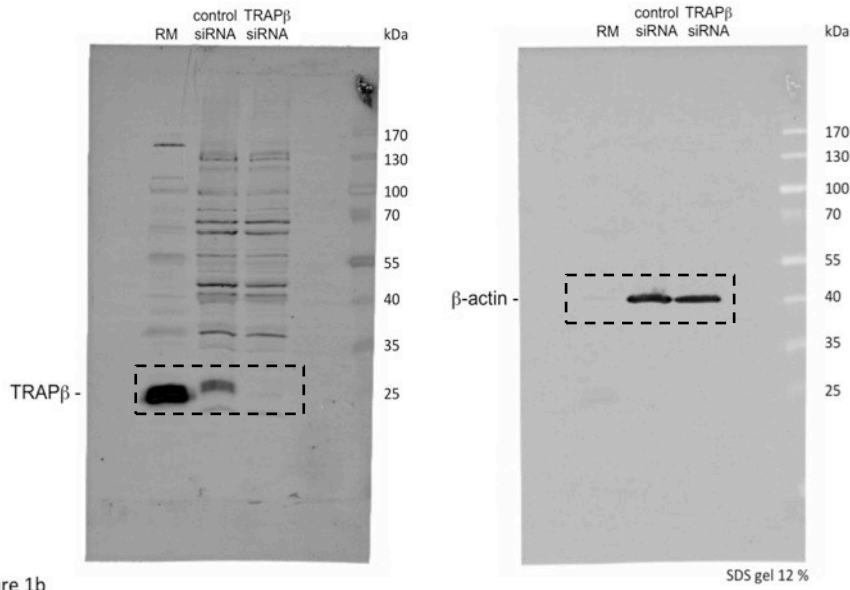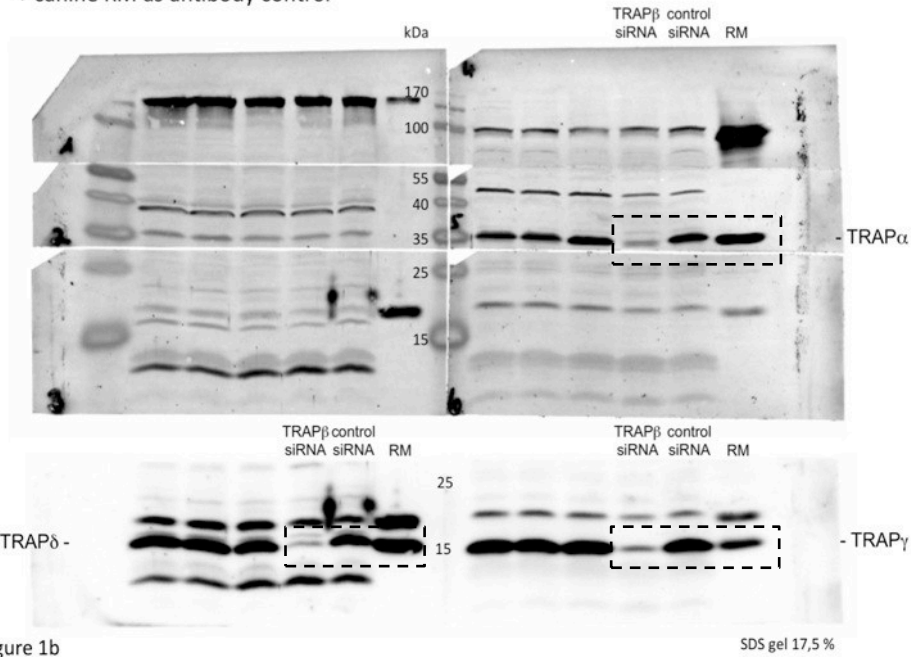
Supplementary Figure S14. Full western blot scans from Figure 1b. Cropped areas are indicated.

Supplementary Figure S15. Full western blot scans from Figure 2a. Cropped areas are indicated.

anti-RibII and -β-actin antibody decoration of RibII silenced cells + canine RM as antibody control

anti-RibI antibody decoration of RibII silenced cells + canine RM as antibody control
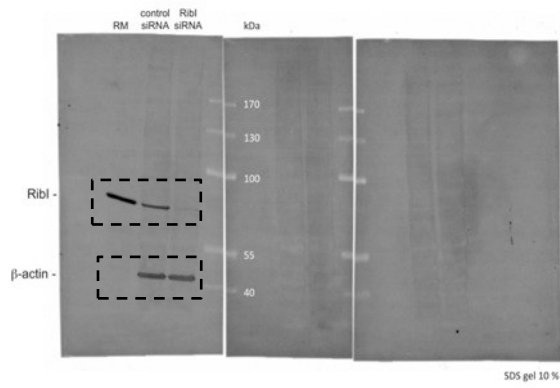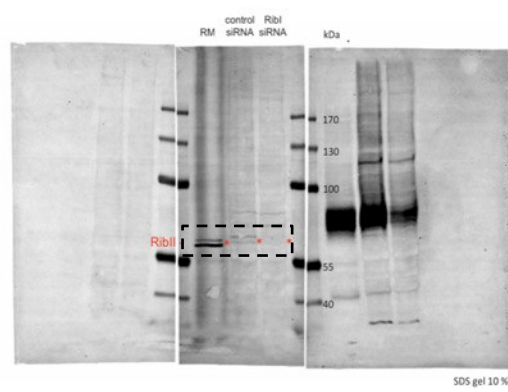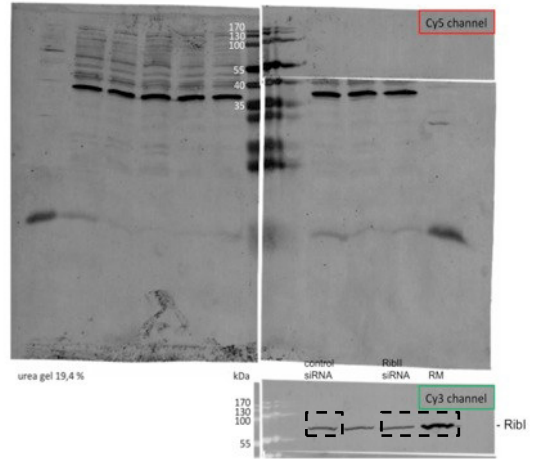
anti-STT3B antibody decoration of RibII silenced cells + canine RM as antibody control
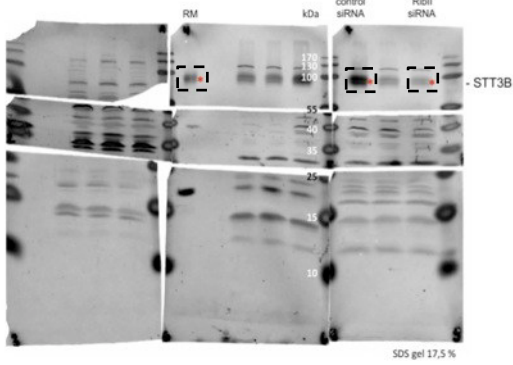
anti-OST48 antibody decoration of RibII silenced cells + canine RM as antibody control
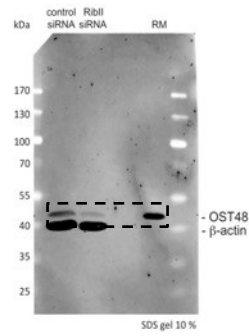
anti-DAD1 antibody decoration of RibII silenced cells + canine RM as antibody control
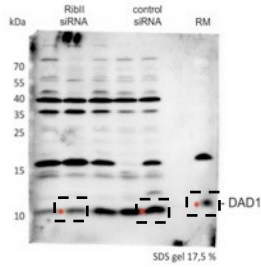
Supplementary Figure S16. Full western blot scans from Figure 2c. Cropped areas are indicated.
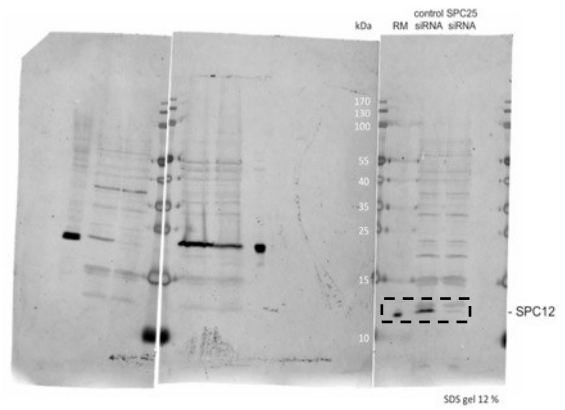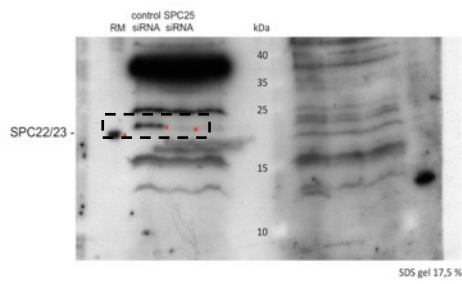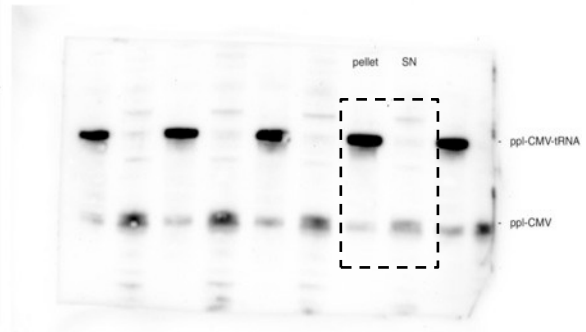
Supplementary Figure S17. Full western blot scans from Supplementary Fig. S6. Cropped areas are indicated.
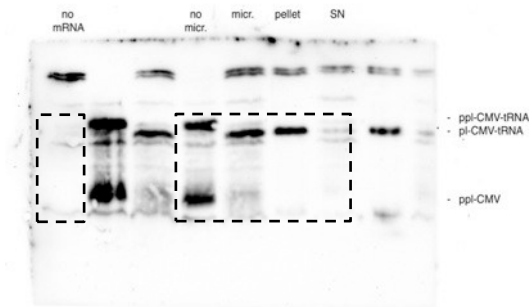
Western blotting using streptavidin coupled horseradish peroxidase
(from Supplementary Figure S7a)
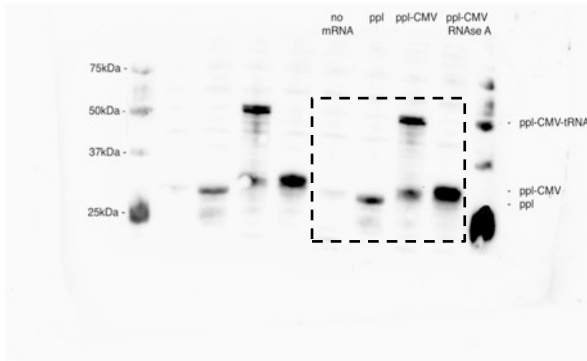
Western blotting using streptavidin coupled horseradish peroxidase
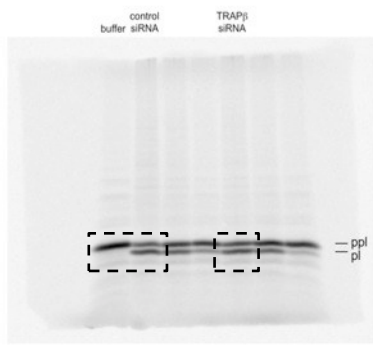(from Supplementary Figure S7a)

Western blotting using streptavidin coupled horseradish peroxidase
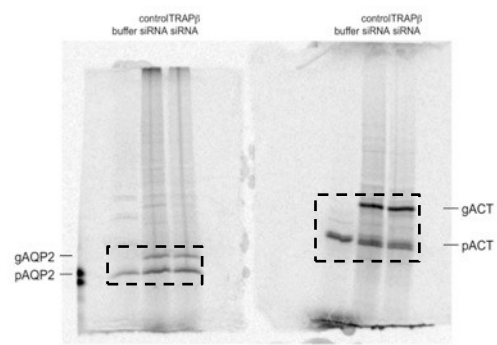(from Supplementary Figure S7b)

Supplementary Figure S18. Full western blot scans from Supplementary Fig. S7. Cropped areas are indicated.
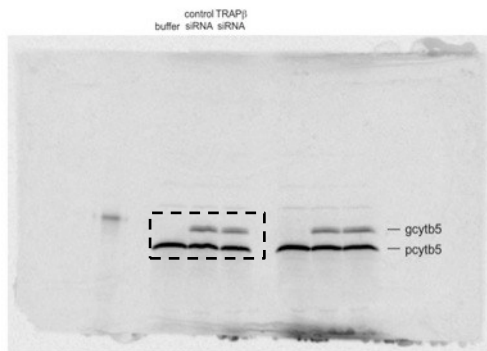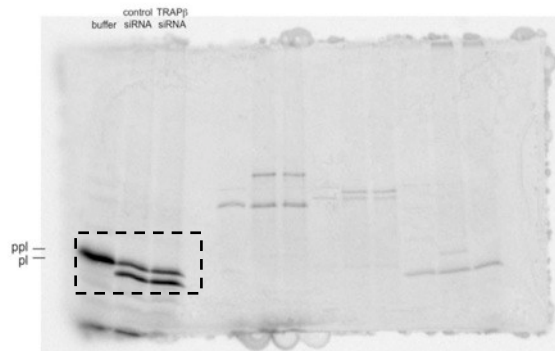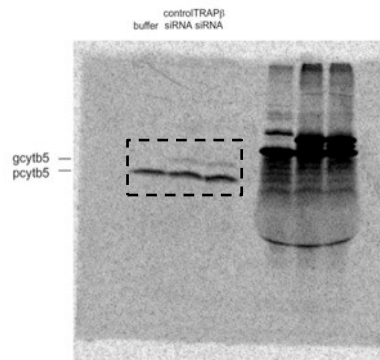
Supplementary Figure S19. Full phosphoimaging scans from Supplementary Fig. S4. Cropped areas are indicated.

Supplementary Table S1. Antibody working dilutions and catalogue numbers of purchased antibodies.

Antibody	Dilution	Company	Catalogue number
Sec61α	1:200		
SPase22/23	1:300		
SPase25	1:300		
Sec62	1:500 WB 1:100 IF		
TRAPα	1:500		
BiP	1:500		
SPase12	1:300		
Grp170	1:500		
TRAPβ	1:500		
SRα	1:500		
GRP94	1:500		
Sec63	1:500		
ERj1	1:500		
Ribophorin I	1:500		
Ribophorin II	1:500		
STT3B	1:500		
DAD1	1:500		
ERp57	1:500		
OST48	1:250	Santa Cruz	sc-74408
Calnexin	1:1000	Stressgene	SPA-860
TRAPγ	1:500	Sigma	HPA014906
TRAPδ	1:500	Sigma	HPA045209
β-actin	1:10.000	Sigma	A5441
anti-rabbit IgG peroxidase conjugated	1:1000	Sigma	A8275
anti-rabbit IgG-Cy5	1:1000	GE	PA45012
anti-mouse IgG-Cy3	1:1000	GE	PA43010
Alexa-Fluor-594	1:1000	Invitrogen	A11012

2.3   Structure of the native Sec61 protein-conducting channel

This manuscript has not been published, yet.

Summary

In this manuscript, we structurally and functionally characterized native, non-solubilized ribosome-Sec61 complexes on pancreatic rough ER vesicles. Using CET and subtomogram analysis, we obtained a structure of the ER-associated ribosome at 9 Å resolution, in which the conformation of Sec61 in the native translocon could be determined unambiguously. Functional characterization by subtomogram classification and deep sequencing of ribosome-protected mRNA fragments (ribosome profiling) revealed that the majority of visualized ER-associated ribosomes were in an idle state, while the subpopulation of active ribosomes were almost exclusively engaged in translation of secretory proteins. Although Sec61 is clearly not in an inserting state in our structure as a consequence, it surprisingly adopts a conformation with an open lateral gate, which was previously thought to be present only transiently during insertion of a nascent transmembrane helix into the lipid bilayer. In contrast to previous mechanistic models for peptide translocation and insertion, all based on structural analysis of the detergent solubilized Sec61 complex, our results suggest that the open conformation of Sec61 is the only major conformation present in the fully assembled ribosome-bound translocon complex, independent of its functional state.

Contribution

For this article, I carried out grid preparation for electron microscopy, acquisition of CET data (including setup of automated data acquisition and extensive pre-screening for optimal acquisition parameters) and the complete workflow for data processing and map interpretation. I wrote major parts of the manuscript and prepared most of the figures.

Structure of the native Sec61 protein-conducting channel

Stefan Pfeffer[1], Laura Burbaum[1], Pia Unverdorben[1], Markus Pech[2], Yuxiang Chen[1], Richard Zimmermann[3], Roland Beckmann[2], Friedrich Förster[1#]

[1] Max-Planck Institute of Biochemistry, Department of Molecular Structural Biology, Martinsried, Germany

[2] Gene Center and Center for integrated Protein Science Munich, Department of Biochemistry, University of Munich, Munich, Germany

[3] Saarland University, Department of Medical Biochemistry and Molecular Biology, Homburg, Germany

[#] Correspondence to: foerster@biochem.mpg.de

Abstract

In mammalian cells, proteins are translocated across or inserted into the endoplasmic reticulum (ER) membrane by the ER protein translocon, a multi-subunit complex located in the ER membrane. The universally conserved protein-conducting channel Sec61 forms the core of the translocon and has been structurally studied by X-ray crystallography and single particle cryo-EM in isolated, detergent solubilized states. Here, we structurally and functionally characterized native, non-solubilized ribosome-Sec61 complexes on pancreatic rough ER vesicles. Using CET and subtomogram analysis, we obtained a structure of the ER-associated ribosome at 9 Å resolution, in which the conformation of Sec61 in the native translocon could be unambiguously determined. Functional characterization by subtomogram classification and deep sequencing of ribosome-protected mRNA fragments revealed that the majority of visualized ER-associated ribosomes were in an idle state, while the subpopulation of active ribosomes were almost exclusively engaged in synthesis of soluble secretory proteins. Although Sec61 is clearly not in an inserting state in our structure as a consequence, it surprisingly adopts a conformation with an open lateral gate, which was thought to be present only transiently during insertion of a nascent transmembrane helix into the lipid bilayer. In contrast to previous mechanistic models for peptide translocation and insertion, our results suggest, that the open conformation of Sec61 is the only major conformation present in the fully assembled ribosome-bound translocon complex, independent of its functional state.

Introduction

In eukaryotic cells, many proteins have to be translocated across or inserted into the endoplasmic reticulum (ER) membrane during their synthesis [1]. These processes are facilitated by the translocon, a multi-subunit complex located in the ER membrane. The universally conserved heterotrimeric protein-conducting channel Sec61 forms the core of the translocon and binds to translating ribosomes for co-translational protein transport. The structure of the prokaryotic Sec61 homolog, the SecY complex, has been extensively studied by X-ray crystallography [2,3]. Single particle cryo-EM studies have provided high-resolution structures of eukaryotic solubilized and purified ribosome-Sec61 complexes [4,5]. On the basis of these structures, a detailed model for protein translocation through a central pore and protein membrane insertion via a lateral gate, formed by two adjacent transmembrane helices (TMHs) of Sec61α, has been proposed [2,5]. Specifically, two major conformations are thought to underlie the two fundamentally different functional states of Sec61: (I) in the 'non-inserting state' (idle or translocating a soluble polypeptide chain), Sec61 is believed to adopt a compact conformation with a closed lateral gate ('closed' conformation); (II) in the 'inserting state' (integration of a TMH into the membrane), Sec61 is supposed to transiently adopt a less compact conformation with an open lateral gate ('open' conformation). Recently, structures of the solubilized ribosome-Sec61 complex purified from porcine pancreas were determined for the two non-inserting conditions, revealing the binding moieties of Sec61 at unprecedented resolution (3.4 and 3.9 Å, respectively) [6]. To date all structural studies that resolved conformations of Sec61 focused on the detergent solubilized protein-conducting channel in the absence of all other canonical translocon components. Thus, the structure of Sec61 in its native context remains uncharted territory.

Cryo-electron tomography (CET) in combination with subtomogram analysis is an excellent method for studying the structures of large macromolecules in their natural environment [7,8]. It

is particularly attractive for studying membrane-embedded and –associated complexes, because detergent solubilization is not required, avoiding destabilization of the complex and possible misinterpretation of the density of the detergent micelle surrounding a solubilized membrane protein. CET provided first insights into the structure of the native translocon [9] and further studies based on isolated rough ER (rER) vesicles from canine and human origin allowed identification of Sec61, the translocon associated protein complex (TRAP) and the oligosaccharyl-transferase (OST) complex in a map of the native translocon at 20 Å-resolution [10]. By classification approaches, the latter study also revealed compositional heterogeneity of the translocon; while TRAP is a stoichiometric component of the ribosome-bound translocon complex, OST was found to be present in only 40-70% of translocon complexes. Subnanometer resolution subtomogram averages of membrane protein complexes have recently been obtained from ~100,000 asymmetric units, which can be collected relatively efficiently for symmetrical samples such as virus coats using automated CET data acquisition [11-13]. Recent revolutionary developments in direct detector technology [14] suggest that subnanometer resolution subtomogram averages are in reach for much smaller datasets and hence for non-symmetrical macromolecules. Benefitting from these developments in direct detector technology, we obtained a subtomogram average of mainly idle mammalian ribosomes bound to the native translocon in rER-vesicles at subnanometer resolution. This structure allowed determining the conformation of native Sec61 in a non-inserting state, revealing an open lateral gate even in the absence of a nascent transmembrane helix, breaking with the current dogma of ER translocation.

Results and Discussion

Structure determination

For structure determination of the ribosome-bound translocon in its native membrane environment, we applied CET and subtomogram analysis to rER-vesicles isolated from dog pancreas. Functional assays and western blotting have shown that these rER-vesicles contain all protein components necessary for co-translational protein transport and membrane protein integration, as well as subsequent maturation steps of nascent peptides [9,10]. In our tomograms, rER-vesicles have a size of 100-300 nm and are densely populated with membrane-bound ribosomes (Extended Data Fig. 1). From 211 single axis tomograms recorded on a Titan Krios (FEI) equipped with energy filter and K2 Summit direct detector (both Gatan), we retrieved 105,500 candidate particles by a six-dimensional cross-correlation search [15] with a ribosome template ('template matching'). In a first round of classification, we separated false positives and the majority of non membrane-bound ribosomes from ER-associated ribosomes (27,500 remaining subtomograms), which were subsequently subjected to iterative subtomogram alignment. In a second round of classification, ribosomes bound to the OST-containing translocon were separated from remaining non membrane-bound ribosomes and ribosomes bound to the OST-lacking translocon (Extended Data Fig. 2). In order to restrict the cumulative electron dose to ~ 30 e/Å^2 and to avoid influence of specimen alteration due to beam damage, the remaining 17,600 subtomograms were reconstructed from projections covering only a reduced tilt range (-20° to 20°).

Overall structure of the native ER translocon

After refinement of the subtomogram alignment, the segment of the resulting subtomogram average (Fig. 1) that represents the ribosome is resolved to approximately 9 Å, as estimated by Fourier cross-resolution (FCR) and Fourier shell correlation (FSC) of averages from two halves of the data (Extended Data Fig. 3a). Distinguishable features, such as rod-like densities

co-localizing with alpha helices in a superposed atomic model of the ribosome (Extended Data Fig. 3b) are consistent with the estimated resolution. Our reconstruction of the ER-associated ribosome is thus the first structure of a non-symmetric macromolecular assembly determined by CET and subtomogram analysis at subnanometer resolution. In the translocon part of the subtomogram average, we clearly distinguish TMHs for Sec61, TRAP and OST (Fig. 1). Consistently, the local resolution for most of the ribosome-associated membrane part of the average is determined to be better than 10 Å (Extended Data Fig. 3c). In contrast, local resolution estimation suggests that the lumenal parts of TRAP and OST are resolved to only 12-15 Å. In line with this observation, we found that ribosome-binding to the translocon is not entirely homogeneous, but allows for minor tilting of the ribosome (up to approximately 5°), along an axis formed by its membrane contacts. While this tilting barely affects directly ribosome-associated translocon density, misalignment of the translocon part increases into the lumen, resulting in worse resolution for the lumenal parts of TRAP and OST. Subtomogram alignment focused on the lumenal parts of the translocon did not yield satisfactory results, probably because the signal of subtomograms excluding the ribosome was insufficient for accurate alignment.

All subtomograms depict ribosome-Sec61 complexes in the non-inserting state

The absence of visible density for tRNAs in our subtomogram average already indicates that the majority of contributing subtomograms correspond to idle ribosome-translocon complexes not engaged in translocation or membrane integration of a nascent peptide. Indeed, unsupervised classification of subtomograms focused on the tRNA binding sites confirms the complete absence of tRNAs for the majority of subtomograms (71%). For a minority of subtomograms (29%), well-defined density for tRNAs is present (Fig. 2a), indicating actively translating ribosomes. In line with the specialization of pancreatic tissue in the synthesis of extracellular digestive enzymes, ribosome profiling reveals that 94% of these actively

translating ribosomes in our rER sample are engaged in the synthesis of soluble secretory proteins (Fig. 2b), in particular of the digestive system. The most abundant reads were those of pancreatic lipases as well as proteases such as anionic trypsin and chymotrypsin C. This suggests that the subtomograms in our dataset depict ribosome-Sec61 complexes almost exclusively in the two non-inserting states (either idle or translocating a soluble protein), which have been proposed to be not completely identical [6] but highly similar, in particular at a resolution of approximately 9 Å [4,5]. Concordantly, structural details and resolution of the density segment representing Sec61 in the native translocon are significantly improved for the complete dataset of 17,600 subtomograms (9.4 Å) compared to the subpopulation of only idle ribosome-Sec61 complexes (12,500 subtomograms, 10.6 Å) (Extended Data Fig. 4). Thus, consistent with previous studies, the idle and translocating states of Sec61 are essentially indistinguishable at the resolution range of 9-10 Å in the native translocon and are therefore referred to as one single 'non-inserting state'.

Native Sec61 adopts an open conformation in the non-inserting state

As classification according to tRNA occupancy revealed that the majority of particles contributing to our subtomogram average (71%) correspond to idle ribosome-translocon complexes, we fitted an atomic model of the complete idle ribosome-Sec61 complex (PDBs 3J7Q and 4W23) into our subtomogram average as a rigid body. With this global fit, we observed excellent co-localization of rod-like densities in the translocon part of the average and α-helices in the atomic model for the C-terminal domain of Sec61α and Sec61γ (Extended Data Fig. 5a). In contrast, for the N-terminal domain of Sec61α and Sec61β, helices in the atomic model and the subtomogram average do not match initially. However, when the N-terminal domain of Sec61α and Sec61β are fitted as a rigid body separately, co-localization of helical densities in the average and α-helices in the atomic model is achieved

also for the N-terminal domain of Sec61α and Sec61β (Extended Data Fig. 5b). The only α-helix, which was not entirely positioned in a rod-like density for either of the two arrangements, is the very C-terminal TMH 10 of Sec61α. A translation of this helix by approximately 13 Å along its axis towards the ribosome entirely embeds it in a well-defined rod-like density (Extended Data Fig. 5c). The model, resulting from the two described rigid body fits and the adjustment of TMH 10 served as an initial model for molecular dynamics flexible fitting (MDFF) [16]. After MDFF all helices of the hetero-trimeric Sec61 complex are unambiguously positioned in the density (Fig. 3), revealing the conformation of native Sec61 in a non-inserting state (Fig. 4a).

Compared to the starting model, the C-terminal domain of Sec61α and consequently the interaction with the ribosome remain largely unaltered with the exception of TMH 10, which moves 13 Å towards the ribosome. This repositioning of TMH 10 into immediate proximity to the ribosome might indicate a functional role in protein transport for this helix, as previously proposed [3]. In contrast to the invariant position of the C-terminal half of Sec61α, the N-terminal domain of Sec61α, in concert with Sec61β, undergoes a rigid body movement (rotation: 22°; translation along rotation axis: 13.8 Å), resulting in an opening of the lateral gate in the native Sec61 complex (Fig. 4b). Thus, when in the context of the complete translocon, native non-inserting Sec61 clearly adopts an open conformation akin to the conformation first observed in an X-ray crystallographic structure of an isolated SecYE complex, which supposedly mimics the inserting state of the protein-conducting channel [3] (Fig. 4c). Similar open conformations have also been described for detergent solubilized Sec61 complexes engaged in the integration of a nascent TMH through the lateral gate into the membrane [5,17].

Implications for the mechanistic model of protein translocation/insertion

The discrepant conformations of native and detergent solubilized Sec61 in the non-inserting state may be explained by the effects of detergent solubilization or by the interaction with the accessory translocon components TRAP and OST. The differing physical properties of a membrane bilayer compared to a detergent micelle and the tight complex formation with TRAP and OST as observed in the native translocon may trigger a conformational change from the 'open' to the 'closed' conformation upon solubilization. However, the presence of a nascent transmembrane helix in the lateral gate seems to stabilize the open state also upon solubilization of Sec61, as indicated by the open conformations observed in recent cryo-EM studies [5,17]. Previous mechanistic models, which were derived from the cryo-EM maps and X-ray structures of detergent-solubilized samples, suggested that ribosome-bound Sec61 is mostly present in a closed conformation and only opens transiently for integration of a nascent transmembrane helix. In contrast, based on the structure of the native ribosome-Sec61 complex in the non-inserting state, we conclude that the 'open' conformation of Sec61 may be the only major conformation present in the fully assembled ribosome-bound translocon complex independent of its functional state (idle, translocating, inserting a nascent TMH). The 'pre-opened' conformation of Sec61 observed in our structure may provide immediate access to the lipid bilayer for hydrophobic nascent polypeptide stretches emerging from the ribosome, such as TMHs or signal sequences, as previously suggested based on site-specific crosslinking [18]. A largely invariant conformation of ribosome-associated Sec61 would also be consistent with a model that membrane integration and folding of membrane proteins is primarily driven by the thermodynamic behavior of the growing nascent chain [19]. The structure of non-ribosome associated Sec61 in the native membrane and its assembly state remain uncharted. Nevertheless, it is likely that Sec61 adopts its closed conformation in a ribosome-free idle state in the native system, in order to maintain the necessary ion permeability barrier. This model would be consistent with a recent analysis using photo-

induced electron transfer, which shows that SecY alone adopts a closed conformation in a lipid environment and undergoes an opening of the lateral gate upon binding of idle ribosomes and ribosome-nascent chain complexes with and without a TMH [20].

Our study highlights the importance of analyzing the structure of membrane proteins in their native membrane environment and in complex with their physiological interaction partners and it suggests that peptide translocation and membrane protein insertion involve much smaller conformational changes of Sec61 than previously thought. Our structure of the translocon not only allows detailed insights into the conformation of Sec61 in the native translocon, but it also represents a solid basis for follow-up studies of both structural and biochemical nature that may results in a detailed mechanistic understanding of protein transport, membrane insertion and maturation facilitated cooperatively by Sec61 and accessory translocon components.

Methods

Sample preparation and CET

Rough microsomes were prepared from dog pancreas as previously described [21], but omitting the nuclease treatment. Microsomes were diluted to 0.25 eq/μl using ribosome buffer (20mM Hepes, pH 7.6; 50mM KCl; 2mM $MgCl_2$) and 3 μl were applied to lacey carbon molybdenum grids (Ted Pella, USA). After an incubation time of 60 s at 22°C, 3 μl of 10-nm colloidal gold in ribosome buffer were added to the grid and the sample was vitrified in liquid ethane using a Vitrobot Mark IV (FEI Company, The Netherlands). Tilt series were acquired using a FEI Titan Krios transmission electron microscope (TEM) equipped with a "K2 summit" direct electron detector (Gatan, USA), operated in movie mode with 4-7 frames per projection image (exposure time 0.8-1.4 s). The TEM was operated at an acceleration voltage of 300 kV, a nominal defocus of 3-4 μm and an object pixel size of 2.62 Å. Single-axis tilt series were recorded from -60° to +60° (first half: -20° to +60°; second half; -22° to -60°) with an angular increment of 2° and a cumulative electron dose of 90-100 electrons/Å^2 using the Serial EM acquisition software [22].

Image processing

Frames from the K2 direct electron detector were aligned using a quasi-expectation maximization protocol implemented in the MATLAB toolbox AV3 [23]. Correction of phase reversals due to the contrast transfer function was performed using MATLAB scripts and PyTom [24] on single projections, as described in [25]. Tomogram reconstruction (object pixel: 2.1 nm) and template matching against a single particle cryo-EM reconstruction of the human 80S ribosome [26] filtered to 5 nm resolution were accomplished using PyTom [24] as described [9]. Subtomograms (object pixel: 2.1 nm) centered at the coordinates of the 500 highest-scoring peaks of the cross correlation function were classified using constrained principal component

analysis (CPCA) [27] focusing on an area encompassing the large ribosomal subunit and the ER membrane. This classification separated ER membrane-associated ribosomes from most false-positive matches, such as gold markers, ER membrane or carbon edges. For the retained coordinates, subtomograms (110^3 voxels, object pixel: 0.524 nm) were reconstructed individually from the weighted projections using the full tilt range (-60° to +60°). After iterative alignment using PyTom [24], a second round of CPCA [27] focused on the translocon part of the subtomograms separated ribosomes bound to the OST-containing translocon from ribosomes bound to the OST-lacking translocon, remaining non membrane-bound ribosomes and false positives. For the retained coordinates, subtomograms (220^3 voxels, object pixel: 0.262 nm) were reconstructed using only a reduced tilt range (-20° to +20°) in order to restrict the cumulative electron dose to 30 electrons/$Å^2$. Subtomograms were iteratively aligned using PyTom [24] and the resolution of the subtomogram average was determined by Fourier shell correlation (FSC=0.5) of two averages from each half of the data and cross resolution (FSC=0.33) with a single particle reconstruction of the human 80S ribosome [26] on appropriately masked maps. Local resolution estimation was performed using BSoft [28]. For visualization the resolution-limited maps were sharpened using a B-factor of -500.

EM-map analysis and flexible fitting

The atomic model of the idle Sec61 complex bound to the 60S ribosome (PDB 3J7Q) was fitted into the subtomogram average as a rigid body using UCSF Chimera [29], resulting in a good initial fit for the C-terminal half of Sec61α and Sec61γ, as judged by colocalization of helices and rod-like densities. Then, the N-terminal half of Sec61α and Sec61β were fitted into the subtomogram average as a rigid body independently of the rest of the atomic model, resulting in a good initial fit for the N-terminal half of Sec61α and Sec61β. Since TMH 10 of Sec61α is neither positioned accurately in the appropriate rod-like density for the rigid body

fit for the C- nor for the N-terminal half of Sec61α, its position was manually adjusted. The resulting atomic model of Sec61 was refined using molecular dynamics flexible fitting [16] (MDFF) in VMD [30] until convergence using a simulated annealing protocol and implicit solvent. For comparing Sec61 conformations, atomic models of Sec61 were structurally aligned according to the C-terminal half of Sec61α using UCSF Chimera.

Ribosome Profiling

Next-generation sequencing libraries of ribosome protected fragments and total RNA were prepared using the ARTseq™ Ribosome Profiling Kit (epicentre®) according to the manufactures protocol with the following modification. After RNase I treatment of rough microsomes 80S monosomes were isolated by sucrose gradient and protected mRNA fragments were recovered by dissociation of the monosomes into subunits. Raw single-end sequencing reads were clipped of the known adaptor sequence. Clipped reads were first mapped to *C. familiaris* rRNA, tRNA and mitochondrial non-coding RNA using Bowtie 1.0.0. Unaligned reads were then mapped to the dog genome assembly (CanFam3.1, Ensemble release 77) using GSNAP (version 2013-10-10) including annotated splice junctions. Unique aligned reads on protein coding genes were counted with HTSeq 0.6.1 and normalized for the length of the coding sequence. For total mRNA sequencing RNase I digestion was omitted.

References

1	Corsi, A. K. & Schekman, R. Mechanism of polypeptide translocation into the endoplasmic reticulum. *J Biol Chem* **271**, 30299-30302 (1996).

2	Van den Berg, B. *et al.* X-ray structure of a protein-conducting channel. *Nature* **427**, 36-44 (2004).

3	Egea, P. F. & Stroud, R. M. Lateral opening of a translocon upon entry of protein suggests the mechanism of insertion into membranes. *Proc. Natl. Acad. Sci. USA* **107**, 17182-17187 (2010).

4	Becker, T. *et al.* Structure of monomeric yeast and mammalian Sec61 complexes interacting with the translating ribosome. *Science* **326**, 1369-1373 (2009).

5	Gogala, M. *et al.* Structures of the Sec61 complex engaged in nascent peptide translocation or membrane insertion. *Nature* **506**, 107-110 (2014).

6	Voorhees, R. M., Fernandez, I. S., Scheres, S. H. & Hegde, R. S. Structure of the mammalian ribosome-Sec61 complex to 3.4 A resolution. *Cell* **157**, 1632-1643 (2014).

7	Briggs, J. A. Structural biology in situ--the potential of subtomogram averaging. *Curr. Opin. Struct. Biol.* **23**, 261-267 (2013).

8	Forster, F. & Hegerl, R. Structure determination in situ by averaging of tomograms. *Methods Cell Biol.* **79**, 741-767 (2007).

9	Pfeffer, S. *et al.* Structure and 3D Arrangement of Endoplasmic Reticulum Membrane-Associated Ribosomes. *Structure* **20**, 1508-1518 (2012).

10	Pfeffer, S. *et al.* Structure of the mammalian oligosaccharyl-transferase complex in the native ER protein translocon. *Nat Commun* **5**, 3072 (2014).

11	Schur, F. K. *et al.* Structure of the immature HIV-1 capsid in intact virus particles at 8.8 A resolution. *Nature* (2014).

12	Bharat, T. A. *et al.* Cryo-electron microscopy of tubular arrays of HIV-1 Gag resolves structures essential for immature virus assembly. *Proc. Natl. Acad. Sci. USA* **111**, 8233-8238 (2014).

13	Schur, F. K., Hagen, W. J., de Marco, A. & Briggs, J. A. Determination of protein structure at 8.5A resolution using cryo-electron tomography and sub-tomogram averaging. *J. Struct. Biol.* **184**, 394-400 (2013).

14	Li, X. *et al.* Electron counting and beam-induced motion correction enable near-atomic-resolution single-particle cryo-EM. *Nat Methods* **10**, 584-590 (2013).

15	Forster, F., Han, B. G. & Beck, M. Visual proteomics. *Methods Enzymol.* **483**, 215-243 (2010).

16	Trabuco, L. G., Villa, E., Mitra, K., Frank, J. & Schulten, K. Flexible fitting of atomic structures into electron microscopy maps using molecular dynamics. *Structure* **16**, 673-683 (2008).

17	Park, E. *et al.* Structure of the SecY channel during initiation of protein translocation. *Nature* **506**, 102-106 (2014).

18	Martoglio, B., Hofmann, M. W., Brunner, J. & Dobberstein, B. The protein-conducting channel in the membrane of the endoplasmic reticulum is open laterally toward the lipid bilayer. *Cell* **81**, 207-214 (1995).

19	Cymer, F., von Heijne, G. & White, S. H. Mechanisms of Integral Membrane Protein Insertion and Folding. *J. Mol. Biol.* **427**, 999-1022 (2015).

20	Ge, Y., Draycheva, A., Bornemann, T., Rodnina, M. V. & Wintermeyer, W. Lateral opening of the bacterial translocon on ribosome binding and signal peptide insertion. *Nat Commun* **5**, 5263 (2014).

21   Watts, C., Wickner, W. & Zimmermann, R. M13 procoat and a pre-immunoglobulin share processing specificity but use different membrane receptor mechanisms. *Proc. Natl. Acad. Sci. USA* **80**, 2809-2813 (1983).

22   Mastronarde, D. N. Automated electron microscope tomography using robust prediction of specimen movements. *J. Struct. Biol.* **152**, 36-51 (2005).

23   Forster, F., Medalia, O., Zauberman, N., Baumeister, W. & Fass, D. Retrovirus envelope protein complex structure in situ studied by cryo-electron tomography. *Proc. Natl. Acad. Sci. USA* **102**, 4729-4734 (2005).

24   Hrabe, T. *et al.* PyTom: a python-based toolbox for localization of macromolecules in cryo-electron tomograms and subtomogram analysis. *J. Struct. Biol.* **178**, 177-188 (2012).

25   Eibauer, M. *et al.* Unraveling the structure of membrane proteins in situ by transfer function corrected cryo-electron tomography. *J. Struct. Biol.* **180**, 488-496 (2012).

26   Anger, A. M. *et al.* Structures of the human and Drosophila 80S ribosome. *Nature* **497**, 80-85 (2013).

27   Forster, F., Pruggnaller, S., Seybert, A. & Frangakis, A. S. Classification of cryo-electron sub-tomograms using constrained correlation. *J. Struct. Biol.* **161**, 276-286 (2008).

28   Cardone, G., Heymann, J. B. & Steven, A. C. One number does not fit all: mapping local variations in resolution in cryo-EM reconstructions. *J. Struct. Biol.* **184**, 226-236 (2013).

29   Pettersen, E. F. *et al.* UCSF Chimera--a visualization system for exploratory research and analysis. *J. Comput. Chem.* **25**, 1605-1612 (2004).

30   Humphrey, W., Dalke, A. & Schulten, K. VMD: visual molecular dynamics. *J Mol Graph* **14**, 33-38, 27-38 (1996).

Author contributions SP and LB carried out the CET analysis. PU performed flexible fitting and YC provided software for CET data processing. MP carried out ribosome profiling. FF, RB and RZ planned and supervised the experiments and together with SP wrote the manuscript.

Author Information The subtomogram average of the ER membrane-associated ribosome at subnanometer resolution has been deposited in the EMDataBank with accession code XX. Atomic coordinates of native Sec61 in the non-inserting state have been deposited in the PDB with accession code XXX. Reprints and permissions information is available at www.nature.com/reprints. The authors declare no competing financial interests. Correspondence and requests for materials should be addressed to F.F (foerster@biochem.mpg.de).
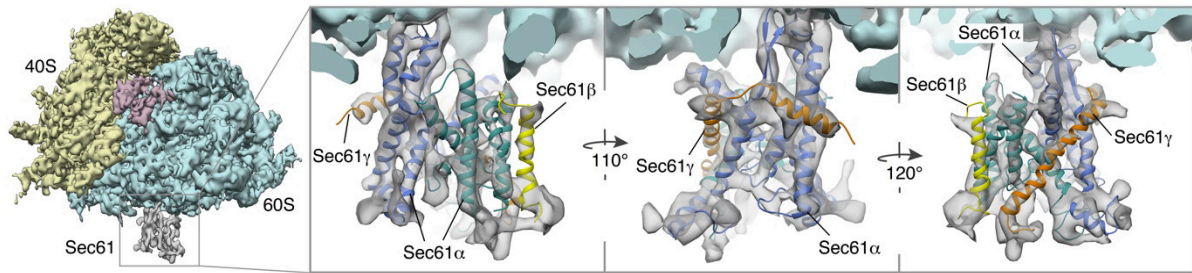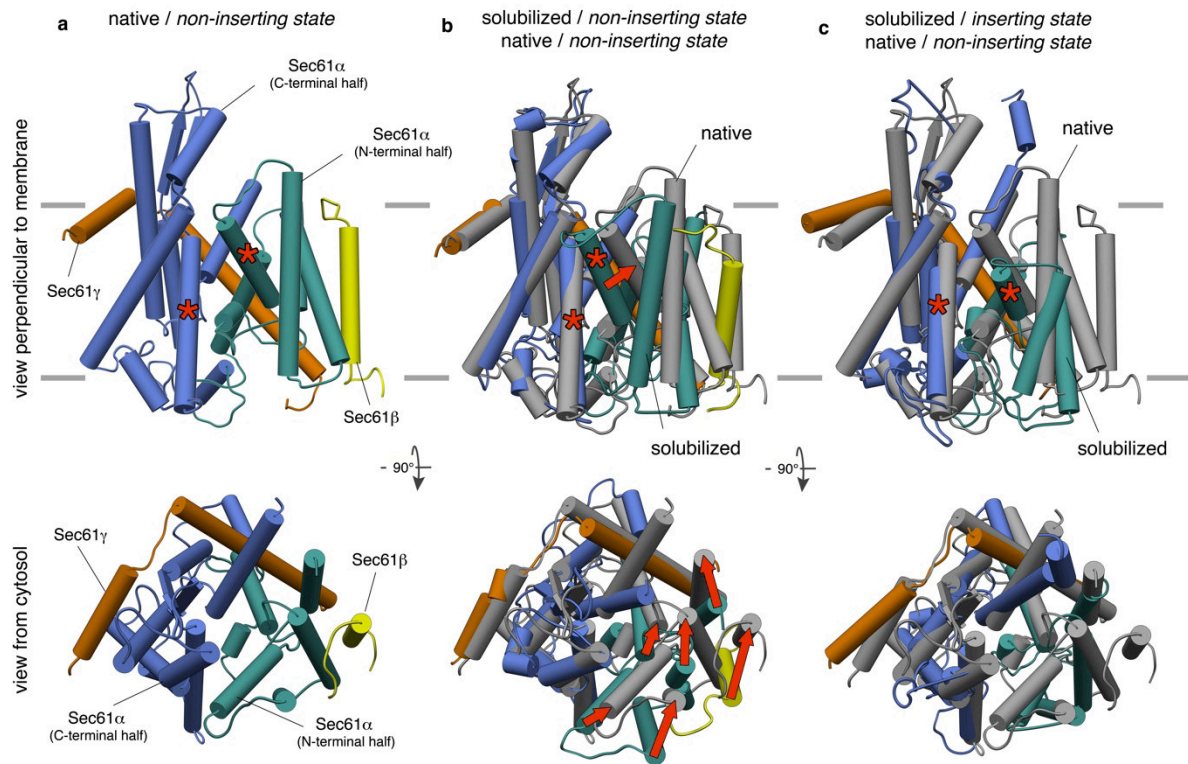
Figures
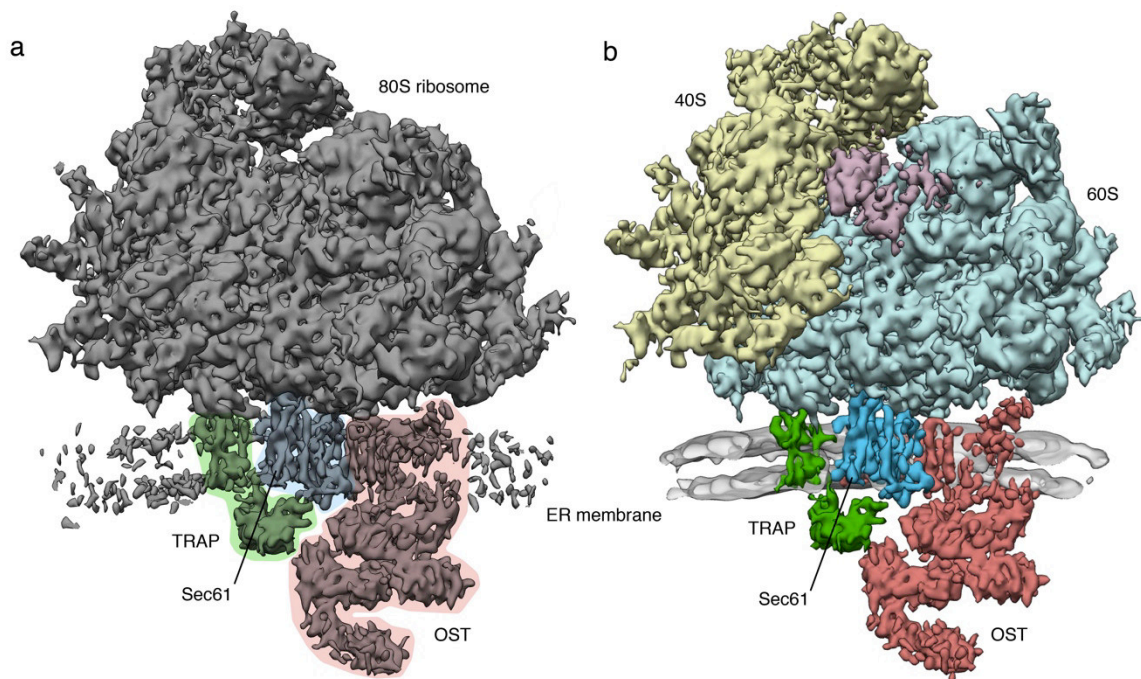
Figure 1: Overall structure of the ER membrane-associated mammalian ribosome. a, Subtomogram average of the ER membrane-associated ribosome filtered to 9.0 Å resolution. In the otherwise unprocessed map, TMHs for Sec61 (blue), TRAP (green) and OST (red) can be distinguished clearly in the membrane. The membrane part of the average has been cut to better visualize the membrane integral parts of the translocon. **b,** Segmented densities for the 40S (yellow) and 60S (light blue) ribosomal subunits, translation elongation factors (magenta), Sec61 (blue), TRAP (green) and OST (red). Density for the ER membrane (gray) has been filtered to 2 nm resolution and cut to emphasize the membrane integral parts of the translocon.
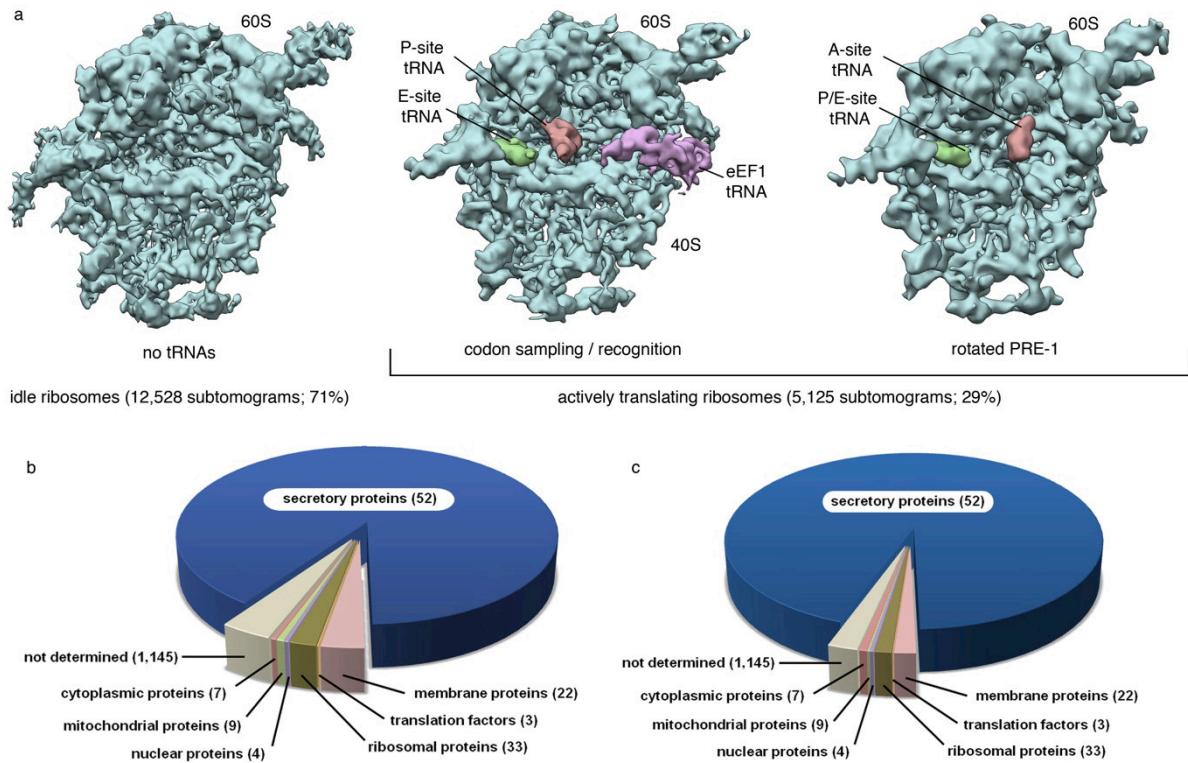
Figure 2: Characterization of Sec61 functional states by classification and mRNA sequencing. a, Classes obtained by unsupervised classification of subtomograms focused on the tRNA binding sites. Only the 60S subunit is shown oriented such that the ER membrane corresponds to the paper plane. Class abundance is specified as absolute number of subtomograms and percentage of all particles. Translational states of classes with defined density for tRNAs have been assigned based on single particle cryo-EM maps of translating ribosomal complexes (EMD 2623 and EMD 5328). **b,c** Characterization of translational activity in the rER sample by sequencing of total mRNA (b) and ribosome protected mRNA fragments (c). 94% of ribosome protected mRNA fragments (c) code for soluble secretory proteins. Numbers of contributing mRNAs are provided in brackets.

Figure 3: Atomic model of native Sec61 in the non-inserting state. Left: Isolated densities for the 40S (yellow) and 60S (light blue) ribosomal subunits, translation elongation factors (magenta) and Sec61 (gray). In the magnified views, the flexibly fitted atomic model of the heterotrimeric Sec61 complex was superposed on the density. The N- and C-terminal halves of Sec61α (green and blue, respectively), Sec61β (yellow) and Sec61γ (orange) are depicted.
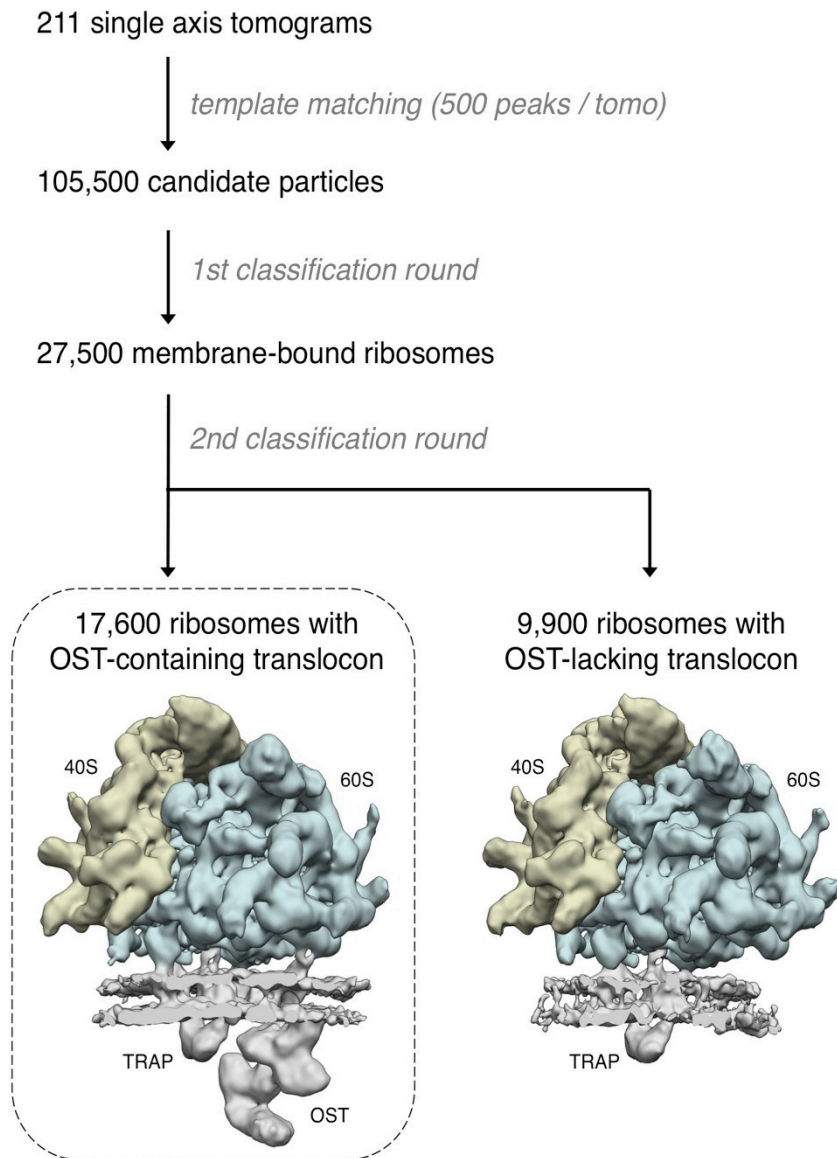
Figure 4: Native Sec61 adopts an open conformation in the non-inserting state. a, Conformation of native Sec61 in the non-inserting state. The N- and C-terminal halves of Sec61α (green and blue, respectively), Sec61β (yellow) and Sec61γ (orange) are depicted. In the views perpendicular to the membrane the asterisks mark the two TMHs forming the lateral gate. **b,** Superposition of native (gray) and solubilized Sec61 (colored as in a; PDBs 3J7Q[6]) in the non-inserting state. Red arrows indicate the motions of TMHs in the N-terminal half of Sec61α and Sec61β linking both conformations. **c,** Conformations of native Sec61 in the non-inserting state (gray) and solubilized SecYE mimicking the inserting state (colored as in a; PDB 3MP7[3]).
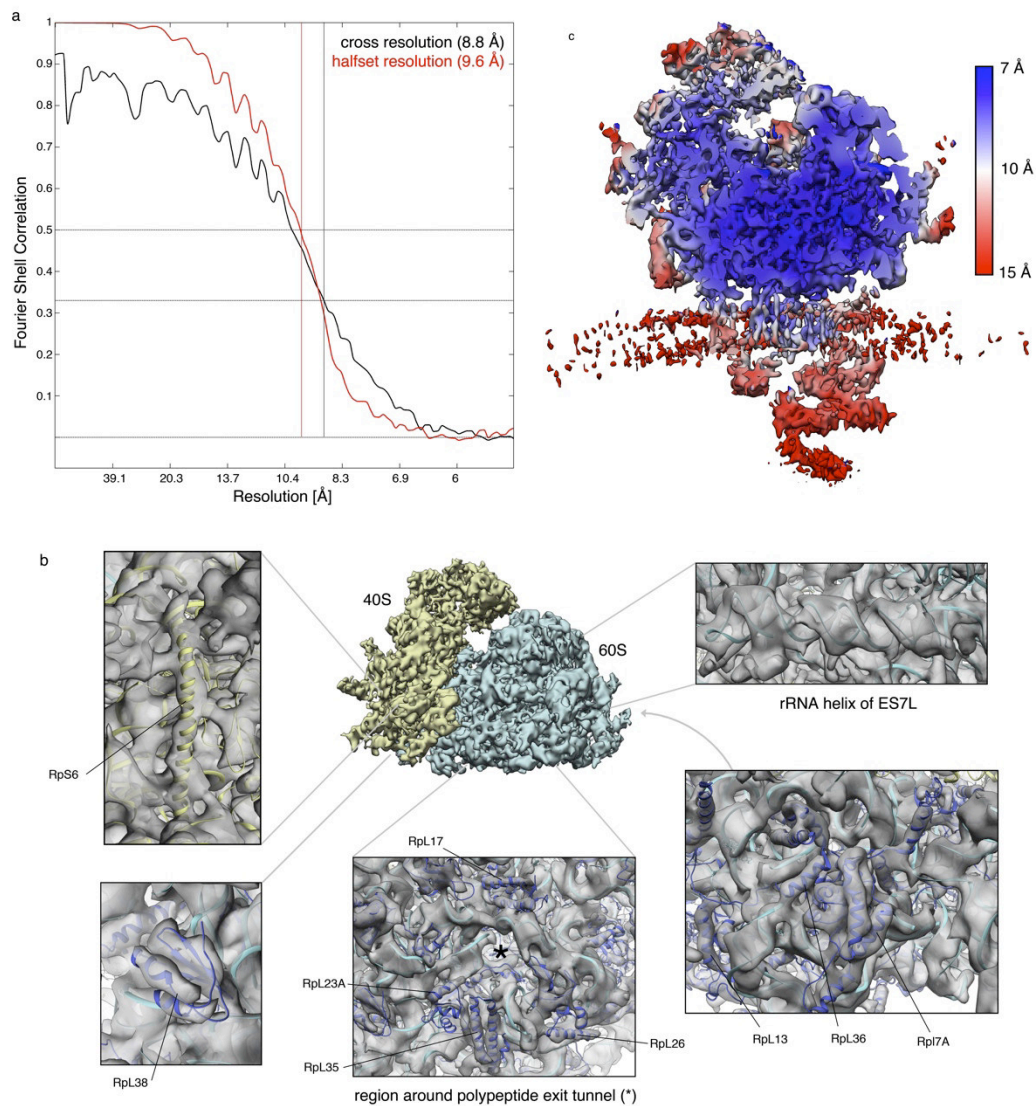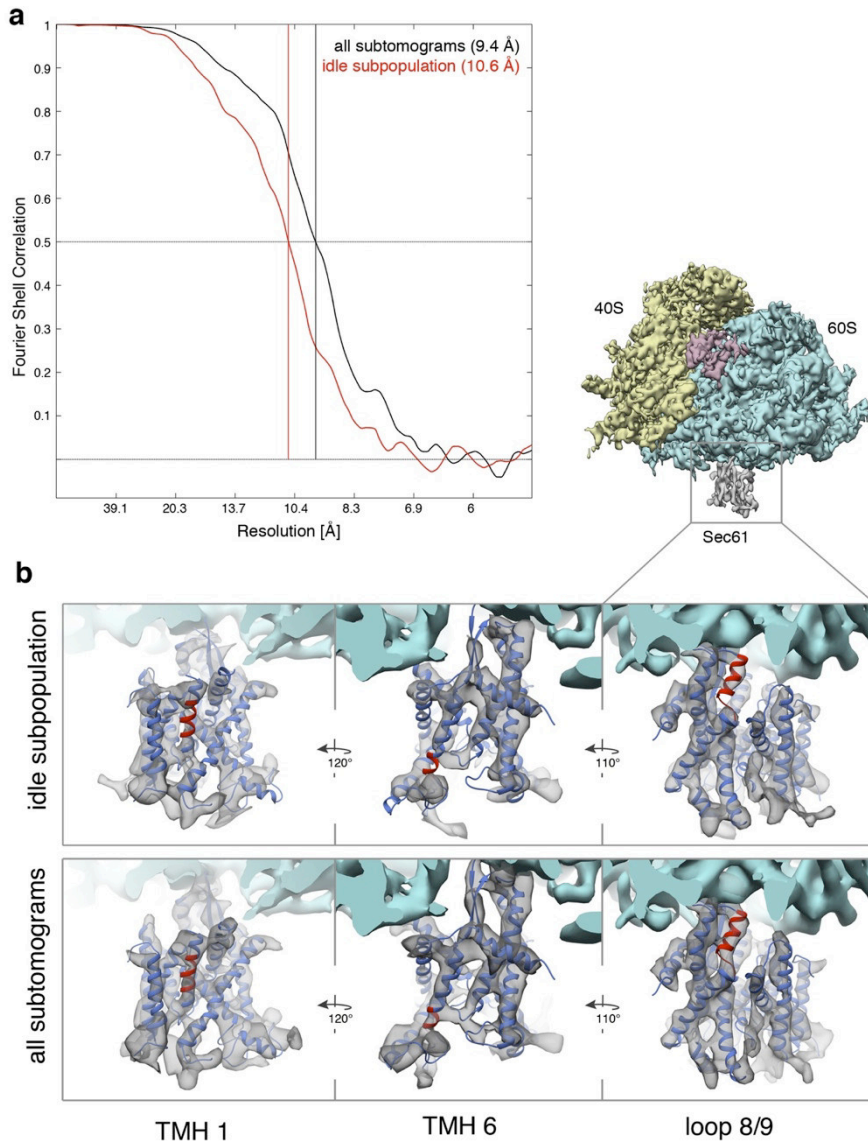
Extended Data Figures
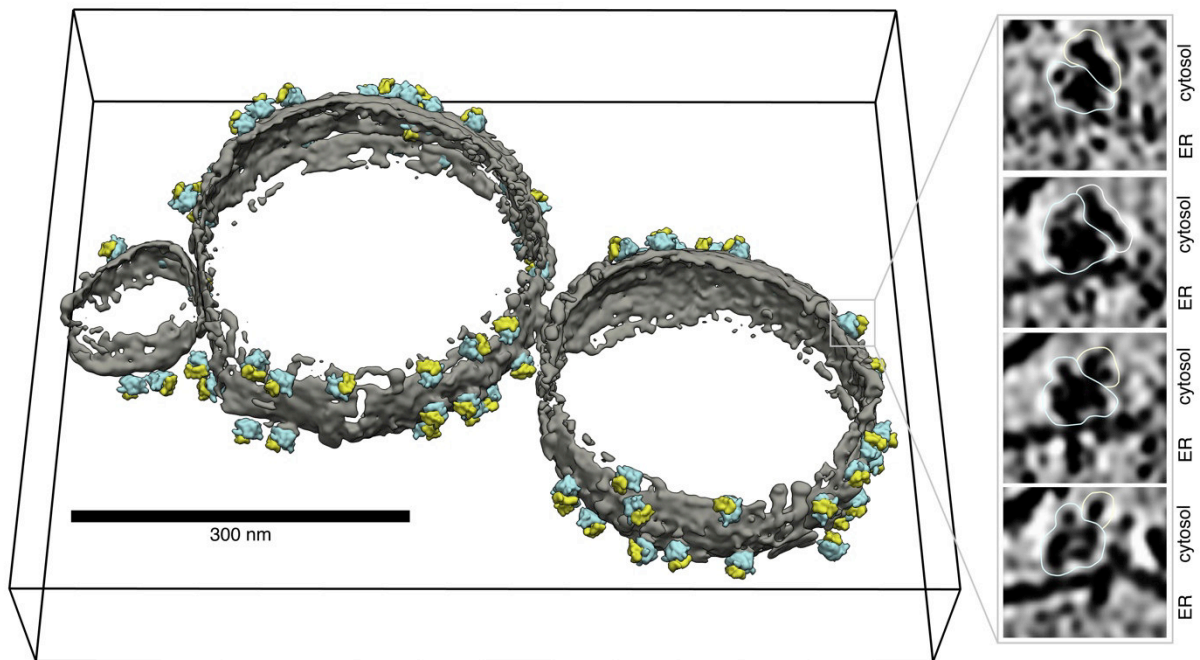
Extended Data Fig. 1: Visualization of a representative tomogram depicting three isolated rER vesicles. The ER membrane is depicted in gray and detected ER-membrane associated ribosomes are represented by the template (40S: yellow, 60S: blue). Scale bar corresponds to 300 nm. Right panel: Slices through a Gaussian-filtered (1.5 nm width) subvolume depicting a single ER membrane-associated ribosome. Density corresponding to the 40S and 60S subunits was annotated (yellow and blue lines delineating density, respectively).

211 single axis tomograms

↓ *template matching (500 peaks / tomo)*

105,500 candidate particles

↓ *1st classification round*

27,500 membrane-bound ribosomes

↓ *2nd classification round*

17,600 ribosomes with OST-containing translocon

40S · 60S · TRAP · OST

9,900 ribosomes with OST-lacking translocon

40S · 60S · TRAP

Extended Data Fig. 2: Subtomogram classification workflow. From 211 single axis tomograms 105,500 candidate particles were obtained by template matching. In two consecutive rounds of classification, ribosomes bound to the OST-containing translocon (17,600 subtomograms) were separated from ribosomes bound to the OST-lacking translocon (9,900 subtomograms), not membrane-bound ribosomes and false positives.

Extended Data Fig.3: Resolution assessment. a, The resolution of the ribosome part of subtomogram average was determined to 9.6 Å by Fourier Shell Correlation (FSC 0.5 criterion) and 8.8 Å by cross-resolution (FSC 0.33 criterion) with a single particle cryo-EM map of the human 80S ribosome (EMD-5592). **b,** Selected areas of the subtomogram average with the atomic model of the porcine 80S ribosome (PDBs 3J7Q, 4W28) superposed. Proteins and rRNA for the large subunit are depicted in dark and light blue, respectively, and components of the small subunit in yellow. **c,** Local resolution assessment of the subtomogram average with an estimated range of 7 Å at the core of the ribosome and below 10 Å in most parts of the ribosome-associated membrane region.

Extended Data Fig. 4: Comparison of Sec61 density for all and only idle ribosome-Sec61 complexes. a, Resolution of the density representing Sec61 for all subtomograms (9.4 Å, black curve) and the subpopulation bound to idle ribosomes (10.6 Å, black curve) estimated by Fourier Shell Correlation (FSC 0.5 criterion). **b,** Isolated density for Sec61 for all subtomograms and the subpopulation bound to idle ribosomes filtered to 9 Å resolution. Visibility of helices for Sec61 even for the smaller population of idle ribosome-Sec61 complexes suggests rather conservative resolution estimation. The model for Sec61 obtained by flexible fitting (blue; see below) is superposed. Helices that are not well resolved in the Sec61 density for idle ribosomes are highlighted in red.
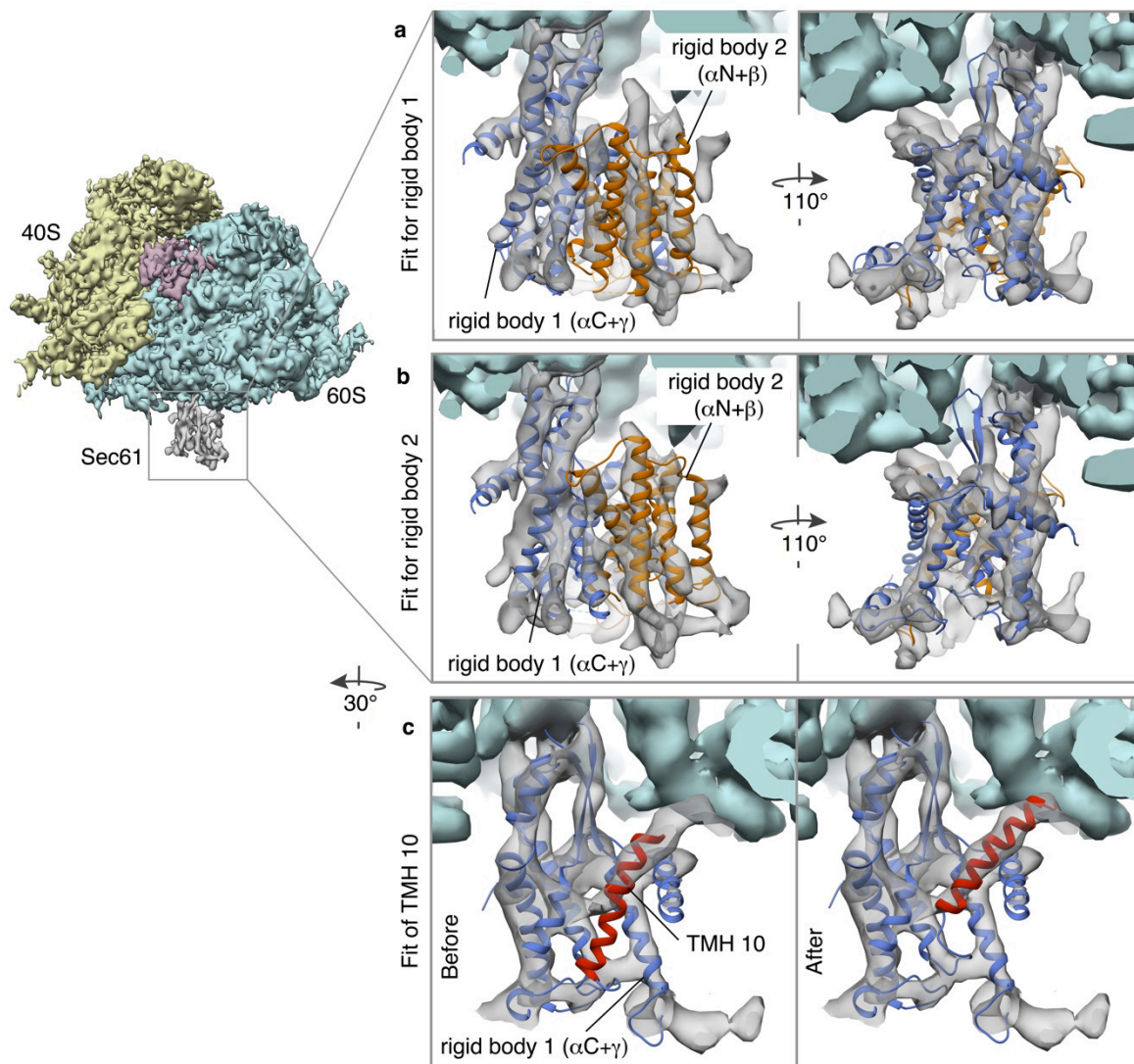
Extended Data Fig. 5: Preparation of the Sec61 model used for MDFF refinement. a,b Segmented densities for the 40S (yellow) and 60S (light blue) ribosomal subunits, translation elongation factors (magenta) and Sec61 (gray). Components of the atomic model for idle Sec61 (PDB 3J7Q) were grouped into two rigid bodies (rigid body 1/blue: C-terminal half of Sec61α + Sec61γ; rigid body 2/orange: N-terminal half of Sec61α + Sec61 β). For both rigid bodies, co-localization between helices in the atomic model and rod-like densities can be achieved after fitting them independently of the other rigid body. **c,** Manually guided repositioning of TMH10 (red) of Sec61α. Density and atomic model were cut to allow for a better view on TMH10.

2.4   Organization of the mitochondrial translation machinery studied *in situ* by cryoelectron tomography

Summary

In this article, we used CET and subtomogram analysis to visualize mitoribosomes in isolated yeast mitochondria, avoiding perturbations during ribosomal purification. In line with their specialization in the synthesis of hydrophobic membrane proteins, most localized mitoribosomes resided in immediate proximity to the inner mitochondrial membrane, forming polyribosomes with a strikingly well defined short-range order. The subtomogram average of membrane-associated mitoribosomes at 28 Å resolution revealed two distinct membrane contact sites. Superposing an atomic model for the large mitoribosomal subunit from yeast, one of these contact sites could be identified as a long ribosomal RNA expansion segment. Tomographic analysis of mitochondria isolated from knockout yeast cells identified the second contact site as the inner membrane protein Mba1. Based on our data, we further hypothesized that Mba1 is not just a passive mitoribosome receptor on the inner membrane, but spatially aligns mitoribosomes with the membrane insertion machinery. In conclusion, this study significantly advanced our understanding of the supramolecular organization of the mitochondrial translation system and its association with the inner mitochondrial membrane in translation-competent mitochondria. It complements the rapidly growing compendium of high-resolution structures available for the mitoribosome by facilitating their molecular interpretation in an organellar context.

Contribution

For this article, I carried out grid preparation for electron microscopy, acquisition of CET data and the complete workflow for data processing and map interpretation. I wrote major parts of the manuscript and prepared most of the figures.

Organization of the mitochondrial translation machinery studied *in situ* by cryoelectron tomography

Stefan Pfeffer[1,*], Michael W. Woellhaf[2,*], Johannes M. Herrmann[2] & Friedrich Förster[1]

Whereas the structure and function of cytosolic ribosomes have been studied in great detail, we know surprisingly little about the structural basis of mitochondrial protein synthesis. Here we used cryoelectron tomography and subtomogram analysis to visualize mitoribosomes in isolated yeast mitochondria, avoiding perturbations during ribosomal purification. Most mitoribosomes reside in immediate proximity to the inner mitochondrial membrane, in line with their specialization in the synthesis of hydrophobic membrane proteins. The subtomogram average of membrane-associated mitoribosomes reveals two distinct membrane contact sites, formed by the 21S rRNA expansion segment 96-ES1 and the inner membrane protein Mba1. On the basis of our data, we further hypothesize that Mba1 is not just a passive mitoribosome receptor on the inner membrane, but that it spatially aligns mitoribosomes with the membrane insertion machinery. This study reveals detailed insights into the supramolecular organization of the mitochondrial translation machinery and its association with the inner membrane in translation-competent mitochondria.

[1] Department of Molecular Structural Biology, Max-Planck Institute of Biochemistry, Am Klopferspitz 18, D-82152 Martinsried, Germany. [2] Cell Biology, University of Kaiserslautern, Erwin-Schrodinger-Strasse 13, 67663 Kaiserslautern, Germany. * These authors contributed equally to this work. Correspondence and requests for materials should be addressed to J.M.H. (email: hannes.herrmann@biologie.uni-kl.de) or to F.F. (email: foerster@biochem.mpg.de).

Mitochondria are essential organelles of eukaryotic cells, which produce ATP by aerobic respiration. They maintained their own translation machinery, mostly for the synthesis of a few highly hydrophobic membrane proteins that form the central reaction centres of the enzymes of the respiratory chain and the ATP synthase[1]. Mitochondrial translation products are co-translationally integrated into the inner membrane in a reaction that depends on two factors in yeast: (1) Oxa1, the homologue of the bacterial YidC, serves as an integrase that inserts its client proteins into the inner membrane[2–5]. (2) Mba1 (mammalian homologue: Mrpl45 or mL45) cooperates with Oxa1 in the membrane recruitment of mitoribosomes[6,7]. Biochemical studies suggest that the mitoribosome remains associated to the inner membrane even in mutants lacking both Oxa1 and Mba1, indicating the presence of additional, so far unidentified membrane tethers[7,8].

Only very recently, high-resolution structures for the large subunit of the mammalian and yeast mitoribosome[9,10] and the small subunit of the mammalian mitoribosome[11] were published. Since the mitoribosomes used in these single particle cryo-electron microscopy (cryo-EM) experiments were recovered from salt-washed detergent extracts, membrane-binding sites remained hypothetical. On the basis of earlier cryo-EM studies it was speculated that the mitoribosome might be partially embedded into the lipid bilayer[12], whereas the recent high-resolution studies led to the hypotheses that the mitoribosome resides in the mitochondrial matrix and contacts the inner membrane either via a mitoribosome-specific protuberance of the large subunit[9] or the peptide exit associated protein Mrpl45 (ref. 10).

To avoid perturbations during ribosomal purification, we used an alternative approach that does not require the purification of ribosomal particles and allows studying the membrane association of mitoribosomes in situ. Cryoelectron tomography (CET) is an excellent method for studying the structure of large molecules in their natural context[13], in particular ribosomal structures and their supramolecular assembly[14–16]. Using this approach, we analysed mitoribosome structure and distribution in purified translation-competent mitochondria revealing detailed insights into the organization of the mitochondrial translation machinery and its association with the inner membrane.

Results

Yeast mitoribosomes are in proximity to the inner membrane. Mitochondria were isolated from wild-type yeast cells and the functionality of their translation and membrane insertion machinery was verified by in organello translation, indicating synthesis and processing of all eight proteins encoded by the mitochondrial genome (Fig. 1a). In tomograms of those mitochondria, mitoribosomes and ATP synthases are the most prominent macromolecular complexes and are readily discernable in the mitochondrial matrix (Fig. 1b). To analyse the spatial distribution of mitoribosomes in mitochondria, candidate particles were located by a six-dimensional cross-correlation search ('template matching') against a single particle cryo-EM reconstruction of the yeast 73S mitoribosome[9]. Features coinciding with cross-correlation peaks were visually inspected to identify true positive matches. For three representative tomograms, we manually traced the mitochondrial inner membrane (Supplementary Fig. 1) and determined the shortest Euclidean distance from all mitoribosome positions to the membrane in these three tomograms. According to the distribution of mitoribosome-membrane distances (Fig. 1c), most mitoribosomes reside in immediate proximity of the inner membrane, with a preferred distance of 17 nm between the membrane and their positional coordinates. Assuming an
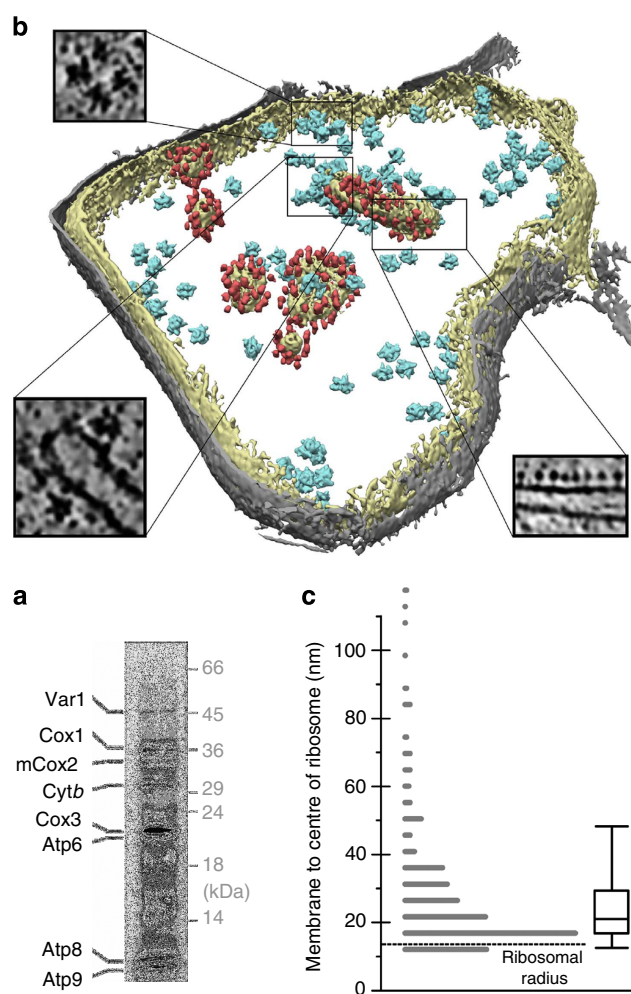
Figure 1 | Distribution of mitoribosomes in translation-competent yeast mitochondria. (a) Isolated mitochondria were labelled for 10 min with radioactive methionine and synthesized proteins were visualized by SDS–PAGE and autoradiography. The synthesized translation products are indicated. mCox2 indicates mature processed Cox2. **(b)** Rendered and segmented version of a tomogram depicting the outer (grey) and inner mitochondrial membrane (yellow) detected mitoribosomes visualized by the template (blue) and a subset of ATP synthases (red). Mitoribosomes and ATP synthases can be readily discerned in mildly Gaussian-filtered (1.5 nm width) slices of the tomogram (boxed areas). **(c)** Distribution of shortest distances between the centre of mass of detected mitoribosomes and the inner mitochondrial membrane represented as histogram and box-whisker plot for 478 mitoribosomes from three tomograms. The box includes the median, upper and lower quartiles of the distribution. Box whiskers include 80% of the data to indicate variability outside the upper and lower quartiles. The dashed line corresponds to the approximate radius of a mitoribosome (14 nm).

approximate radius of 13–14 nm for the mitoribosome, this corresponds to a preferred distance of 3–4 nm between the ribosomal surface and the membrane. This finding strongly supports the notion that in yeast the vast majority of mitoribosomes is tethered to the inner mitochondrial membrane.

Mitoribosomes show a pronounced short-range order. In our tomograms, mitoribosomes are typically organized in clusters on the inner mitochondrial membrane (Fig. 1b), suggesting the presence of membrane-bound polyribosomes. Both, membrane-[15] and non-membrane-bound[16,17] cytosolic polyribosomes

109

typically show a specific close-range order between adjacent ribosomes, resulting in a characteristic architecture of the polyribosome. In order to analyse the three-dimensional (3D) arrangement of membrane-bound mitoribosomes, we pursued a strategy similar to our analysis of ribosome arrangements on the ER membrane[15]. First, we extracted a list of pairwise mitoribosome arrangements from the positional coordinates, which was filtered to arrangements complying with a preferred Euclidean interparticle distance (20–40 nm, Supplementary Fig. 2a) and membrane inclination (0–50°, Supplementary Fig. 2b). For a detailed analysis, we chose a coordinate system, in which the mitochondrial inner membrane (as observed in the subtomogram average described below) corresponds to the paper plane. In this coordinate system, we defined two angles describing the relative position (α) and relative orientation (β) of adjacent mitoribosomes (Fig. 2a). Plotting of α against β yielded two highly populated classes (I and II) on a scarcely populated background (Fig. 2b). Visualization of these two arrangements by replicates of the template structure, positioned according to averaged coordinates and rotations of the classes, indicates that both classes represent the same linear arrangement of mitoribosomes, corresponding to the left and the right neighbours in the polyribosome, respectively. This arrangement of mitoribosomes results in a slightly curved architecture of the polyribosome with a smooth pathway of modelled polysomal mRNA interconnecting neighbouring mitoribosomes (Fig. 2c). Within the two classes, α and β are strongly correlated. To visualize the consequences of this correlation of relative neighbour position and orientation on

polysome architecture, we subdivided class I into three equally populated subclasses (I–I to I–III) according to the relative position of adjacent mitoribosomes (Fig. 2d). In the resulting arrangements (Fig. 2e), we observed that the local correlation of relative positions and orientations within the class causes a radial movement of the neighbour around the mitoribosome under scrutiny, likely guided by their physical interaction via the polysomal mRNA.

Mitoribosomes bind to the inner membrane in a defined way. In order to obtain detailed insights into the association of mitoribosomes with the inner membrane, subtomograms depicting mitoribosomes were individually reconstructed at full resolution, iteratively aligned and sorted by two consecutive unsupervised classification rounds. In the first sorting round, classification of 1,674 initial subtomograms from 12 tomograms was focused on the 37S subunit to separate 73S mitoribosomes from small populations of 54S ribosomal subunits (7%) and 73S mitoribosomes with a hyper-rotated 37S subunit (3%; Fig. 3a). In the second round of classification, focused on the membrane region and the 54S subunit, subtomograms with clearly visible density for the inner mitochondrial membrane were enriched (Fig. 3b). Iterative re-alignment of the remaining 900 subtomograms yielded a structure of the 73S mitoribosome bound to the mitochondrial inner membrane (Fig. 4a) with an overall resolution of 28 Å (Fig. 5a). The local resolution of the map varies according to position, with an approximate value of 22 Å at the
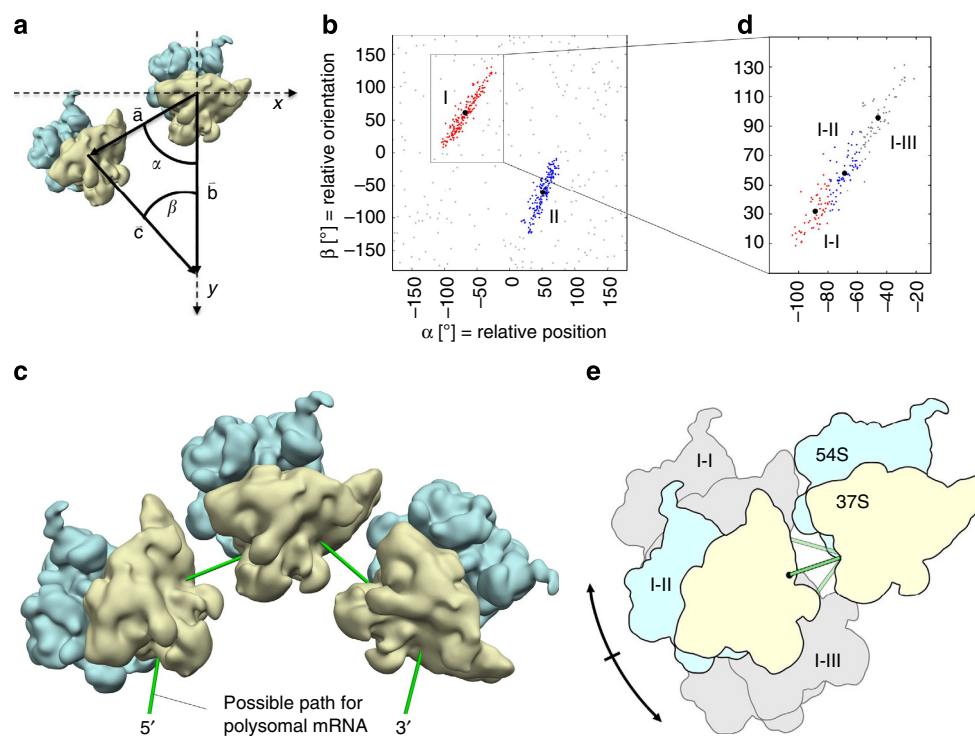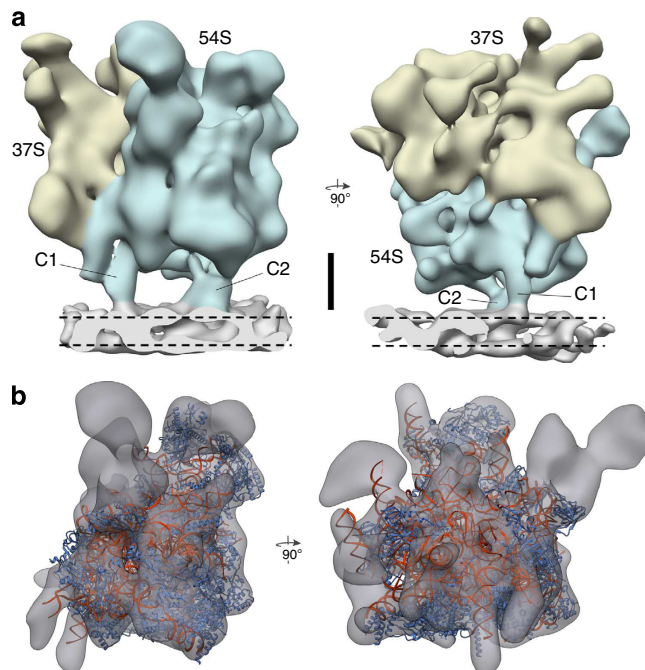

Figure 2 | Three-dimensional arrangement of mitoribosomes in membrane-bound polyribosomes. (**a**) For the analysis of the 3D distribution of mitoribosomes, two angles were defined: the angle α between the y axis of the mitoribosome under scrutiny and the centre-to-centre vector $\vec{a}$ of another mitoribosome describes their relative positions, while the angle β between the vectors $\vec{b}$ and $\vec{c}$ of the two mitoribosomes captures their relative orientation. (**b**) The plot of α against β and subsequent clustering of the data set (730 pairwise mitoribosome arrangements) reveals two highly populated classes I and II that represent the left and right neighbour in the same 3D arrangement of mitoribosomes. (**c**) Preferred 3D arrangement of membrane-bound mitoribosomes, visualized by replicates of the template structure, looking down on the inner membrane. The shortest path between mRNA entry and exit sites of adjacent mitoribosomes was indicated (green) to visualize a possible pathway for polysomal mRNA. (**d**) Class I from **b** was further subdivided into three equally populated clusters (I–I to I–III) according to the relative position of adjacent mitoribosomes. (**e**) Schematic representation of the ribosomal arrangements represented by classes I–I to I–III and the modelled pathways of polysomal mRNA.

110
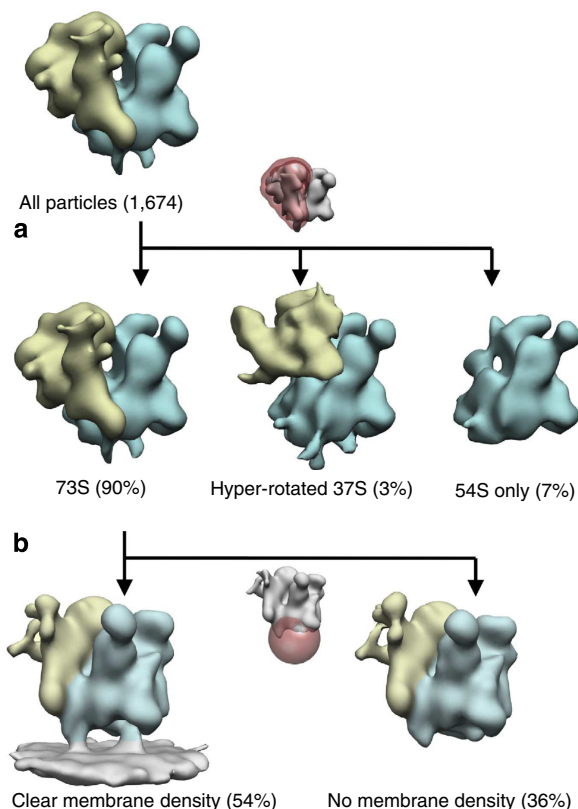
Figure 3 | Classification of subtomograms from wild-type mitochondria.
(**a**) In a first round, classification was focused on the 37S subunit of the mitoribosome (classification mask depicted in red) and separated 73S mitoribosomes from 54S subunits and mitoribosomes with a hyper-rotated 37S subunit. (**b**) In a second round, classification was focused on the membrane and parts of the 54S subunit (classification mask depicted in red) and enriched subtomograms with clear density for the inner mitochondrial membrane. Absence of the membrane density is mostly due to orientations of particles that do not allow resolving the membrane as a consequence of the 'missing wedge effect' in CET. Class abundance is given as percentage of all particles. For classification round 1, the membrane region of the subtomogram average is not shown.

**Figure 4 | Structure of the membrane-bound mitoribosome.**
(**a**) Subtomogram average filtered to 28 Å resolution. The 54S (blue) and 37S (yellow) subunits, the inner mitochondrial membrane (grey) and two distinct contact sites between the mitoribosome and the membrane (C1 and C2) are resolved. Dashed lines indicate the two leaflets of the membrane bilayer. The scale bar corresponds to 5 nm. (**b**) Atomic model of the 54S subunit (modelled proteins blue, modelled rRNA orange, PDB 1VW3, 1VW4) fitted into the 54S density of the subtomogram average (transparent grey). Some flexible parts of the 54S subunit are not included in the atomic model.

core of the mitoribosome and ~30 Å in the membrane region (Fig. 5b). Consistently, Fourier shell correlation between a cryo-EM single particle structure of the 73S yeast mitoribosome[9] and the subtomogram average indicates a resolution of 23 Å for the ribosome part of the subtomogram average (Fig. 5a). The atomic model for the yeast 54S subunit[9] (PDB 1VW3, 1VW4) derived from this single particle structure shows an excellent rigid body fit into the 54S density of the subtomogram average (Fig. 4b). Consistent with previous cryo-EM studies[9,10,18], the mitoribosome depicted in our subtomogram average is considerably larger than its bacterial counterpart, matching the dimensions of cytosolic 80S ribosomes (Supplementary Fig. 3). Notably, a ribosome-associated density resolved in the subtomogram average close to the mRNA exit site on the 37S subunit (Supplementary Fig. 4a) coincides with the expected path of polysomal mRNA (Supplementary Fig. 4b) in the preferred arrangement described in Fig. 2c. The biochemical nature of this density is unclear, as similar structures were not present for polyribosomes of the bacterial or eukaryotic cytosol[15–17]. Despite its specialization on the translation of a small number of very hydrophobic membrane proteins, the yeast mitoribosome is by no means embedded in the inner membrane, as previously speculated for the mammalian mitoribosome[12]. On the contrary,

the distance between the inner mitochondrial membrane and the canonical peptide exit site on the mitoribosome even exceeds that observed between eukaryotic ribosomes and the ER membrane during co-translational protein translocation (Supplementary Fig. 5)[14].

Mitoribosomes are membrane-tethered by two contact sites. The orientation and position of the mitoribosome on the inner membrane differs from a previous hypothesis on the basis of the putative involvement of a mitoribosome-specific protuberance of the large subunit in membrane tethering[9]. Instead, the mitoribosome is tethered to the inner membrane by two prominent contact sites, C1 and C2, located on opposing sites of the canonical ('bacterial') peptide exit tunnel (Fig. 4a). Superposition of the atomic model of the yeast 54S ribosomal subunit[9] (PDB 1VW3, 1VW4) to the subtomogram average reveals that one of these contacts (C1) is mediated by the 21S rRNA expansion segment 96-ES1 (Fig. 6).

On the basis of biochemical analyses and knockout experiments, Mba1 was suggested to act as a mitoribosome receptor on the inner membrane and, together with Oxa1, was shown to be required for efficient membrane integration of nascent proteins[7]. Consistent with the proposed function as a mitoribosome receptor, Mba1 fractionates like a *bona fide* inner membrane protein in flotation gradients (Supplementary Fig. 6a) and—upon lysis of membranes with detergents—with mitoribosomes in sedimentation gradients (Supplementary Fig. 6b). Moreover, superposition of an atomic model of the mammalian mitochondrial 39S subunit[10] (PDB 4CE4) on the subtomogram average reveals spatial overlap of the modelled fragment of the

111
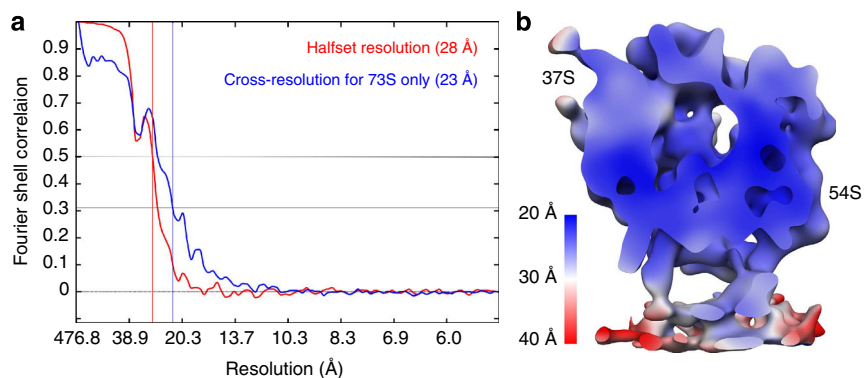
Figure 5 | Resolution assessment via FSC and cross-resolution. (**a**) The resolution of the subtomogram average was determined to 28 Å by FSC 0.5 criterion with a mask, encompassing the whole 73S mitoribosome and most of the inner mitochondrial membrane. For validation, the cross-resolution between the yeast 73S mitoribosome as determined by single particle cryo-EM[9] and the 73S part of the subtomogram average was determined to 23 Å (FSC 0.33 criterion). (**b**) Local resolution assessment of the subtomogram average with an estimated range of 22 Å at the core of the mitoribosome and ~30 Å in the mitoribosome-associated membrane region.
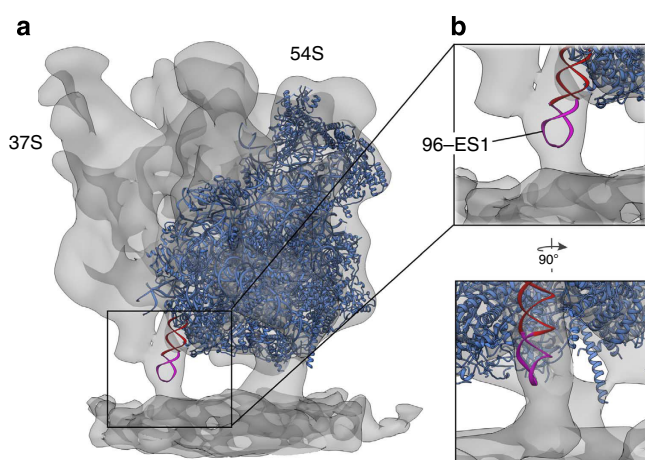
Figure 6 | Large subunit ribosomal RNA 96-ES1 constitutes the C1 contact site. (**a**) Atomic model of the 54S subunit (blue, PDB 1VW3, 1VW4) with 96-ES1 highlighted in red/magenta fitted into the subtomogram average (transparent grey) as a rigid body. Twenty residues of 96-ES1 (magenta) were not included in the original model and were extended using the tip of a random rRNA ES. (**b**) Zoomed views of the boxed area in **a** showing colocalization of 96-ES1 and the C1 contact site in more detail.

mammalian Mba1 homologue Mrpl45 and C2 (Supplementary Fig. 7). Taken together, these findings make Mba1 a genuine candidate for mediating the C2 contact. To test this hypothesis, we generated an Mba1 deletion mutant (Fig. 7a), which showed defects in the membrane insertion of nascent chains resulting in the accumulation of the precursor form of subunit 2 of cytochrome oxidase (Fig. 7b). From this strain, mitochondria were isolated and the *in situ* structure of the membrane-bound mitoribosome was determined (Supplementary Fig. 8). Consistent with earlier biochemical studies[7,8], the mitoribosome remains tethered to the inner membrane (Fig. 7c), likely due to the contribution of 96-ES1 to membrane association of the mitoribosome. Essentially all density assigned to the C2 contact site disappeared, which is also highly significant (>7 s.d.'s) in the difference map to the wild-type structure (Fig. 7d). Thus, we identified the second membrane tether of the mitoribosome in the subtomogram average as Mba1 and show where it binds to the mitoribosome to perform its established function as a mitoribosome receptor on the inner membrane.

**Mba1 aligns the exit tunnel with membrane-embedded density.** On the basis of the high-resolution cryo-EM single particle reconstruction of the yeast 54S mitoribosome subunit, the mitoribosomal peptide exit site has been located ~3.5 nm away from the canonical ('bacterial') peptide exit, which is blocked by a long mitoribosome-specific extension of Mrpl23 (ref. 9). This mitoribosomal peptide channel emerges from the 54S subunit perfectly aligned and face-to-face with Mba1 (Fig. 8a), suggesting that Mba1 might be in close contact with nascent peptides emerging from the mitoribosome. Indeed, Mba1 can be chemically crosslinked to nascent but not to mature mitochondrial translation products (Supplementary Fig. 9). In a pull down experiment, immobilized Mba1 can, furthermore, pull down the Oxa1 insertase from mitochondrial extracts, suggesting that Mba1 has the ability to recruit the insertion machinery to the mitoribosome (Supplementary Fig. 10). Indeed, in direct contact with Mba1, an area of particularly high density is discernable inside the inner mitochondrial membrane (Fig. 8b and Supplementary Fig. 11). Thus, in the spatial arrangement observed here, Mba1 may act not only as a passive mitoribosome receptor, but it also may align the membrane-bound mitoribosome with membrane-integral components of the translation machinery, such as the membrane insertion machinery necessary for co-translational protein membrane insertion.

Discussion

With the help of direct electron detector technology, we could directly visualize mitoribosomes bound to the native inner membrane structures of translation-competent mitochondria *in situ*, revealing the supramolecular organization of the mitochondrial translation machinery and its association with the inner membrane.

Purification and cryopreparation can alter the overall morphology of yeast mitochondria slightly compared with their native counterparts. However, the full functionality in terms of translation and protein membrane insertion (Fig. 1a), the structurally well-defined interaction between mitoribosomes and the inner membrane (Fig. 4), and finally the strikingly well-preserved architecture of the delicate polysomal assemblies on the inner membrane (Fig. 2) argue for a mild preparation procedure in our study, preserving the native state of mitochondria with respect to the structural features of its translational machinery.

The analysis of mitoribosome arrangements in our study suggests that mitoribosomes are predominantly organized in membrane-bound polyribosomes. The preferred architecture
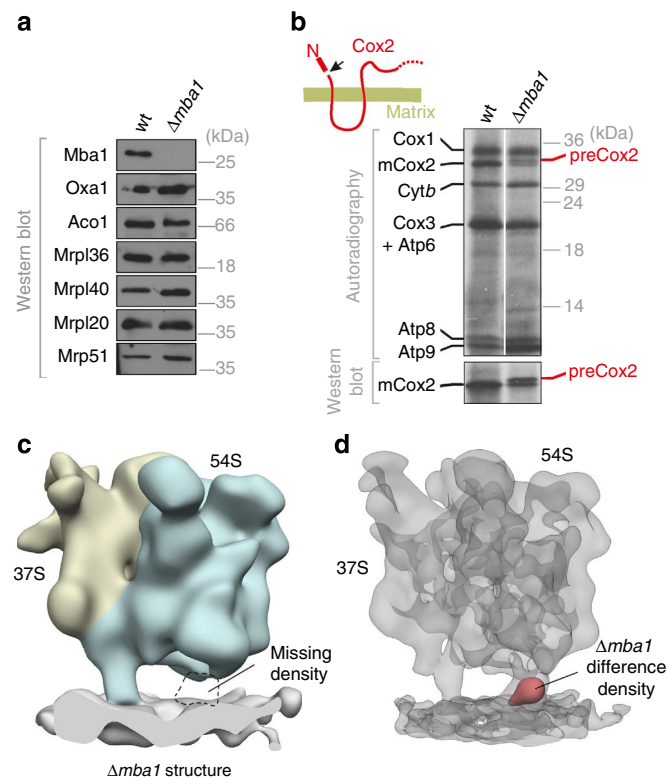
Figure 7 | The inner membrane protein Mba1 constitutes the C2 contact site. (**a**) Western blot against the mitochondrial proteins Mba1, Aco1, Oxa1, Mrpl36, Mrpl40, Mrpl20 and Mrp51 in isolated wild-type and *Δmba1* mitochondria[30]. Please note that the absence of Mba1 does neither affect the steady-state levels of proteins of the mitoribosome (Mrpl36, Mrpl40, Mrpl20 and Mrp51) nor of the membrane insertase Oxa1. (**b**) Translation products were radiolabelled for 20 min with [^{35}S]-methionine in isolated wild-type (wt) and *Δmba1* mitochondria. Synthesized proteins were visualized by SDS–PAGE and autoradiography. The same samples were probed with Cox2-specific antibodies to visualize steady-state levels of endogenous Cox2. Cox2 is initially synthesized in the matrix as a precursor protein (preCox2), which is proteolytically matured after its insertion into the inner membrane by the Imp1 protease in the intermembrane space; mature Cox2 (mCox2) thus depends on the co-translational membrane insertion of Cox2, which is compromised in the absence of Mba1. (**c**) Subtomogram average of the membrane-bound mitoribosome from *Δmba1* mitochondria. Essentially all density assigned to C2 disappeared. (**d**) Normalized difference density (red) between the structures from *Δmba1* and wild-type mitochondria, isosurface-rendered at 7 s.d.'s, superposed to the subtomogram average from wild-type mitochondria (transparent grey). The difference density co-localizes with contact site C2.

of these polyribosomes is similar to the architecture of poly-ribosomes bound to the mammalian endoplasmic reticulum[15]. This similarity suggests that the organization of membrane-bound polyribosomes is evolutionarily conserved, probably due to the invariant basic topological requirements for threading an mRNA molecule from one ribosome to next while translocating a nascent peptide across the membrane.

Our subtomogram average unveils that the membrane-bound yeast mitoribosome is tethered to the inner mitochondrial membrane by two distinct contacts, one of them the rRNA expansion segment 96-ES1. Involvement of rRNA expansion segments in membrane binding has already been observed for the ER membrane-associated 80S ribosome *in situ*[15], suggesting that contribution of rRNA to membrane tethering is a common principle. Whether the negatively charged phosphate residues of
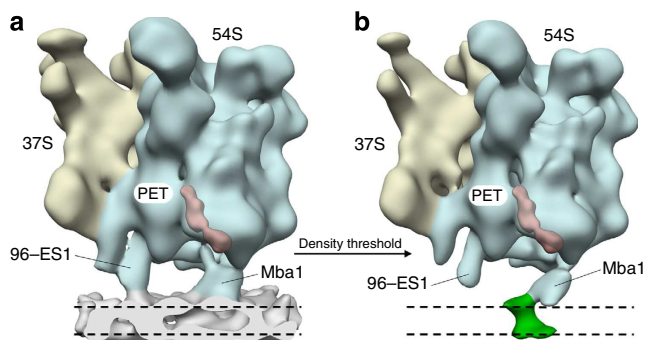
Figure 8 | Mba1 aligns the ribosomal exit tunnel with a membrane-embedded protein density. (**a**) Cavity of the peptide exit tunnel (red; PET), as resolved in a single particle reconstruction of the 54S subunit of the yeast mitoribosome[9], superposed to the subtomogram average. The peptide exit tunnel emerges from the mitoribosome face-to-face with Mba1. (**b**) Subtomogram average shown at a higher density threshold level than in **a** to visualize an Mba1-associated, membrane-embedded density (green). Dashed lines indicate the two leaflets of the membrane bilayer.

the rRNA backbone interact with positively charged head groups of the phospholipids constituting the membrane bilayer, or whether the rRNA specifically interacts with acceptor proteins in the inner mitochondrial membrane, remains to be investigated. The second distinct contact between the mitoribosome and the inner membrane, which is resolved in the subtomogram average, is mediated by the inner membrane protein Mba1. Mba1 is rather ubiquitously found in eukaryotes but absent in bacteria[19], indicating that this membrane tether might be a general feature of mitoribosomes. In consistence, the mammalian Mba1 homologue Mrpl45 was found in the equivalent position on the mammalian mitoribosome[10]; however, in that study the position of the membrane remained unclear.

In direct contact with Mba1, an area of particularly high density is discernable inside the well-resolved membrane bilayer. The position of this density close to the mitoribosome and its alignment with the peptide exit tunnel suggest that this density could represent a membrane-integral component of the transla-tion machinery, such as the membrane insertion machinery necessary for co-translational protein membrane insertion. The adjacent position of Mba1, together with the multiple reported genetic and biochemical interactions of Mba1 and the Oxa1 insertase, indicate that Mba1 is not simply a passive membrane tether, but rather actively supports mitochondrial protein synthesis by aligning the peptide exit tunnel of the membrane-bound mitoribosome with the membrane insertion machinery. Potentially, Mba1 even supports the transfer of the very hydrophobic mitochondrial translation products towards the membrane insertion machinery to facilitate their fast and reliable insertion (Fig. 9). This would explain the defects in membrane insertion associated with Mba1 deletion (Fig. 7b)[7,8].

In summary, our analysis of the membrane-bound yeast mitoribosome unveils that, concomitant with the remodelling of the mitoribosomal polypeptide exit tunnel, its membrane association—and potentially also its mode of membrane insertion—have been radically reshaped during evolution. Finally, it demonstrates the power of *in situ* tomography for the molecular analysis of complex intracellular structures, in particular of those that are as labile as mitochondrial ribosomes.

Methods

Yeast strains and growth media. For imaging of wild-type mitoribosomes, mitochondria were isolated from the wild-type strain D273-10B[20]. Yeast cultures were grown at 30 °C in YP (1% yeast extract, 2% peptone) medium supplemented

113
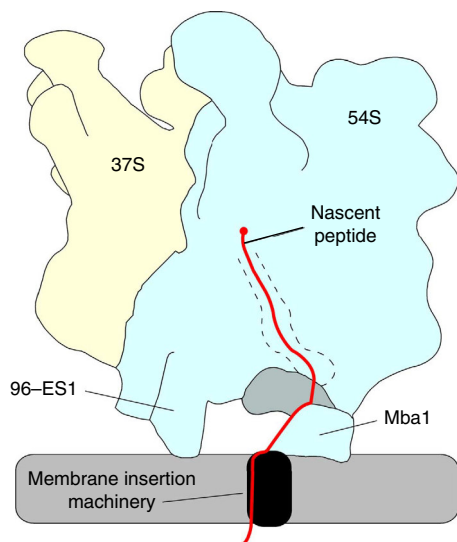
Figure 9 | Hypothetical model for co-translational membrane protein insertion in yeast mitochondria. The inner membrane protein Mba1 aligns the mitochondrial peptide exit tunnel (dashed lines) with the membrane insertion machinery (black box) and supports the transfer of the very hydrophobic mitochondrial nascent peptides (red line) towards the membrane to facilitate their fast and reliable insertion.

with 2% galactose[20]. Mitochondria were isolated as described[21]. In brief, for isolation of mitochondria, yeast cells were converted to spheroplasts by incubation with zymolyase (5 mg g^{-1} wet weight) in 1.2 M sorbitol, 20 mM potassium phosphate for 30 min at 30 °C. Cells were resuspended in homogenization buffer (0.6 M sorbitol, 10 mM Tris-HCl, pH 7.4, 1 mM EDTA, 0.2% (w/v) bovine serum albumin, 1 mM phenylmethylsulphonyl fluoride) and opened in a glass dounce homogenizer. After a clarifying spin for 5 min at 5,000 g, mitochondria were pelleted by centrifugation for 12 min at 12,000 g at 4 °C and resuspended in 0.6 M sorbitol, 20 mM HEPES, pH 7.4 at a protein concentration of 10 mg ml^{-1}.

In organello translation experiments. Translation products were labelled in mitochondria as described[21,22]. In brief, mitochondria (40 μg protein) were incubated in translation buffer (0.6 M sorbitol, 150 mM KCl, 15 mM KH$_2$PO$_4$, 13 mM MgSO$_4$, 0.15 mg ml^{-1} of all amino acids except methionine, 4 mM ATP, 0.5 mM GTP, 5 mM α-ketoglutarate, 5 mM phosphoenolpyruvate, 3 mg ml^{-1} fatty acid-free bovine serum albumin, 20 mM Tris/HCl pH 7.4) containing 0.6 U ml^{-1} pyruvate kinase and 10 μCi [^{35}S]-methionine. Samples were incubated for 30 min at 24 °C. Labelling was stopped by addition of 25 mM unlabelled methionine. The samples were further incubated for 5 min to complete synthesis and mitochondria were isolated by centrifugation, washed in 1 ml 0.6 M sorbitol, 20 mM Hepes/HCl, pH 7.4 and lysed in 25 μl sample buffer (2% sodium dodecyl sulfate, 10% glycerol, 2.5% β-mercaptoethanol, 0.02% bromophenolblue, 60 mM Tris/HCl pH 6.8). Samples were shaken at 4 °C for 10 min before loading on the gel.

Western blotting. Western blotting was performed according to the standard protocols. Full scans of all cropped western blots are shown in Supplementary Figs 12–17. All antisera were raised in rabbits. The antibody against Mrp51 was a kind gift from Tom Fox and the sera against Tim50 was a kind gift from Dejana Mokranjac. Working dilutions of all antibodies are listed in Supplementary Table 1.

Flotation of Mba1 with mitochondrial vesicles. Mitochondria (250 μg) were resuspended in 250 mM KCl, 5 mM EDTA, 1 mM phenylmethylsulphonyl fluoride (PMSF), 20 mM Hepes/KOH, pH 7.4 and ruptured by repeated freeze-thawing. One half of the sample was directly applied to SDS–PAGE (total), the other was adjusted to 1.6 M sucrose (300 μl), placed into a centrifugation tube and overlayed with layers of 250-μl 1.2 M sucrose and 100-μl 0.2 M sucrose. The samples were centrifuged in a Beckman SW60 rotor for 16 h at 230,000 g at 4 °C. The gradient was split into a top and bottom fraction and proteins contained were precipitated by addition of trichloroacetic acid (TCA). Aconitase and Oxa1 served as controls for soluble and membrane-embedded proteins, respectively.

Sedimentation of Mba1 with mitoribosomes. Mitochondria (250 μg) were lysed in 400 μl 1% Triton X-100, 50 mM KCl, 1 mM PMSF, 20 mM Hepes/KOH, pH 7.4. After a clarifying spin for 15 min at 18,000 g at 4 °C, the extract was loaded on a sucrose cushion (100-μl 1.2 M sucrose in lysis buffer) and centrifuged for 1 h at

214,000 g at 4 °C. The supernatant was collected and proteins were prepared by TCA precipitation. Proteins from the pellet (containing mitochondrial ribosomes) were directly dissolved in sample buffer. A total sample containing a comparable amount of mitochondria dissolved in sample buffer was loaded for control.

Pull down of Oxa1 with immobilized Mba1 fusion protein. Maltose-binding protein (MBP) or an MBP-Mba1 fusion protein[7] was immobilized on amylose beads. Mitochondria (500 μg) were lysed with 1% Triton X-100, 50 mM KCl, 20 mM Hepes/KOH, pH 7.4. The extract was cleared by centrifugation and either directly subjected to SDS–PAGE (4%) or incubated with the MBP proteins as indicated (equivalents to 40%). Proteins were transferred to nitrocellulose and either stained by Ponceau S (lower panel) or probed with Oxa1-specific antibodies.

Cryoelectron tomography. Translation-competent mitochondria (2 μl) were applied to lacey carbon molybdenum grids (Ted Pella, USA) and incubated for 60 s at 22 °C. Directly before vitrification of the sample in liquid ethane using a Vitrobot Mark IV (FEI, the Netherlands), 4 μl of 10 nm colloidal gold in tomography buffer (20 mM Hepes pH 7.6, 50 mM KCl, 2 mM MgCl$_2$) were added to the grid. Tilt series were acquired using a FEI Titan Krios TEM equipped with a 'K2 summit' direct electron detector (Gatan, USA), operated in frame mode with five to seven frames per projection image. The TEM was operated at an acceleration voltage of 300 kV. Single-axis tilt series were recorded from −60° to +60° with an angular increment of 2° at a nominal defocus of 4–8 μm and an object pixel size of 2.62 Å using the Serial EM acquisition software[23]. The cumulative electron dose was 100–120 electrons Å^{-2}.

Image processing. Frames from the K2 DDD were aligned using a quasi-expectation maximization protocol implemented in the MATLAB toolbox AV3 (ref. 24). Correction of phase reversals due to the contrast transfer function was performed using MATLAB scripts on single projections, as described in ref. 25. Tomogram reconstruction (object pixel: 2.1 nm) and template matching against a single particle cryo-EM reconstruction of the 73S yeast mitoribosome[9] filtered to 5 nm resolution were accomplished using PyTom[26]. Different rotations of the template were sampled with an angular increment of 12.85°. Tomogram areas corresponding to cross-correlation peaks within mitochondria (distance of distinct peaks > 18.9 nm) were visually inspected to identify true-positive matches. For the retained coordinates, unbinned subtomograms (200^3 voxels, object pixel: 0.262 nm) were reconstructed individually from the weighted projections and iteratively aligned using PyTom[26]. Before each iteration, the average was filtered according to its resolution. The optimal translations and rotations of the subtomograms were determined using the constrained correlation function; this similarity measure constrains the correlation between two volumes to their commonly sampled segments in Fourier space. In a first round of Constrained Principal Component Analysis[27] focused on the 37S subunit, 73S mitoribosomes could be separated from remaining false-positives, which could not be excluded by visual inspection, 54S ribosomal subunits and 73S mitoribosomes with a hyper-rotated 37S subunit. In a second round of Constrained Principal Component Analysis focused on the 54S subunit and the membrane region, subtomograms depicting mitoribosomes with clearly visible density for the inner mitochondrial membrane were enriched. The resolution of the resulting averages was determined by Fourier shell correlation (FSC = 0.5) and cross resolution (FSC = 0.33) with the single particle reconstruction of the 73S yeast mitoribosome[9] on appropriately masked averages. Local resolution estimation was performed using the Bsoft software package[28]. Normalized density difference maps were generated from normalized subtomogram averages, filtered to their respective resolution. The analysis of polyribosome arrangements was carried out in a coordinate system with the z-axis perpendicular to the inner mitochondrial membrane using the full data set of 900 classified mitoribosomes. First, a Gaussian distribution was fitted to the radial pair distribution function of all mitoribosomes in a radius of 100 nm. Only ribosomes within three s.d.'s around the mean distance were used for further analysis. Next, a Gaussian distribution was fitted to the distribution of membrane inclination angles θ in the retained mitoribosome pairs and only mitoribosomes within one s.d. of the mean value were used for further analysis. For each ribosome, we calculated the angle α, describing the relative position of neighbouring ribosomes, and the angle β, describing the relative orientation of neighbouring ribosomes (Fig. 2a). The data set was clustered hierarchically in these two dimensions in MATLAB (Mathworks, USA) using the 'single' linkage and 'distance' clustering criterion.

EM-map analysis and tomogram visualization. For EM-map analysis, fitting of atomic models, fitting of EM maps, segmentation and visualization, we used the UCSF Chimera software package[29]. Colouration of the EM-maps was performed either on images in Photoshop (Adobe, USA) by applying coloured layers ('multiply' style) to the image or in Chimera on segmented densities. For visualization of a whole tomogram in Fig. 1 and analysis of mitoribosome-membrane distances, mitochondrial membranes and selected ATP synthases were segmented manually in Amira (FEI, USA) and the template density of the mitoribosome was positioned according to the coordinates and orientations determined by template matching.

114

References

1. Daley, D. O. & Whelan, J. Why genes persist in organelle genomes. *Genome Biol.* **6,** 110 (2005).
2. He, S. & Fox, T. D. Membrane translocation of mitochondrially coded Cox2p: distinct requirements for export of N and C termini and dependence on the conserved protein Oxa1p. *Mol. Biol. Cell* **8,** 1449–1460 (1997).
3. Hell, K., Herrmann, J., Pratje, E., Neupert, W. & Stuart, R. A. Oxa1p mediates the export of the N- and C-termini of pCoxII from the mitochondrial matrix to the intermembrane space. *FEBS Lett.* **418,** 367–370 (1997).
4. Hell, K., Neupert, W. & Stuart, R. A. Oxa1p acts as a general membrane insertion machinery for proteins encoded by mitochondrial DNA. *EMBO J.* **20,** 1281–1288 (2001).
5. Bonnefoy, N., Chalvet, F., Hamel, P., Slonimski, P. P. & Dujardin, G. OXA1, a *Saccharomyces cerevisiae* nuclear gene whose sequence is conserved from prokaryotes to eukaryotes controls cytochrome oxidase biogenesis. *J. Mol. Biol.* **239,** 201–212 (1994).
6. Preuss, M. *et al.* Mba1, a novel component of the mitochondrial protein export machinery of the yeast *Saccharomyces cerevisiae*. *J. Cell Biol.* **153,** 1085–1096 (2001).
7. Ott, M. *et al.* Mba1, a membrane-associated ribosome receptor in mitochondria. *EMBO J.* **25,** 1603–1610 (2006).
8. Bauerschmitt, H. *et al.* Ribosome-binding proteins Mdm38 and Mba1 display overlapping functions for regulation of mitochondrial translation. *Mol. Biol. Cell* **21,** 1937–1944 (2010).
9. Amunts, A. *et al.* Structure of the yeast mitochondrial large ribosomal subunit. *Science* **343,** 1485–1489 (2014).
10. Greber, B. J. *et al.* Architecture of the large subunit of the mammalian mitochondrial ribosome. *Nature* **505,** 515–519 (2014).
11. Kaushal, P. S. *et al.* Cryo-EM structure of the small subunit of the mammalian mitochondrial ribosome. *Proc. Natl Acad. Sci. USA* **111,** 7284–7289 (2014).
12. Agrawal, R. K. & Sharma, M. R. Structural aspects of mitochondrial translational apparatus. *Curr. Opin. Struct. Biol.* **22,** 797–803 (2012).
13. Lucic, V., Forster, F. & Baumeister, W. Structural studies by electron tomography: from cells to molecules. *Annu. Rev. Biochem.* **74,** 833–865 (2005).
14. Pfeffer, S. *et al.* Structure of the mammalian oligosaccharyl-transferase complex in the native ER protein translocon. *Nat. Commun.* **5,** 3072 (2014).
15. Pfeffer, S. *et al.* Structure and 3D arrangement of endoplasmic reticulum membrane-associated ribosomes. *Structure* **20,** 1508–1518 (2012).
16. Brandt, F. *et al.* The native 3D organization of bacterial polysomes. *Cell* **136,** 261–271 (2009).
17. Brandt, F., Carlson, L. A., Hartl, F. U., Baumeister, W. & Grunewald, K. The three-dimensional organization of polyribosomes in intact human cells. *Mol. Cell* **39,** 560–569 (2010).
18. Sharma, M. R., Booth, T. M., Simpson, L., Maslov, D. A. & Agrawal, R. K. Structure of a mitochondrial ribosome with minimal RNA. *Proc. Natl Acad. Sci. USA* **106,** 9637–9642 (2009).
19. Smits, P., Smeitink, J. A., van den Heuvel, L. P., Huynen, M. A. & Ettema, T. J. Reconstructing the evolution of the mitochondrial ribosomal proteome. *Nucleic Acids Res.* **35,** 4686–4703 (2007).
20. Sherman, F., Fink, G. R. & Hicks, J. *Methods in Yeast Genetics: A Laboratory Course* (Cold Spring Harbor Laboratory Press, 1986).
21. Bauerschmitt, H., Funes, S. & Herrmann, J. M. Synthesis and sorting of mitochondrial translation products. *Methods Mol. Biol.* **457,** 95–112 (2008).
22. McKee, E. E. & Poyton, R. O. Mitochondrial gene expression in *Saccharomyces cerevisiae*. I. Optimal conditions for protein synthesis in isolated mitochondria. *J. Biol. Chem.* **259,** 9320–9331 (1984).
23. Mastronarde, D. N. Automated electron microscope tomography using robust prediction of specimen movements. *J. Struct. Biol.* **152,** 36–51 (2005).
24. Forster, F., Medalia, O., Zauberman, N., Baumeister, W. & Fass, D. Retrovirus envelope protein complex structure in situ studied by cryo-electron tomography. *Proc. Natl Acad. Sci. USA* **102,** 4729–4734 (2005).
25. Eibauer, M. *et al.* Unraveling the structure of membrane proteins in situ by transfer function corrected cryo-electron tomography. *J. Struct. Biol.* **180,** 488–496 (2012).
26. Hrabe, T. *et al.* PyTom: a python-based toolbox for localization of macromolecules in cryo-electron tomograms and subtomogram analysis. *J. Struct. Biol.* **178,** 177–188 (2012).
27. Forster, F., Pruggnaller, S., Seybert, A. & Frangakis, A. S. Classification of cryo-electron sub-tomograms using constrained correlation. *J. Struct. Biol.* **161,** 276–286 (2008).
28. Cardone, G., Heymann, J. B. & Steven, A. C. One number does not fit all: mapping local variations in resolution in cryo-EM reconstructions. *J. Struct. Biol.* **184,** 226–236 (2013).
29. Goddard, T. D., Huang, C. C. & Ferrin, T. E. Visualizing density maps with UCSF Chimera. *J. Struct. Biol.* **157,** 281–287 (2007).
30. Brachmann, C. B. *et al.* Designer deletion strains derived from Saccharomyces cerevisiae S288C: a useful set of strains and plasmids for PCR-mediated gene disruption and other applications. *Yeast* **14,** 115–132 (1998).

Acknowledgements

Author contributions

Additional information

Supplementary Fig. 1. Manually traced inner mitochondrial membrane. For three tomograms the inner mitochondrial membrane was manually traced (transparent yellow) and positions of detected mitoribosomes were indicated by the template (blue).

$$y = a1 \cdot e^{-\left(\frac{x-b1}{c1}\right)^2} + a2 \cdot e^{-\left(\frac{x-b2}{c2}\right)^2}$$

$a1 = 70.73, b1 = 30.74, c1 = 3.254$
$a2 = 97.96, b2 = 84.74, c2 = 50.07$

$$y = a1 \cdot e^{-\left(\frac{x-b1}{c1}\right)^2}$$

$a1 = 100.61, b1 = 24.31, c1 = 27.19$
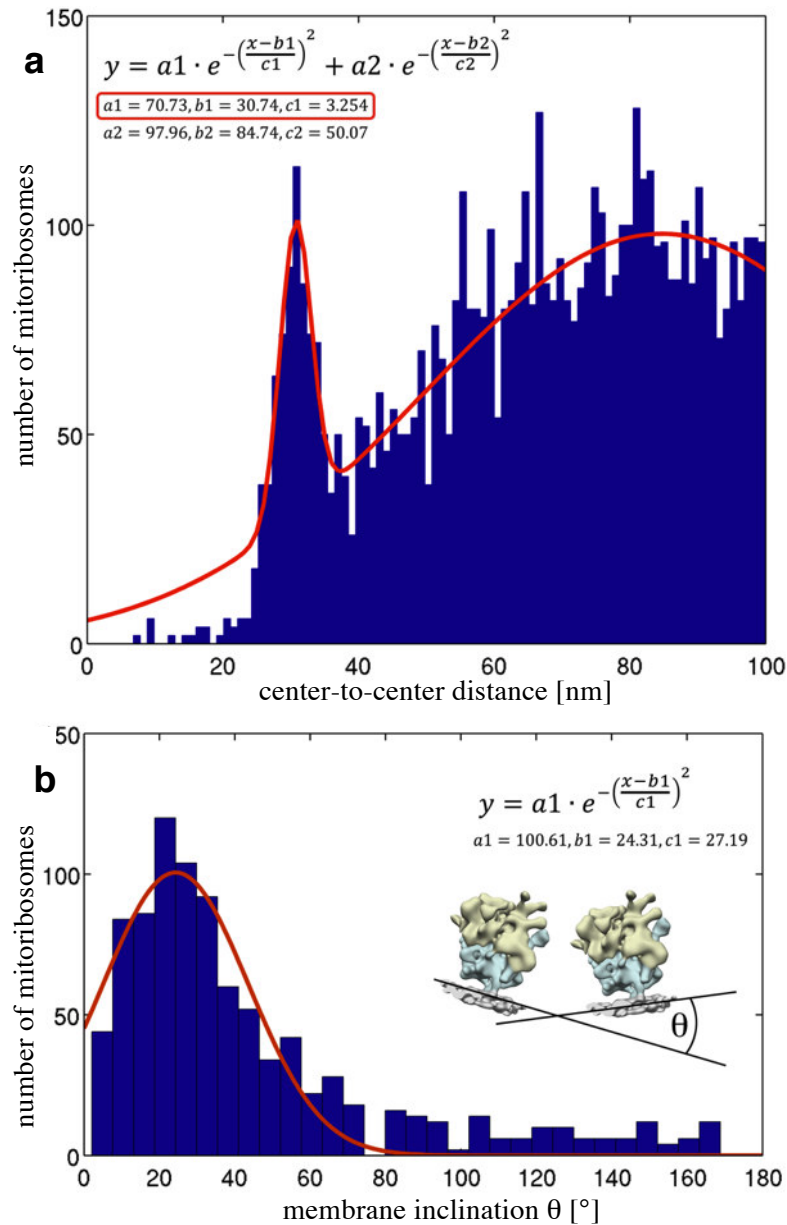
Supplementary Fig. 2. Extraction of a set of preferred pairwise mitoribosome arrangements. a, For each mitoribosome, the center-to-center distance distribution of all neighbors within a radius of 100 nm was analyzed, resulting in 9,160 observed pairwise mitoribosome arrangements. A Gaussian-like distribution with a preferred inter-ribosome distance of 30.7 nm and a standard deviation of 3.3 nm was observed, overlaid with the Gaussian-like signal of non-specifically positioned mitoribosomes. **b,** Distribution of membrane inclination θ (as defined in the insert) between 928 mitoribosome pairs residing in the preferred inter-ribosome distance of 20 - 40 nm. A Gaussian-like distribution with a preferred membrane inclination of 21.3° and a standard deviation of 27.2° was observed.

117
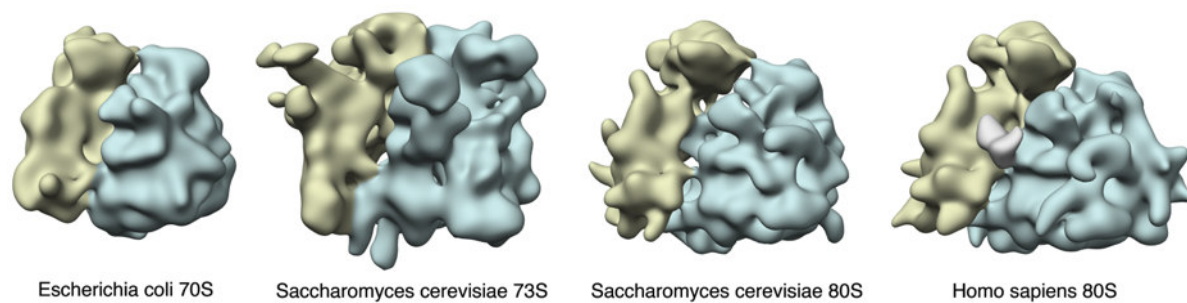
Supplementary Fig. 3. Comparison of ribosome size. The *Escherichia coli* 70S ribosome (EMD 5799), the yeast 73S mitoribosome from this study, the yeast 80S ribosome (EMD 2275) and the human 80S ribosome (EMD 5592) are depicted. All structures were filtered to 28 Å resolution. The large and small ribosomal subunits were colored in blue and yellow, respectively. In the human 80S structure, a ribosome-bound elongation factor is shown in gray.
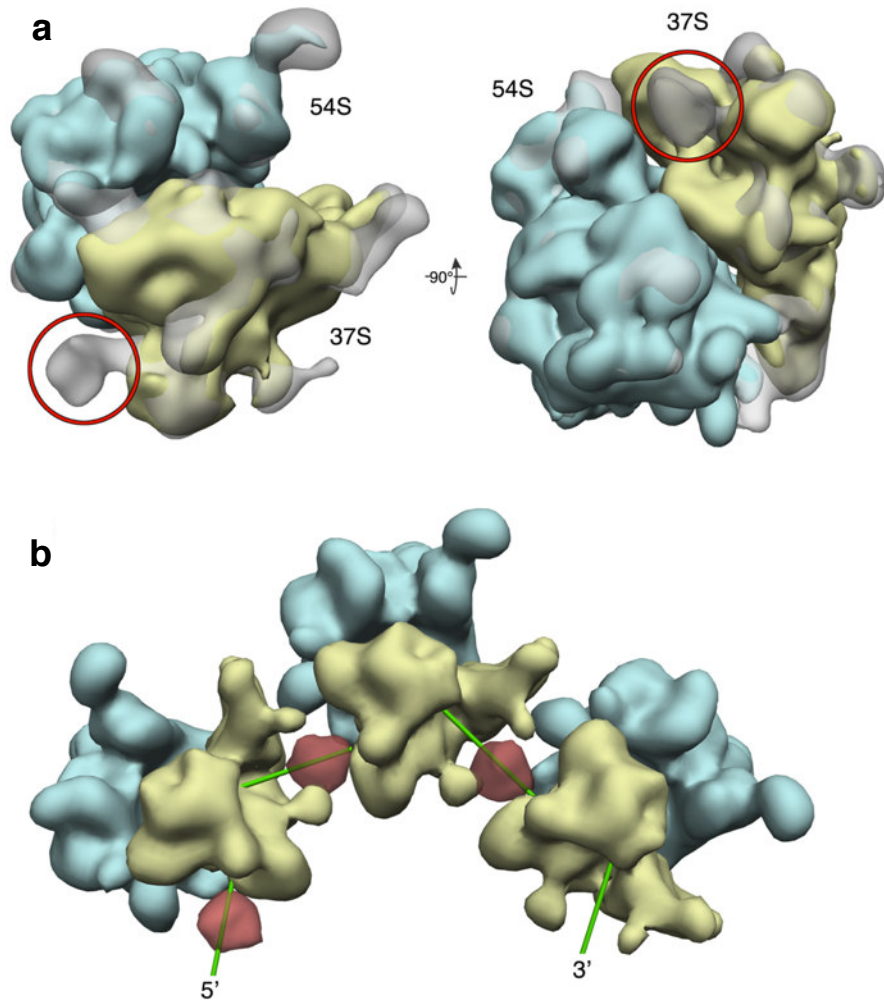
Supplementary Fig. 4. A mitoribosome-associated density on the 37S subunit coincides with polysomal mRNA. a, The subtomogram average of the mitoribosome (transparent gray) was superimposed on the template structure (37S subunit: yellow, 54S subunit: blue). The mitoribosome is oriented as the central mitoribosome in the polysomal arrangement shown in (b) (left) and rotated 90° as indicated. Close to the mRNA exit site on the 37S subunit, a density not present in the template structure is resolved in the subtomogram average (red circle). The membrane part of the average is not shown. **b,** Preferred polysomal arrangement described in Fig. 2c, visualized using the subtomogram average (37S subunit: yellow, 54S subunit: blue) instead of the template structure. The density on the 37S subunit (red) coincides with the path of modeled polysomal mRNA (green).
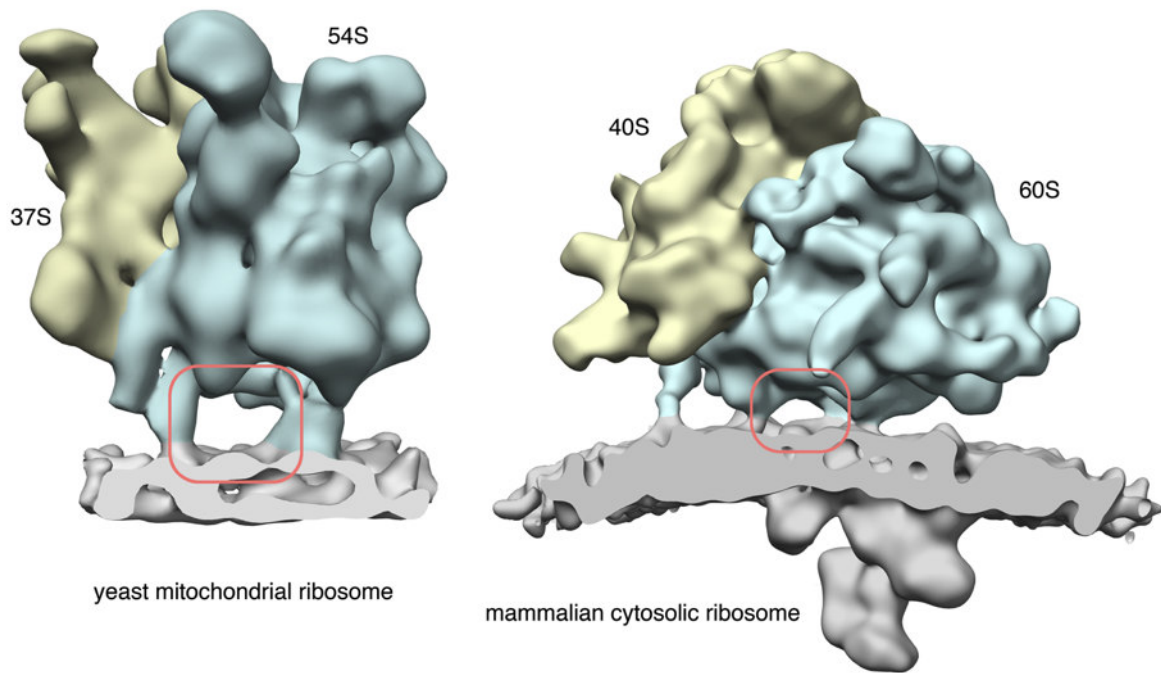
Supplementary Fig. 5. Comparison of membrane positions on the yeast mitoribosome and the mammalian cytosolic 80S ribosome. Comparison of the subtomogram averages of the membrane bound 73S (left) and the ER membrane-associated 80S ribosome (right, EMD 2519) shown to scale. Large and small ribosomal subunits are colored blue and yellow, respectively. The associated membranes (and ER-lumenal complexes) are colored gray. The gap between the large ribosomal subunits and the associated membranes is highlighted (red boxes).
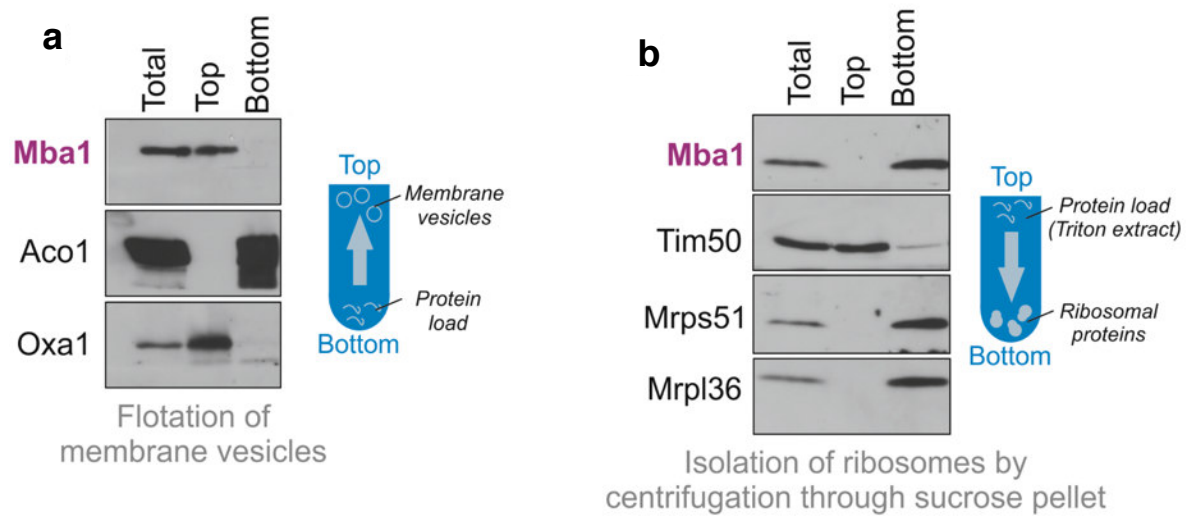
Supplementary Fig. 6. Mba1 is a mitoribosome receptor on the inner mitochondrial membrane. a, Western blot against the mitochondrial proteins Mba1, Aco1 and Oxa1 after flotation of inner membrane vesicles obtained by repeated freeze thawing of mitochondria on a sucrose gradient. Mba1 behaves like a mitochondrial membrane protein. **b,** Western blot against the mitochondrial proteins Mba1, Tim50, Mrps51 and Mrpl36 after sedimentation of mitoribosomes from mitochondrial detergent extracts. Mba1 sediments with mitoribosomes.
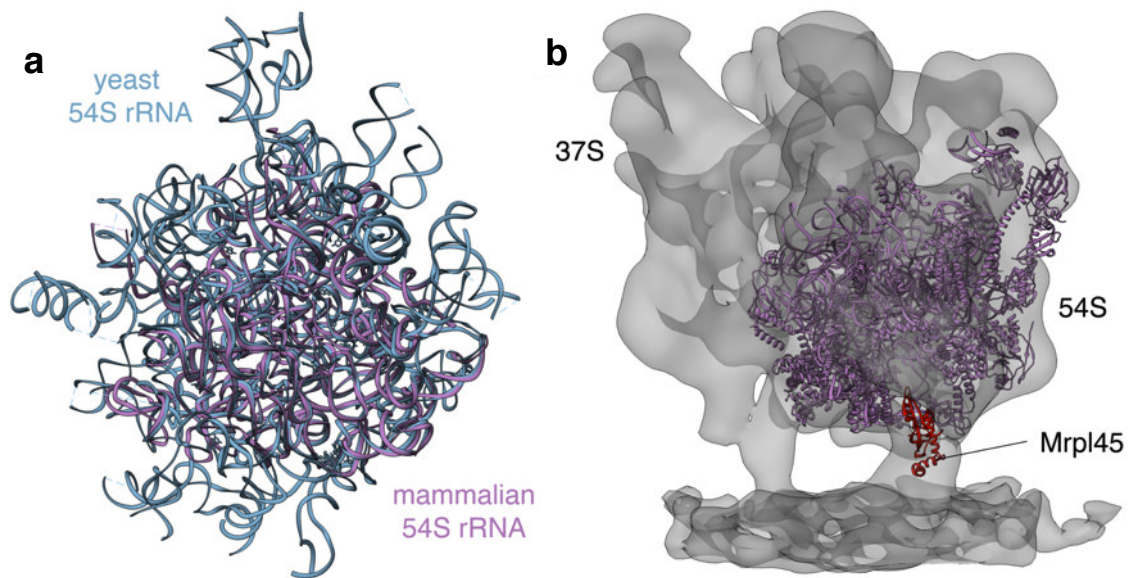
Supplementary Fig. 7. Mrpl45, the mammalian homologue of Mba1, is in spatial proximity to the C2 contact site. a, The atomic models of the mammalian and yeast mitochondrial 54S subunits were structurally aligned to each other according to the large subunit rRNA (mammalian 54S rRNA: purple, PDB 4CE4-A; yeast 54S rRNA: blue, PDB 1VW3-A) using UCSF Chimera. **b,** Atomic model of the mammalian mitochondrial 54S subunit (purple, PDB: 4CE4) superposed to the subtomogram average according to the alignment in **a**. The modeled fragment of the mammalian Mba1 homologue Mrpl45 (red) overlaps with the C2 contact site.
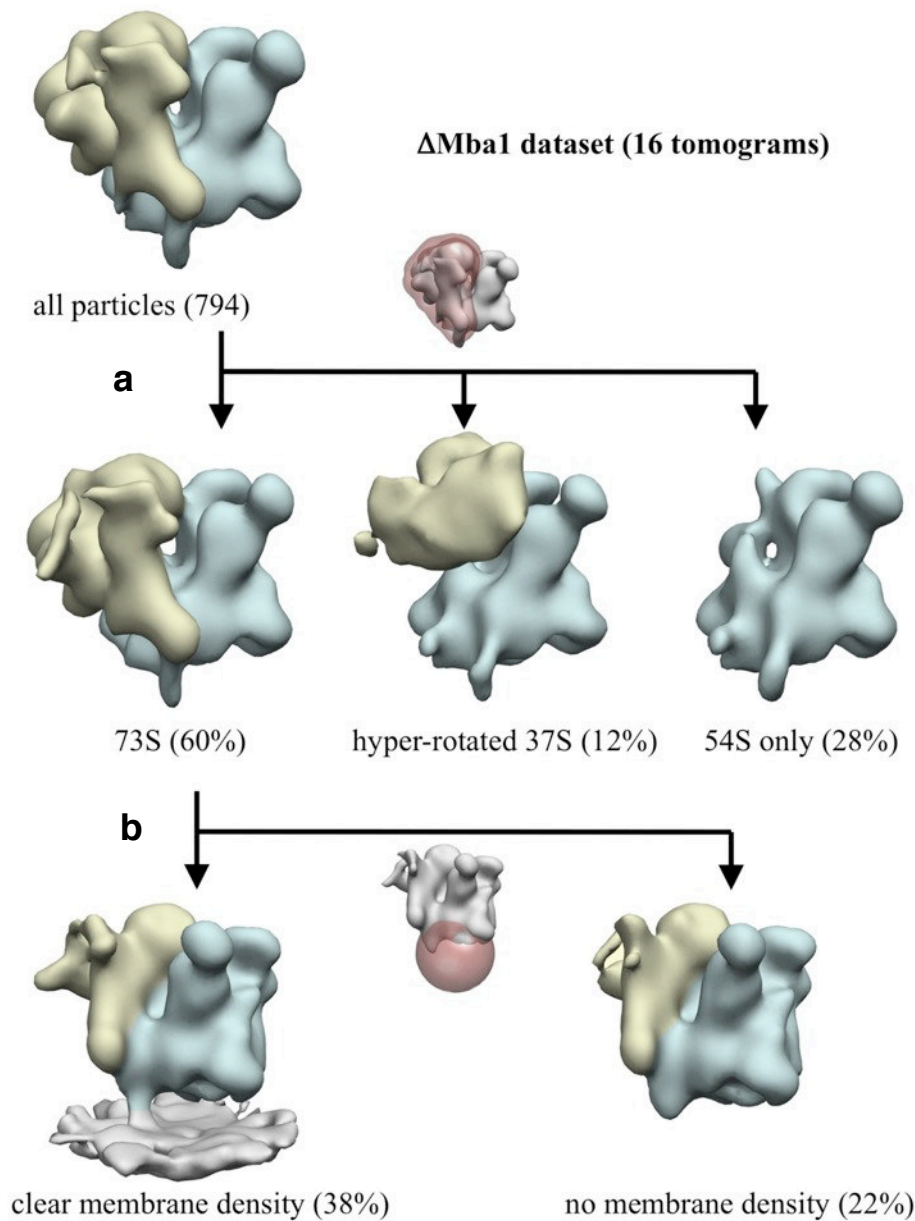
Supplementary Fig. 8. Classification of subtomograms from *Δmba1* mitochondria. a, In a first round, classification was focused on the 37S subunit of the mitoribosome and separated 73S mitoribosomes from 54S subunits and mitoribosomes with a hyper-rotated 37S subunit. **b,** In a second round, classification was focused on the membrane and parts of the 54S subunit and enriched subtomograms with clear density for the inner mitochondrial membrane. Class abundance is given as percentage of all particles. For classification round 1, the membrane region of the subtomogram average is not shown.
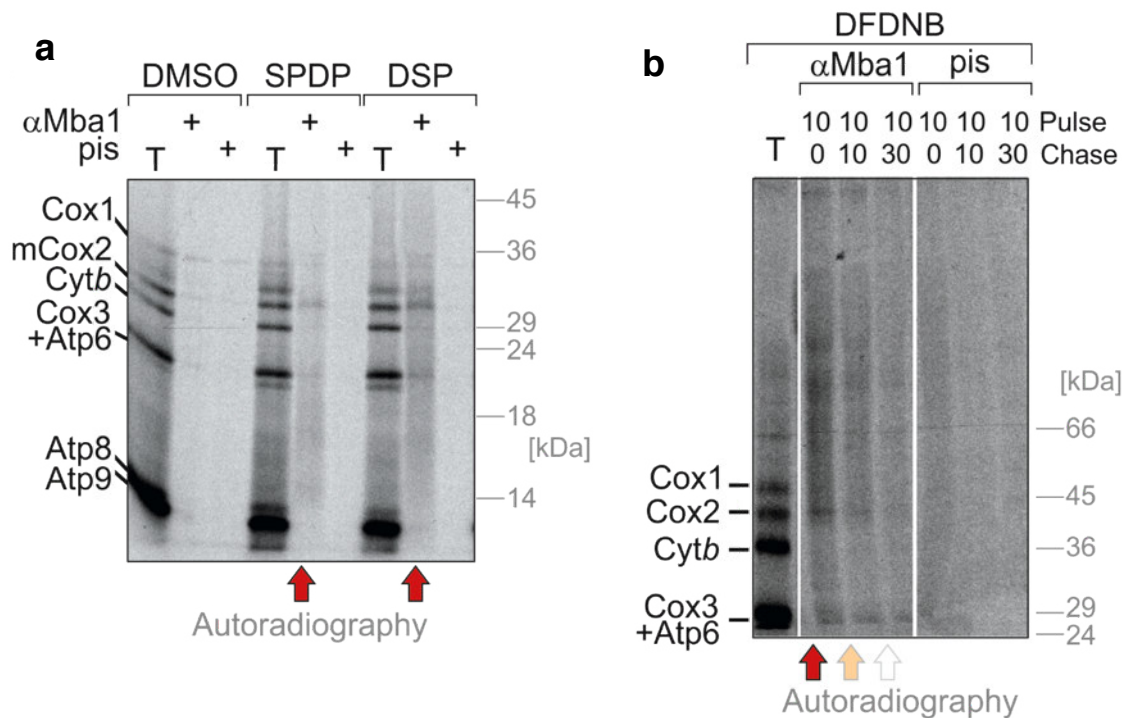
Supplementary Fig. 9. Mba1 can be chemically crosslinked to nascent polypeptide chains. a, Translation products were radiolabeled in isolated wild type mitochondria for 20 min. The sample was split into three aliquots to which 500 µM of the cleavable crosslinkers sulfosuccinimidyl 6-[3′(2-pyridyldithio)-propionamido] hexanoate (SPDP), dithiobis [succinimidyl propionate] or only the solvent demethylsulfoxide (DMSO, 1% final) were added. After incubation for 15 min, the crosslinkers were quenched with 0.2 M glycine. Mitochondria were washed, lysed and the resulting extracts used for immunoprecipitation with Mba1-specific antibodies or preimmune serum (pis) for control. Lanes labeled with T show 10 percent of the total extract used per immunoprecipitation reaction. Before loading to the SDS gel, the crosslinks were resolved by boiling the samples in 4% 2-mercaptoethanol. Please note that nascent chains were specifically pulled down with the Mba1 antibody upon crosslinking. Due to their heterogeneity in size, these chains migrate as a smear-like signal. In contrast, completed translation products were not recovered with Mba1. **b,** Translation products were radiolabeled for 10 min in wild type mitochondria. Labeling was quenched by addition of unlabeled methionine. The sample was divided into three aliquots which were

chased for 0, 10 or 30 min before 500 µM of the non-cleavable short-distance (3 Å) crosslinker 1,5-difluoro-2,4-dinitrobenzene (DFDNB) was added for 15 min. The samples were further treated as described for (a) with the exception that the crosslinks were not broken before SDS PAGE. Crosslinking was only observed during translation but decreased during the chase reaction, indicating that Mba1 interacts with these products during or directly subsequent to their synthesis on mitoribosomes.
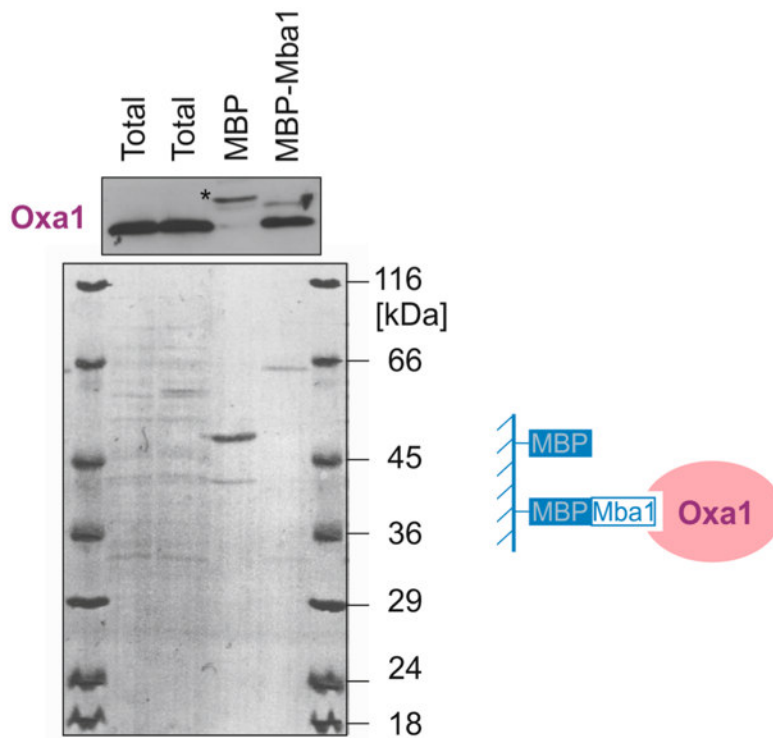
Supplementary Fig. 10. Oxa1 can be pulled-down with immobilized Mba1 fusion proteins. Maltose-binding protein (MBP) or an MBP-Mba1 fusion protein [1] were immobilized on amylose beads. Mitochondrial extract was either directly subjected to SDS-PAGE (4%) or incubated with the MBP proteins as indicated (equivalents to 40%). Proteins were transferred to nitrocellulose and either stained by Ponceau S (lower panel) or probed with Oxa1-specific antibodies. The asterisk depicts a crossreaction of the Oxa1 antibody with the MBP-containing fraction.
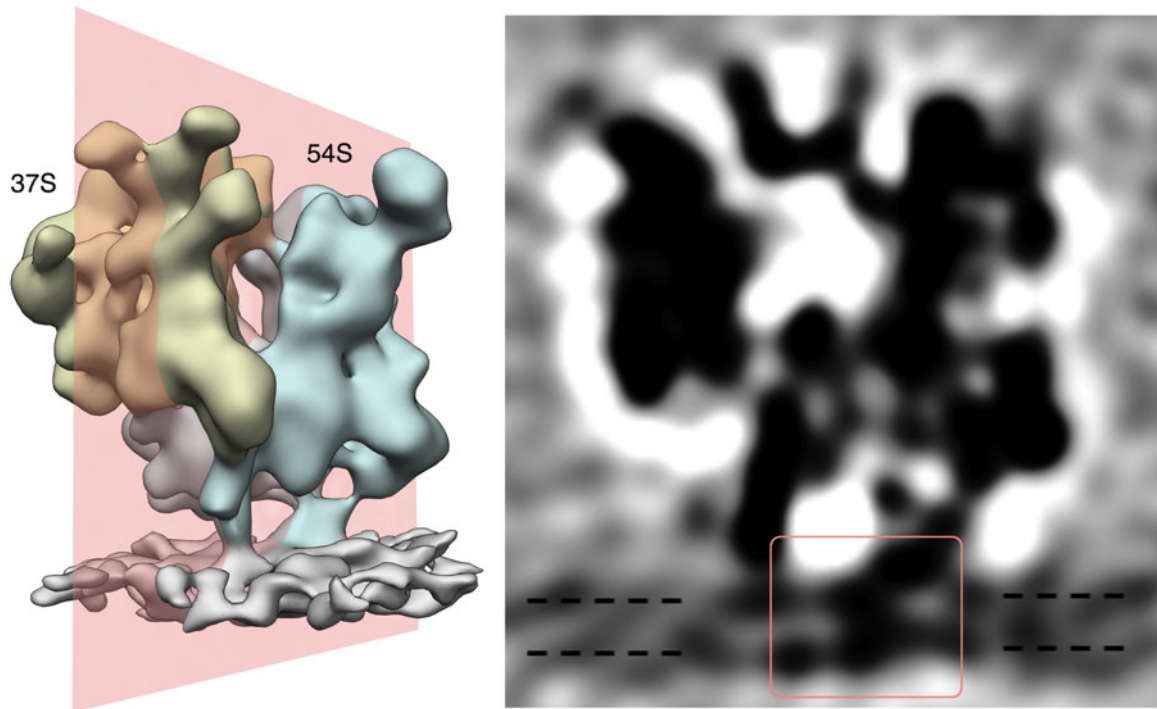
Supplementary Fig. 11. A high-density feature is resolved in the inner membrane. In a density slice though the subtomogram average (right), oriented as indicated by the red plane in the left panel, a high-density feature inside the inner mitochondrial membrane can be discerned in the center of the red box. Dashed lines indicate the position of the two leaflets of the membrane bilayer.
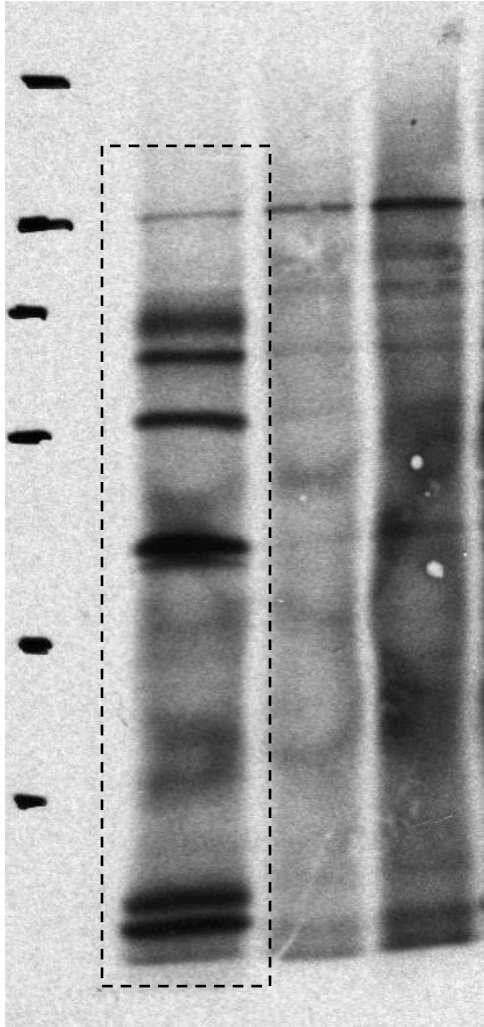
Supplementary Fig. 12. Full phosphoimaging scan from Figure 1a. The cropped areas is indicated.
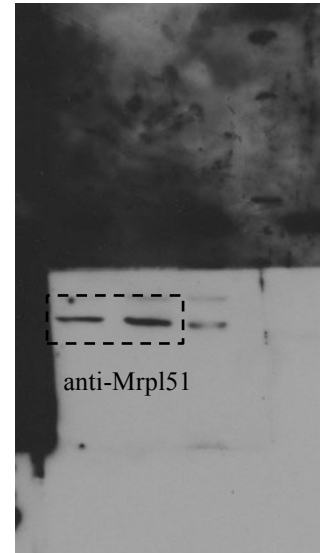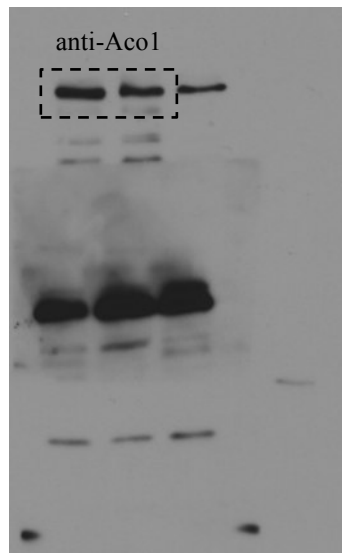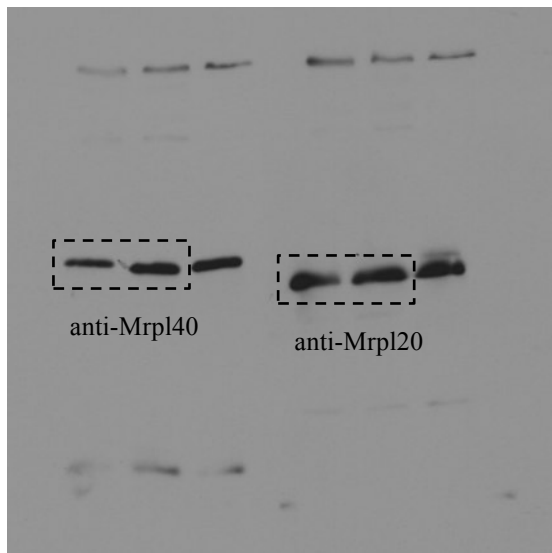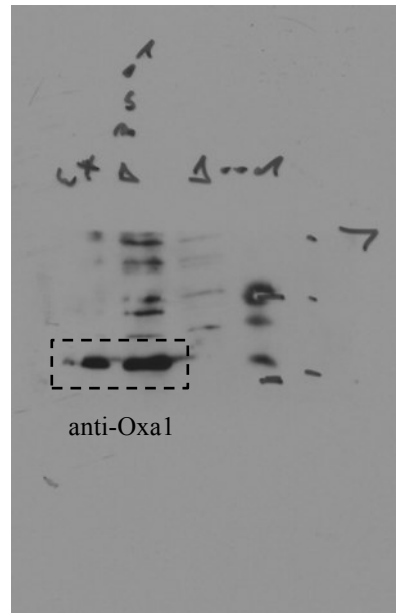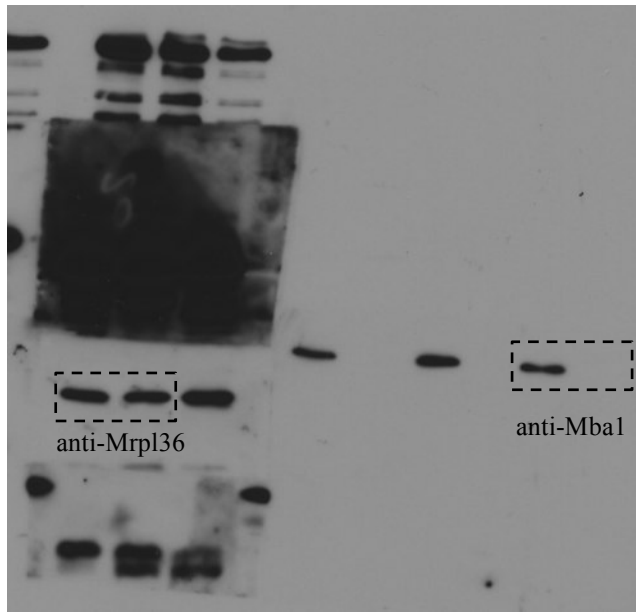
Supplementary Fig. 13. Full western blot scans from Figure 7a. Cropped areas are indicated.
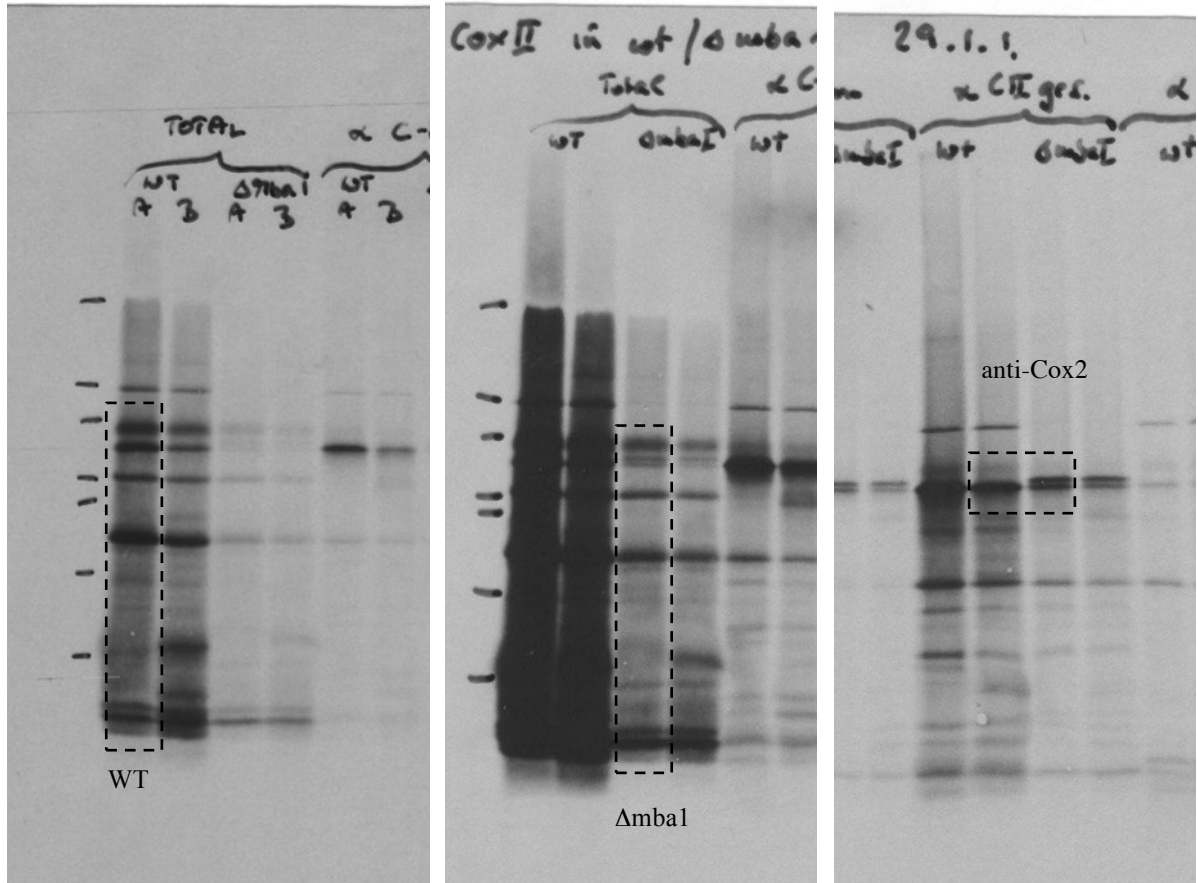
Supplementary Fig. 14. Full phosphoimaging and western blot scans from Figure 7b.

Cropped areas are indicated.
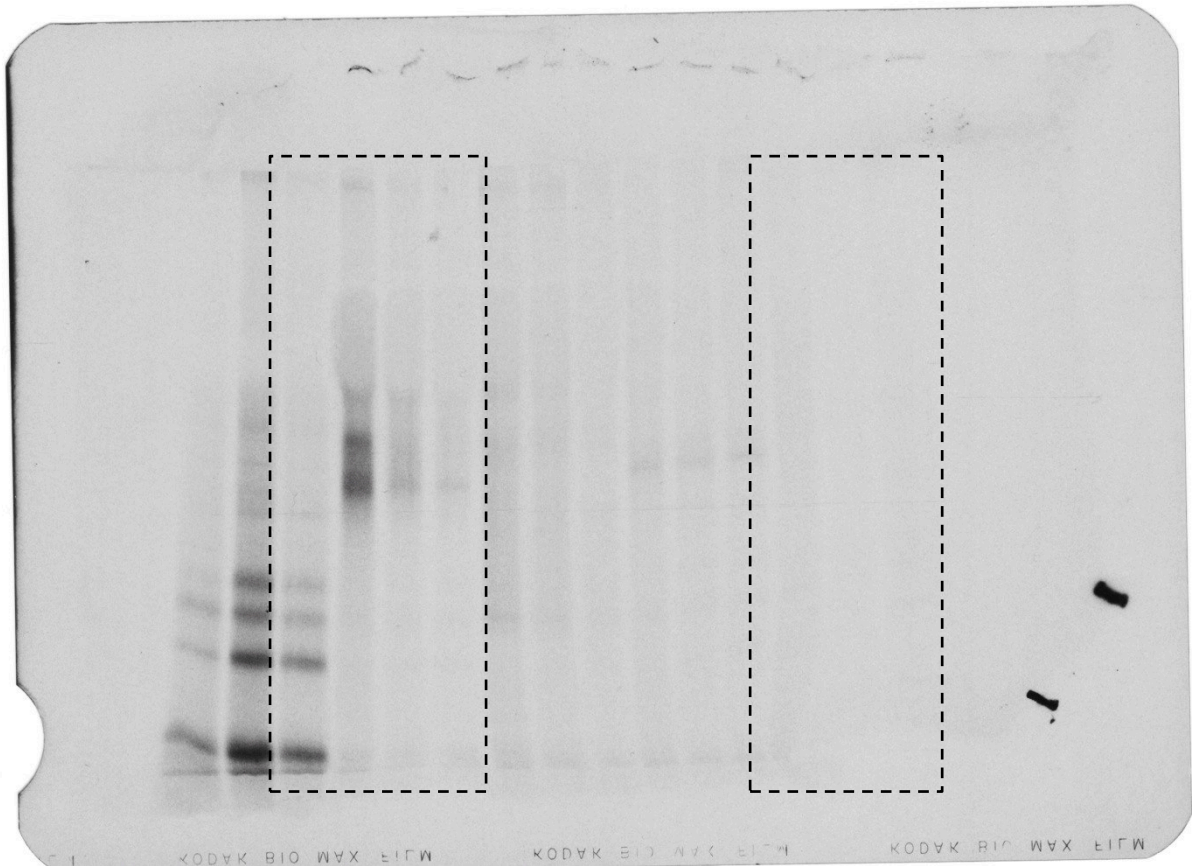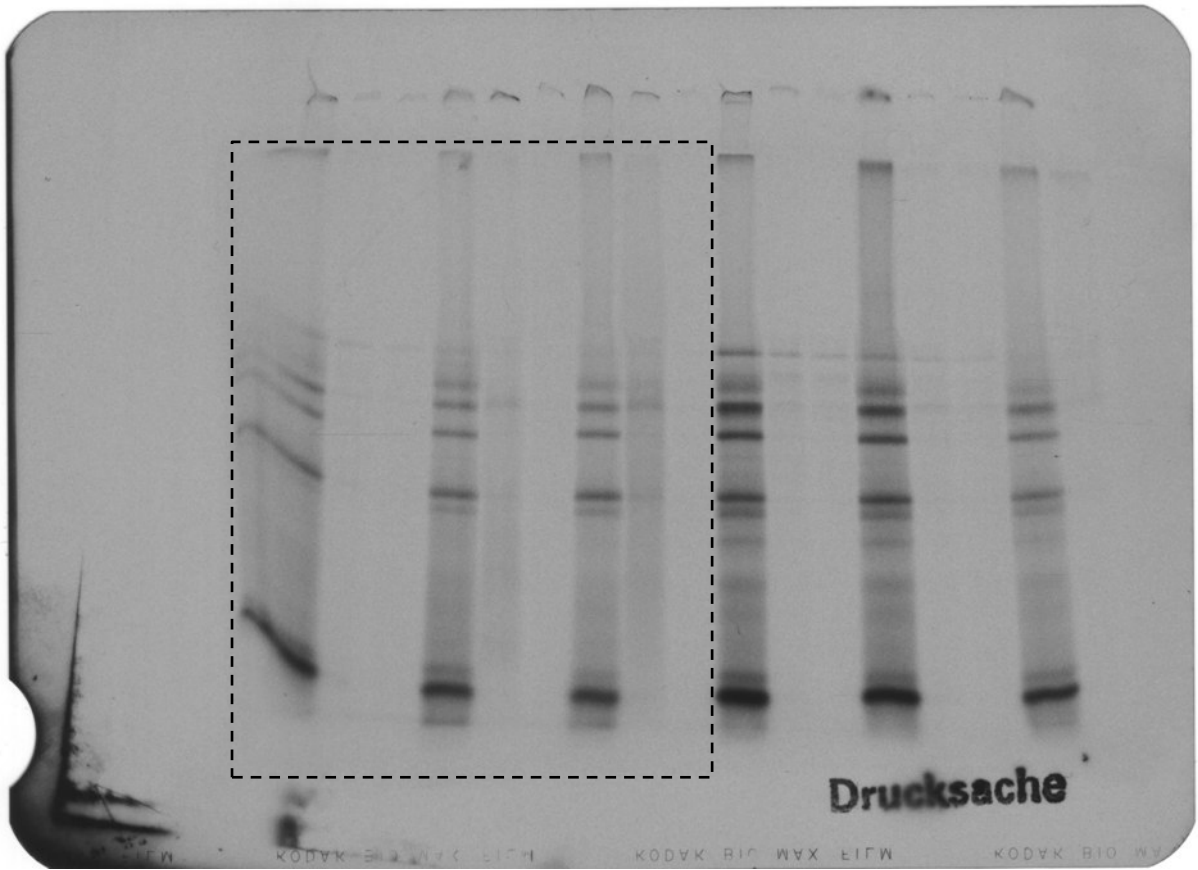
Supplementary Fig. 15. Full phosphoimaging scans from Supplementary Fig. XX. Cropped areas are indicated.
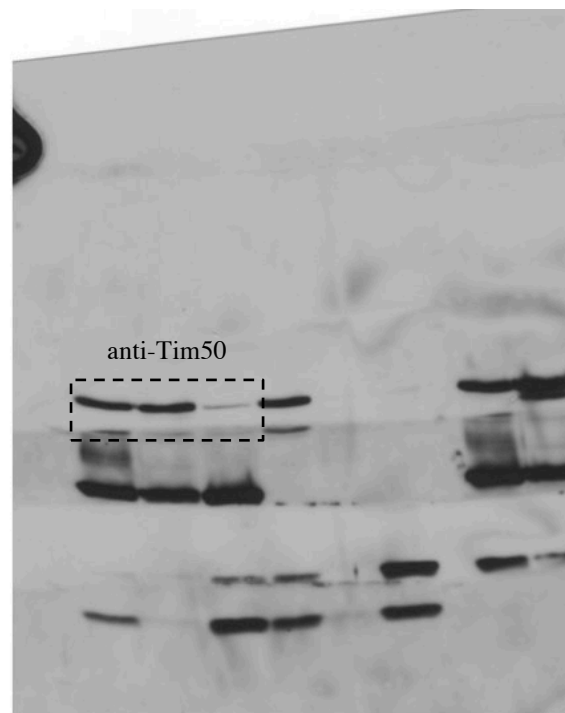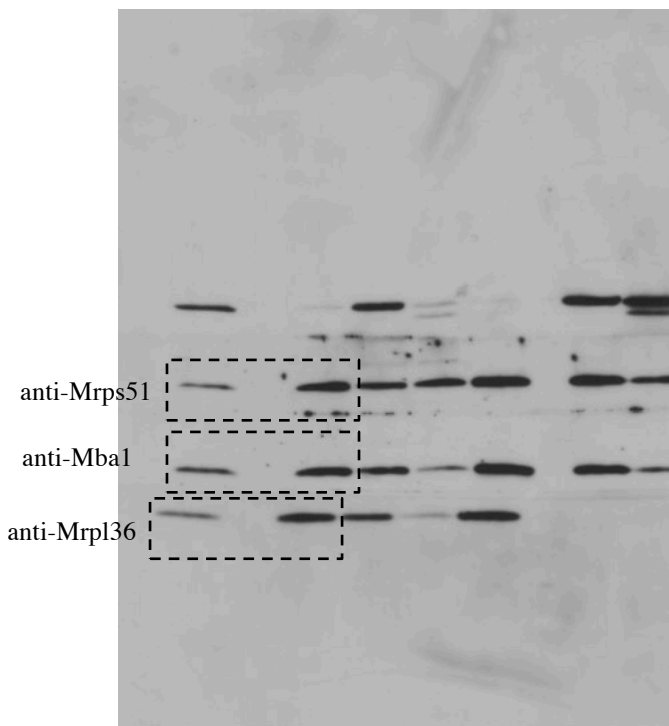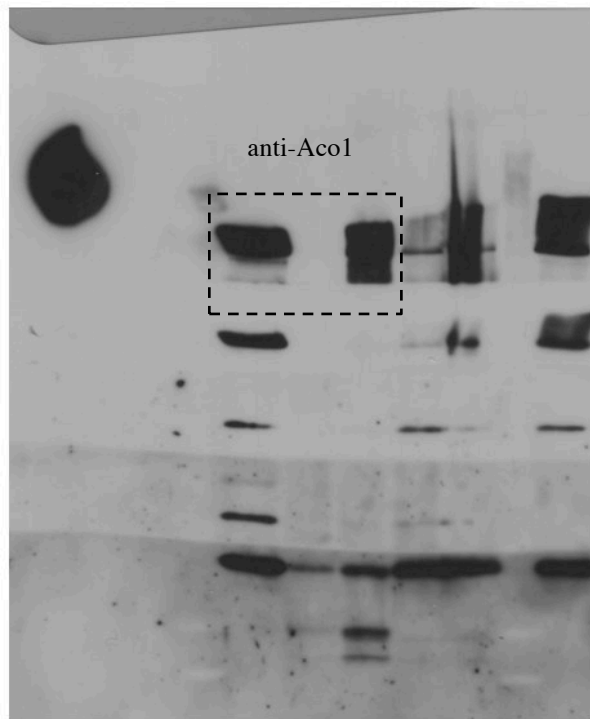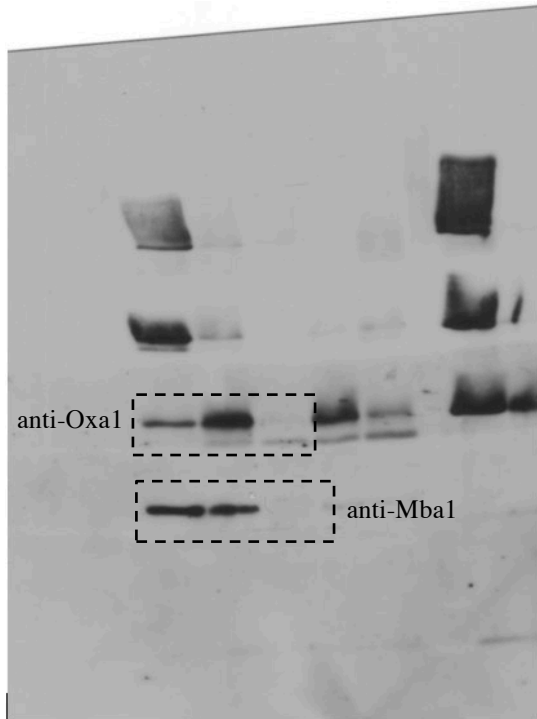
Supplementary Fig. 16. Full western blot scans from Supplementary Fig. XX. Cropped areas are indicated.
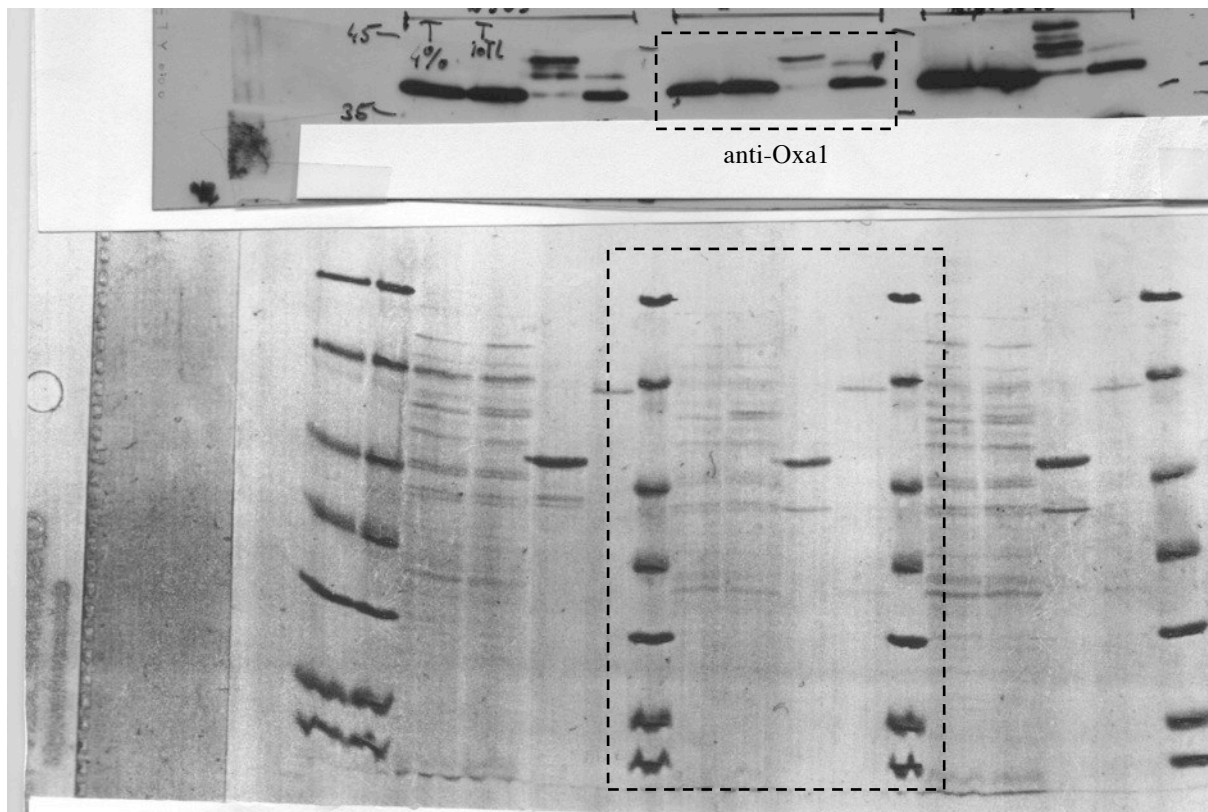
Supplementary Fig. 17. Full western blot and Ponceau S scans from Supplementary Fig. XX. Cropped areas are indicated.

Supplementary Table S1. Antibody working dilutions.

Antibody	Dilution
Aco1	1:2000
Mba1	1:500
Mrp51	1:10000
Mrpl20	1:500
Mrpl36	1:1000
Mrpl40	1:1000
Oxa1	1:1000
Tim50	1:1000

1   Ott, M. *et al.* Mba1, a membrane-associated ribosome receptor in mitochondria. *EMBO J.* **25**, 1603-1610, doi:10.1038/sj.emboj.7601070 (2006).

3 Discussion and Perspectives

3.1 Structure of the mammalian ER protein translocon

The first major achievement of my PhD work was to shed light on the structure and architecture of the native mammalian ER protein translocon. To date essentially all structural information available on this complex machinery in its membrane-embedded form results from my PhD studies. Using CET and subtomogram processing to analyze canine rough ER vesicles, we initially described the overall structure of the ER membrane-associated ribosome, obtaining structural insights into membrane attachment of ribosomes via several previously unknown contact sites, the molecular architecture of the ER translocon, and polyribosome formation on the ER membrane (section 2.1). Combining this set of methodologies with siRNA mediated gene silencing to manipulate the translocon composition in human cells, we could later identify Sec61, TRAP and OST in the native translocon and describe the spatial organization of these three major translocon constituents in unprecedented detail (section 2.2). Using latest direct electron detector technology and automated batch data acquisition, we were finally able to refine our structure to subnanometer resolution and determine the conformation of Sec61 in the native translocon at a defined functional state. The fundamental differences between the conformations of solubilized and native Sec61 suggest that peptide translocation and membrane protein insertion involve much smaller conformational changes of Sec61 than previously believed (section 2.3).

3.1.1 Detailed structural dissection of the core translocon

For molecular interpretation of our translocon structures, assignment of the four, respectively seven subunits of the TRAP and OST complexes is pivotal. In order to localize single subunits in the overall densities for TRAP and OST, several approaches are conceivable. One approach aims at genetic manipulation of cell lines to either deplete single TRAP/OST subunits or fuse a tag detectable by CET and subtomogram analysis. While depletion of

TRAPβ or Ribophorin 1 and Ribophorin 2 led to a concomitant "down regulation" of all other TRAP/OST subunits (Fig. 2.2.1, Fig. 2.2.2), it is conceivable that depletion of other complex subunits leaves the remaining sub-complexes intact and bound to the translocon. This would allow assignment of the depleted subunits to density missing in the subtomogram averages from depleted cells. Fusing suitable tags to the N- or C-termini of specific subunits would also reveal their positions in the subtomogram average. These tags must be sufficiently large or electron dense to be recognizable in difference maps of subtomogram averages. Maltose binding protein (42.5 kDa) or the gold nanoclusters assembled on Metallothionein could be explored as potential clonable tags.

A second approach for localizing single subunits in the overall densities for TRAP and OST relies on docking of atomic models into our subtomogram average of the ER-associated ribosome at subnanometer resolution (Fig. 2.3.1). Although computational analysis reveals that the folds of most lumenal segments of OST and TRAP subunits can be predicted, models accurate enough for unambiguous positioning cannot be generated, because the template structures are evolutionary too distant (sequence similarity < 20%). Thus, the availability of atomic structures with higher sequence similarity to the mammalian TRAP or OST subunits in the future is essential for a detailed molecular interpretation of our subtomogram average. Primary targets for crystallization efforts could be the lumenal segments of Ribophorin 1, Ribophorin 2, Ost48, TRAPα, TRAPβ and TRAPδ, with a focus on those fragments that are predicted to adopt a well-defined and crystallographically accessible fold.

Once several subunits of TRAP and OST have been located in our translocon structures, a third approach based on a combination of cross-linking and mass spectrometry (XL/MS) could prove very useful. XL/MS has emerged as a powerful method to obtain information on physical proximities of specific peptides, which are very valuable if they describe the

interaction of two subunits in a complex [99]. Thus, this method provides reliable distance restraints that can be used to place remaining subunits of TRAP and OST into the framework of our translocon structures. For XL/MS, purification of the complex of interest is typically beneficial, because the search space for crosslinked peptides during computational processing of the MS data increases significantly with increasing sample complexity. Thus, XL/MS experiments should be preferably performed rather with RAMP fractions that contain purified ribosomes bound to the detergent-solubilized ER translocon [100] than intact rough ER vesicles.

Eventually, the obtained structural information can be computationally combined to determine the most likely positioning of subunits in the framework of our translocon structures [101]. Localization data derived from depletion or tagging of subunits and docking of atomic models restrict the absolute positioning of subunits, while the inter-protein interactions from XL/MS constitute distance restraints on the involved subunits.

3.1.2   Exploring the compositional landscape of the translocon

Co-translational translocation or membrane protein insertion via the ER translocon requires concerted action of various associated cofactors and enzymes. Many of the involved modules are thought to associate transiently or in a substrate-specific manner to the core translocon, giving rise to a manifold of translocon types [102]. Our structural studies on ER-derived microsomes from canine pancreatic and HeLa cells have characterized OST as one of these substoichiometric components (Fig. S2.2.2), which is present in only 35-70% of translocon complexes. Analysis of translocon particles from whole Mouse Embryonic Fibroblast (MEF) cells showed a similar OST abundance as in microsomal preparations (Fig. 3.1), indicating that the OST distribution observed in microsomes is indeed physiological. A systematic screening of OST abundance in translocon complexes translocating stalling substrates with different chain lengths could elucidate whether OST associates transiently with the translocon during specific translocation phases or whether different stable translocon types co-exist.
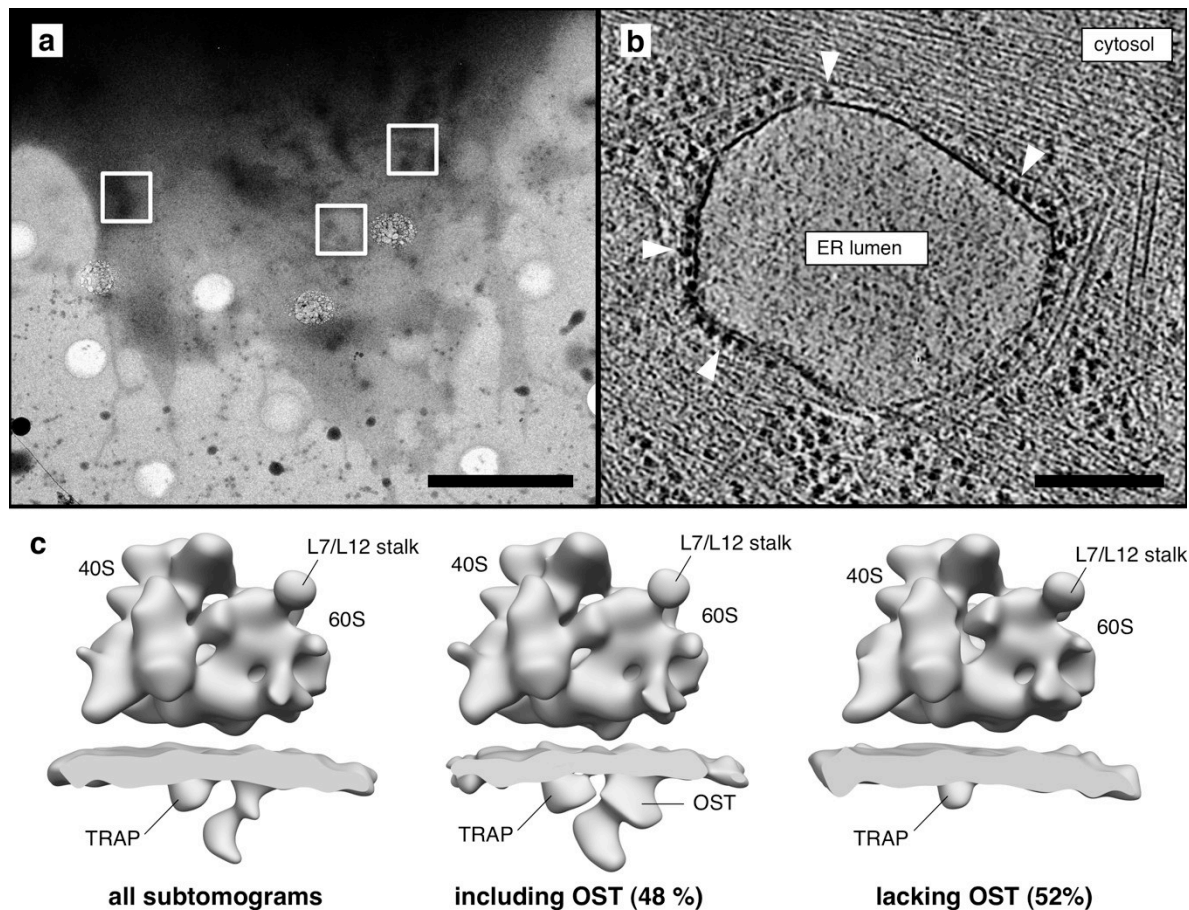
Fig. 3.1: Two distinct, ribosome-bound translocon populations are present in intact murine cells. a, Low-magnified projection of the periphery of a MEF cell, that was grown on a carbon-coated gold grid and vitrified in liquid ethane. White frames indicate tomogram positions. In vicinity to the tomogram positions, areas for automated focusing and tracking during tomogram acquisition can be identified by beam damage ("bubbling" of the carbon film). Scale bar corresponds to 5 μm. **b,** Representative tomogram of rough ER in the cell periphery. Membrane-bound ribosomes (arrowheads), cytosolic ribosomes and a dense network of cytoskeletal filaments can be observed. Scale bar corresponds to 200 nm. **c,** From left to right: subtomogram averages of the unclassified dataset (528 particles), the OST-containing translocon (254 particles) and the OST-free translocon (274 particles). All structures were filtered to a resolution of 45 Å.

In a first attempt to locate the position of additional substoichiometric or transiently associated translocon components, we used our established siRNA based gene silencing approach to manipulate translocon composition in HeLa cells and silenced subunits of the signal peptidase complex (Fig. S2.2.6), the SRP receptor, the Sec62/Sec63 complex or the

138

Hsp40 co-chaperone ERj1. Although western blotting indicated nearly quantitative depletion of the target proteins, comparison of translocon structures from wild type and knockdown samples did not yield significant density differences. As all silenced translocon components possess substantial (> 30 kDa) lumenal or cytosolic segments, the absence of a significant density difference suggests that they are significantly underrepresented in the average translocon from the beginning as expected. To compensate for this substoichiometry, the components of interest could be enriched on the translocon by over-expressing a specific substrate fused to a stalling peptide or by mechanistic stalling of the recruitment and translocation process at certain stages. Another approach could rely on acquiring massive amounts of data and extensive classification to obtain a good coverage of translocon types, essentially defining all long-lived states.

3.2   Organization of the mitochondrial translation machinery

The second achievement of my PhD work was to shed light on the still not well-understood mitochondrial translation system. Our study using CET could provide detailed insights into the supramolecular organization of the mitochondrial translation machinery and its association with the inner membrane in intact mitochondria (section 2.4). It revealed that yeast mitoribosomes are predominantly located in immediate proximity of the inner mitochondrial membrane and bind via two distinct contact sites, formed by a long rRNA expansion segments and the inner membrane protein Mba1. Results demonstrate, that concomitant with the remodeling of the mitoribosomal polypeptide exit tunnel, the mode of membrane association has been radically reshaped during evolution.

In our subtomogram average of the membrane-bound mitoribosome from yeast, a ribosome-associated density is resolved close to the mRNA exit site on the small subunit (Fig. S2.4.4). It coincides with the expected path of mRNA in mitochondrial polyribosomes and has not

been observed for bacterial or eukaryotic cytosolic (poly) ribosomes. Thus, it is conceivable, that this ribosome-associated density corresponds to an mRNA-binding complex specific for mitochondria. In mitochondria, a number of specific mRNA helicases and mRNA-binding translational activators are known to be required for efficient translation [103] and are thus genuine candidates. Isolation and mass spectrometric analysis of mitochondrial polyribosomes could narrow down the number of candidate proteins. Since yeast mitoribosomes are very delicate and disassemble easily upon isolation, polysome preparation and analysis should be performed using organisms with more stable mitoribosomes, potentially *Neurospora crassa* or *Euglena gracilis*, for which preparation of mitochondrial polyribosomes has already been reported [104]. Once promising candidates have been identified, the effects of depletion or tagging experiments on the ribosome-associated density can be assessed via CET and subtomogram analysis to confirm or refute its identity.

Finding an organism with a more stable mitochondrial translation machinery also could provide an opportunity to obtain a subtomogram average at higher resolution and thus might lead to a more detailed understanding of how nascent peptides are transferred towards the membrane insertion machinery. Using intact mitochondria, resolution is restricted by sample thickness and the very dense mitochondrial matrix. Thus, isolation of mitoribosomes bound to the membrane insertion machinery, preferably in form of inverted vesicles of the inner mitochondrial membrane, would be a prerequisite for further studies. Protocols for isolation of inverted inner membrane vesicles are available [105], but the sonication steps included in the protocols demand for a very stable association between the mitoribosome and the inner membrane. Once appropriate preparations are available, a subtomogram average at subnanometer resolution can now routinely be obtained with the streamlined acquisition and processing pipeline established in the lab for ribosome-associated complexes during my PhD work.

In our subtomogram average, the mitoribosome is tethered to the inner mitochondrial membrane by two distinct contact sites formed by a long rRNA expansion segment and the inner membrane protein Mba1. These two contact sites align the mitoribosomal peptide exit tunnel with a high-density feature within the well-resolved membrane bilayer (Fig. 2.4.8). It is conceivable that this membrane-embedded density corresponds to the Oxa1 insertase, which receives nascent peptides from the mitoribosome for integration into the inner membrane. Due to the weak intrinsic signal of membrane integral proteins in low-resolution cryo-EM densities, a simple deletion of Oxa1 did not yield sufficient difference signal for reliable confirmation of its position. Thus, tagging of Oxa1 with an electron dense or very big label would be required for specific detection. Tagging of Oxa1, however, is very challenging in general: the N-terminus is bearing the mitochondrial targeting signal and thus cannot be modified; the C-terminal portion of Oxa1 is crucial for its interaction with the mitoribosome and, hence, any bulky C-terminal tag would be unsuitable here.
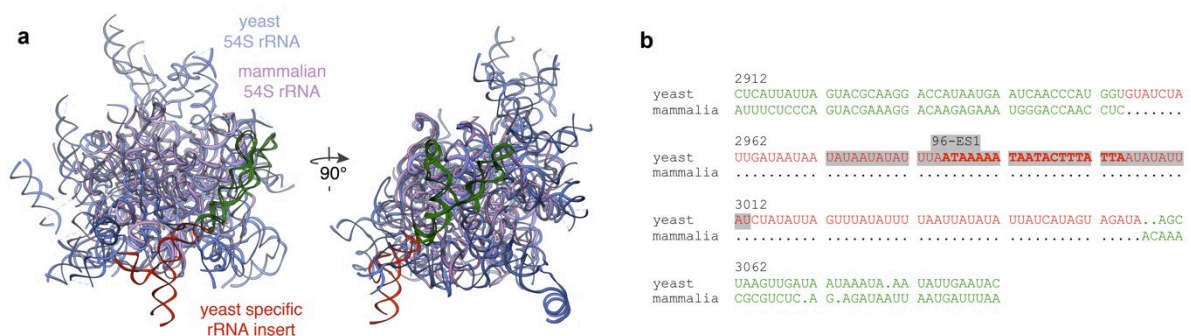
Fig. 3.2. Mammalian mitoribosomes lack yeast mitochondrial rRNA 96-ES1. a, Atomic models of the mammalian (purple, PDB 4CE4-A) and yeast (blue, PDB 1VW3-A) large subunit rRNA were aligned to each other. A yeast-specific rRNA insert (red) as well as flanking regions in the yeast and mammalian rRNA (green) are depicted. b, Alignment of yeast and mammalian rRNA around a yeast specific insert (red letters) comprising 96-ES1, based on the structural alignment of (a). Residues of 96-ES1 not included in the atomic model of yeast rRNA are depicted in bold letters. Flanking regions are depicted in green.

Structure based sequence alignment of the yeast and mammalian mitochondrial rRNA reveals that the rRNA insert containing 96-ES1 in yeast is not present in mammalian mitochondrial rRNA (Fig. 3.2), suggesting that membrane tethering in mammalian and yeast mitochondria is different. Thus, it would be desirable to obtain a subtomogram average for the mammalian membrane-bound mitoribosome and compare their modes of membrane-association. Since intact mammalian mitochondria are typically too thick and dense for CET, sample preparation by FIB milling would be a prerequisite for such an analysis.

4   Conclusions

This work makes a substantial contribution to our understanding of the structure and architecture of macromolecular machineries involved in co-translational protein transport and membrane insertion at the ER and the inner mitochondrial membrane of eukaryotic cells. Our structure of the native ER protein translocon represents a solid basis for follow-up studies of both, structural and biochemical nature aiming at a detailed mechanistic understanding of protein transport, membrane insertion and maturation facilitated cooperatively by Sec61 and accessory translocon components. The study of isolated yeast mitochondria in this thesis significantly advanced our understanding of the supramolecular organization of the mitochondrial translation system and its association with the inner mitochondrial membrane. It complements the rapidly growing compendium of high-resolution structures available for the mitoribosome by facilitating their molecular interpretation in an organellar context. Finally, this work demonstrates the limitations of analyzing membrane protein complexes in an isolated, detergent-extracted form and advocates studying their structure in a native membrane environment and in context of their native interaction partners.

Abbreviations

3D	three-dimensional
ATP	adenosine triphosphate
CCD	charge coupled device
CCF	cross correlation function
CET	cryo electron tomography
CPCA	constrained principal-component analysis
CTF	contrast transfer function
eEF	eukaryotic elongation factor
EM	electron microscopy
EMDB	electron microscopy data bank
ER	endoplasmic reticulum
ES	expansion segment
FIB	focused ion beam
FCR	Fourier cross resolution
FSC	Fourier shell correlation
GDP	guanosine diphosphate
GTP	guanosine triphosphate
Hsp	heat shock protein
LD	lumenal density
MA	membrane anchor
MEF	mouse embryonic fibroblast
mRNA	messenger RNA
MS	mass spectrometry
OST	oligosaccharyl-transferase

PDB   protein data bank

PET   polypeptide exit tunnel

RAMP   ribosome-associated membrane proteins

rER   rough endoplasmic reticulum

RM   rough microsomes

RNA   ribonucleic acid

RNC   ribosome nascent chain

rRNA   ribosomal RNA

siRNA   small interfering RNA

SPA   single particle analysis

SRP   signal recognition particle

SPC   signal peptidase complex

TEM   transmission electron microscopy

TM/TMH   transmembrane helix

TRAM   translocon associated membrane protein

TRAP   translocon associated protein complex

tRNA   transfer RNA

WT   wild type

XL   cross-linking

Bibliography

1   Pfeffer, S. *et al*. Structure and 3D Arrangement of Endoplasmic Reticulum Membrane-Associated Ribosomes. *Structure* **20**, 1508-1518 (2012).

2   Pfeffer, S. *et al*. Structure of the mammalian oligosaccharyl-transferase complex in the native ER protein translocon. *Nat Commun* **5**, 3072 (2014).

3   Pfeffer, S., Woellhaf, M. W., Herrmann, J. M. & Forster, F. Organization of the mitochondrial translation machinery studied in situ by cryoelectron tomography. *Nat Commun* **6**, 6019 (2015).

4   Steitz, T. A. A structural understanding of the dynamic ribosome machine. *Nature reviews. Molecular cell biology* **9**, 242-253 (2008).

5   Pestova, T. V. *et al*. Molecular mechanisms of translation initiation in eukaryotes. *Proc. Natl. Acad. Sci. USA* **98**, 7029-7036 (2001).

6   Voorhees, R. M., Fernandez, I. S., Scheres, S. H. & Hegde, R. S. Structure of the mammalian ribosome-Sec61 complex to 3.4 A resolution. *Cell* **157**, 1632-1643 (2014).

7   Rodnina, M. V. & Wintermeyer, W. Recent mechanistic insights into eukaryotic ribosomes. *Curr Opin Cell Biol* **21**, 435-443 (2009).

8   Loh, P. G. & Song, H. Structural and mechanistic insights into translation termination. *Curr. Opin. Struct. Biol.* **20**, 98-103 (2010).

9   Dana, A. & Tuller, T. Properties and determinants of codon decoding time distributions. *BMC Genomics* **15**, S13 (2014).

10   Staehelin, T., Brinton, C. C., Wettstein, F. O. & Noll, H. Structure and Function of E. Coli Ergosomes. *Nature* **199**, 865-870 (1963).

11   Lee, S. Y., Krsmanovic, V. & Brawerman, G. Attachment of ribosomes to membranes during polysome formation in mouse sarcoma 180 cells. *J Cell Biol* **49**, 683-691 (1971).

12   Warner, J. R., Knopf, P. M. & Rich, A. A multiple ribosomal structure in protein synthesis. *Proc. Natl. Acad. Sci. USA* **49**, 122-129 (1963).

13   Blobel, G. *et al*. Translocation of proteins across membranes: the signal hypothesis and beyond. *Symp Soc Exp Biol* **33**, 9-36 (1979).

14   Corsi, A. K. & Schekman, R. Mechanism of polypeptide translocation into the endoplasmic reticulum. *J Biol Chem* **271**, 30299-30302 (1996).

15   Halic, M. *et al*. Following the signal sequence from ribosomal tunnel exit to signal recognition particle. *Nature* **444**, 507-511 (2006).

16   Shen, K., Arslan, S., Akopian, D., Ha, T. & Shan, S. O. Activated GTPase movement on an RNA scaffold drives co-translational protein targeting. *Nature* **492**, 271-275 (2012).

17   Jagannathan, S., Reid, D. W., Cox, A. H. & Nicchitta, C. V. De novo translation initiation on membrane-bound ribosomes as a mechanism for localization of cytosolic protein mRNAs to the endoplasmic reticulum. *Rna* **20**, 1489-1498 (2014).

18   Van den Berg, B. *et al*. X-ray structure of a protein-conducting channel. *Nature* **427**, 36-44 (2004).

19   Egea, P. F. & Stroud, R. M. Lateral opening of a translocon upon entry of protein suggests the mechanism of insertion into membranes. *Proc. Natl. Acad. Sci. USA* **107**, 17182-17187 (2010).

20   Becker, T. *et al*. Structure of monomeric yeast and mammalian Sec61 complexes interacting with the translating ribosome. *Science* **326**, 1369-1373 (2009).

21   Gogala, M. *et al*. Structures of the Sec61 complex engaged in nascent peptide translocation or membrane insertion. *Nature* **506**, 107-110 (2014).

22   Dejgaard, K. *et al*. Organization of the Sec61 translocon, studied by high resolution native electrophoresis. *J. Proteome Res*. **9**, 1763-1771 (2010).

23   Shibatani, T., David, L. L., McCormack, A. L., Frueh, K. & Skach, W. R. Proteomic analysis of mammalian oligosaccharyltransferase reveals multiple subcomplexes that contain Sec61, TRAP, and two potential new subunits. *Biochemistry* **44**, 5982-5992 (2005).

24   Wang, L. & Dobberstein, B. Oligomeric complexes involved in translocation of proteins across the membrane of the endoplasmic reticulum. *FEBS lett*. **457**, 316-322 (1999).

25   Evans, E. A., Gilmore, R. & Blobel, G. Purification of microsomal signal peptidase as a complex. *Proc. Natl. Acad. Sci. USA* **83**, 581-585 (1986).

26   Mohorko, E., Glockshuber, R. & Aebi, M. Oligosaccharyltransferase: the central enzyme of N-linked protein glycosylation. *Journal of inherited metabolic disease* **34**, 869-878 (2011).

27   Kelleher, D. J. & Gilmore, R. An evolving view of the eukaryotic oligosaccharyltransferase. *Glycobiology* **16**, 47R-62R (2006).

28   Chavan, M. & Lennarz, W. The molecular basis of coupling of translocation and N-glycosylation. *Trends Biochem. Sci*. **31**, 17-20 (2006).

29   Mohorko, E. *et al*. Structural basis of substrate specificity of human oligosaccharyl transferase subunit N33/Tusc3 and its role in regulating protein N-glycosylation. *Structure* **22**, 590-601 (2014).

30   Crimaudo, C., Hortsch, M., Gausepohl, H. & Meyer, D. I. Human ribophorins I and II: the primary structure and membrane topology of two highly conserved rough endoplasmic reticulum-specific glycoproteins. *EMBO J*. **6**, 75-82 (1987).

31   Sauri, A., McCormick, P. J., Johnson, A. E. & Mingarro, I. Sec61alpha and TRAM are sequentially adjacent to a nascent viral membrane protein during its ER integration. *J. Mol. Biol*. **366**, 366-374 (2007).

32   Sommer, N., Junne, T., Kalies, K. U., Spiess, M. & Hartmann, E. TRAP assists membrane protein topogenesis at the mammalian ER membrane. *Biochim Biophys Acta* **1833**, 3104-3111 (2013).

33   Lang, S. *et al*. Different effects of Sec61alpha, Sec62 and Sec63 depletion on transport of polypeptides into the endoplasmic reticulum of mammalian cells. *J. Cell Sci*. **125**, 1958-1969 (2012).

34   Tyedmers, J., Lerner, M., Wiedmann, M., Volkmer, J. & Zimmermann, R. Polypeptide-binding proteins mediate completion of co-translational protein translocation into the mammalian endoplasmic reticulum. *EMBO reports* **4**, 505-510 (2003).

35   Neupert, W. A mitochondrial odyssey. *Annu. Rev. Biochem*. **81**, 1-33 (2012).

36   Daley, D. O. & Whelan, J. Why genes persist in organelle genomes. *Genome biology* **6**, 110 (2005).

37   Amunts, A. *et al*. Structure of the yeast mitochondrial large ribosomal subunit. *Science* **343**, 1485-1489 (2014).

38   Greber, B. J. *et al*. Architecture of the large subunit of the mammalian mitochondrial ribosome. *Nature* **505**, 515-519 (2014).

39   Brown, A. *et al*. Structure of the large ribosomal subunit from human mitochondria. *Science* **346**, 718-722 (2014).

40   Greber, B. J. *et al*. The complete structure of the large subunit of the mammalian mitochondrial ribosome. *Nature* **515**, 283-286 (2014).

41   He, S. & Fox, T. D. Membrane translocation of mitochondrially coded Cox2p: distinct requirements for export of N and C termini and dependence on the conserved protein Oxa1p. *Mol. Biol. Cell* **8**, 1449-1460 (1997).

42   Hell, K., Herrmann, J., Pratje, E., Neupert, W. & Stuart, R. A. Oxa1p mediates the export of the N- and C-termini of pCoxII from the mitochondrial matrix to the intermembrane space. *FEBS lett*. **418**, 367-370 (1997).

43   Hell, K., Neupert, W. & Stuart, R. A. Oxa1p acts as a general membrane insertion machinery for proteins encoded by mitochondrial DNA. *EMBO J*. **20**, 1281-1288 (2001).

44   Bonnefoy, N., Chalvet, F., Hamel, P., Slonimski, P. P. & Dujardin, G. OXA1, a Saccharomyces cerevisiae nuclear gene whose sequence is conserved from prokaryotes to eukaryotes controls cytochrome oxidase biogenesis. *J. Mol. Biol*. **239**, 201-212 (1994).

45   Kumazaki, K. *et al*. Crystal structure of Escherichia coli YidC, a membrane protein chaperone and insertase. *Sci Rep* **4**, 7299 (2014).

46   Wickles, S. *et al*. A structural model of the active ribosome-bound membrane protein insertase YidC. *Elife* **3**, e03035 (2014).

47   Kumazaki, K. *et al*. Structural basis of Sec-independent membrane protein insertion by YidC. *Nature* **509**, 516-520 (2014).

48   Preuss, M. *et al*. Mba1, a novel component of the mitochondrial protein export machinery of the yeast Saccharomyces cerevisiae. *J Cell Biol* **153**, 1085-1096 (2001).

49   Ott, M. *et al*. Mba1, a membrane-associated ribosome receptor in mitochondria. *EMBO J*. **25**, 1603-1610 (2006).

50   Bauerschmitt, H. *et al*. Ribosome-binding proteins Mdm38 and Mba1 display overlapping functions for regulation of mitochondrial translation. *Mol. Biol. Cell* **21**, 1937-1944 (2010).

51   Agrawal, R. K. & Sharma, M. R. Structural aspects of mitochondrial translational apparatus. *Curr. Opin. Struct. Biol*. **22**, 797-803 (2012).

52   Lucic, V., Rigort, A. & Baumeister, W. Cryo-electron tomography: the challenge of doing structural biology in situ. *J Cell Biol* **202**, 407-419 (2013).

53   Brandt, F. *et al*. The native 3D organization of bacterial polysomes. *Cell* **136**, 261-271 (2009).

54   Afonina, Z. A., Myasnikov, A. G., Shirokov, V. A., Klaholz, B. P. & Spirin, A. S. Conformation transitions of eukaryotic polyribosomes during multi-round translation. *Nucleic acids research* **43**, 618-628 (2015).

55   Mrazek, J. *et al*. Polyribosomes are molecular 3D nanoprinters that orchestrate the assembly of vault particles. *ACS Nano* **8**, 11552-11559 (2014).

56   Afonina, Z. A., Myasnikov, A. G., Shirokov, V. A., Klaholz, B. P. & Spirin, A. S. Formation of circular polyribosomes on eukaryotic mRNA without cap-structure and poly(A)-tail: a cryo electron tomography study. *Nucleic acids research* **42**, 9461-9469 (2014).

57   Myasnikov, A. G. *et al*. The molecular structure of the left-handed supra-molecular helix of eukaryotic polyribosomes. *Nat Commun* **5**, 5294 (2014).

58   Davies, K. M. *et al*. Visualization of ATP synthase dimers in mitochondria by electron cryo-tomography. *J Vis Exp*, 51228 (2014).

59   Daum, B., Walter, A., Horst, A., Osiewacz, H. D. & Kuhlbrandt, W. Age-dependent dissociation of ATP synthase dimers and loss of inner-membrane cristae in mitochondria. *Proc. Natl. Acad. Sci. USA* **110**, 15301-15306 (2013).

60   Strauss, M., Hofhaus, G., Schroder, R. R. & Kuhlbrandt, W. Dimer ribbons of ATP synthase shape the inner mitochondrial membrane. *EMBO J*. **27**, 1154-1160 (2008).

61   Davies, K. M. *et al*. Macromolecular organization of ATP synthase and complex I in whole mitochondria. *Proc. Natl. Acad. Sci. USA* **108**, 14121-14126 (2011).

62   Gold, V. A. *et al*. Visualizing active membrane protein complexes by electron cryotomography. *Nat Commun* **5**, 4129 (2014).

63   Nicastro, D., Frangakis, A. S., Typke, D. & Baumeister, W. Cryo-electron tomography of neurospora mitochondria. *J. Struct. Biol.* **129**, 48-56 (2000).

64   Beck, M. *et al*. Nuclear pore complex structure and dynamics revealed by cryoelectron tomography. *Science* **306**, 1387-1390 (2004).

65   Brandt, F., Carlson, L. A., Hartl, F. U., Baumeister, W. & Grunewald, K. The three-dimensional organization of polyribosomes in intact human cells. *Mol. Cell* **39**, 560-569 (2010).

66   Ortiz, J. O. *et al*. Structure of hibernating ribosomes studied by cryoelectron tomography in vitro and in situ. *J Cell Biol* **190**, 613-621 (2010).

67   Ortiz, J. O., Forster, F., Kurner, J., Linaroudis, A. A. & Baumeister, W. Mapping 70S ribosomes in intact cells by cryoelectron tomography and pattern recognition. *J. Struct. Biol.* **156**, 334-341 (2006).

68   Koning, R. I. Cryo-electron tomography of cellular microtubules. *Methods Cell Biol.* **97**, 455-473 (2010).

69   Engel, B. D. *et al*. Native architecture of the Chlamydomonas chloroplast revealed by in situ cryo-electron tomography. *Elife* **4** (2015).

70   Rigort, A. *et al*. Focused ion beam micromachining of eukaryotic cells for cryoelectron tomography. *Proc. Natl. Acad. Sci. USA* **109**, 4449-4454 (2012).

71   Rigort, A. *et al*. Micromachining tools and correlative approaches for cellular cryo-electron tomography. *J. Struct. Biol.* **172**, 169-179 (2010).

72   Villa, E., Schaffer, M., Plitzko, J. M. & Baumeister, W. Opening windows into the cell: focused-ion-beam milling for cryo-electron tomography. *Curr. Opin. Struct. Biol.* **23**, 771-777 (2013).

73   Bui, K. H. *et al*. Integrated structural analysis of the human nuclear pore complex scaffold. *Cell* **155**, 1233-1243 (2013).

74   Lin, J., Okada, K., Raytchev, M., Smith, M. C. & Nicastro, D. Structural mechanism of the dynein power stroke. *Nat. Cell. Biol.* **16**, 479-485 (2014).

75   Carbajal-Gonzalez, B. I. *et al*. Conserved structural motifs in the central pair complex of eukaryotic flagella. *Cytoskeleton (Hoboken)* **70**, 101-120 (2013).

76   Barber, C. F., Heuser, T., Carbajal-Gonzalez, B. I., Botchkarev, V. V., Jr. & Nicastro, D. Three-dimensional structure of the radial spokes reveals heterogeneity and interactions with dyneins in Chlamydomonas flagella. *Mol. Biol. Cell* **23**, 111-120 (2012).

77   Li, X. *et al*. Electron counting and beam-induced motion correction enable near-atomic-resolution single-particle cryo-EM. *Nat Methods* **10**, 584-590 (2013).

78   Chen, Y., Pfeffer, S., Hrabe, T., Schuller, J. M. & Forster, F. Fast and Accurate Reference-Free Alignment of Subtomograms. *J. Struct. Biol.* (2013).

79   Hrabe, T. *et al*. PyTom: a python-based toolbox for localization of macromolecules in cryo-electron tomograms and subtomogram analysis. *J. Struct. Biol.* **178**, 177-188 (2012).

80   Bharat, T. A. *et al*. Cryo-electron microscopy of tubular arrays of HIV-1 Gag resolves structures essential for immature virus assembly. *Proc. Natl. Acad. Sci. USA* **111**, 8233-8238 (2014).

81   Schur, F. K., Hagen, W. J., de Marco, A. & Briggs, J. A. Determination of protein structure at 8.5A resolution using cryo-electron tomography and sub-tomogram averaging. *J. Struct. Biol.* **184**, 394-400 (2013).

82   Schur, F. K. *et al*. Structure of the immature HIV-1 capsid in intact virus particles at 8.8 A resolution. *Nature* (2014).

83   Lawrence, M. C. in *Electron tomography*   (ed J. Frank) 197-204 (Plenum Press, New York, 1992).

84   Gilbert, P. F. The reconstruction of a three-dimensional structure from projections and its application to electron microscopy. II. Direct methods. *Proc R Soc Lond B Biol Sci* **182**, 89-102 (1972).

85   Harauz, G. & Heel, M. v. Exact Filters for General Geometry 3-Dimensional Reconstruction. *Optik* **73**, 146-156 (1986).

86   Koster, A. J. *et al*. Perspectives of molecular and cellular electron tomography. *J. Struct. Biol.* **120**, 276-308 (1997).

87   Carragher, B. *et al*. Leginon: an automated system for acquisition of images from vitreous ice specimens. *J. Struct. Biol.* **132**, 33-45 (2000).

88   Mastronarde, D. N. Automated electron microscope tomography using robust prediction of specimen movements. *J. Struct. Biol.* **152**, 36-51 (2005).

89   Zheng, S. Q. *et al*. UCSF tomography: an integrated software suite for real-time electron microscopic tomographic data collection, alignment, and reconstruction. *J. Struct. Biol.* **157**, 138-147 (2007).

90   Forster, F., Han, B. G. & Beck, M. Visual proteomics. *Methods Enzymol.* **483**, 215-243 (2010).

91   Walz, J. *et al*. Electron Tomography of Single Ice-Embedded Macromolecules: Three-Dimensional Alignment and Classification. *J. Struct. Biol.* **120**, 387-395 (1997).

92   Forster, F., Medalia, O., Zauberman, N., Baumeister, W. & Fass, D. Retrovirus envelope protein complex structure in situ studied by cryo-electron tomography. *Proc. Natl. Acad. Sci. USA* **102**, 4729-4734 (2005).

93   Grigorieff, N. Resolution measurement in structures derived from single particles. *Acta Crystallogr. D Biol. Crystallogr.* **56**, 1270-1277 (2000).

94   Scheres, S. H. RELION: implementation of a Bayesian approach to cryo-EM structure determination. *J. Struct. Biol.* **180**, 519-530 (2012).

95   Bartesaghi, A. *et al*. Classification and 3D averaging with missing wedge correction in biological electron tomography. *J. Struct. Biol.* **162**, 436-450 (2008).

96   Forster, F., Pruggnaller, S., Seybert, A. & Frangakis, A. S. Classification of cryo-electron sub-tomograms using constrained correlation. *J. Struct. Biol.* **161**, 276-286 (2008).

97   Fernandez, J. J., Li, S. & Crowther, R. A. CTF determination and correction in electron cryotomography. *Ultramicroscopy* **106**, 587-596 (2006).

98   Zanetti, G., Riches, J. D., Fuller, S. D. & Briggs, J. A. Contrast transfer function correction applied to cryo-electron tomography and sub-tomogram averaging. *J. Struct. Biol.* **168**, 305-312 (2009).

99   Leitner, A. *et al*. Probing native protein structures by chemical cross-linking, mass spectrometry and bioinformatics. *Mol Cell Proteomics* **9**, 1634-1649 (2010).

100   Potter, M. D. & Nicchitta, C. V. Endoplasmic reticulum-bound ribosomes reside in stable association with the translocon following termination of protein synthesis. *J Biol Chem* **277**, 23314-23320 (2002).

101   Lasker, K. *et al*. Molecular architecture of the 26S proteasome holocomplex determined by an integrative approach. *Proc. Natl. Acad. Sci. USA* **109**, 1380-1387 (2012).

102   Schnell, D. J. & Hebert, D. N. Protein translocons: multifunctional mediators of protein translocation across membranes. *Cell* **112**, 491-505 (2003).

103   Herrmann, J. M., Woellhaf, M. W. & Bonnefoy, N. Control of protein synthesis in yeast mitochondria: the concept of translational activators. *Biochim Biophys Acta* **1833**, 286-294 (2013).

104   Avadhani, N. G. & Buetow, D. E. Isolation of active polyribosomes from the cytoplasm, mitochondria and chloroplasts of Euglena gracilis. *The Biochemical journal* **128**, 353-365 (1972).

105   Ono, H., Yoshida, T. & Tuboi, S. Transport of prepro-albumin into inverted vesicles prepared from the inner membrane of rat liver mitochondria. *FEBS lett*. **318**, 273-276 (1993).

Wöllhaf from the Technical University Kaiserslautern for great collaboration, many fruitful

discussions and a constant supply of high-quality samples for electron microscopy.